

Effect of Pressurization and Expulsion of Entrapped Air in Pipelines

A Thesis

Presented to

The Academic Faculty

By

Nahm Ho Lee

In Partial Fulfillment

of the Requirements for the Degree

Doctor of Philosophy in the

School of Civil and Environmental Engineering

Georgia Institute of Technology

August 2005

EFFECT OF  
PRESSURIZATION AND EXPULSION OF  
ENTRAPPED AIR IN PIPELINES

Approved by:

Dr. C. SAMUEL MARTIN, Advisor  
School of Civil and Environmental  
Engineering  
*Georgia Institute of Technology*

Dr. TERRY W. STURM  
School of Civil and Environmental  
Engineering  
*Georgia Institute of Technology*

Dr. PHILIP ROBERT  
School of Civil and Environmental  
Engineering  
*Georgia Institute of Technology*

Dr. DAVID. C. WIGGERT  
School of Mechanical Engineering  
*Michigan State University*

DR. FREDERICK. J. MOODY  
Consulting Engineer

Date Approved: July 15, 2005

Dedicated To

My Parents

My lovely wife Choon Hee

My little wonderful boy Michael

## ACKNOWLEDGMENTS

Thanks to God. He gave me extraordinary strength and patience to complete this work.

I would like to thank my advisor, Dr. C. S. Martin, who has given me useful advice and encouragement to overcome the difficulties. He has been a advisor and teacher of my life. Thanks the members of my committee for patient reading. I would like to thank Andy Udell for all his help in constructing experimental set up.

I also would like to express my thanks to my family members, wife, Choon Hee Kim, parents in Korea and brother Dal Ho.

## TABLE OF CONTENTS

ACKNOWLEDGMENTS	iv
LIST OF TABLES	viii
LIST OF FIGURES	ix
NOMENCLATURE	xvi
SUMMARY	xviii
CHAPTER 1 INTRODUCTION	1
1.1 Locations of Air	1
1.2 Entrapped Air	1
1.3 Air Venting or Expulsion	2
CHAPTER 2 LITERATURE REVIEW	3
2.1 Methods of Analysis	3
2.2 Historical Review	3
2.3 Objective of Study	8
CHAPTER 3 BASIC THEORY	10
3.1 Introduction	10
3.2 Governing Equations of Mass, Momentum, and Energy	11
3.2.1 Confined System	11
3.2.1.1 Lumped Liquid and Lumped Gas Mass (Cases I and II)	11
3.2.1.2 Elastic Liquid and Lumped Gas Mass (Case III)	18
3.2.1.3 Elastic Liquid and Acoustic Gas Mass (Case IV)	22
3.3 Dimensional Analysis	26
3.3.1 Lumped Liquid and Gas Mass (Cases I and II)	29
3.3.1.1 Variable Liquid Length (Case I)	29
3.3.1.2 Constant Liquid Length (Case II)	31
3.3.2 Acoustic Liquid and Gas Mass (Case III)	32

3.3.3	Acoustic Liquid and Acoustic Gas Mass (Case IV)	33
3.4	Comparison of Different Analytical Models	33
3.4.1	Effect of Wave Action In Liquid and Gas Phases (Case IV)	34
3.4.2	Effect of Thermodynamic Process	37
3.4.3	Effect of Liquid Length in Rigid Column Analysis (Cases I and II)	38
3.5	Gas Venting System	45
3.6	Heat Transfer	46
3.7	Frequency Analysis	47
<b>CHAPTER 4</b>	<b>EXPERIMENTAL APPARATUS &amp; INSTRUMENTATION</b>	<b>50</b>
4.1	Description of Test Facility	50
4.2	Description of Instrumentation	52
4.2.1	Data Acquisition System	52
4.2.2	Turbine Flow Meter	54
4.2.3	Ball Valve	55
4.2.4	Rotary Variable Differential Transformer (RVDT)	55
4.3	Hydraulic Characteristics of System Components	56
4.3.1	Hydraulic Characteristics of Straight Pipe	57
4.3.2	Head-Loss Characteristics of Ball Valve	57
4.3.3	Head-Loss Characteristics of Flow Meter and Entire Piping System	57
4.4	Pressure Transducers	60
4.5	Orifice Flow Characteristics	61
<b>CHAPTER 5</b>	<b>EXPERIMENTAL RESULTS</b>	<b>65</b>
5.1	Confined System of Entrapped Air	65
5.1.1	Experimental Procedure	67

5.1.2	Entrapped Air Experimental Results	68
5.1.3	Maximum Entrapped Air Pressures	73
5.1.4	Frequency of Oscillation	73
5.2	Air Venting System	78
5.2.1	Maximum Venting Pressures	85
CHAPTER 6 COMPARISON BETWEEN ANALYTICAL AND EXPERIMENTAL RESULTS		88
6.1	Confined System	88
6.1.1	Maximum Pressure	89
6.1.2	Thermal Damping and Frequency	92
6.2	Air Venting System	95
CHAPTER 7 CONCLUSION AND RECOMMENDATIONS		99
APPENDIX A ENTRAPPED AIR EXPERIMENTAL RESULTS		101
APPENDIX B AIR VENTING EXPERIMENTAL RESULTS		109
APPENDIX C ENTRAPPED AIR ANALYSIS		121
APPENDIX D AIR VENTING ANALYSIS		127
REFERENCES		144
VITA		149

## LIST OF TABLES

Table 2-1	Methods of Analysis	3
Table 4.1	Summary of Experimental Configuration with Dead End (Entrapped Air)	53
Table 4.2	Summary of Experimental Configurations with Orifice (Venting)	53
Table 5.1	Period of Oscillation of Entrapped Gas Tests and Small Amplitude Theory	76

## LIST OF FIGURES

Figure 3.1	Control Volume of Pipe with Entrapped Gas	11
Figure 3.2	Initial Acceleration ( $H/b = 40$ ; $B/b = 30$ )	15
Figure 3.3	Definition Sketch in x-t Plane with Fixed Grid and Interfacial Path Line	20
Figure 3.4	Portion of Grid Employed for Elastic Liquid and Acoustic Gas Analysis	25
Figure 3.5	Results for Three Models (Cases I, III and IV)	35
Figure 3.6	Effect of Varying Acoustic Velocity of Liquid (Cases I and III)	35
Figure 3.7	Comparison of Various Analytical Models (Cases I, II, III, and IV)	38
Figure 3.8	Comparison of Inelastic Liquid Column Models (Cases I and II)	43
Figure 3.9	Entrapped Air Solution for Inelastic Liquid Column (Cases I and II)	44
Figure 3.10	Thermal Damping Effect on Variable Length Rigid Column Modeling	48
Figure 3.11	Thermal Damping Effect on Lumped Mass Stiffness (Air Spring Effect)	49
Figure 4.1	Schematic of Test Facility for Entrapped Air Experiments with Dead End	51
Figure 4.2	Schematic of Test Facility for Air Venting Experiments with Orifice	51
Figure 4.3	Schematic of Data Acquisition System	54
Figure 4.4	Calibration of Turbine Flow Meter	55
Figure 4.5	Characteristics of Rotary Variable Differential Transducer (RVDT)	56
Figure 4.6	Measured Darcy Friction Factor for Plexiglass Pipe	58
Figure 4.7	Measured Head Loss Characteristics of Ball Valve	59
Figure 4.8	Pipe System Head Loss Characteristics	59

Figure 4.9	Calibration of Pressure Transducers with Dead Weight Tester	60
Figure 4.10	Free Jet Orifice Characteristics	62
Figure 4.11	Submerged Jet Orifice Characteristics	63
Figure 4.12	Variation of Orifice Discharge Coefficient with Size and Reynolds Number	64
Figure 5.1	Schematic of Entrapped Transient Air Phases	66
Figure 5.2	Typical Variation of Ball Valve Angle $\theta$ During Opening	68
Figure 5.3	Entrapped Air Pressure Time Histories for $L_A = 16.23$ ft ( $\alpha_0 = 0.4481$ )	70
Figure 5.4	Entrapped Air Pressure Time Histories for $L_A = 4.85$ ft ( $\alpha_0 = 0.1952$ )	71
Figure 5.5	Entrapped Air Pressure Time Histories for $L_A = 1.23$ ft ( $\alpha_0 = 0.0580$ )	72
Figure 5.6	Entrapped Air Pressure Time Histories with Air Space Partially Filled with Water for $L_A = 10.1$ ft ( $\alpha_0 = 0.1980$ )	74
Figure 5.7	Correlation of Maximum Pressure with Pressure Ratio and Air Column Length	75
Figure 5.8	Determination of Measured Period of Oscillation for $P_R = 5$	75
Figure 5.9	Correlation of Measured Period of Oscillation with Theoretical	77
Figure 5.10	Schematic of Air Venting Transient Phases	79
Figure 5.11	Pressure and Velocity Time Histories for Air Venting ( $P_R = 2$ ; $d = 0$ )	82
Figure 5.12	Pressure and Velocity Time Histories for Air Venting ( $P_R = 2$ ; $d = 1/16$ Inch)	82
Figure 5.13	Pressure and Velocity Time Histories for Air Venting ( $P_R = 2$ ; $d = 3/16$ Inch)	83
Figure 5.14	Pressure and Velocity Time Histories for Air Venting ( $P_R = 2$ ; $d = 1/4$ Inch)	83

Figure 5.15	Pressure and Velocity Time Histories for Air Venting ( $P_R = 2$ ; $d = 3/8$ Inch)	84
Figure 5.16	Pressure and Velocity Time Histories for Air Venting ( $P_R = 2$ ; $d = 1/2$ Inch)	84
Figure 5.17	Maximum Pressure at Orifice (PT3) for $\alpha_0 = 0.4481$	85
Figure 5.18	Maximum Pressure at Orifice (PT3) for $\alpha_0 = 0.3357$	86
Figure 5.19	Maximum Pressure at Orifice (PT3) for $\alpha_0 = 0.1952$	86
Figure 5.20	Maximum Pressure at Orifice (PT3) for $\alpha_0 = 0.1217$	87
Figure 5.21	Maximum Pressure at Orifice (PT3) for $\alpha_0 = 0.0580$	87
Figure 6.1	Entrapped Air Analysis for $L_A = 16.23$ ft ( $\alpha_0 = 0.4481$ ) ; $P_R = 2$	90
Figure 6.2	Entrapped Air Analysis for $L_A = 16.23$ ft ( $\alpha_0 = 0.4481$ ) ; $P_R = 4$	90
Figure 6.3	Entrapped Air Analysis for $L_A = 16.23$ ft ( $\alpha_0 = 0.4481$ ) ; $P_R = 6$	90
Figure 6.4	Entrapped Air Analysis for $L_A = 10.1$ ft ( $\alpha_0 = 0.3357$ ) ; $P_R = 2$	91
Figure 6.5	Entrapped Air Analysis for $L_A = 10.1$ ft ( $\alpha_0 = 0.3357$ ) ; $P_R = 4$	91
Figure 6.6	Entrapped Air Analysis for $L_A = 10.1$ ft ( $\alpha_0 = 0.3357$ ) ; $P_R = 6$	91
Figure 6.7	Analytical and Experimental Entrapped Air Results for Various Air Lengths $L_A$ and Tank Pressures $P_R$	92
Figure 6.8	Effect of Thermal Damping on Entrapped Air for $L_A = 16.23$ ft	93
Figure 6.9	Effect of Thermal Damping on Entrapped Air Frequency for $L_A = 16.23$ ft	94
Figure 6.10	Venting Analysis for $\alpha_0 = 0.4481$ ; $P_R = 3$ ; and $d = 1/16$ Inch	96
Figure 6.11	Venting Analysis for $\alpha_0 = 0.4481$ ; $P_R = 3$ ; and $d = 1/8$ Inch	96
Figure 6.12	Venting Analysis for $\alpha_0 = 0.4481$ ; $P_R = 3$ ; and $d = 1/4$ Inch	97
Figure A.1	Entrapped Air Pressure Time Histories for $L_A = 16.23$ ft ( $\alpha_0 = 0.4481$ )	102

Figure A.2	Entrapped Air Pressure Time Histories for $L_A = 10.1$ ft ( $\alpha_0 = 0.3357$ )	103
Figure A.3	Entrapped Air Pressure Time Histories for $L_A = 4.85$ ft ( $\alpha_0 = 0.1952$ )	104
Figure A.4	Entrapped Air Pressure Time Histories for $L_A = 2.77$ ft ( $\alpha_0 = 0.1217$ )	105
Figure A.5	Entrapped Air Pressure Time Histories for $L_A = 1.23$ ft ( $\alpha_0 = 0.0580$ )	106
Figure A.6	Entrapped Air Pressure Time Histories with Air Space Partially Filled with Water for $L_A = 16.23$ ft ( $\alpha_0 = 0.2558$ )	107
Figure A.7	Entrapped Air Pressure Time Histories with Air Space Partially Filled with Water for $L_A = 10.1$ ft ( $\alpha_0 = 0.1980$ )	108
Figure B.1	Pressure and Velocity Time Histories for Air Venting ( $P_R = 2$ ; $d = 0$ )	110
Figure B.2	Pressure and Velocity Time Histories for Air Venting ( $P_R = 2$ ; $d = 1/16$ Inch)	110
Figure B.3	Pressure and Velocity Time Histories for Air Venting ( $P_R = 2$ ; $d = 1/8$ Inch)	111
Figure B.4	Pressure and Velocity Time Histories for Air Venting ( $P_R = 2$ ; $d = 3/16$ Inch)	111
Figure B.5	Pressure and Velocity Time Histories for Air Venting ( $P_R = 2$ ; $d = 1/4$ Inch)	112
Figure B.6	Pressure and Velocity Time Histories for Air Venting ( $P_R = 2$ ; $d = 5/16$ Inch)	112
Figure B.7	Pressure and Velocity Time Histories for Air Venting ( $P_R = 2$ ; $d = 3/8$ Inch)	113
Figure B.8	Pressure and Velocity Time Histories for Air Venting ( $P_R = 2$ ; $d = 7/16$ Inch)	113
Figure B.9	Pressure and Velocity Time Histories for Air Venting ( $P_R = 2$ ; $d = 1/2$ Inch)	114
Figure B.10	Pressure and Velocity Time Histories for Air Venting ( $P_R = 3$ ; $d = 0$ )	114

Figure B.11	Pressure and Velocity Time Histories for Air Venting ( $P_R = 3$ ; $d = 1/16$ Inch)	115
Figure B.12	Pressure and Velocity Time Histories for Air Venting ( $P_R = 3$ ; $d = 1/8$ Inch)	115
Figure B.13	Pressure and Velocity Time Histories for Air Venting ( $P_R = 3$ ; $d = 3/16$ Inch)	116
Figure B.14	Pressure and Velocity Time Histories for Air Venting ( $P_R = 3$ ; $d = 1/4$ Inch)	116
Figure B.15	Pressure and Velocity Time Histories for Air Venting ( $P_R = 3$ ; $d = 5/16$ Inch)	117
Figure B.16	Pressure and Velocity Time Histories for Air Venting ( $P_R = 3$ ; $d = 3/8$ Inch)	117
Figure B.17	Pressure and Velocity Time Histories for Air Venting ( $P_R = 3$ ; $d = 7/16$ Inch)	118
Figure B.18	Pressure and Velocity Time Histories for Air Venting ( $P_R = 3$ ; $d = 1/2$ Inch)	118
Figure B.19	Pressure and Velocity Transients for Air Venting ( $P_R = 4$ ; $d = 1/16, 1/8$ Inch)	119
Figure B.20	Pressure and Velocity Transients for Air Venting ( $P_R = 4$ ; $d = 3/16, 1/4$ Inch)	119
Figure B.21	Pressure and Velocity Transients for Air Venting ( $P_R = 4$ ; $d = 5/16, 3/8$ Inch)	120
Figure B.22	Pressure and Velocity Transients for Air Venting ( $P_R = 4$ ; $d = 7/16, 1/2$ Inch)	120
Figure C.1	Entrapped Air Analysis for $L_A = 16.23$ ft ( $\alpha_0 = 0.4481$ ) ; $P_R = 2$	122
Figure C.2	Entrapped Air Analysis for $L_A = 16.23$ ft ( $\alpha_0 = 0.4481$ ) ; $P_R = 4$	122
Figure C.3	Entrapped Air Analysis for $L_A = 16.23$ ft ( $\alpha_0 = 0.4481$ ) ; $P_R = 6$	122
Figure C.4	Entrapped Air Analysis for $L_A = 10.1$ ft ( $\alpha_0 = 0.3357$ ) ; $P_R = 2$	123

Figure C.5	Entrapped Air Analysis for $L_A = 10.1$ ft ( $\alpha_0 = 0.3357$ ) ; $P_R = 4$	123
Figure C.6	Entrapped Air Analysis for $L_A = 10.1$ ft ( $\alpha_0 = 0.3357$ ) ; $P_R = 6$	123
Figure C.7	Entrapped Air Analysis for $L_A = 4.85$ ft ( $\alpha_0 = 0.1952$ ) ; $P_R = 2$	124
Figure C.8	Entrapped Air Analysis for $L_A = 4.85$ ft ( $\alpha_0 = 0.1952$ ) ; $P_R = 4$	124
Figure C.9	Entrapped Air Analysis for $L_A = 4.85$ ft ( $\alpha_0 = 0.1952$ ) ; $P_R = 6$	124
Figure C.10	Entrapped Air Analysis for $L_A = 2.77$ ft ( $\alpha_0 = 0.1212$ ) ; $P_R = 2$	125
Figure C.11	Entrapped Air Analysis for $L_A = 2.77$ ft ( $\alpha_0 = 0.1212$ ) ; $P_R = 4$	125
Figure C.12	Entrapped Air Analysis for $L_A = 2.77$ ft ( $\alpha_0 = 0.1212$ ) ; $P_R = 6$	125
Figure C.13	Entrapped Air Analysis for $L_A = 1.23$ ft ( $\alpha_0 = 0.0580$ ) ; $P_R = 2$	126
Figure C.14	Entrapped Air Analysis for $L_A = 1.23$ ft ( $\alpha_0 = 0.0580$ ) ; $P_R = 4$	126
Figure D.1	Venting Analysis for $L_A = 16.2$ ft ( $\alpha_0 = 0.4481$ ) ; $P_R = 2$ ; $d = 1/16$ Inch	128
Figure D.2.	Venting Analysis for $L_A = 16.2$ ft ( $\alpha_0 = 0.4481$ ) ; $P_R = 2$ ; $d = 1/8$ Inch	128
Figure D.3.	Venting Analysis for $L_A = 16.2$ ft ( $\alpha_0 = 0.4481$ ) ; $P_R = 2$ ; $d = 3/16$ Inch	129
Figure D.4.	Venting Analysis for $L_A = 16.2$ ft ( $\alpha_0 = 0.4481$ ) ; $P_R = 2$ ; $d = 1/4$ Inch	129
Figure D.5.	Venting Analysis for $L_A = 16.2$ ft ( $\alpha_0 = 0.4481$ ) ; $P_R = 3$ ; $d = 1/16$ Inch	130
Figure D.6.	Venting Analysis for $L_A = 16.2$ ft ( $\alpha_0 = 0.4481$ ) ; $P_R = 3$ ; $d = 1/8$ Inch	130
Figure D.7.	Venting Analysis for $L_A = 16.2$ ft ( $\alpha_0 = 0.4481$ ) ; $P_R = 3$ ; $d = 3/16$ Inch	131
Figure D.8.	Venting Analysis for $L_A = 16.2$ ft ( $\alpha_0 = 0.4481$ ) ; $P_R = 3$ ; $d = 1/4$ Inch	131
Figure D.9.	Venting Analysis for $L_A = 10.1$ ft ( $\alpha_0 = 0.3357$ ) ; $P_R = 2$ ; $d = 1/16$ Inch	132
Figure D.10.	Venting Analysis for $L_A = 10.1$ ft ( $\alpha_0 = 0.3357$ ) ; $P_R = 2$ ; $d = 1/8$ Inch	132
Figure D.11.	Venting Analysis for $L_A = 10.1$ ft ( $\alpha_0 = 0.3357$ ) ; $P_R = 2$ ; $d = 3/16$ Inch	133
Figure D.12.	Venting Analysis for $L_A = 10.1$ ft ( $\alpha_0 = 0.3357$ ) ; $P_R = 2$ ; $d = 1/4$ Inch	133

- Figure D.13. Venting Analysis for  $L_A = 10.1$  ft ( $\alpha_0 = 0.3357$ ) ;  $P_R = 3$  ;  $d = 1/16$  Inch 134
- Figure D.14. Venting Analysis for  $L_A = 10.1$  ft ( $\alpha_0 = 0.3357$ ) ;  $P_R = 3$  ;  $d = 1/8$  Inch 134
- Figure D.15. Venting Analysis for  $L_A = 10.1$  ft ( $\alpha_0 = 0.3357$ ) ;  $P_R = 3$  ;  $d = 3/16$  Inch 135
- Figure D.16. Venting Analysis for  $L_A = 10.1$  ft ( $\alpha_0 = 0.3357$ ) ;  $P_R = 3$  ;  $d = 1/4$  Inch 135
- Figure D.17 Venting Analysis for  $L_A = 4.85$  ft ( $\alpha_0 = 0.1952$ ) ;  $P_R = 2$  ;  $d = 1/16$  Inch 136
- Figure D.18 Venting Analysis for  $L_A = 4.85$  ft ( $\alpha_0 = 0.1952$ ) ;  $P_R = 2$  ;  $d = 1/8$  Inch 136
- Figure D.19 Venting Analysis for  $L_A = 4.85$  ft ( $\alpha_0 = 0.1952$ ) ;  $P_R = 2$  ;  $d = 3/16$  Inch 137
- Figure D.20 Venting Analysis for  $L_A = 4.85$  ft ( $\alpha_0 = 0.1952$ ) ;  $P_R = 2$  ;  $d = 1/4$  Inch 137
- Figure D.21 Venting Analysis for  $L_A = 4.85$  ft ( $\alpha_0 = 0.1952$ ) ;  $P_R = 3$  ;  $d = 1/16$  Inch 138
- Figure D.22 Venting Analysis for  $L_A = 4.85$  ft ( $\alpha_0 = 0.1952$ ) ;  $P_R = 3$  ;  $d = 1/8$  Inch 138
- Figure D.23 Venting Analysis for  $L_A = 4.85$  ft ( $\alpha_0 = 0.1952$ ) ;  $P_R = 3$  ;  $d = 3/16$  Inch 139
- Figure D.24 Venting Analysis for  $L_A = 4.85$  ft ( $\alpha_0 = 0.1952$ ) ;  $P_R = 3$  ;  $d = 1/4$  Inch 139
- Figure D.25 Venting Analysis for  $L_A = 2.77$  ft ( $\alpha_0 = 0.1217$ ) ;  $P_R = 2$  ;  $d = 1/16$  Inch 140
- Figure D.26 Venting Analysis for  $L_A = 2.77$  ft ( $\alpha_0 = 0.1217$ ) ;  $P_R = 2$  ;  $d = 1/8$  Inch 140
- Figure D.27 Venting Analysis for  $L_A = 2.77$  ft ( $\alpha_0 = 0.1217$ ) ;  $P_R = 2$  ;  $d = 3/16$  Inch 141
- Figure D.28 Venting Analysis for  $L_A = 2.77$  ft ( $\alpha_0 = 0.1217$ ) ;  $P_R = 2$  ;  $d = 1/4$  Inch 141
- Figure D.29 Venting Analysis for  $L_A = 2.77$  ft ( $\alpha_0 = 0.1217$ ) ;  $P_R = 3$  ;  $d = 1/16$  Inch 142
- Figure D.30 Venting Analysis for  $L_A = 2.77$  ft ( $\alpha_0 = 0.1217$ ) ;  $P_R = 3$  ;  $d = 1/8$  Inch 142
- Figure D.31 Venting Analysis for  $L_A = 2.77$  ft ( $\alpha_0 = 0.1217$ ) ;  $P_R = 3$  ;  $d = 3/16$  Inch 143
- Figure D.32 Venting Analysis for  $L_A = 2.77$  ft ( $\alpha_0 = 0.1217$ ) ;  $P_R = 3$  ;  $d = 1/4$  Inch 143

## NOMENCLATURE

A	Cross sectional area of pipe
$a_g$	Acoustic speed of gas
$a_l$	Acoustic speed of liquid
B	Reservoir tank diameter
b	Channel diameter of added mass analysis
$C_d$	Orifice discharge coefficient
$c_p$	Specific heat of gas at constant temperature
$c_v$	Specific heat of gas at constant pressure
D	Inside pipe diameter
d	Orifice diameter
f	Darcy-Weisbach resistance coefficient
H	Piezometric head
k	Isentropic exponent
$K_L$	Head-loss coefficient of element
$K_M$	Head-loss coefficient of flow meter element
$L_g$	Initial length of gas column
$L_l$	Initial length of liquid column
m	Gas mass
n	Polytropic index
p	Pressure
$p_0$	Initial pressure in gas space
$p_b$	Barometric pressure
$p_R$	Reservoir pressure
P	Pressure ratio

$P_M$	Pressure ratio $p_M/p_0$
$P_R$	Pressure ratio $p_R/p_0$
$t$	Time
$T$	Gas temperature
$T_0$	Initial gas temperature
$V$	Velocity of liquid or gaseous fluid (one-dimensional)
$V_\ell$	Liquid velocity
$V_r$	Relative velocity
$x$	Horizontal distance from liquid and gas interface
$Y$	Gas expansion factor
$z$	Elevation of liquid or pipe
$\lambda = fL_g/D$	Entrapped gas dimensionless parameter
$\nabla$	Gas Volume
$\nabla_0$	Initial Gas Volume
$\alpha$	Void fraction
$\alpha_0$	Initial void fraction
$\beta$	Parameter in added-mass analysis
$\theta$	Angle of ball valve
$\rho_g$	Gas density
$\rho_\ell$	Liquid density

## SUMMARY

Analytical and experimental laboratory studies were conducted for rapid pressurizing of entrapped gas at the end of a horizontal liquid pipeline. Analytical models were studied considering acoustic effect of both liquid and gas side. Closed form of solutions were derived for a lumped liquid and lumped gas model if pipeline is a horizontal. Experiments were conducted for a range of reservoir pressure from two times of ambient pressure to seven times with five different configurations. Comparison of analytical and experimental model results were presented. Analytical model predicted well first peak. Both results of experimental and analytical model shows that pressure can be increased or reduced depending on the liquid acceleration. Thermal damping effects were studied to account for a consequential damping mechanism and frequency shortening whereas pipe friction and minor loss do not change a frequency.

Laboratory investigations and analytical model development were performed for a gas venting system. Experiments were conducted for a range of orifice from closed end to one half size of pipe diameter with reservoir pressure two, three and four times of ambient pressure for five different configurations. Experimental results shows that significant pressure was caused through a critical range of the area ratio of orifice to pipe. Pressure surge at the orifice has following effects for small amount of entrapped gas and waterhammer, which was traced from laboratory pressure time history. Only the smallest orifices and orifices greater than a critical value reduce the pressure surge compared to closed system. Comparison of analytical model and experiments were presented.

# CHAPTER 1

## INTRODUCTION

### 1.1 Locations of Air

In pipelines gases can be present in the form of dissolved or entrained or both. As described by Martin (1976, 1993 and 1996), some sources of gases are :

- Incomplete removal of gas during the filling operation
- Action of an air vacuum breaker or check valve admitting air during low pressure transients
- Gradual evolution of gas from solution due to a pressure drop or temperature increase above saturation levels
- Air admitting vortex action at an intake or at the riser of a surge tank or air chamber
- Evolution of dissolved gas from solution
- Starting of pumps in partially empty pipelines
- Water wave impact in caves in coastal areas

### 1.2 Entrapped Air

Once gas is introduced into a liquid pipeline, liquid and gas flow simultaneously. The effect of gas release (evolution of dissolved gas) can be beneficial because the acoustic velocity can drop dramatically. Free gas (bubbly or slug flow) is often beneficial under depressurization transient or sudden deceleration but a sudden pressurization transient may be critical. Entrapped gas in large pockets; for example in slugs, can be beneficial under depressurization, but quite detrimental under pressurization or startup of pumps

Entrapped gas can cause unwanted higher transient pressures depending on the amount and location of gas. For example large amount of gas ,similar to an accumulator, yield inconsequential pressure maxima. Indeed, the effectiveness of accumulators depends

upon large amounts of gas. However, as demonstrated by Martin (1976) entrapped gas located in either a closed end or between two liquid columns can lead to higher pressure compared to the driving pressure because of the non-linear spring action of the gas. Free gas can be beneficial because the speed of sound drops dramatically for even small concentrations. Entrapped gas (slug flow) can be beneficial under depressurization, but quite detrimental under pressurization or startup of pumps.

### **1.3 Air Venting or Expulsion**

Venting of gas followed by liquid can cause serious waterhammer pressures due to expulsion of gas at orifices or valves followed by liquid slugs in piping subject to rapid filling . Venting systems such as a slightly opened valves, or small orifices, can lead to very serious pressure surges if the gas is trapped at the top of the opening. There can be a sudden deceleration by virtue of the usually large difference in fluid density (water/air  $\sim 800$ ). The pressure surge of a gas venting system is very sensitive to the size of opening. For very small open area the constriction can aid in reducing any entrapped air spring effect. For intermediate areas for which the air is expelled quite readily the liquid can attain a high velocity, resulting in impact as the liquid column strikes the constriction. As the open area is increased the velocity of the accelerating liquid column becomes higher, but impact may be minimal inasmuch as there would not be significant flow deceleration.

For intermediate areas for which the air is expelled quite readily the liquid can attain a high velocity, resulting in impact as the liquid column strikes the constriction. As the open area is increased the velocity of the accelerating liquid column becomes higher, but impact may be minimal inasmuch as there would not be significant flow deceleration

The research concerns the pressurizing gas pocket at the end of liquid line and venting through an orifice at its end.

## CHAPTER 2

### LITERATURE REVIEW

#### 2.1 Methods of Analysis

Entrapped gas is an important subject in the field of hydraulic transients. Analysis of this problems can be classified by various methods which may or may not consider elasticity of liquid as well as acoustic effects in gaseous phase. Some simple models disregard liquid elasticity by assuming only its inertia (rigid column approach). Regarding the gaseous phase most models represent the mass of air as elastic, but without acoustic effects. Table 2.1 has been prepared to refer to the various methods of analysis employed by researchers and in thesis.

Table 2-1 Methods of Analysis

Case	Elasticity	Liquid Length	Gas
I	Inelastic (Rigid Column)	Variable	Elastic Lumped Mass
II	Inelastic (Rigid Column)	Constant	Elastic Lumped Mass
III	Elastic	Variable	Elastic Lumped Mass
IV	Elastic	Variable	Elastic Acoustic

#### 2.2 Historical Review

Effect of entrapped gas can be either beneficial or detrimental. As an example of a beneficial effect, Safwat (1972) demonstrated that a small volume of air trapped at the top of the condenser in cooling water systems of thermal power plants could reduce pressure surges during transient conditions, mainly attributed to a reduction in the acoustic velocity of the air-water mixture. Another example, presented by Griffiths (1972), is that entrapped

air near a tank can serve as an advantage in cushioning a back surge in a long penstock tunnel of an hydroelectric scheme.

Entrapped gas cannot always be beneficial. In most cases, it causes a pressure surge during hydraulic transient or reduces the efficiency of steady operation because of additional head loss through the gas pocket, as described by Streeter and Wylie (1993).

Using analysis tools for Case II Martin (1976) showed that entrapped air located either in a closed end or between liquid columns could lead to higher peak pressures than those of a single liquid phase if the transient is applied rapidly. He provided a parametric study to predict maximum head caused by entrapped air in the pipeline under an instantaneous valve opening condition. He assumed that elastic effect of liquid and the variation of liquid length could be neglected in the case of pipelines containing air pockets separated by very long columns of liquid which was free of gas.

Ocasio (1976) conducted a careful set of experiments in which an air pocket was located between the dead end and a closed valve. He demonstrated that entrapped air, under conditions of instantaneous valve opening, could lead to unwanted high-pressure surges. He also demonstrated that as initial air volume increases, maximum pressure surge decreases. His experimental results showed that pipe inclination does not affect the history of the pressure surge for a relatively short pipeline. However, a horizontal pipeline yields higher peak pressure surges than does a vertical pipeline.

Agudelo (1988) studied entrapped air in a vertical pipeline. He considered variation of liquid length in the Case I model. His results showed that the significance of variable liquid length on maximum pressures is negligible if the ratio of air to liquid column length is less than 0.10. Maximum pressures are only significant when either relatively short pipeline or relatively large air volumes within the pipelines are involved. However, variable liquid length does affect the magnitude of the maximum velocity

Cabrera et al (1991,1992) studied validity range of Case II model comparing to the

results of Case I and II models. They also found that both Case I and II models have the same peak pressure values based on the numerical results if a simple pipeline system is horizontal. However, they did not prove explicitly why the maximum pressures were the same for both models in the case of frictional system even though they presented the closed solutions of model of Cases I and II in a frictionless system.

Guara et al (1996) investigated elastic effects comparing the results of Cases I and III. His results showed that as entrapped air volume decreases case I model provides more conservative maximum pressures than those of Case III model does.

Qui and Burrows (1996) demonstrated that entrapped air pocket can lead a serious pressure surge during a pump shutdown.

If vapor cavity forms in a pipeline, pressure surges can be more severe than those of air pocket if a sudden acceleration is applied to liquid-side. Nakagawa and Takenaka (1993 and 1994) researched a pressure surge involving cooling cavities in a pipeline. Cooling vapor cavities form after operation is stopped and liquid is enclosed if the surrounding temperature is lower than that of transporting liquid in a pipeline. Their results showed that maximum pressure surge was recorded 10.1 times greater than the impression pressure difference between reservoir and initial pressure in the cooling cavity. They observed high-damping waveforms of pressure history and period shortening.

Entrapped gas may cause self-ignition if pipelines carry a combustible liquid because combustible liquid piston compressing a trapped gas works identically to a compression-ignition engine, as described by Thorley and Main (1986). Thornton (1983) investigated an explosion in a process plant in which a pump started up with a combustible liquid. He demonstrated that 250 C° temperatures were recorded in the gas space before being quenched by the moving liquid and this was because of the presence of trapped gas. He had difficulty measuring temperature trace in gas space because a) a heavy incursion of liquid cooled the entire gas volume and cut off temperature trace before the peak and b) there was

a possible lag caused by the thermal capacity of the element. Later Thorley and Main (1986) researched same explosion study addressed by Thornton. They focused on theoretical model based on Case I model, lumped gas such as vapor cavities. They presented that extremely high pressure and temperatures can occur in a vapor cavity under transient conditions. They stated that "the rapid opening of a valve can easily produce explosive conditions in a trapped vapor cavity." Thorley and Spurrett (1990) presented that experimental measurements of peak pressures and temperature in pipeline cavities. Theoretical models both for Cases I, II and III were developed to compare with experimental results. Their results showed that Case III model predicted peak pressures quite well. Case I and II models gave conservative peak pressures.

Kitagawa (1979) studied optimal design of a nozzle in the air chamber located at the downstream to absorb pressure surges that caused by presence of trapped air or gases.

Gas venting system where trapped gas is located either at the end or between liquid columns can be beneficial or detrimental. Edwards and Farmer (1984) showed that trapped gas could develop higher jet velocity and remove oscillation under instantaneous valve opening conditions.

However, a gas-venting system as a means of reducing a pressure surge due to the presence of trapped gas needs very careful design and operation. Not many researchers have studied pressure surge following the collision of a liquid column with the gas venting system. Albertson and Andrews (1971) reported that the release of air at an air release valve by means of surge relief can cause dangerous transient pressures if abrupt flow deceleration happened at the air release valve. As Martin (1976) pointed out that "the discharge of a mixture of air and water out of an orifice can lead to significant pressure surges if the two-phase flow is in the slug flow regime." He presented a theoretical parametric curve to predict the reduced maximum pressure surge resulting from the effect of an orifice as a gas venting system.

Ocasio (1976) performed experimental measurements of pressure histories using different sizes of orifice. His experimental results demonstrated that if the ratio of orifice diameter to pipe diameter is between 0.10 and 0.20, then very high-pressure surges were observed at the time of mixture of liquid and gas hit an orifice. Agudelo (1988) conducted experimental work with a range of 1/16 inch to 3/8 inch orifice diameters in a 1.0088 inch diameter pipe. His experimental and theoretical results demonstrated that smallest orifice, a 1/16 inches, always-reduced pressure surge due to the pressure relieving effect of the orifice.

Hashimoto *et al* (1988) set up experiments similar to those of Ocasio and Agudelo. They considered a larger size of orifice diameter relative to pipe diameter,  $D_o/D$ , with a range from 0.40 to 0.86. Pressure surges in this range of diameter ratio are less than or close to pressure surges of confined systems. Their measurement showed that effective elastic speed was reduced to 500 m/s.

Norman and Sorenson (1996) performed experimental measurements of transient pressure at the valves and nozzles of a water column driven by piston in the combustion chamber. They demonstrated that the presence of an air cavity close to valves or nozzles can cause a very high-pressure surge development in the pipeline system.

Zhou, Hicks and Stefler (2002) studied a phenomenon in which the entire manhole structure was blown off the sewer line in the city of Edmonton, Canada 1995 due to a storm frequency of 300 years return-period. Surface flow drained into the sewer lines, causing the sewers downstream of the manhole to become overloaded. A reverse flow caused by the downstream pressure developed, instead of gravity flow that would under normal condition. The pressurized flow rapidly compressed the air pocket trapped upstream of a trunk sewer. The compressed air pocket force was enough to blow the manhole structures of sewer line.

Graze (1968 and 1972) studied thermodynamic air behavior in an air chamber. He proposed RHT (Rational Heat Transfer) process, which allows heat transfer during the

compression and expansion of the gas volume. His results showed that RHT process provided better results than did those of Cases I, II, and III models such as polytropic relation did. He reported that period of calculated by RHT process agreed well with experimental results. Graze (1996) also conducted experiments with entrapped air in an air chamber in order to investigate a heat transfer coefficient term in the RHT process. His experimental results showed that heat transfer coefficient varies continuously with transient conditions and value of averaged constant heat transfer coefficient is higher than steady state value of McAdam's equation, which value was used in the RHT process in the previous papers. Nakagawa and Takenaka (1994) studied thermodynamic behavior of vapor cavities in the pipeline. They reported that heat transfer term allows additional damping other than pipe friction or minor loss in the analytical model.

### **2.3 Objective of Study**

The object of this study is to analyze sudden pressurization of entrapped gas and venting or expulsion of gas through restrictions. The effect of both phenomena is evaluated by both analytical (numerical) methods and carefully designed experiments with a single straight pipe with upstream pressure source and a quick-opening valve. One-dimensional analysis is employed to consider wave action in both liquid and gas. Numerical models are developed for the Cases I, II, III, and IV. Closed solutions of Cases I and II are derived for frictional and frictionless system. Period shortening and large damping phenomena of the second and third peak pressures are investigated with corporations of heat transfer.

Carefully designed experiments were performed to calibrate the analysis as well as provide insight into the phenomena, especially with respect to two-phase flow regimes and the attendant thermodynamic processes. Experiments were conducted with a 10-m long straight pipe to investigate pressurization of entrapped gas and gas venting. A valve actuator was mounted to improve experimentally repeatable accuracy of instant valve opening time. For a range of initial gas volumes and driving pressures, the effects of entrapped gas were

ascertained by measurement of transient pressures with pressure transducers and transient flow with a rapid response turbine flow meter. The phenomenon associated with venting was investigated utilizing the same apparatus with orifices of various diameters located at the end of the test pipe. Careful measurement of transient gas pressure and liquid flow showed that effect of impact at the orifice is due to entrapped gas, waterhammer and two-phase flow. In the case of impact by entrapped gas, a modified entrapped gas model is utilized to simulate maximum pressure with experiment.

## CHAPTER 3

### BASIC THEORY

#### 3.1 Introduction

The focus of this research is to analyze the rise, from rest, of transient pressure and velocity due to the presence of a gas pocket at the start up of a liquid column. Entrapped gas in a confined system can be serious because of higher pressure rises than occur in a single phase system. The simple ideal case of a single system is considered in Figure 3.1. Entrapped gas is located between the valve and either the dead end of the confined system or the orifice of the gas venting system. The initial gas length  $L_g$  and the initial liquid length  $L_l$  are separated by a valve. The valve motion is assumed to be rapid. Initial pressure is the ambient atmosphere pressure,  $p_0$ . The reservoir pressure,  $p_R$  is assumed to be constant during the transient period.

One-dimensional analysis is employed to consider wave action in both liquid and gas. The acoustic effects of both liquid and gas are studied. Added mass effect is considered when water inside the reservoir accelerates due to rapid valve opening. Heat transfer through the wall is considered even though it does not effect peak pressure. However, it does relate to the frequency of pressure time history. Assumptions made in the mathematical formulation are explained as follows:

- Liquid and gas have a sharp vertical interface;
- The thermodynamic process can be isentropic, empirical polytropic, or heat transfer
- Liquid can be inelastic (rigid column) or elastic (acoustic)
- Gas is assumed to be either lumped mass or acoustic
- All analyses are base on 1-D (one-dimensional) theory

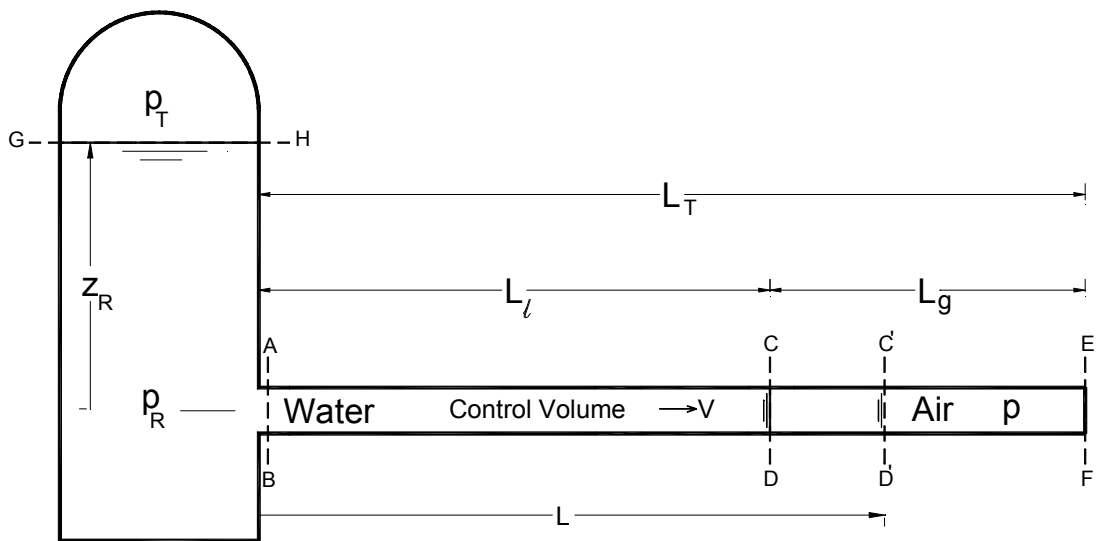


Figure 3.1 Control Volume of Pipe with Entrapped Gas

### 3.2 Governing Equations of Mass, Momentum, and Energy

#### 3.2.1 Confined System

##### 3.2.1.1 Lumped Liquid and Lumped Gas Mass (Cases I and II)

In this section, the governing one-dimensional equations of mass, momentum, and energy are derived employing Reynolds transport theorem, which is applied separately to the control volume of both the liquid and gas sides. The ball valve located at the section CD is assumed to be an interface of liquid and gas and is treated as a thin, vertical line. Firstly, the liquid side of the governing equations is derived. Reynolds transport theorem is applied to a moving control volume section ABCD of water in the pipeline, shown in Figure 3.1, Munson *et al* (1990). The control volume has a fixed surfaces at pipe section AB and the pipe walls, but at section CD (and C'D') the control surface is moving at velocity  $\vec{w}$ , which

is identical to the fluid velocity  $\vec{V}$ . For the control volume analysis the relative velocity is defined

$$\vec{V}_r = \vec{V} - \vec{w} \quad (3-1)$$

In terms of a fixed and moving control volume the mass conservation equation of liquid can be expressed as:

$$\frac{D}{Dt} \int_{\forall_s(t)} \rho_l dV = \frac{d}{dt} \int_{\forall(t)} \rho_l dV + \int_{A(t)} \rho_l \vec{V}_r \cdot \vec{n} dA \quad (3-2)$$

where  $\rho_l$  is the liquid (water) density,  $\forall_s(t)$  is the system volume and  $\forall(t)$  the control volume. Since the left hand side of the term is zero from the law of conservation mass for a non-reacting fluid, the equation becomes:

$$0 = \frac{d}{dt} \int_{\forall(t)} \rho_l dV + \sum_{CD} \rho_l (V - w) A - \sum_{AB} \rho_l (V - w) A \quad (3-3)$$

Relative velocity  $V_r$  at section CD is zero since  $V = w$  for the moving boundary condition. However, at section AB  $w = 0$ , while the fluid velocity is  $V$ . The fluid density for the lumped mass (rigid column) analysis can be eliminated inasmuch as  $\rho_l$  is a constant. If  $x$  is measured from entrance AB then the integral

$$\frac{d}{dt} \int_{\forall(t)} dV = \frac{d}{dt} \int_0^{L(t)} A dx = A \frac{dL}{dt} \quad (3-4)$$

Hence, the final form of the mass conservation equation is written as:

$$0 = A \frac{dL}{dt} - VA \quad (3-5)$$

Or

$$V = \frac{dL}{dt} \quad (3-6)$$

The momentum equation of the liquid phase with control volume ABCD is:

$$\frac{d}{dt} \int_{\forall_s(t)} \rho_l \vec{V} dV = \frac{d}{dt} \int_{\forall(t)} \rho_l \vec{V} dV + \int_{A(t)} \rho_l \vec{V} \vec{V}_r \cdot \vec{n} dA \quad (3-7)$$

Invoking Newton's second law for the system term on the left hand side, the one-dimensional x component becomes

$$\Sigma F = \frac{d}{dt} \int_{\forall(t)} \rho_l V dV + \sum_{CD} \rho_l V(V - w) A - \sum_{AB} \rho_l V(V - w) A \quad (3-8)$$

The pressure force over the liquid column is based on the difference between  $p_{AB}$  at the pipe entrance and the gas pressure  $p$ . In the opposite direction is the boundary shear stress  $\tau_0 PL$ . Hence the momentum equation becomes

$$(p_{AB} - p) A - \tau_0 \pi D L = \rho_l \frac{d}{dt} \int_{\forall(t)} V dV + \rho_l \sum_{CD} V(V - w) A - \rho_l \sum_{AB} V(V - w) A \quad (3-9)$$

The boundary shear stress is based upon the Darcy-Weisbach resistance coefficient  $f$ , defined as

$$\tau_0 = \frac{f \rho_l V |V|}{4} \quad (3-10)$$

where the absolute value is employed to allow shear reversal with flow reversal.

The unsteady momentum integral term has variable limits, necessitating the use of Leibnitz's rule. Moreover, the inertial effect in the reservoir is included as well utilizing theoretical results available from Sarpkaya (1962)

$$\frac{d}{dt} \int_{\forall(t)} V dV = \frac{d}{dt} \int_0^{L(t)} VA dx + \int_{Res} \frac{\partial V}{\partial t} A ds = A \left[ V \frac{dL}{dt} + \int_0^{L(t)} \frac{dV}{dt} dx \right] + \int_{Res} \frac{\partial V}{\partial t} A ds \quad (3-11)$$

Realizing that the two uniform flow terms become  $-\rho_l AV^2$  due to the contribution at section AB, and applying the mean-value theorem to the second term on the right hand side (RHS) of Equation (3-11), the x-momentum equation reduces to

$$(p_{AB} - p)A - \tau_0 \pi D L = \rho_l \int_{Res} \frac{\partial V}{\partial t} A ds + \rho_l V^2 A - \rho_l V^2 A + \rho_l L \frac{dV}{dt} \quad (3-12)$$

The first term on the RHS can be estimated by theoretical analysis by Sarpkaya (1962) using conformal mapping, albeit a two-dimensional solution. The integration represents the reservoir (and liquid column) added mass or induced length due to sudden acceleration.

Sarpkaya (1962) suggested the exact solution of the integration term is as follows

$$\frac{dV}{dt} = \frac{g H/L}{1 + \beta \frac{b}{L} + \frac{b}{B} \left[ \frac{H}{L} - \frac{1}{2} \frac{b}{L} \right]} \quad (3-13)$$

where b is channel height (pipe diameter); B is reservoir tank dimension; and  $\beta$  represents induced length, or added reservoir effect. The solution for  $\beta$  is

$$\beta = \frac{2}{\pi} \left[ \ln \left( \frac{1 + \frac{B^2}{b^2}}{4 \frac{B}{b}} \right) + \frac{B}{b} \tan^{-1} \frac{b}{B} + \frac{b}{B} \tan^{-1} \frac{B}{b} \right] \quad (3-14)$$

In the absence of added mass, the simple solution is based on the following one-dimensional differential equation

$$\frac{dV}{dt} = g \frac{H}{L} \quad (3-15)$$

Figure 3.2 illustrates the effect of added mass as the ratio of the Equation (3-15) neglecting added mass divided by the Equation (3-14) including both terms. The solution, while based on two-dimensional potential flow solution, is expected to have the same general trend as the three-dimensional case for the experimental results report in this thesis. Indeed, the parameters chosen for the solution plotted in Figure 3.2 correspond to the geometry of the experimental apparatus tested.

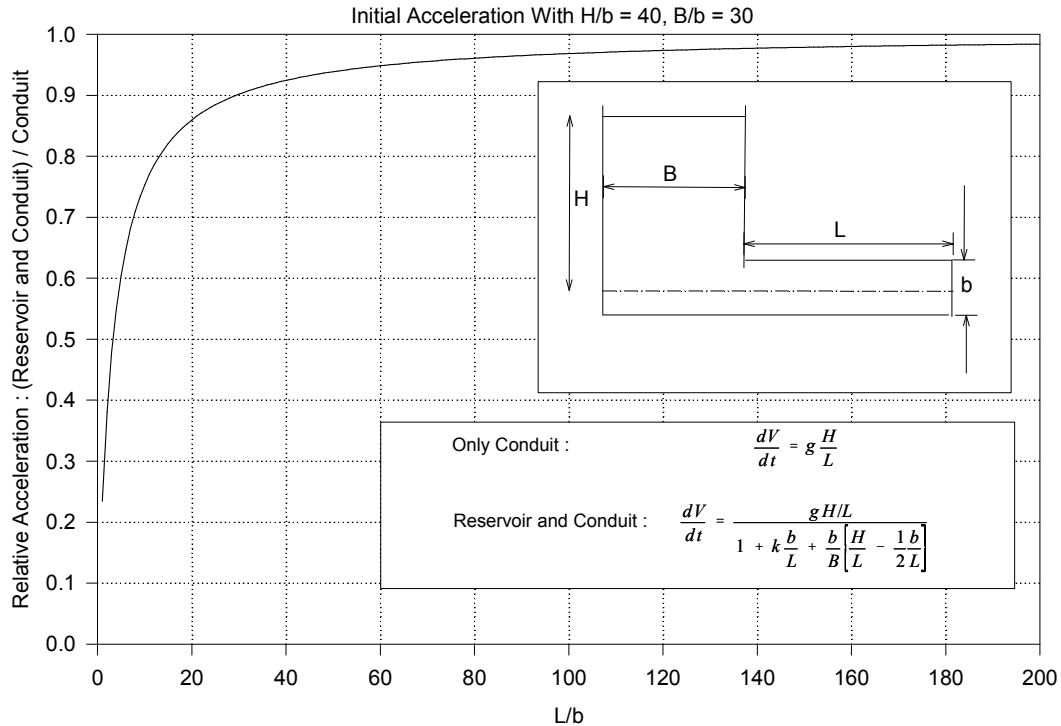


Figure 3.2 Initial Acceleration ( $H/b = 40 ; B/b = 30$ )

Continuing by neglecting the reservoir term (added mass)

$$(p_{AB} - p)A - \tau_0 \pi D L = \rho_t L \frac{dV}{dt} \quad (3-16)$$

Rearranging and inserting the Darcy-Weisbach based shear stress

$$\frac{dV}{dt} = \frac{1}{\rho_t} \frac{p_{AB} - p}{L} - \frac{f}{2D} V |V| \quad (3-17)$$

Finally, in terms of the reservoir pressure on the pipe centerline  $p_R$ , which is related to  $p_{AB}$  by

$$p_R = p_{AB} + \frac{\rho_l V^2}{2} \quad (3-18)$$

the final form of the one-dimensional momentum equation for incompressible flow is

$$\frac{dV}{dt} = \frac{1}{\rho_l} \frac{p_R - p}{L} - \frac{V^2}{2L} - \frac{f}{2D} V|V| \quad (3-19)$$

For analysis based on constant liquid length  $L = L_l$  and  $dL/dt = 0$  the equation is often expressed as

$$\frac{dV}{dt} = \frac{1}{\rho_l} \frac{p_R - p}{L_l} - \frac{f}{2D} V|V| \quad (3-20)$$

Equation (3-17) represents the linear pressure variation along the pipeline from the reservoir to the liquid and gas interface point, which is based on rigid column theory.

The mass conservation equation of gas phase with control volume CDEF is:

$$\frac{D}{Dt} \int_{\forall s(t)} \rho_g dV = \frac{d}{dt} \int_{\forall(t)} \rho_g dV + \int_{A(t)} \rho_g \vec{V}_r \cdot \vec{n} dA \quad (3-21)$$

For a non-reacting gas, the mass conservation equation of the gas phase becomes:

$$\rho_g A \frac{dL_g}{dt} + \sum_{EF} \rho_g V_r A - \sum_{CD} \rho_g V_r A = 0 \quad (3-22)$$

With the moving boundary condition, the gas volume change can be related to the rate of change of the liquid column

$$\frac{dV}{dt} = -AV \quad (3-23)$$

Energy with moving control volume CDEF in the pipeline, Figure 3.1 is:

$$\frac{D}{Dt} \int_{CV} e \rho_g dV + \int_{CS} e \rho_g \vec{V}_r \cdot \hat{n} dA = \dot{Q} + \dot{W} - \int_{CS} p \vec{V} \cdot \hat{n} dA \quad (3-24)$$

Apply the following assumptions to the energy equation:

- No shaft work;
- No heat transfer across boundaries;
- Negligible kinetic energy change of gas in control volume compared to kinetic energy of water;
- At interface  $V_r = 0$ ;
- For entrapped gas  $w = V = 0$  at closed end and on pipe walls;
- Ideal gas  $p = \rho_g RT$  and  $R = c_p - c_v$

The first law equation reduces to the rate of change of internal energy balanced by work

$$\frac{dU}{dt} = -p \frac{dV}{dt} \quad (3-25)$$

Since  $m = \rho_g V$  and  $U = mu = m c_v T$ :

$$p \frac{dV}{dt} + mc_v \frac{dT}{dt} = 0 \quad (3-26)$$

Integrating results in the reversible adiabatic process:

$$\frac{p}{p_o} = \left( \frac{V_0}{V} \right)^k \quad (3-27)$$

$$\frac{T}{T_0} = \left( \frac{V}{V_0} \right)^{k-1} \quad (3-28)$$

The differential form of the Equation (3-25) is:

$$\frac{dp}{dt} = -k \frac{p}{V} \frac{dV}{dt} + k \frac{p}{m} \frac{dm}{dt} \quad (3-29)$$

Since the  $dm/dt$  term is zero for a confined system, the final form of the energy equation for the entrapped gas can be written as:

$$\frac{dp}{dt} = -k \frac{p}{V} \frac{dV}{dt} = \frac{k p A V}{V} \quad (3-30)$$

Since the adiabatic process is a special quasi-equilibrium process of the polytropic process, in this thesis the energy equation for a gas phase also includes the polytropic relation as an energy equation to be more general.

### 3.2.1.2 Elastic Liquid and Lumped Gas Mass (Case III)

The method of characteristics was developed to study wave action in the liquid phase --Wylie and Streeter (1993), and Watters (1980) and was applied in this study. A characteristic grid line was adopted to avoid interpolation error. Assumptions and initial conditions are the same as those for lumped liquid and gas mass. Applying the mass conservation and momentum equations to control volume ABCD yields:

$$\frac{\partial p}{\partial t} + \rho_l a_l^2 \frac{\partial V}{\partial x} = 0 \quad (3-31)$$

$$\frac{1}{\rho_l} \frac{\partial p}{\partial x} + \frac{\partial V}{\partial t} + \frac{f}{2D} V |V| = 0 \quad (3-32)$$

The transformed total characteristic forms are:

$$\frac{dx}{dt} = \pm a_l \quad (3-33)$$

$$\pm \frac{1}{\rho_l a_l} \frac{dp}{dt} + \frac{dV}{dt} + \frac{f}{2D} V |V| = 0 \quad (3-34)$$

The forward characteristic, C<sup>+</sup>, is:

$$\frac{dx}{dt} = a_l \quad (3-35)$$

$$\frac{1}{\rho a_l} \frac{dp}{dt} + \frac{dV}{dt} + \frac{f}{2D} V |V| = 0 \quad (3-36)$$

The backward characteristic, C<sup>-</sup>, is :

$$\frac{dx}{dt} = -a_l \quad (3-37)$$

$$-\frac{1}{\rho a_l} \frac{dp}{dt} + \frac{dV}{dt} + \frac{f}{2D} V |V| = 0 \quad (3-38)$$

Integration of C<sup>+</sup> along characteristic lines from interior (fixed grid) point A to Point P in Figure 3.3 :

$$V_P = V_A - \frac{1}{\rho_l a_l} (p_P - p_A) - \frac{f}{2D} V_A |V_A| (t_P - t_A) \quad (3-39)$$

$$x_P = a_l (t_P - t_A) + x_A \quad (3-40)$$

Integration of C<sup>-</sup> along characteristic from Point B to Point P:

$$V_P = V_B + \frac{1}{\rho_l a_l} (p_P - p_B) - \frac{f}{2D} V_B |V_B| (t_P - t_B) \quad (3-41)$$

$$x_P = -a_l (t_P - t_B) + x_B \quad (3-42)$$

For interior point P Equations (3-39) and (3-41) can be solved simultaneously to yield both velocity V<sub>P</sub> and p<sub>P</sub>.

$$V_P = \frac{1}{2} \left[ V_A + V_B + \frac{1}{\rho_l a_l} (p_A - p_B) - \frac{f}{2D} (|V_A| |V_A| + |V_B| |V_B|) \Delta t \right] \quad (3-43)$$

$$p_P = \frac{1}{2} \left[ \rho_l a_l (V_A + V_B) + p_A + p_B - \frac{f \rho_l a_l}{2D} (|V_A| |V_A| - |V_B| |V_B|) \Delta t \right] \quad (3-44)$$

where the time increment  $\Delta t$  must satisfy the Courant condition

$$(t_P - t_A) = \Delta t = \frac{(x_P - x_A)}{a_l} = \frac{\Delta x}{a_l} \quad (3-45)$$

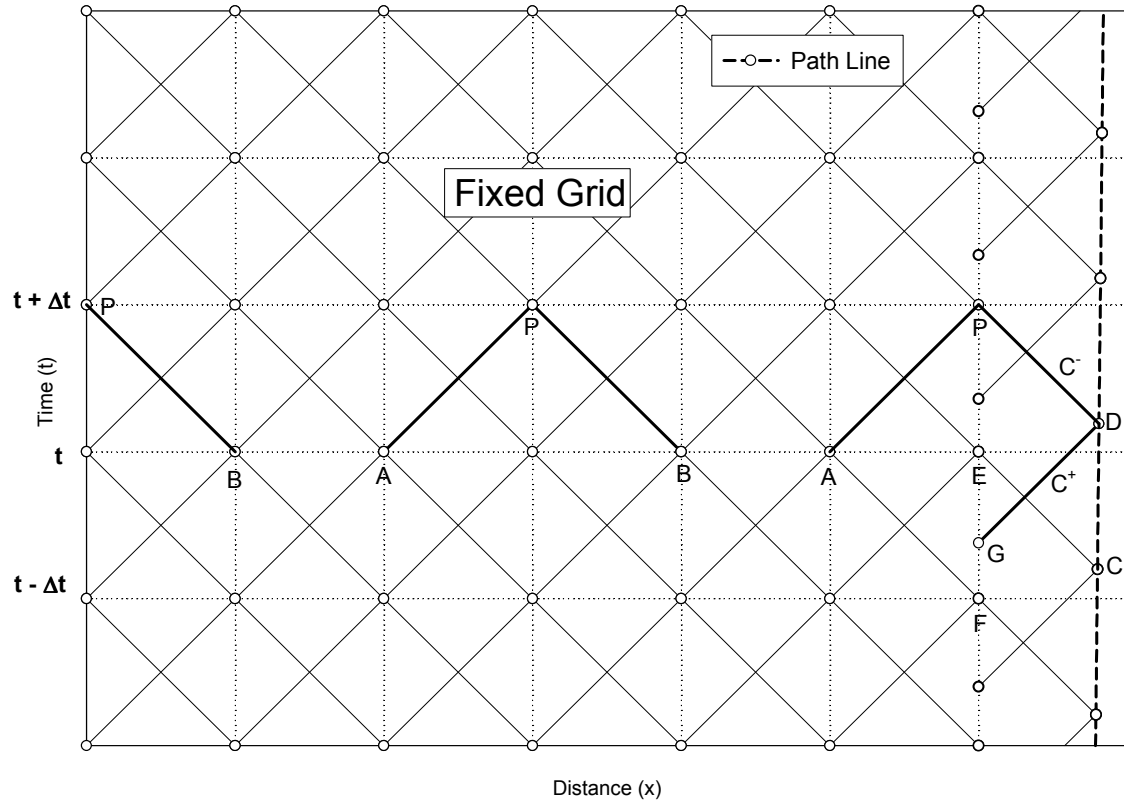


Figure 3.3 Definition Sketch in x-t Plane with Fixed Grid and Interfacial Path Line

The upstream boundary condition of constant reservoir pressure  $p_R$ , is:

a) For positive Flow:

$$p_P = p_R - \frac{\rho V_P^2}{2} \quad (3-46)$$

b) For negative Flow:

$$p_P = p_R \quad (3-47)$$

To formulate a solution at the liquid-gas interface on the far right of Figure 3.4, there is an iterative solution joining  $C^+$  characteristics from A to P and from G to D,  $C^-$  characteristic from D to P, and the path line from C to D. The values of pressure and velocity at Point G is based on interpolation between Points F and E, or for some grids between Points E and P.

From point G to D on  $C^+$  :

$$V_D = V_G - \frac{1}{\rho_l a_l} (p_D - p_G) - \frac{f}{2D} V_G |V_G| (t_D - t_G) \quad (3-48)$$

$$x_D = a_l (t_D - t_G) + x_G \quad (3-49)$$

From point D to P on  $C^-$  :

$$V_P = V_D + \frac{1}{\rho_l a_l} (p_P - p_D) - \frac{f}{2D} V_D |V_D| (t_P - t_D) \quad (3-50)$$

$$x_P = -a_l (t_P - t_D) + x_D \quad (3-51)$$

From point C to D on pathline :

$$x_D = x_C + \frac{1}{2} (V_D + V_C) (t_D - t_C) \quad (3-52)$$

Polytropic process in gas at liquid-gas interface :

$$p_D = p_0 \left( \frac{L_g}{L_T - x_D} \right)^n \quad (3-53)$$

Combining the two equations for  $C^+$ , one equation for  $C^-$ , pathline, and the polytropic relation yields:

$$x_D - x_C - \frac{1}{2} [V_C - \frac{1}{\rho_l a_l} (p_0 (\frac{L_g}{L_T - x_D})^n - p_C) - f V_C | V_C | \frac{(x_D - x_C)}{2 a_l D} + V_C] [\frac{(x_D + a_l t_C - x_C)}{a_l} - t_C] = 0$$

The Newton-Raphson method presented by Atkinson (1989) was employed to find the root  $x_D$ .

### 3.2.1.3 Acoustic Liquid and Acoustic Gas Mass (Case IV)

The method of characteristics was employed to analyze wave action in both the liquid side and the gas side Anderson (1990). The characteristic equations of the liquid side are similar to those for acoustic liquid and lumped gas mass. Friction was neglected for a gas phase. Mass conservation and momentum equations with control volume CDEF are:

$$\frac{\partial p}{\partial t} + V \frac{\partial p}{\partial x} + \rho_g a_g^2 \frac{\partial V}{\partial x} = 0 \quad (3-55)$$

$$\frac{1}{\rho_g} \frac{\partial p}{\partial x} + V \frac{\partial V}{\partial x} + \frac{\partial V}{\partial t} = 0 \quad (3-56)$$

The transformation of governing equations for acoustic gas mass yields characteristic lines and compatibility equations, which are:

$$\pm \frac{1}{\rho_g a_g} \frac{dp}{dt} + \frac{dV}{dt} = 0 \quad (3-57)$$

$$\frac{dx}{dt} = V \pm a_g \quad (3-58)$$

Calorically perfect gas:

$$\rho_g = \frac{kp}{a_g^2} \quad (3-59)$$

Assuming an isentropic process for rapid transients :

$$dp = c_2 \left( \frac{2k}{k-1} \right) a_g^{\frac{k+1}{k-1}} da_g \quad (3-60)$$

Substituting Equation (3-60) into (3-59) yields:

$$\rho_g = c_2 k a_g^{\frac{2}{k-1}} \quad (3-61)$$

Substitute Equation (3-60) and (3-61) into (3-57):

$$dV \pm \frac{2}{k-1} da_g = 0 \quad (3-62)$$

The forward characteristic, C<sup>+</sup>, is :

$$\frac{dx}{dt} = V + a_g \quad (3-63)$$

$$dV + \frac{2}{k-1} da_g = 0 \quad (3-64)$$

The backward characteristic, C<sup>-</sup>, is :

$$\frac{dx}{dt} = V - a_g \quad (3-65)$$

$$dV - \frac{2}{k-1} da_g = 0 \quad (3-66)$$

Integrate along C<sup>+</sup> :

$$x_P = V_A(t_P - t_A) + a_{gR}(t_P - t_A) + x_A \quad (3-67)$$

$$V_P = -\frac{2}{k-1}(a_{gP} - a_{gA}) + u_A \quad (3-68)$$

Integrate along C<sup>+</sup>:

$$x_P = V_B(t_P - t_B) - a_{gB}(t_P - t_B) + x_B \quad (3-69)$$

$$V_P = \frac{2}{k-1}(a_{gP} - a_{gB}) + u_B \quad (3-70)$$

The upstream boundary condition of the liquid-side is the same as that of the acoustic liquid and lumped gas mass. The downstream boundary of the gas phase is a dead-end -- velocity V is zero. Since position x and velocity V are known values at the end, a<sub>p</sub> and t<sub>p</sub> can be expressed in the following form:

$$t_p = \frac{t_A(V_A + a_{gA}) + x_p - x_A}{V_A - a_{gA}} \quad (3-71)$$

$$a_{gp} = \frac{k-1}{2}(V_p - V_A) + a_{gA} \quad (3-72)$$

The interface boundary, downstream of the liquid phase or upstream of the gas phase, has a condition such that velocity and pressure are the same at the interface. The interface boundary condition has the following equations: C<sup>+</sup> from the liquid phase, C<sup>-</sup> from the gas phase, and pathline in Figure 3.4.

Forward characteristic C<sup>+</sup> in liquid:

$$V_p = V_A - \frac{1}{\rho_l a_l} (p_p - p_A) - \frac{f}{2D} V_A |V_A| (t_p - t_A) \quad (3-73)$$

$$x_p = a_l (t_p - t_A) + x_A \quad (3-74)$$

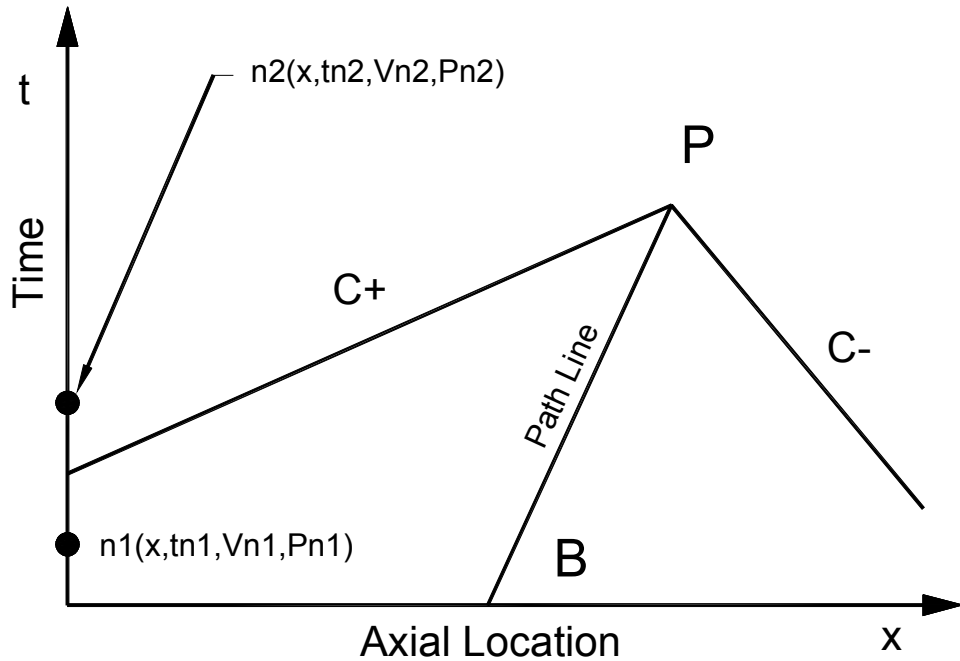


Figure 3.4 Portion of Grid Employed for Elastic Liquid and Acoustic Gas Analysis

Backward characteristic  $C^-$  in gas:

$$V_P = V_S - \frac{2}{k-1} (a_{gP} - a_{gS}) \quad (3-75)$$

$$x_P = V_S(t_P - t_S) - a_{gS}(t_P - t_S) + x_S \quad (3-76)$$

Path Line :

$$x_P = x_B + \frac{1}{2} (V_P + V_B)(t_P - t_B) \quad (3-77)$$

Iteration Procedure

1. Assume  $t_A$ , interpolate  $V_A$ :

$$V_A = V_{nl} + \frac{V_{n2} - V_{nl}}{t_A - t_{nl}} (t_{n2} - t_{nl}) \quad (3-78)$$

2.  $a_{gp}$  can be expressed in the following way:

$$a_{gp} = a_{g0} \left( \frac{p_p}{p_0} \right)^{\frac{k-1}{2k}} \quad (3-79)$$

3. Combining two compatibility equations yields:

$$\frac{2}{k-1} \left[ a_{g0} \left( \frac{p_p}{p_0} \right)^{\frac{k-1}{2k}} - a_{gs} \right] + u_B - V_A + \frac{1}{\rho_l a_l} (p_p - p_A) + \frac{f}{2D} V_A |V_A| (t_p - t_A) = 0 \quad (3-80)$$

4. Solve for  $p_p$  with the Newton-Raphson method.

5. Combining two characteristic line equations yields

$$t_p = \frac{x_s - x_A - t_s (V_s - a_{gs}) + t_A - a_l}{a_l - (V_s - a_{gs})} \quad (3-81)$$

6. Solve for  $t_p$ .

7. Compute  $V_p$  from the liquid side compatibility equation.

8. Compute  $x_p$  from the liquid phase characteristic line equation.

9. Compute  $x_{p1}$  from the pathline equation.

10. Compare  $x_p$  and  $x_{p1}$ .

11. Iterate until  $|x_p - x_{p1}| \leq \text{Tolerance}$ .

### 3.3 Dimensional Analysis

Dimensional analysis was done to present results of numerical analysis more efficiently. Similarity parameters were derived by nondimensionalizing the governing equations with normalization or scaling of dimensionless groups. Similarity parameters can be conveniently presented as parametric relations, such as the influence of liquid and gas length ratio and the effect of acoustic liquid and gas. The following dimensionless parameters were used to nondimensionalize the governing equations Martin (1976):

Ratio of Imposed Pressure to Initial Air Pressure:

$$P_R = \frac{p_R}{p_0} \quad (3-82)$$

Ratio of Maximum Pressure to Initial Air Pressure:

$$P_M = \frac{p_M}{p_0} \quad (3-83)$$

Definition of Initial Void Fraction:

$$\alpha_0 = \frac{L_g}{L_l + L_g} = \frac{L_A}{L_w + L_A} \quad (3-84)$$

Various Dimensionless Parameters:

$$\text{Pressure} : p^* = \frac{p}{p_0} = P \quad (3-85a)$$

$$\text{Velocity} : V^* = \frac{V}{\sqrt{\frac{p_0 \nabla_0}{\rho_l L_l A}}} \quad (3-85b)$$

$$\text{Time} : t^* = \frac{t}{\sqrt{\frac{\rho_l L_l \nabla_0}{p_0 A}}} \quad (3-85c)$$

$$\text{Liquid Length} : L^* = \frac{LA}{\nabla_0} = \frac{L}{L_g} \quad (3-85d)$$

$$\text{Volume of gas} : \nabla^* = \frac{\nabla}{\nabla_0} \quad (3-85e)$$

List of Variables:

$$p_M = F(p_0, p_R, L_\ell, D, f, \forall_0, \rho_\ell, a_\ell, \rho_g, a_g, n) \quad (3-86)$$

Definition of  $\Pi$  Parameters:

$$\Pi_1 = \frac{p_M}{p_0} = P_M; \quad \Pi_2 = \frac{p_R}{p_0} = P_R; \quad \Pi_3 = \frac{f\forall_0}{D^3}; \quad \Pi_4 = \frac{\forall_0}{L_\ell A} \quad (3-87)$$

$$\Pi_5 = \frac{\rho_\ell a_\ell^2}{p_R}; \quad \Pi_6 = \frac{\rho_g a_g^2}{p_R}; \quad \Pi_7 = \frac{\rho_g a_g}{\rho_\ell a_\ell} \quad (3-88)$$

Parameter  $\Pi_3$  can also be written

$$\Pi_3 = \frac{f\forall_0}{D^3} = \frac{\pi f \forall_0}{4DA} = \frac{\pi f L_g}{4D} = \frac{\pi}{4} \lambda \quad (3-89)$$

Also, parameter  $\Pi_4$  can be expressed in terms of initial void fraction  $\alpha_0$

$$\Pi_4 = \frac{\forall_0}{L_\ell A} = \frac{L_g}{L_\ell} = \frac{\alpha_0}{1 - \alpha_0} \quad (3-90)$$

List of  $\Pi$  Groups becomes:

$$F(\Pi_1, \Pi_2, \Pi_3, \Pi_4, \Pi_5, \Pi_6, \Pi_7) = 0 \quad (3-91)$$

Definition of Cauchy and Mach Numbers:

$$C = \frac{\rho a^2}{kp} = M^2 \quad (3-92)$$

General List of Dimensionless Functions:

$$p^* = P_M = \frac{p_M}{p_0} = \Psi_1 \left( P_R, \frac{fL_g}{D}, \alpha_0, \frac{\rho_\ell a_\ell^2}{p_R}, \frac{\rho_g a_g^2}{p_R}, \frac{\rho_g a_g}{\rho_\ell a_\ell}, n \right) \quad (3-93a)$$

$$t_{p_M}^* = \frac{t_{p_M}}{\sqrt{\frac{\rho_l L_l V_0}{p_0 A}}} = \Phi_2 \left( P_R, \frac{fL_g}{D}, \alpha_0, \frac{\rho_l a_l^2}{p_R}, \frac{\rho_g a_g^2}{p_R}, \frac{\rho_g a_g}{\rho_l a_l}, n \right) \quad (3-93b)$$

$$V_M^* = \frac{V_M}{\sqrt{\frac{p_0 V_0}{\rho_l L_l A}}} = \Phi_3 \left( P_R, \frac{fL_g}{D}, \alpha_0, \frac{\rho_l a_l^2}{p_R}, \frac{\rho_g a_g^2}{p_R}, \frac{\rho_g a_g}{\rho_l a_l}, n \right) \quad (3-93c)$$

$$t_{V_M}^* = \frac{t_{V_M}}{\sqrt{\frac{\rho_l L_l V_0}{p_0 A}}} = \Phi_4 \left( P_R, \frac{fL_g}{D}, \alpha_0, \frac{\rho_l a_l^2}{p_R}, \frac{\rho_g a_g^2}{p_R}, \frac{\rho_g a_g}{\rho_l a_l}, n \right) \quad (3-93d)$$

$$V_{\min}^* = \frac{V_{\min}}{V_0} = \Phi_5 \left( P_R, \frac{fL_g}{D}, \alpha_0, \frac{\rho_l a_l^2}{p_R}, \frac{\rho_g a_g^2}{p_R}, \frac{\rho_g a_g}{\rho_l a_l}, n \right) \quad (3-93e)$$

Definition of Acoustic Impedance Related Power Parameter

$$\varrho = \frac{4 \frac{\rho_g a_g}{\rho_l a_l}}{\left( 1 + \frac{\rho_g a_g}{\rho_l a_l} \right)^2} \quad (3-94)$$

The final solution for the maximum value of the pressure ratio  $P_M$  becomes

$$P_M = \varphi(P_R, \lambda, \alpha_0, C_l, C_g, \varrho, n) \quad (3-95)$$

### 3.3.1 Lumped Liquid and Gas Mass (Cases I and II)

#### 3.3.1.1 Variable Liquid Length (Case I)

The governing equations in the variable liquid length case were nondimensionalized using dimensionless groups. Momentum equation for variable liquid length

$$\frac{dV}{dt} = \frac{1}{\rho_l} \frac{P_R - P}{L} - \frac{V^2}{2L} - \frac{f}{2D} V|V| \quad (3-96)$$

The dimensionless momentum equation of the liquid phase is:

$$\frac{dV^*}{dt^*} = \frac{L_A}{\nabla_0} \frac{P_R - P}{L^*} - \frac{V^{*2}}{2L^*} - \frac{f\nabla_0}{2DA} V^*|V^*| \quad (3-97)$$

Variable length

$$\frac{dL}{dt} = V \quad (3-98)$$

Dimensionless variable liquid length

$$\frac{dL^*}{dt^*} = V^* \quad (3-99)$$

Gas volume and liquid length

$$\frac{d\nabla}{dt} = -AV \quad (3-100)$$

Dimensionless gas volume and liquid length

$$\frac{d\nabla^*}{dt^*} = -V^* \quad (3-101)$$

Dimensional energy equation of the gas phase

$$\frac{dp}{dt} = -n \frac{p}{\nabla} \frac{d\nabla}{dt} = \frac{n p A V}{\nabla} \quad (3-102)$$

Dimensionless energy equation of the gas phase

$$\frac{dp^*}{dt^*} = -n \frac{p^*}{\nabla^*} \frac{d\nabla^*}{dt^*} = \frac{n p^* V^*}{\nabla^*} \quad (3-103)$$

It is shown that pressure ratio, pipe friction, the ratio of gas volume and pipe diameter, thermodynamic parameter, and length ratio of liquid and gas appear as similarity parameters. Ideal frictionless case similarity parameters are reduced to three groups which are: pressure ratio, thermodynamic parameters, and length ratio of liquid and gas. Functional relationships of dimensionless ratio of maximum pressure, maximum velocity, minimum gas unit volume, and corresponding times can be expressed with these five similarity parameters:

### 3.3.1.2 Constant Liquid Length (Case II)

The dimensionless forms of governing equations are the same for the variable liquid length case except for the momentum equation. The dimensionless momentum equation of liquid phase is:

$$\frac{dV^*}{dt^*} = P_R - P - \frac{fV_0}{2DA} V^* |V^*| = P_R - P - \frac{\lambda}{2} V^* |V^*| \quad (3-104)$$

If we regard liquid length as constant rather than variable, then we can dispense with dimensionless length ratio of liquid and gas as a similarity parameter. The functional relationship of the dimensionless ratio of maximum pressure, maximum velocity, minimum gas unit volume, and corresponding times are:

$$P_M = \frac{p_M}{p_0} = \varphi(P_R, \lambda, \alpha_0, k) \quad (3-105)$$

Maximum pressure is independent of initial liquid length since initial liquid length is not listed on the similarity parameters of maximum pressure. However initial liquid length does influence the timing of maximum pressure, magnitude of maximum velocity, and minimum gas volume. Furthermore, maximum pressure is totally independent of the initial length of liquid and gas for an ideal frictionless case. Maximum pressure depends only on pressure ratio,  $p/p_R$ . Validity range will be compared to other models later in the thesis.

### 3.3.2 Acoustic Liquid and Gas Mass(Case III)

The total ordinary differential equations with in the liquid phase are:

$$\frac{dx}{dt} = \pm a_l \quad (3-106)$$

$$\frac{dV}{dt} \pm \frac{1}{\rho_l a_l} \frac{dp}{dt} + \frac{f}{2D} V |V| = 0 \quad (3-107)$$

The nondimensional form of characteristic lines and the compatibility equation are:

$$\frac{dx^*}{dt^*} = \pm \sqrt{\frac{\rho_l a_l^2}{p_R} \frac{p_R}{p_0} \frac{L_l A}{V_0}} \quad (3-108)$$

and

$$\pm \sqrt{\frac{p_R}{\rho_l a_l^2} \frac{p_R}{p_0} \frac{L_l A}{V_0}} \frac{dp^*}{dt^*} + \frac{dV^*}{dt^*} + \frac{f V_0}{2DA} V^* |V^*| = 0 \quad (3-109)$$

Dimensionless form of polytropic relationship as a moving interface boundary condition is:

$$P = p^* = \left[ \frac{1}{V^*} \right]^k \quad (3-110)$$

Acoustic liquid and gas mass theory introduces the acoustic effect of liquid as a similarity parameter. The rest of the similarity parameters are the same as those of lumped liquid and gas mass theory.

### 3.3.3 Acoustic Liquid and Acoustic Gas Mass (Case IV)

The governing equations of gas phase are:

$$\frac{dx}{dt} = \pm a_g \quad (3-111)$$

$$\pm \frac{1}{\rho_g a_g} \frac{dp}{dt} + \frac{dV}{dt} = 0 \quad (3-112)$$

yielding the non-dimensional form

$$\frac{dx^*}{dt^*} = V^* \pm \sqrt{\frac{\rho_g a_g^2}{p_R} \frac{p_R}{p_0} \frac{L_t A}{V_0}} \quad (3-113)$$

$$\pm \frac{\rho_t}{\rho_g} \sqrt{\frac{p_R}{\rho_t a_g^2} \frac{p_R}{p_0} \frac{L_t A}{V_0}} \frac{dp^*}{dt^*} + \frac{dV^*}{dt^*} = 0 \quad (3-114)$$

The dimensionless form of transformed governing equations of liquid phase are the same as those of acoustic liquid and lumped gas mass. Qualitative analysis was done for the moving interface boundary condition. When a pressure wave is transmitted from one fluid medium to another, the power transmission coefficient can be expressed with specific impedance of each fluid medium, Kinsler and Frey (1962):

Acoustic liquid and acoustic gas theory introduces the acoustic effect of gas and specific impedance ratio as a similarity parameter. The rest of the similarity parameters are the same as those of acoustic liquid and lumped gas mass. Similarity parameters for same pipe diameter are:

### 3.4 Comparison of Different Analytical Models

The frictionless ideal case was considered to present the effects of: liquid length, wave action in the gas phase, and thermodynamic process. To compare maximum interface

pressure variation to that of a single liquid phase case following pressure ratio, a dimensionless parameter was introduced.

### 3.4.1 Effect of Wave Action in Liquid and Gas Phases (Case IV)

To study wave action in the gas phase, liquid length was set to be  $L_l = 40$  m with the gas length  $L_g$  variable. The process was assumed isentropic with the specific heat ratio based on air, for which  $k = 1.4$ . In Figure 3.5, dimensionless maximum interface pressures were plotted using three different models. It is clearly shown in Figure 3.5 that acoustic effect of the gas phase is almost negligible. The effect of the variation of the acoustic velocity of the liquid phase is compared with inelastic liquid (rigid column) with variable length  $L_l$  and  $L_g = 10$  m in Figure 3.6.

Clearly, there is a limited acoustic effect of the gas phase, but negligible compared to the acoustic effect of the liquid phase. Figures 3.5 and 3.6 show that differences in the lumped liquid and lumped gas mass models are caused by the acoustic effect of liquid and not by the acoustic effect of the gas phase. The more important acoustic effect is caused by the liquid phase. The reason for this is that the power transmission coefficient defined by Equation (3-94) is so low for most liquid and gas cases. For example, the typical value in the case of water and air is 0.001. When pressure waves pass through water to air or from air to water, the magnitude of transmitted pressure waves is reduced by a factor of 0.001.

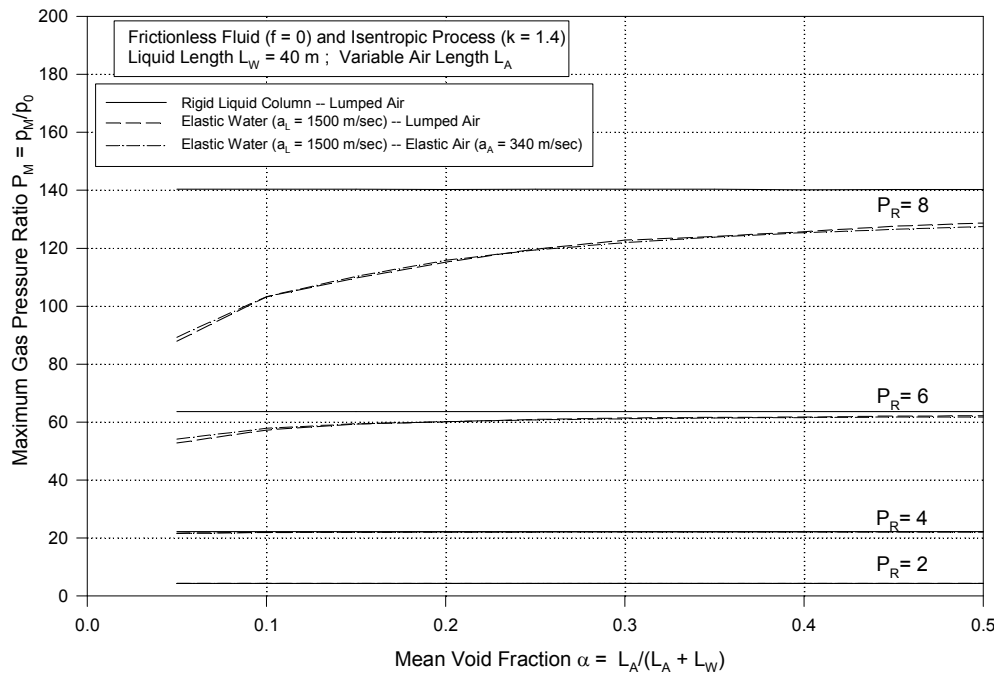


Figure 3.5 Results for Three Models (Cases I, III and IV)

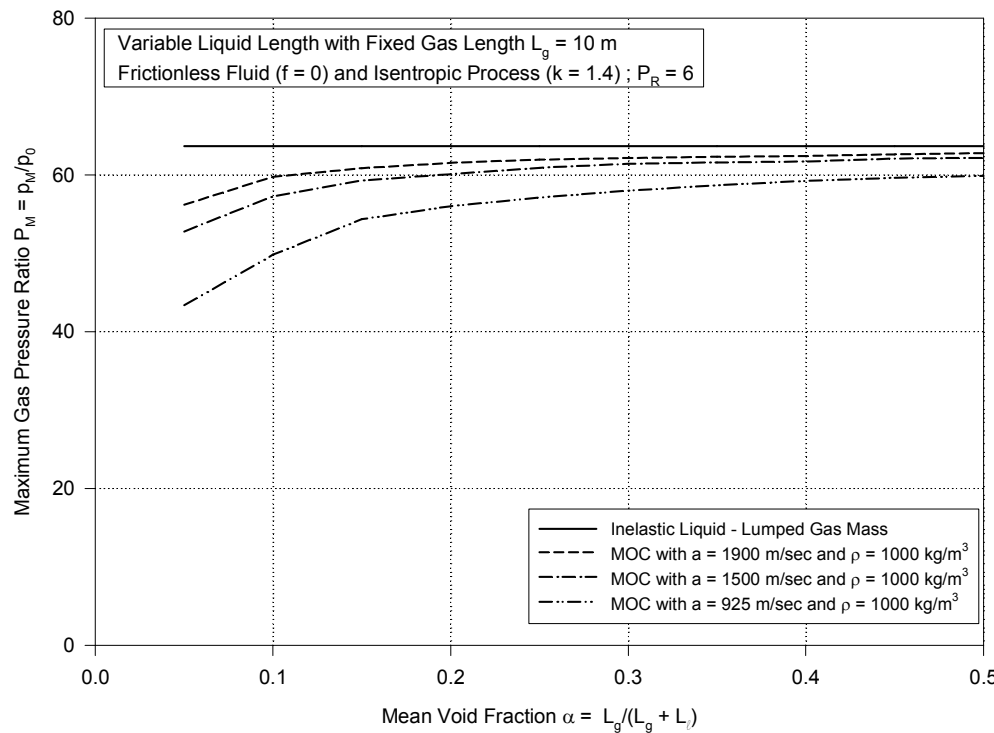


Figure 3.6 Effect of Varying Acoustic Velocity of Liquid (Cases I and III)

The trend of acoustic liquid and lumped gas mass is as follows: As void fraction  $\alpha_0$  increases, interface maximum pressure asymptotically approaches the interface maximum pressure of lumped liquid and lumped gas mass. The increase in pressure ratio  $P_R$  yields higher values of maximum pressure  $P_M$  as lumped gas mass gets larger. The reason for this is that there is less acoustic effect of liquid as the void fraction increases, which means liquid length decreases. For example, when pressure ratio  $P_R = 6$ , the void fraction decreases the acoustic effect of liquid increase. However, if the void fraction is increased beyond 0.3, then there is much less acoustic effect of liquid. That is why interface maximum pressure asymptotically approaches interface maximum pressure of lumped liquid and lumped gas mass. As pressure ratio  $P_R$  increases, the acoustic effect of liquid also increases. With the highest pressure ratio of 8 the acoustic effect of liquid always exists regardless of the void fraction. However, moderate pressure ratio ranges; that is, for  $P_R$  from 2 to 4, result in an interface pressure from acoustic liquid and lumped gas mass almost the same as the values of lumped liquid and lumped gas mass, which means that there is no acoustic effect of liquid regardless of the void fraction.

Trends of three different kinds of liquid are similar to each other – as the void fraction  $\alpha_0$ , increases, interface maximum pressure asymptotically approaches the interface maximum pressure of lumped liquid and lumped gas mass. However as speed of sound increases, the difference to interface maximum pressure of lumped liquid and lumped gas mass gets smaller. That is true because, according to rigid column theory, liquid is lumped in the case of infinite speed of sound. Liquid density also influences maximum interface pressure. Liquid density has much less influence than speed of sound since the similarity parameter shows that speed of sound is in square proportion to infinite in a lumped liquid case. The three acoustic parameters in the dimensionless grouping have been defined as

$$\Pi_5 = \frac{\rho_l a_l^2}{P_R}; \quad \Pi_6 = \frac{\rho_g a_g^2}{P_R}; \quad \Pi_7 = \frac{\rho_g a_g}{\rho_l a_l} \quad (3-115)$$

It is clearly shown in Figure 3.6 that as speed of sound of the liquid phase decreases, the difference in maximum interface pressure between acoustic liquid and lumped gas mass and lumped liquid and lumped gas mass increases because of the greater acoustic effect of liquid, which is also known as packing effect.

### **3.4.2 Effect of Thermodynamic Process**

Air as a gas and water as a liquid were used to present the effect of thermodynamic parameters. The thermodynamic behavior in terms of polytopic process ( $n = 1.2$ ) compared to adiabatic with  $k = 1.4$  are plotted in Figure 3.7. Even though  $n$  may change with compression and expansion of air gas, a constant  $n$  value was used for the sake of simplicity Graze (1996) reported that the "compression (acceleration) period is close to the adiabatic condition because of much less heat transfer, however expansion(deceleration) period shows unstable flow by the possibility of large heat transfer." Behavior of  $n = 1.2$  was based on empirical results for air chambers Parmarkian (1963) and  $n = 1.4$  was for the adiabatic process. Fast transient phenomena are often assumed to be adiabatic processes.

It is shown that results of adiabatic process ( $n = k = 1.4$ ) are much less than maximum interface pressures of air chambers ( $n = 1.2$ ). The results of adiabatic process from acoustic liquid and lumped gas mass model agree very well with maximum interface pressures of acoustic liquid and acoustic gas, since there is less acoustic effect of gas and the same assumption of adiabatic process and acoustic effect of liquid. An isentropic process with  $k = 1.4$  was assumed for this analysis since hydraulic transient phenomena were fast.

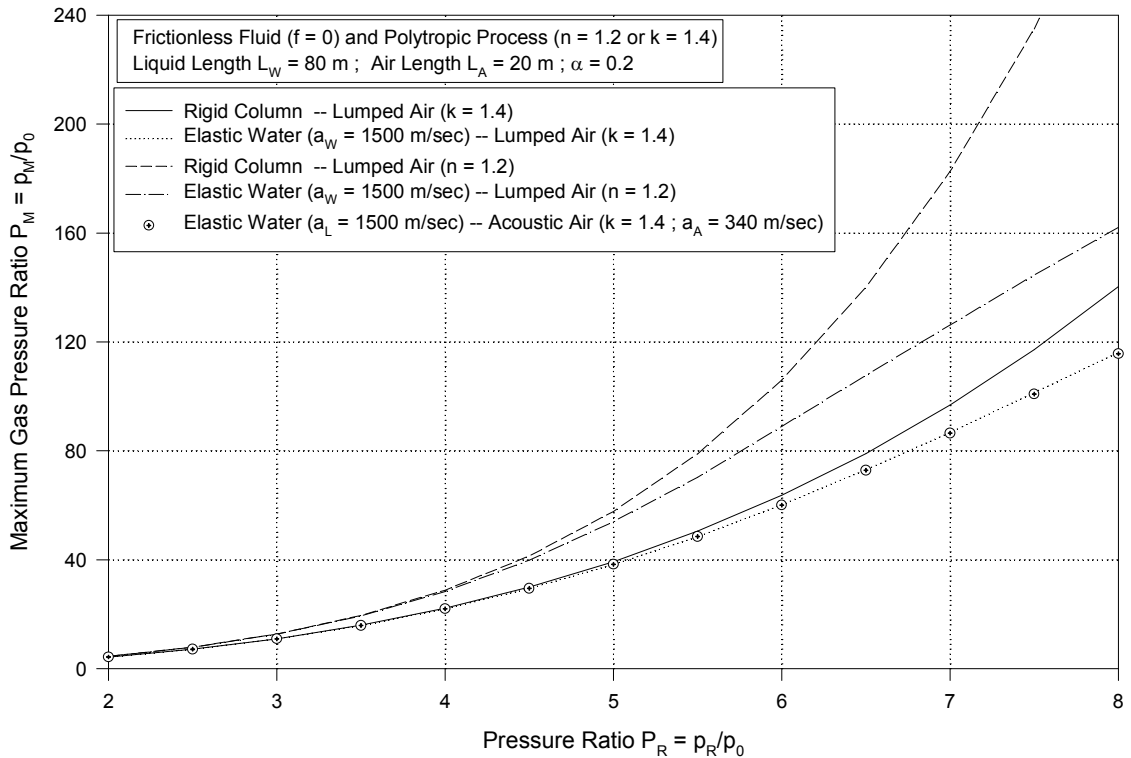


Figure 3.7 Comparison of Various Analytical Models (Cases I, II, III, and IV)

### 3.4.3 Effect of Liquid Length in Rigid Column Analysis

The two models for rigid column analysis for the liquid phase coupled with lumped air mass undergoing either polytropic or isentropic behavior are for (1) variable liquid length, and (2) assumption of constant length. The solution for either model can either be numerical employing finite difference techniques such as Runge-Kutta, or if the only hydraulic resistance is that of straight pipe friction, closed form solution is possible, as follows. The momentum equation for variable length may be expressed

$$\rho_l(L_l + x) \frac{dV}{dt} = p_r - p - \frac{\rho_l V^2}{2} - (L_l + x) \frac{\rho_l f V^2}{2D} \quad (3-116)$$

where the variable liquid length  $L$  shown in Figure 3.1 may be written in terms of  $x$ , whose origin is the initial liquid-gas interface

$$L = L_\ell + x \quad (3-117)$$

Variable liquid length is related to liquid column velocity

$$\frac{dL}{dt} = \frac{dx}{dt} = V \quad (3-118)$$

Assuming isentropic process (which is not necessary)

$$P = \frac{p}{p_o} = \left[ \frac{L_g}{L_g - x} \right]^k \quad (3-119)$$

Then

$$\frac{dP}{dt} = \frac{k}{L_g} P^{\frac{k+1}{k}} \frac{dx}{dt} = \frac{kV}{L_g} P^{\frac{k+1}{k}} \quad (3-120)$$

Combining momentum and gas process

$$\frac{\rho_\ell L}{p_o} \frac{V dV}{dP} = \frac{L_g}{k} \left[ P_R - P - \left( 1 + \frac{fL}{D} \right) \frac{\rho_\ell V^2}{2p_o} \right] P^{-\frac{k+1}{k}} \quad (3-121)$$

Defining dimensionless parameter F

$$F = \frac{\rho_\ell V^2}{2p_o} ; \quad V dV = \frac{p_o dF}{\rho_\ell} \quad (3-122)$$

Using parameters  $\lambda$  and  $\alpha_0$

$$\lambda = \frac{fL_g}{D} ; \quad \alpha_0 = \frac{L_g}{L_\ell + L_g} \quad (3-123)$$

$$k \frac{L}{L_t} dF = \left[ \frac{\alpha_0}{1 - \alpha_0} (P_R - P - F) - \frac{\lambda L}{L_t} F \right] P^{-\frac{k+1}{k}} dP \quad (3-124)$$

Grouping F terms on LHS

$$k \frac{L}{L_t} dF + \left[ \frac{\alpha_0}{1 - \alpha_0} + \frac{\lambda L}{L_t} \right] F P^{-\frac{k+1}{k}} dP = \frac{\alpha_0}{1 - \alpha_0} (P_R - P) P^{-\frac{k+1}{k}} dP \quad (3-125)$$

For transformation multiply by

$$\exp(-\lambda P^{-\frac{1}{k}}) \quad (3-126)$$

This results in perfect differential on LHS and two integrals on RHS

$$k \int_0^M d \left[ \frac{L}{L_t} F \exp(-\lambda P^{-\frac{1}{k}}) \right] = \frac{\alpha_0}{1 - \alpha_0} \int_{P_0}^{P_M} \exp(-\lambda P^{-\frac{1}{k}}) (P_R P^{-\frac{k+1}{k}} - P^{-\frac{1}{k}}) dP \quad (3-127)$$

Solutions are

$$LHS = k \frac{\rho_t V_M^2 L_M}{2 p_0 L_t} \exp(-\lambda P_M^{-\frac{1}{k}}) - k \frac{\rho_t V_0^2 L_0}{2 p_0 L_t} \exp(-\lambda P_0^{-\frac{1}{k}}) \quad (3-128)$$

and

$$RHS = \frac{\alpha_0}{1 - \alpha_0} \left[ P_R \int_{P_0}^{P_M} \exp(-\lambda P^{-\frac{1}{k}}) P^{-\frac{k+1}{k}} dP - \int_{P_0}^{P_M} \exp(-\lambda P^{-\frac{1}{k}}) P^{-\frac{1}{k}} dP \right] \quad (3-129)$$

Integrating the first integral on RHS

$$RHS = \frac{\alpha_0}{1 - \alpha_0} \left[ \frac{k P_R}{\lambda} \left( \exp(-\lambda P_M^{-\frac{1}{k}}) - \exp(-\lambda P_0^{-\frac{1}{k}}) \right) - \int_{P_0}^{P_M} \exp(-\lambda P^{-\frac{1}{k}}) P^{-\frac{1}{k}} dP \right]$$

A special case is for entrapped air problem for which the liquid column is at rest and integration is from initial condition to maximum pressure , for which  $P = P_M$ . The limits are :  $x_0 = 0$  ;  $L_0 = L$  ;  $V_0 = 0$  ; and  $V_M = 0$ . Since, for this special case the LHS vanishes,

$$0 = \frac{k P_R}{\lambda} \left[ \exp(-\lambda P_M^{-\frac{1}{k}}) - \exp(-\lambda) \right] - \int_{P_0}^{P_M} \exp(-\lambda P^{-\frac{1}{k}}) P^{-\frac{1}{k}} dP \quad (3-131)$$

The implicit solution in terms of  $P_R$  is

$$P_R = \frac{\lambda I(P_M)}{k \left[ \exp(-\lambda P_M^{-\frac{1}{k}}) - \exp(-\lambda P_0^{-\frac{1}{k}}) \right]} \quad (3-132)$$

where the integral  $I(P_M)$  is related to the incomplete Gamma function, Abramowitz (1965)

$$I(P_M) = \int_{P_0}^{P_M} \exp(-\lambda P^{-\frac{1}{k}}) P^{-\frac{1}{k}} dP \quad (3-133)$$

$$I(P_M) = k \Gamma(1-k) [P_0^{\frac{k-1}{k}} \gamma^*(1-k, \lambda P_0^{-1/k}) - P_M^{\frac{k-1}{k}} \gamma^*(1-k, \lambda P_M^{-1/k})] \quad (3-134)$$

$$\gamma^*(a, x) = \frac{x^{-a} \gamma(a, x)}{\Gamma(a)} \quad (3-135)$$

for which  $a = 1 - k$ . Using IMSL functions for the incomplete gamma function  $\gamma^*$  Equation (3-132) can be solved for  $P_M$  as a function of  $P_R$  and  $\lambda$ .

The momentum equation for constant length  $L_\ell$  may be expressed

$$\rho_\ell L_\ell \frac{dV}{dt} = p_R - p - L_\ell \frac{\rho_\ell f V^2}{2D} \quad (3-136)$$

It can be shown that this equation coupled with Equation (3-119) yields Equation (3-129) as well, resulting in the same result. In fact, finite difference solutions of both variable length Equation (3-116) and constant length Equation (3-136) prove that the initial liquid length  $L_\ell$  is not a variable in the case of entrapped air from rest.

The similarity parameter of the thermodynamic parameter of the polytropic relation constant  $n$  was set to be 1.4. Dimensionless maximum interface pressure, velocity, and gas volume of lumped liquid and lumped gas mass methods are presented in Figure 3.8. The time of peak interface pressure and the magnitude of maximum interface velocity are different; however, the magnitude of peak interface pressure and minimum gas volume are, as expected, the same for both the constant and the variable liquid length model.

The closed form of interface  $P_M$  solutions – for the Case I model with variable length, and the Case II model with constant length – are exactly same. That means interface  $P_M$  is the same for both the variable liquid length and the constant length model, regardless of the friction term. Furthermore, interface  $P_M$  for both models is independent of initial liquid and length for the frictionless case, even though variable liquid length analysis includes the similarity parameter of initial length ratio of liquid and gas in the dimensionless governing equation. The size of initial gas length influences interface  $P_M$  only when a friction term is introduced. Initial liquid length does not have any influence on interface  $P_M$ , even with the friction term because the closed forms of interface  $P_M$  solutions do not include the initial length of liquid. Minimum gas volume is the same for both constant and variable liquid length as expected. Because of the closed form of  $x_M$  solutions for the variable length model,

and solutions for the constant length model are exactly the same.

This means that the values of maximum interface pressure are the same for both Cases I and II in both friction and frictionless cases. Cabrera(1992) investigated these results based on his numerical results. He tried to prove the same maximum pressure for both Case I and II, based on his mathematical findings. Additional liquid length in Case I is canceled by the additional term . There was a discussion about this problem between Cabrera(1992) and Karney (1994), but neither of them was able to prove a closed form of solution.

The reason that interfaces  $P_M$  and  $x_M$  are the same in both models is that increased momentum due to additional liquid length is canceled due to momentum flux,  $\rho V^2/2$  Cabrera. *et al* (1992), and Karney *et al*, (1994). However, the time history of interface pressure and gas volume, as shown in Figure 3.8, is different in each model. Moreover, time history of interface velocity and magnitude of maximum interface velocity as shown in Figure 3.8 are different in each model.

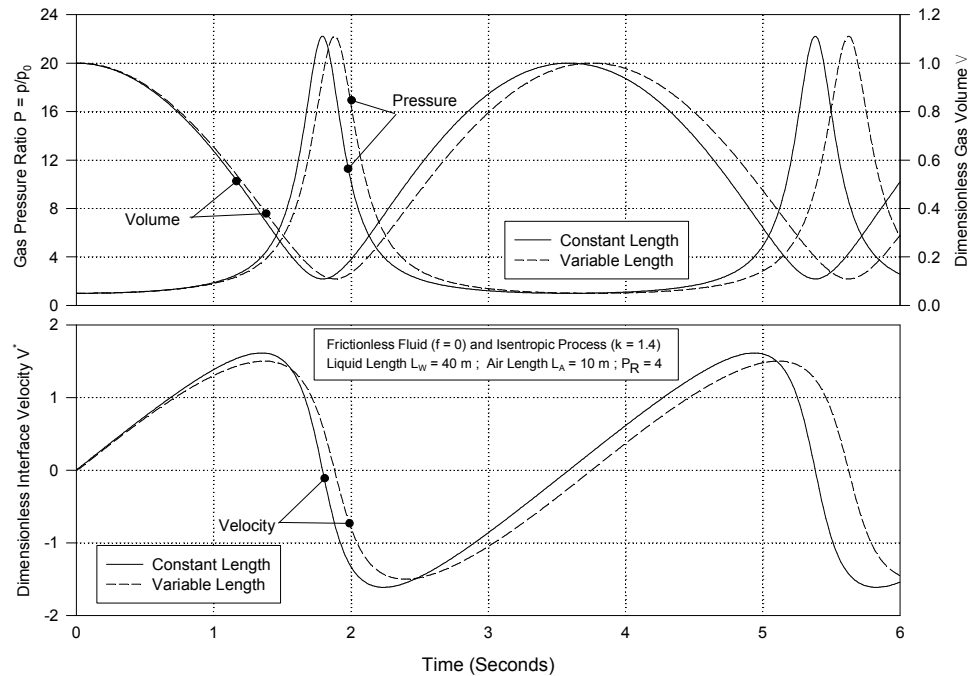


Figure 3.8 Comparison of Inelastic Liquid Column Models (Cases I and II)

The results of the closed form solution are presented in Figure 3.9, which shows that maximum pressure increased as  $\lambda$ , which can be increased by either volume of air and/or Darcy friction coefficient  $f$ . Both finite difference and closed form solutions yield exactly the same result for the entrapped gas solution. In fact, the assumptions correspond to the parameters in Equation (3-105); that is,  $P_M$  depends only on  $P_R$ ,  $\lambda$ , and  $\alpha_0$  for a constant  $k$ , in this instance 1.4 for air. Actually, for the entrapped air problem with the liquid column starting from rest the peak pressure  $P_M$  at  $V_M = 0$  can be shown to be independent of  $\alpha_0$ . Indeed the main parameter associated with the gas phase is  $\lambda = f L_g / D$ .

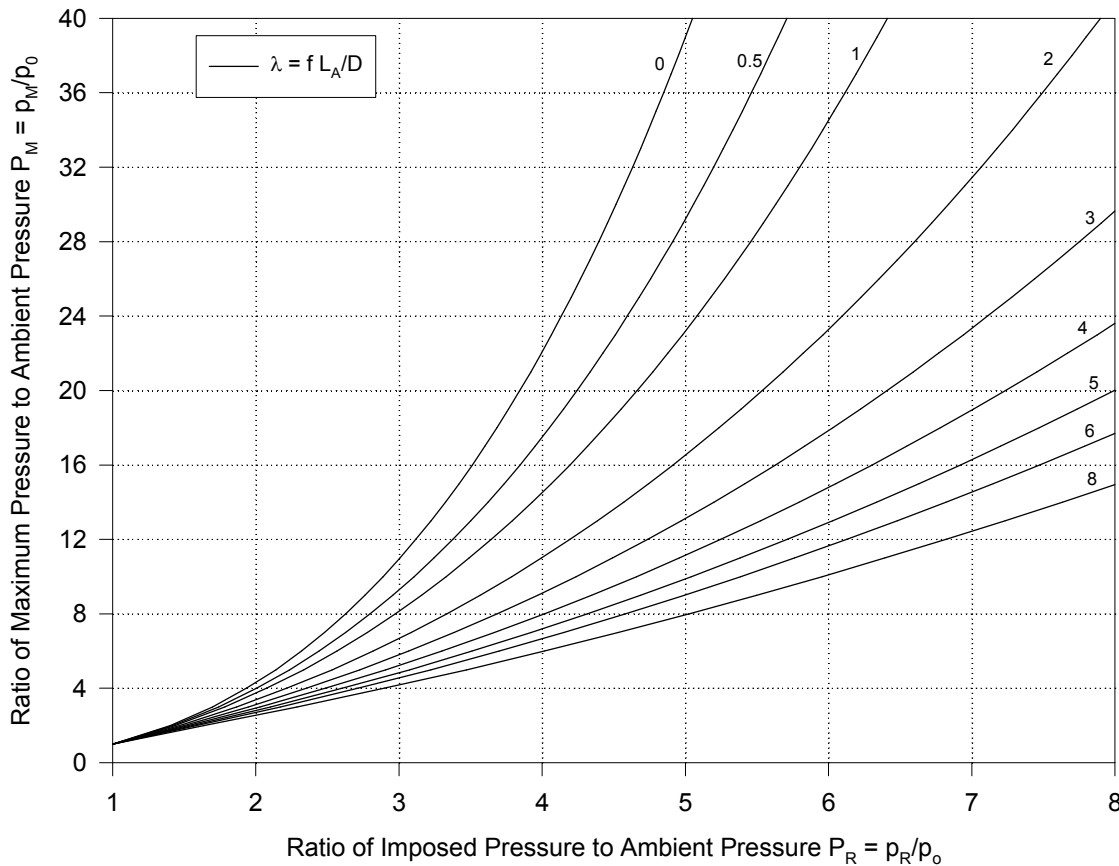


Figure 3.9 Entrapped Air Solution for Inelastic Liquid Column (Cases I and II)

### 3.5 Gas Venting System

Entrapped gas in a confined system can cause unwanted higher transient pressure. Either slow opening of an upstream valve or a gas venting system may reduce undesirable higher transient pressure. An orifice was regarded as a gas venting system as shown in Figure 3.7. Analysis of the whole system was assumed to be an adiabatic process. The lumped liquid and gas mass method was applied to derive governing equations. Mass conservation equations of the liquid and gas phases are valid in the gas venting system. The momentum equation is also valid. It is unlikely that the gas mass of a confined system is variable. The energy equation of the gas phase is:

$$\frac{dp}{dt} = -k \frac{p}{\nabla} \frac{d\nabla}{dt} + k \frac{p}{m} \frac{dm}{dt} \quad (3-137)$$

Mass flow rate out of the orifice opening,  $dm/dt$ , is defined by:

$$\frac{dm}{dt} = -C_d A_0 \rho_g Y \sqrt{\frac{2(p-p_b)}{\rho_g}} \quad (3-138)$$

The expansion factor for adiabatic flow is defined by:

$$Y = \sqrt{\frac{\frac{k}{k-1} \left(\frac{p_b}{p}\right)^{\frac{2}{k}} \frac{1-\left(\frac{p_b}{p}\right)^{\frac{k-1}{k}}}{1-\frac{p_b}{p}}}{\left(\frac{2}{k+1}\right)^{\frac{k+1}{k-1}} \frac{k}{2\left(1-\frac{p_b}{p}\right)}}} \quad (3-139)$$

If  $p_b/p$  is less than 0.528 (air;  $k = 1.4$ ), then the orifice becomes choked:

$$Y = \sqrt{\left(\frac{2}{k+1}\right)^{\frac{k+1}{k-1}} \frac{k}{2\left(1-\frac{p_b}{p}\right)}} \quad (3-140)$$

### 3.6 Heat Transfer

The thermodynamic parameter, n, in the empirical polytropic relation is usually assumed to be constant. However, it does change with compression and expansion of gas Graze (1996). Moreover it does not reproduce high damping and frequency shortening of experimental data of pressure time history. Particularly, if the pressure of entrapped gas is below atmospheric pressure, such as in the case of a cavity, damping is huge. It cannot be regenerated with only pipe friction and minor loss such as valve and flowmeter, (Graze 1968) and Nakagawa and Takenaka (1994). That means heat transfer plays an important role in the frequency and additional damping of each peak in the pressure time history. In this analysis, the temperature of gas was assumed to be between freezing and boiling temperature of liquid. Latent heat was not considered.

The energy equation with control volume CDEF in Figure 3.1 including the heat transfer term can be expressed in the following form, Graze (1972) and Moody (1990)

$$p \frac{dV}{dt} - q + \frac{dU}{dt} = 0 \quad (3-141)$$

Applying the perfect gas state equations:

$$U = \frac{pV}{k-1} \quad (3-142)$$

$$pV = M_g R_g T, p_0 V_0 = M_g R_g T_0 \quad (3-143)$$

The conduction and radiation heat transfer rates are relatively negligible. Convection heat transfer is dominant. The heat transfer term, q, can be defined as follows:

$$q = HA_q(T_0 - T) \quad (3-144)$$

The energy equation becomes:

$$\frac{dp}{dt} = -\frac{k}{\forall} p \frac{d\forall}{dt} + \frac{(k-1)HA_q p_0 \forall_0}{\forall M_g R_g} \left( 1 - \frac{p\forall}{p_0 \forall_0} \right) \quad (3-145)$$

The difficult part of energy equations is how to define the heat transfer coefficient, H. Even though the process of convection heat transfer is transient, a steady state condition was assumed because of complexities. Although convection heat transfer can be both free and forced, free convection theory was applied. In fact, Graze (1996) performed an experiment with air gas and a glass cylinder to determine the heat transfer coefficient, H, based on the idea of a simplified equation for air gas case with vertical plane case, McAdam (1954)

$$H = \alpha |\Delta T|^{1/3} \quad (3-146)$$

Graze (1996) suggested the average value of 3.5 for  $\alpha$  in the case of S.I. units, even though  $\alpha$  varies with the compression and expansion of air gas, Graze (1996). The value 3.5 is higher than McAdam's value 1.4, which is based only on free convection heat transfer with vertical planes. The Runge-Kutta method was applied to solve energy and mass conservation equations of gas phase, and mass conservation and momentum equation of liquid phase with the same initial conditions for a variable liquid length case of lumped liquid and gas mass.

### 3.7 Frequency Analysis

The results of thermal damping effect are presented in Figure 3.10. The heat transfer coefficient for an air and glass pipe as recommended by Graze (1996) is:

$$H = 3.5 |\Delta T|^{1/3} \quad (3-147)$$

Figure 3.10 shows that there is additional damping without pipe friction and minor loss, and the period of maximum interface pressure is shortened. The first peak of both model agrees

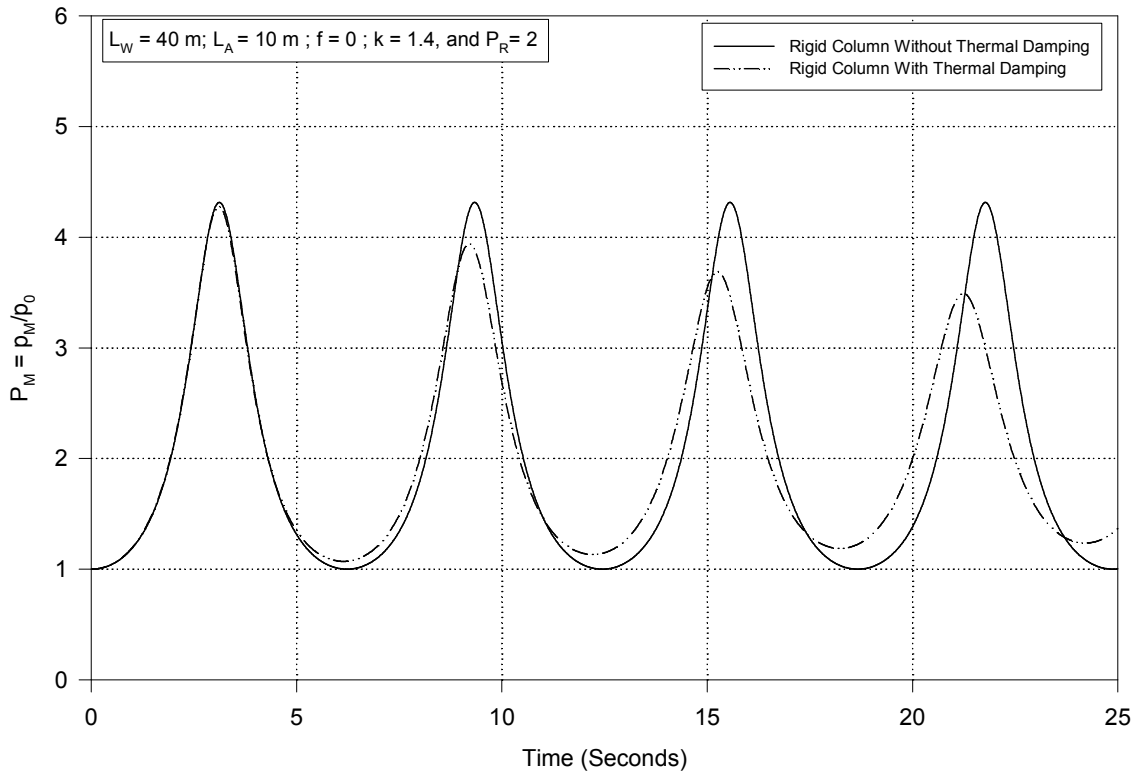


Figure 3.10 Thermal Damping Effect on Variable Length Rigid Column Modeling

very well since the compression period is close to the adiabatic condition. After the first peak, differences of maximum interface pressure between the two models increases as the number of peaks pass. This is because once expansion (deceleration) started, large amounts of heat transfer were introduced. Additional damping by heat transfer explains why there is always extra damping in the measurement pressure wave data compared to the numerical model, which includes only pipe friction and minor loss.

The phenomenon of period shortening is common in the measurement data. Pipe friction and minor loss terms cannot change the period of peak pressure; instead they only reduce the magnitude of pressure and velocity. However, the heat transfer term can change the period of peak pressure and also reduce the magnitude of pressure and velocity. This is because the heat transfer term changes the stiffness of an entrapped gas system, whereas pipe

friction and minor loss do not. It is clearly shown in Figure 3.11 that the stiffness of an entrapped gas system without thermal damping models, with  $f = 0$  and  $f = 0.03$ , coincides with different maximum displacement. However the stiffness of air mass with a thermal damping model is changed.

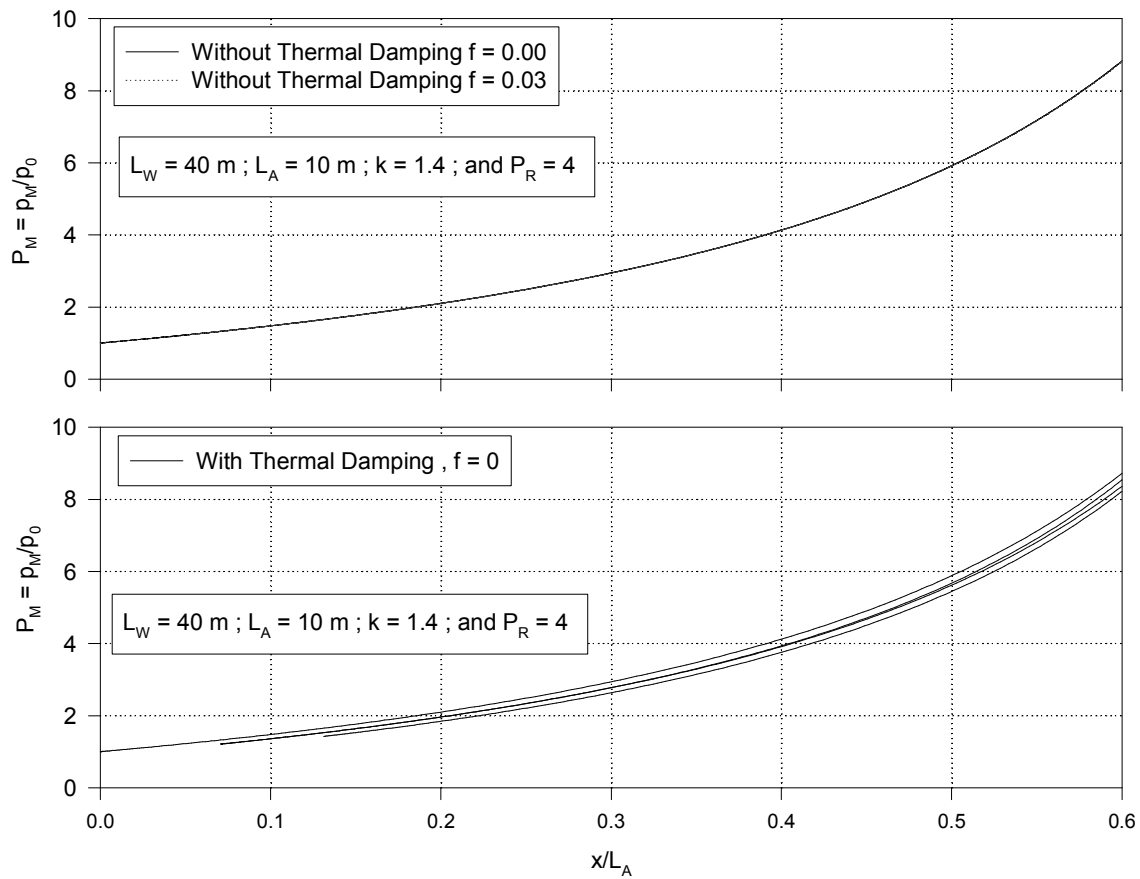


Figure 3.11 Thermal Damping Effect on Lumped Mass Stiffness (Air Spring Effect)

# CHAPTER 4

## EXPERIMENTAL APPARATUS AND INSTRUMENTATION

### **4.1 Description of Test Facility**

Laboratory experiments were conducted in the Hydraulics Laboratory of the School of Civil and Environmental Engineering of the Georgia Institute of Technology for the purpose of ascertaining the effect of entrapped air on pipeline transients. The experimental apparatus depicted in Figures 4.1 and 4.2 consists of a pressure tank and an acrylic plastic (Plexiglass) pipe of maximum total length  $L_T = 36.22$  feet with internal diameter  $D = 1.025$  inches and wall thickness  $e = 0.25$  inch.

At the upstream end of the pipe system is an ASME certified pressure tank which is 30 inches in diameter and approximately 48 inches tall, with a sight glass for water level control and measurement, and regulated air pressure which could be controlled up to 100 psig. The air pressure was measured by a test gauge with 0.5 psi divisions. For air venting tests, a turbine flow meter with high frequency response was installed at a distance of 7 ft from the pipe entrance, as shown in Figure 4.2. The ball valve utilized to generate the transient was always at a fixed location of 20.0 ft from the pressure tank. For all tests, the pipe was completely full of water from the pressure tank to the ball valve, corresponding to a fixed length of water column, defined by  $L_W = 20.0$  ft. Beyond the valve up to the end of the test facility, different lengths of acrylic pipe  $L_A$  were attached. Finally, the test pipe terminated either at: (a) a blanked end cap for entrapped air experiments, or (b) an orifice plate for air venting tests. In both instances, the end of the pipe was securely fixed with a robust strut to minimize axial motion due to the severe transient caused by rapid opening of the ball valve.

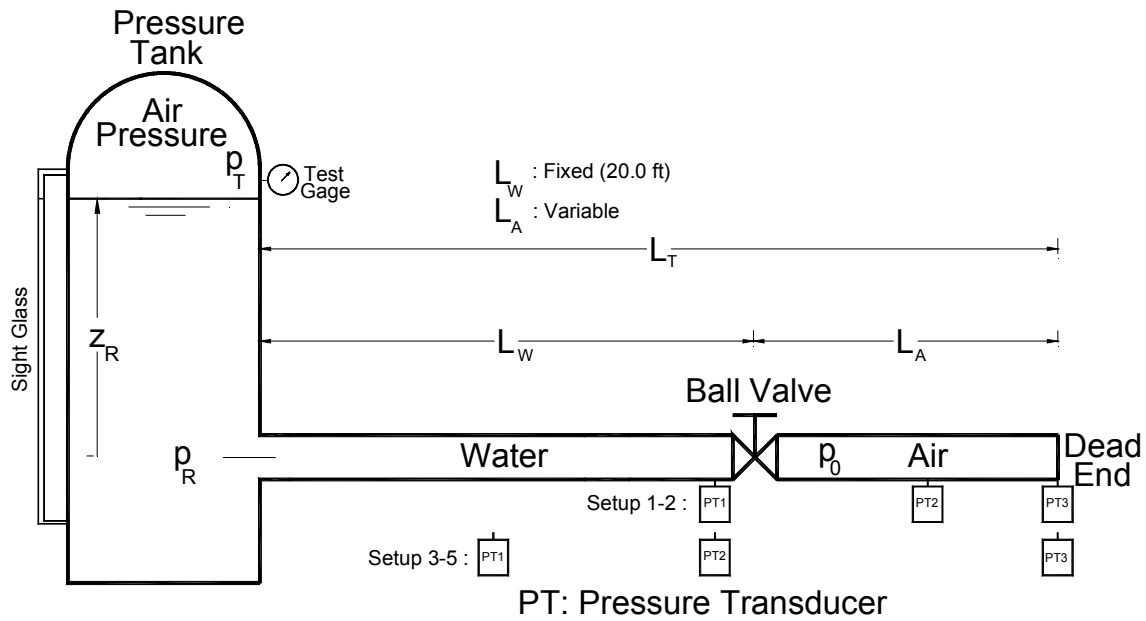


Figure 4-1. Schematic of Test Facility for Entrapped Air Experiments with Dead End

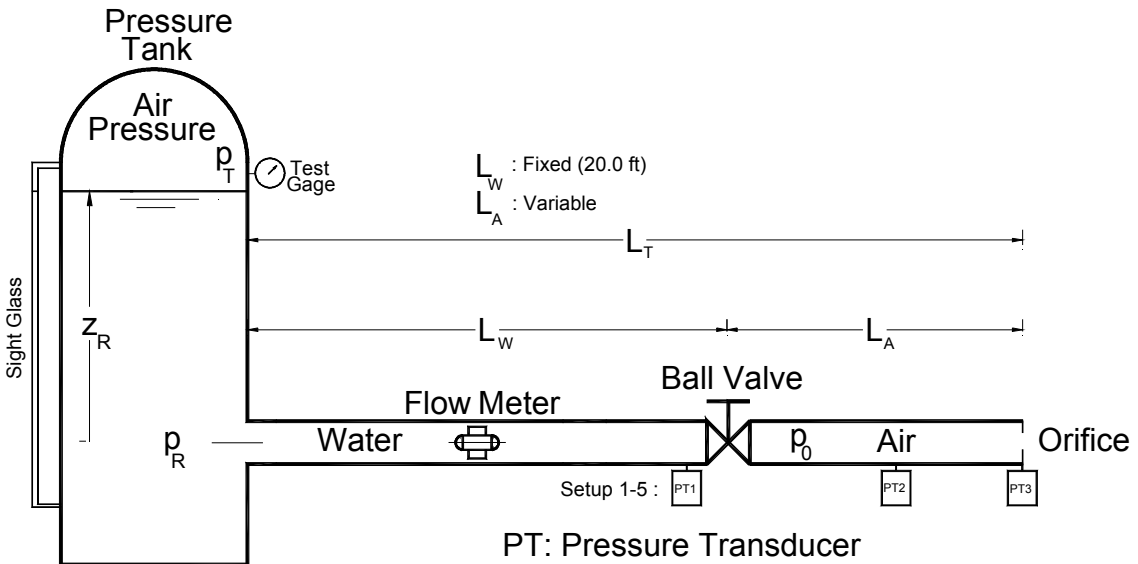


Figure 4-2. Schematic of Test Facility for Air Venting Experiments with Orifice

The length of the piping beyond the ball valve was varied by swapping various sections of the Plexiglass pipe, which was flanged on each end. Short and long pre-fabricated sections of pipe could be inserted to vary the length of the air column from the actuated ball valve to the end of the pipe. Five lengths of piping from the ball valve to the terminal end of pipe were tested. The lengths of the five air column lengths  $L_A = 16.23$  ft,  $10.10$  ft,  $4.85$  ft,  $2.77$  ft, and  $1.23$  ft, and corresponding mean void fractions  $\alpha_0 = L_A / (L_W + L_A)$  are tabulated in Tables 4.1 and 4.2. For the venting experiments, sharp-edged orifices having nominal diameters ranging from  $1/16$ -inch to  $1/2$ -inch in steps of  $1/16$  inch were mounted at the end of pipeline.

## **4.2 Description of Instrumentation**

The tank reference pressure  $p_R$  was determined by means of the test gauge  $p_T$  and the water level in the sight glass shown in Figures 4.1 and 4.2. For transient flow measurement for the venting experiments, a turbine flow meter was installed 7 ft from the pressure tank. A rotary variable differential transformer (RVDT) was mounted on the shaft of the ball valve to have a continuous output of valve angle during the opening phase of the valve. Three diaphragm-type pressure transducers were utilized at various locations along the pipe to sense transient pressure.

### **4.2.1 Data Acquisition System**

A fast response data acquisition system was utilized to collect, digitize, and record voltages from five transient signals; namely, ball valve angle  $\theta$ , flow  $Q$ , and three pressures. National Instruments software LABVIEW was programmed to collect the data using a PC. A schematic flow chart of the data acquisition system is presented in Figure 4.3. The five DC signals were fed into a National Instruments 12-bit A-D card, Model AT-MIO-16-H, which has a  $2.5$  mV resolution between  $0$  and  $10$  volts. The software used to collect data was LABVIEW VER. 5.0. Data were taken at a rate of  $2000$  readings/second.

Table 4.1 Summary of Experimental Configurations with Dead End (Entrapped Air)

Setup	Air Length $L_A$ (ft)	Air Void Fraction $\alpha_0$	Pressure Transducer Location From Reservoir (ft)		
			PT1	PT2	PT3
1	16.23	0.4481	19.7 (Valve)	30.1 (Mid-Air)	36.2 (Dead End)
2	10.10	0.3357	19.7 (Valve)	24.8 (Mid-Air)	30.1 (Dead End)
3	4.85	0.1952	10.9 (Mid-Water)	19.7 (Valve)	24.8 (Dead End)
4	2.77	0.1217	10.9 (Mid-Water)	19.7 (Valve)	22.8 (Dead End)
5	1.23	0.0580	10.9 (Mid-Water)	19.7 (Valve)	21.2 (Dead End)

Table 4.2 Summary of Experimental Configurations with Orifice (Venting)

Setup	Air Length $L_A$ (ft)	Air Void Fraction $\alpha_0$	Pressure Transducer Location From Reservoir (ft)		
			PT1	PT2	PT3
1	16.23	0.4481	19.7 (Valve)	30.1 (Mid-Air)	36.2 (Orifice)
2	10.10	0.3357	19.7 (Valve)	24.8 (Mid-Air)	30.1 (Orifice)
3	4.85	0.1952	19.7 (Valve)	22.8 (Mid-Air)	24.8 (Orifice)
4	2.77	0.1217	19.7 (Valve)	21.2 (Mid-Air)	22.8 (Orifice)
5	1.23	0.0580	19.7 (Valve)	20.1 (Mid-Air)	21.2 (Orifice)

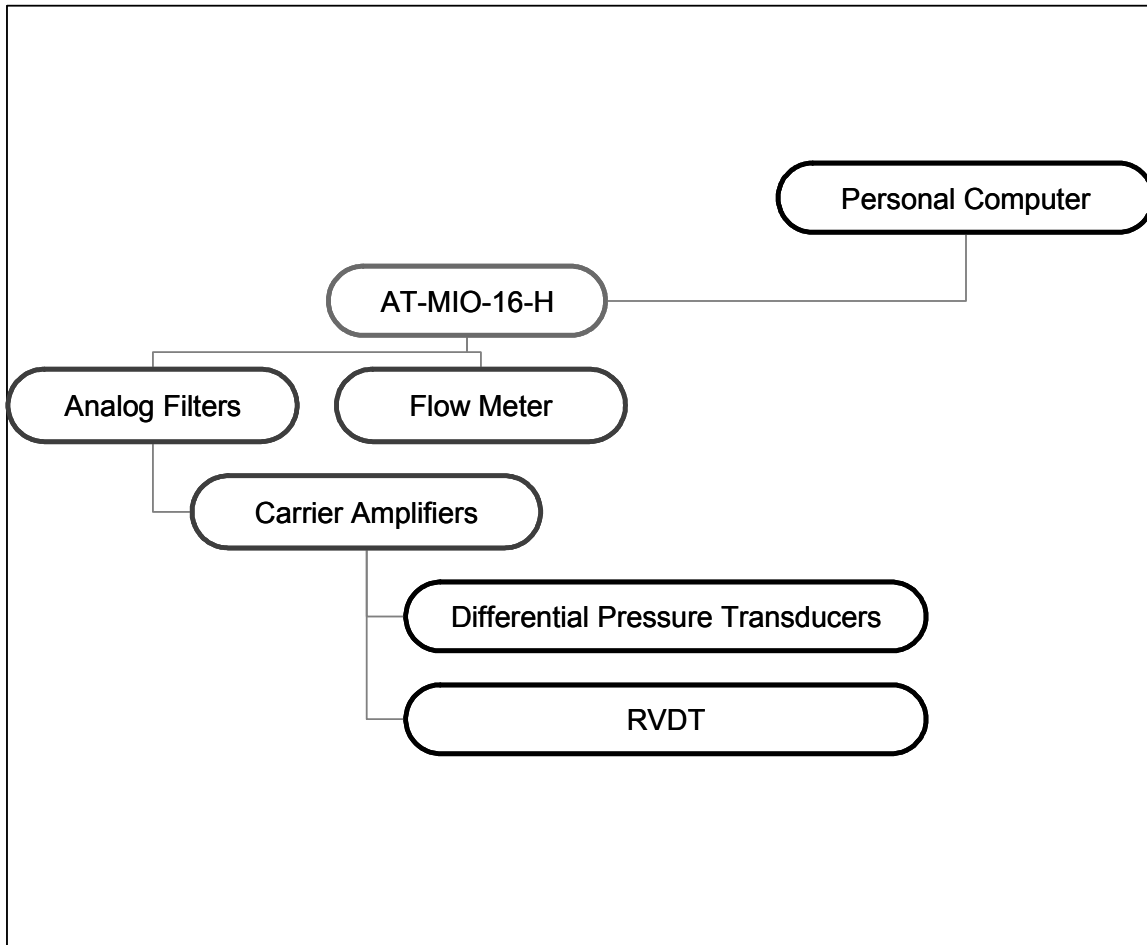


Figure 4.3 Schematic of Data Acquisition System

#### 4.2.2 Turbine Flow Meter

A Flow Technology Model FT turbine flow meter was installed 7 feet from the pressure tank. Signal conditioning provided by the manufacturer generated a 0 -10 Volt DC output that was read in by the data acquisition card. The manufacturer provided a certified calibration curve, relating flow rate to output DC voltage. The flow characteristics were confirmed gravimetrically with water for a range of discharges. Figure 4.4 shows both calibrations.

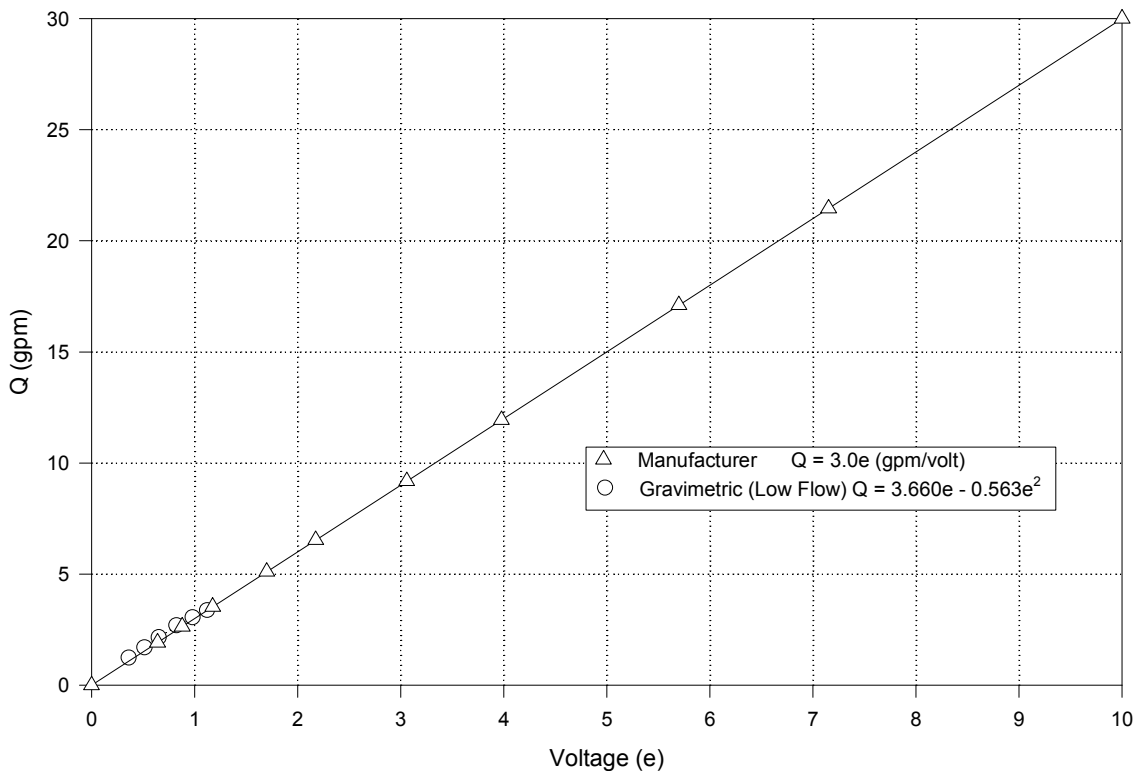


Figure 4.4 Calibration of Turbine Flow Meter

#### 4.2.3 Ball Valve

A Jamesbury Model F-515-S6-F-66 ball valve was installed at the end of the water column, 20.0 ft from the pressure tank. The ball valve was controlled by a ROTORK pneumatic actuator, Model R180SR12, mounted on the top of the valve. By maintaining constant air pressure by means of a pressure regulator, the repeatability of the valve opening time was ensured.

#### 4.2.4 Rotary Variable Differential Transformer (RVDT)

For accurate determination of the angular position of the ball valve, a rotary variable differential transformer (RVDT), Schaevitz Model R30A was mounted on the top of the valve actuator. The AC type transducer was excited by a carrier amplifier with frequency of 2400 Hz. The DC output ranged from - 5 to + 5 volts and was accurately calibrated against a large protractor. Figure 4.5 shows the results of RVDT calibration.

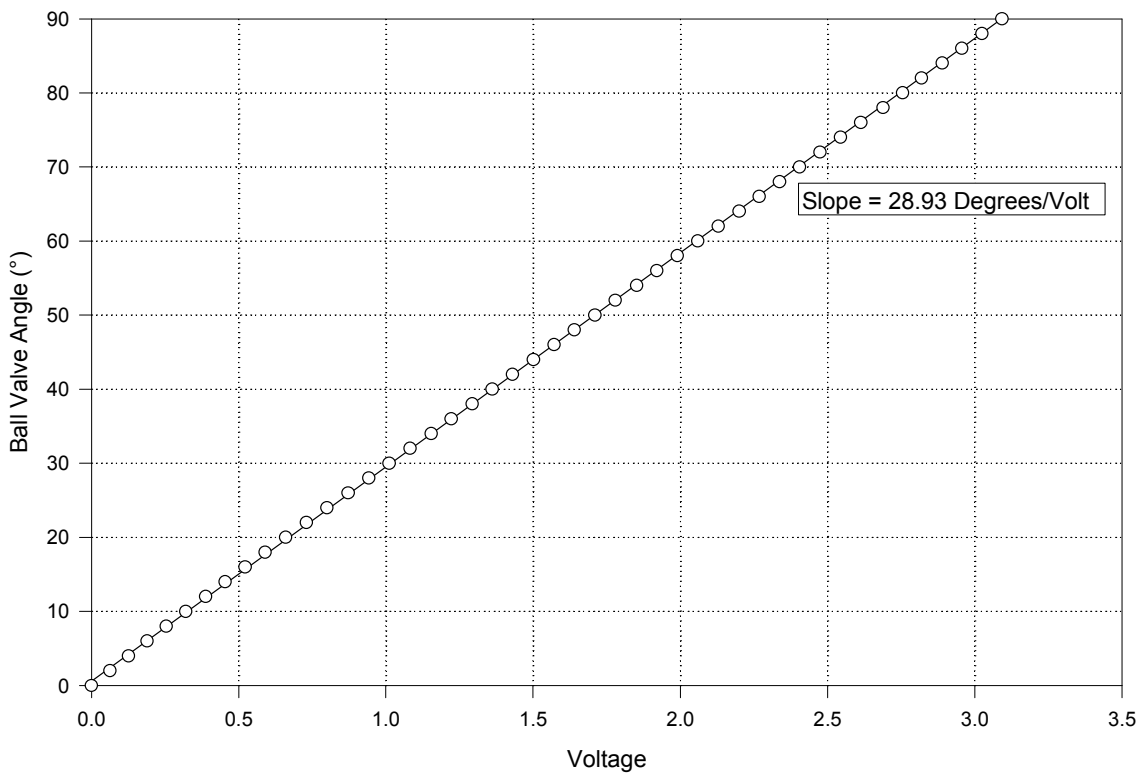


Figure 4.5 Characteristics of Rotary Variable Differential Transducer (RVDT)

### 4.3 Hydraulic Characteristics of System Components

Fluid resistance of the piping system consists of pipe friction and minor losses such as those caused by the flow meter and the valve. The flow characteristics of turbine flow meter, ball valve, and eight orifices were determined under steady flow conditions. In addition, the resistance characteristics of the pipe entrance, straight pipe, flow meter, and ball valve were measured over a range of flow rates. Using air-water and mercury manometers for head-loss measurements and the turbine flow meter for flow determination, head-loss data were determined for four different configurations : (1) straight pipe head loss without ball valve or turbine flow meter, (2) head loss across ball valve itself, (3) head loss across turbine flow meter, and (4) finally, the entire head loss from pressure tank to downstream side of orifice at end of test pipe.

### **4.3.1 Hydraulic Resistance Characteristics of Straight Pipe**

Based upon careful steady-state measurements of straight pipe head loss the Darcy-Weisbach resistance coefficient  $f$  was determined over a range of Reynolds numbers, the results of which are correlated in Figure 4.6. It is contended that the empirical correlation yields Darcy  $f$  values greater than those for smooth pipe behavior because of offset at flanges, and the existence of nonuniform internal diameters. The energy equation was used to calculate the head loss  $H_L$  due to friction factor  $f$  and minor loss  $K_L$  from section 1 to 2

$$h_1 + \frac{V_1^2}{2g} = h_2 + \frac{V_2^2}{2g} + \left( \frac{fL}{D} + \Sigma K_L \right) \frac{V^2}{2g} \quad (4-1)$$

### **4.3.2 Head-Loss Characteristics of Ball Valve**

Pressure drop measurements were made at distances 10 ft upstream and downstream of the ball valve under steady flow conditions. Care was taken to establish steady flow with the ball valve fixed at various openings, ranging from fully open down to closed position  $\theta$  in  $5^\circ$  increments. For valve angles greater than  $\theta = 22.5^\circ$  there was water on both sides of the valve. However, for angles less than  $\theta = 22.5^\circ$ , and especially for quite small openings, the very small flow rate negated the use of the turbine flow meter. For these small ball valve openings the downstream flange connection to the valve was removed, allowing for direct discharge into air, whereupon the water flow was determined gravimetrically. For all tests the variation of the ball valve head-loss coefficient  $K_L$  with rotary angle  $\theta$  is plotted in Figure 4.7.

### **4.3.3 Head-Loss Characteristics of Flow Meter and Entire Piping System**

The resistance characteristics of the entire pipe system, including full open ball valve, pipe entrance, straight pipe, orifice, and flow meter are correlated in Figure 4.8 in terms of total loss coefficient  $\Sigma K_L$ . It is noticed that the Reynolds number effect is not only due to

the straight pipe effect attributed to the Darcy  $f$  (Figure 4.6), but also affected by the flow meter, which definitely shows a Reynolds number influence reflected by  $\Sigma K_M$ .

The smaller 3/4-inch diameter turbine flow meter compared to the 1-inch internal diameter  $D$  of the Plexiglass resulted in considerable hydraulic resistance compared to the pipe itself. Indeed, 20 ft of 1-inch pipe with a Darcy  $f = 0.025$  yields the ratio  $fL_w/D = 6$ , compared to values of  $\Sigma K_M$  ranging from above 26 to nearly 34.

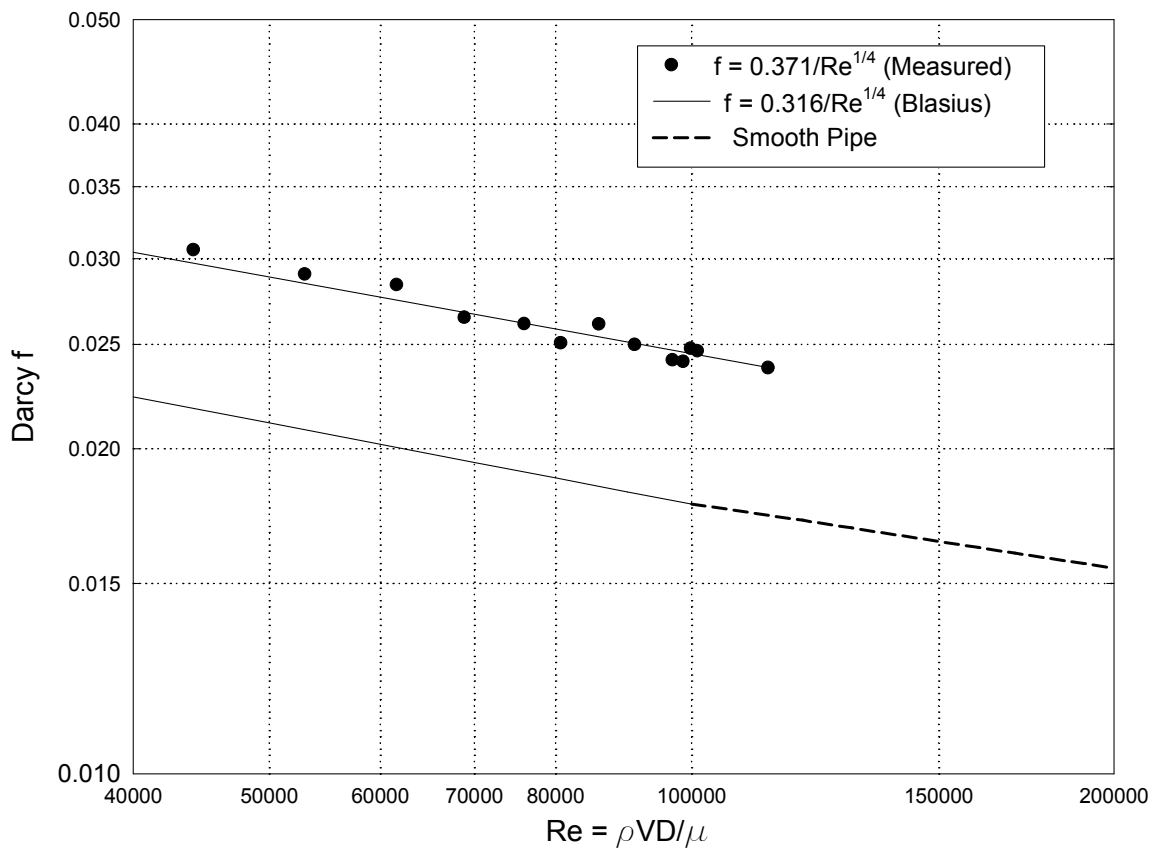


Figure 4.6 Measured Darcy Friction Factor for Plexiglass Pipe

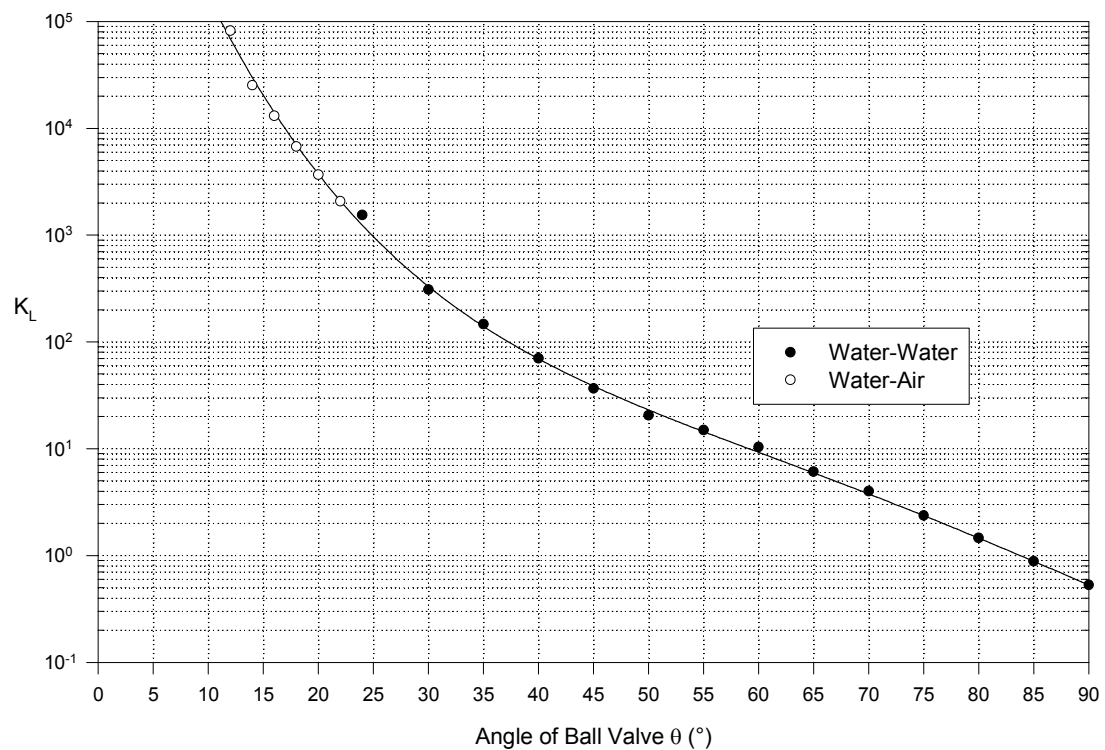


Figure 4.7 Measured Head Loss Characteristics of Ball Valve

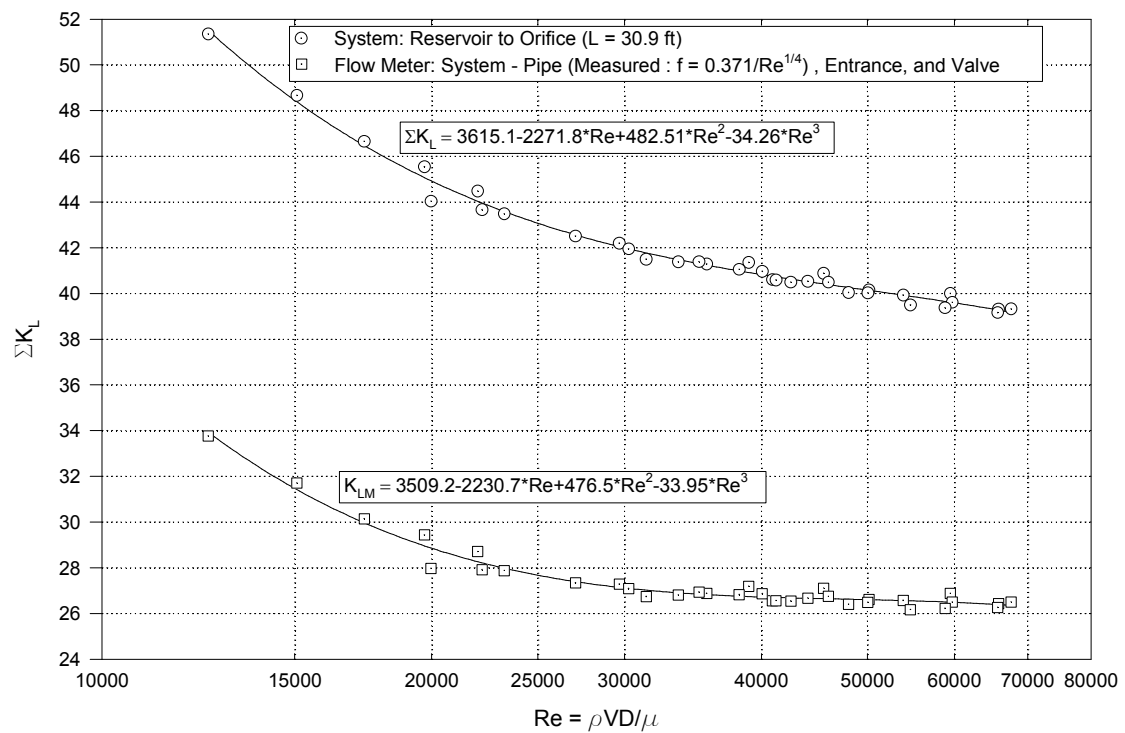


Figure 4.8 Pipe System Head Loss Characteristics

#### 4.4 Pressure Transducers

Three Model KP15 Pace differential reluctance diaphragm type pressure transducers were mounted at flanges along the test pipe. The actual location PT1, PT2, and PT3 of the three transducers for various tests can be found in Tables 4.1 and 4.2. Distance is given in feet from the pressure tank. Each transducer had a stainless steel diaphragm with nominal rating of 500 psid. A rack type carrier amplifier system provided excitation and signal conditioning for the reluctance type pressure transducers, resulting in a DC voltage output ranging from - 5 to + 5 volts. Attenuator settings of X200, X100, and X50 were utilized to improve resolution for various pressure ranges. The transducers were calibrated with a dead weight tester from 0 to 500 psig, for which the results are shown in Figure 4.9.

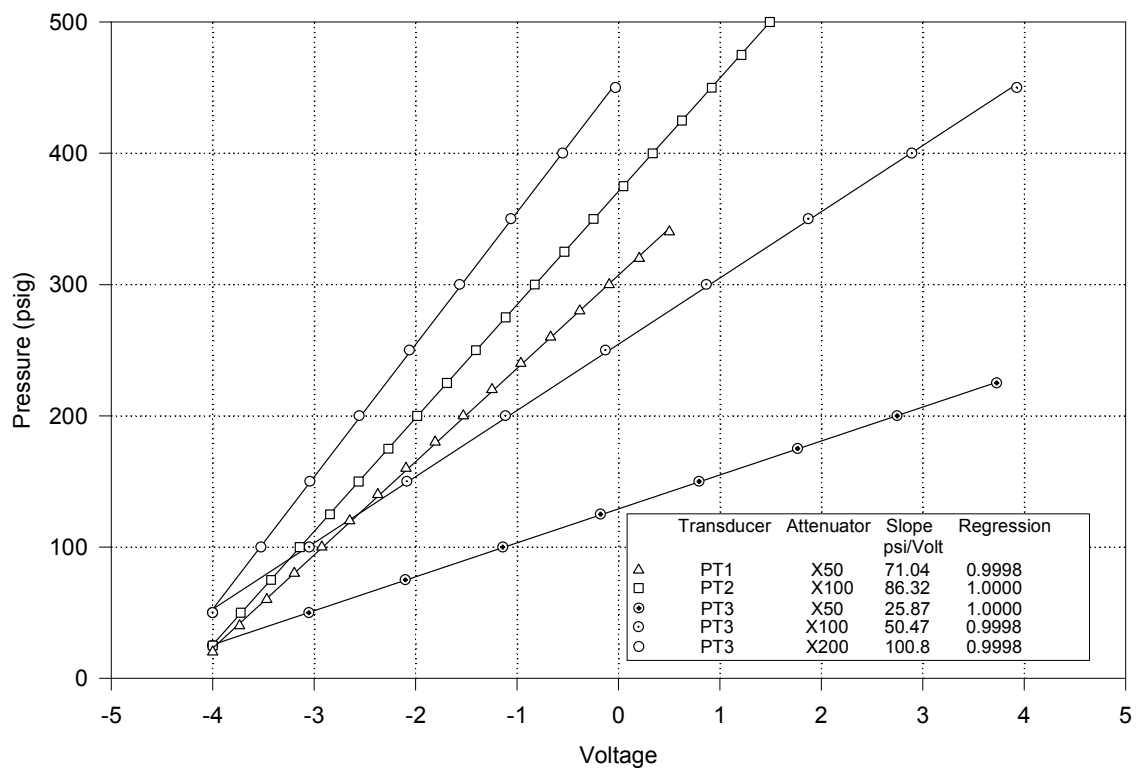


Figure 4.9 Calibration of Pressure Transducers with Dead Weight Tester

#### 4.5 Orifice Flow Characteristics

Sharp-edged orifices ranging in size from 1/16-inch to 1/2-inch were installed for determining quasi-steady transient flow. The orifice discharge coefficient  $C_d$  is defined by

$$Q = C_d A_0 \sqrt{\frac{2\Delta p}{\rho}} \quad (4-2)$$

where  $Q$  is the volumetric flow,  $A_0$  is the area of the orifice hole, and  $\Delta p$  is the differential

$$A_0 = \frac{\pi}{4} d^2 \quad (4-3)$$

pressure across the orifice flange. For a smaller size of orifice, it is acceptable to maintain the atmospheric pressure as an exit ambient pressure. However for larger orifices, it is technically difficult to measure the orifice discharge coefficients with atmospheric pressure as an exit ambient pressure because of the small spaces available to collect large volumes of discharge. Orifice discharge coefficients for larger orifices ranging from 1/4-inch to 1/2-inch were calculated using pressure difference across the orifice with water on both sides. Results correlating the measured flow with ideal flow are presented in Figures 4.10 and 4.11, showing a linear relationship. The averaged orifice discharge coefficient for each orifice was obtained from linear regressions.

The discharge coefficient  $C_d$  under both free jet (Figure 4.10) and submerged jet (Figure 4.11) conditions is correlated with the orifice Reynolds number in Figure 4.12. The orifice Reynolds number is defined as

$$Re = \frac{\rho V d}{\mu} \quad (4-4)$$

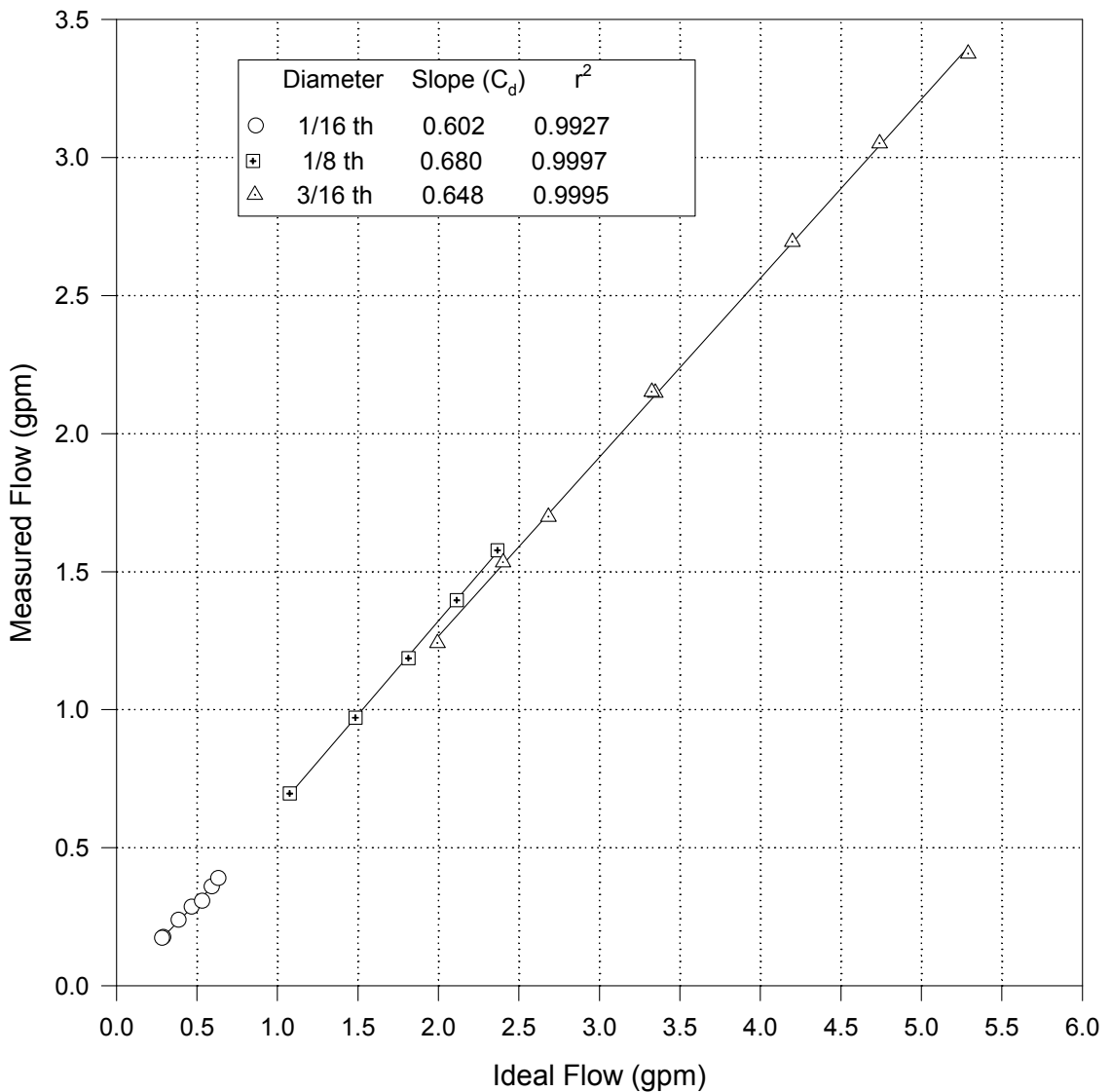


Figure 4.10 Free Jet Orifice Characteristics

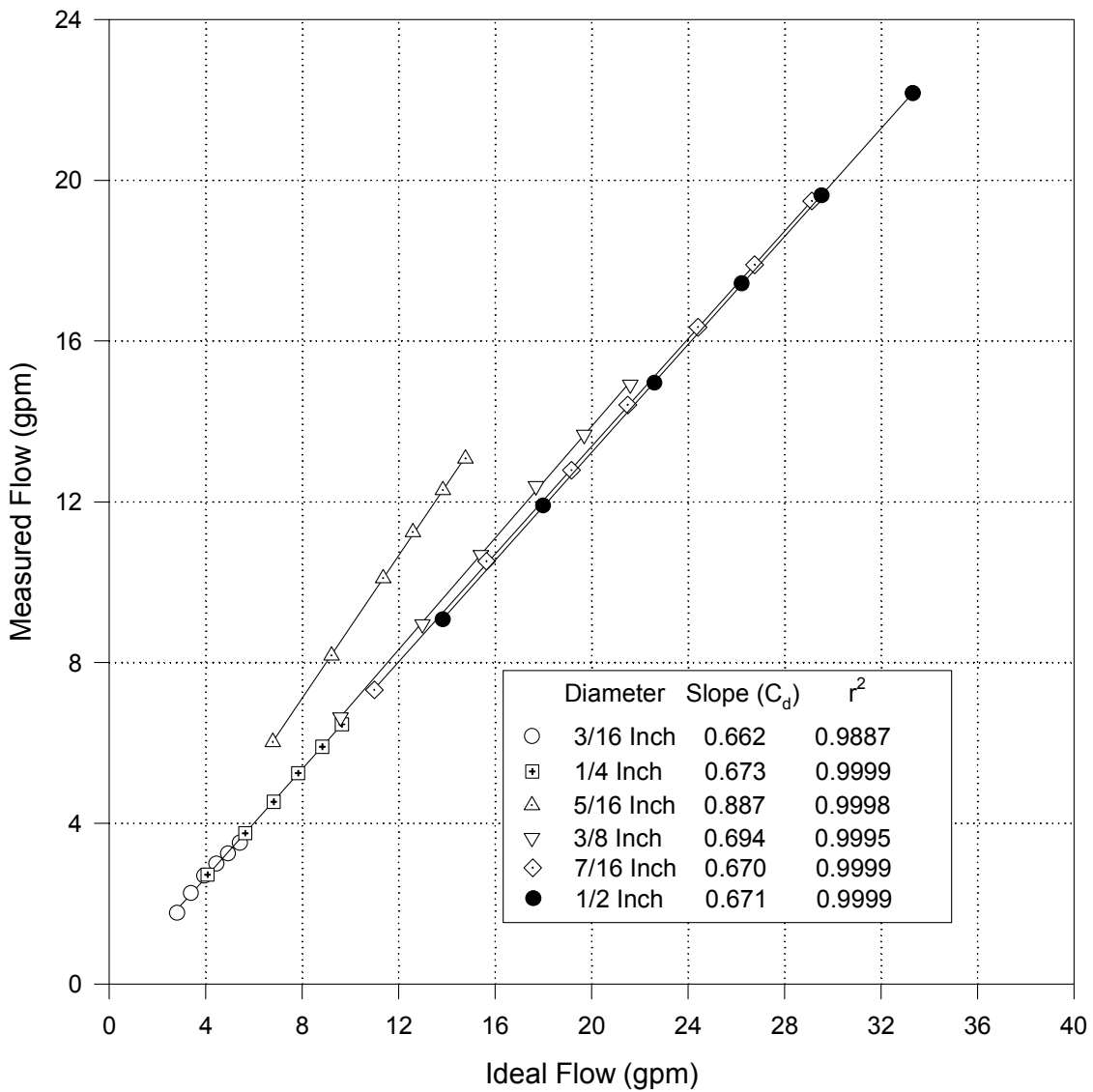


Figure 4.11 Submerged Jet Orifice Characteristics

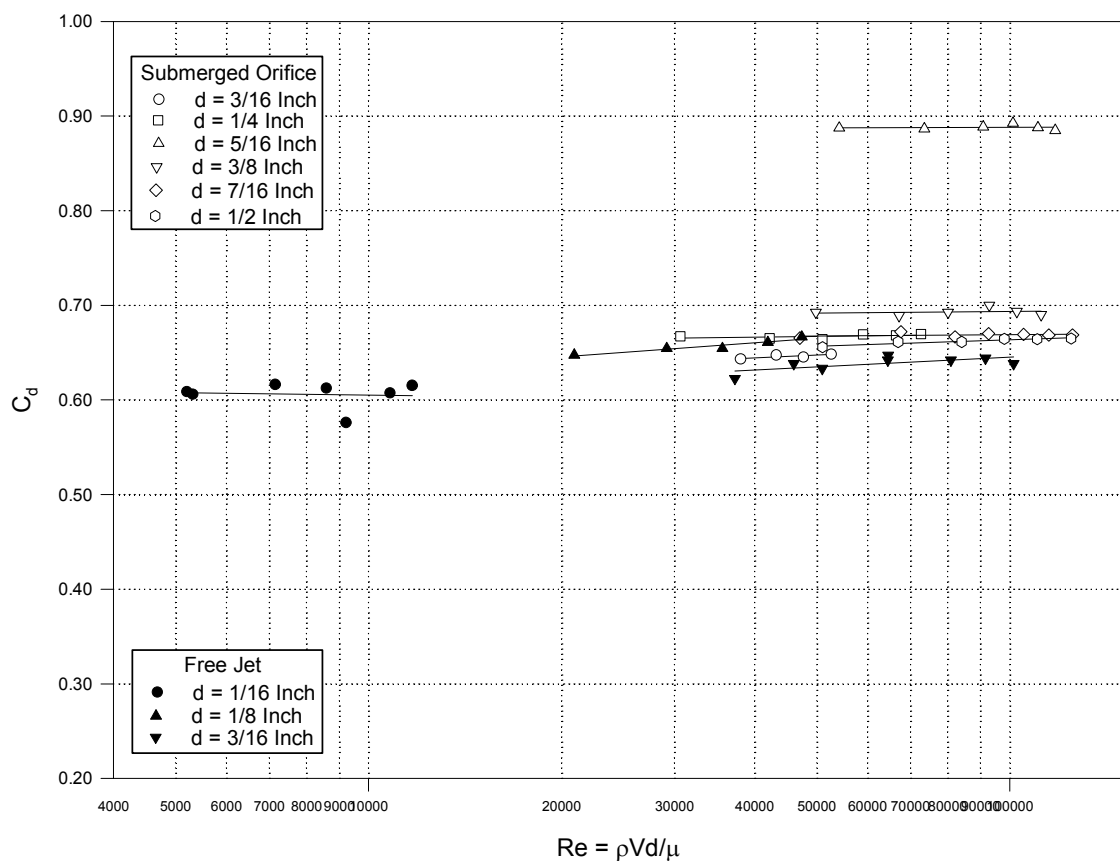


Figure 4.12 Variation of Orifice Discharge Coefficient with Size and Reynolds Number

## CHAPTER 5

### EXPERIMENTAL RESULTS

#### 5.1 Confined System of Entrapped Air

Physical observations for this experiment are illustrated in Figure 5.1. The sequence of events during the entrapped air transient are described in Figure 5.1 as follows: (a) Initial conditions of tank pressure  $p_R$  being applied up to the closed ball valve with atmospheric pressure  $p_0$  beyond the closed ball valve; (b) Air pocket compressed by accelerating water column – the water column starts accelerating due to ball valve opening, causing the air pocket to compress; (c) Compressing air pocket by decelerating water column -- the pressure in the air pocket is enough to change the positive acceleration to negative acceleration of the water column while the air pocket is kept compressed; (d) Maximum pressure at air pocket when the water column reaches stationary position -- pressure in the air pocket reaches its maximum state at the moment water is stationary; (e) Expanding the air pocket by positively accelerating the water column with negative velocity -- pressure in the air pocket starts to decrease from its maximum state as the compressed air pocket expands. The water column changes its flow direction toward the pressure tank due to the stored energy of pressure accumulated in the air pocket by the water column. Here the air pocket acts as a nonlinear spring.

At the moment the reverse flow is arrested the air pressure attains a low value that is typically above the initial pressure  $p_0$  atmospheric. The process repeats itself from (b) to (e). Pressure inside the air pocket oscillates, the driving pressure being pressure tank pressure  $p_R$ . As time passes, the whole system reaches equilibrium at a given pressure in the tank due to dissipative action.

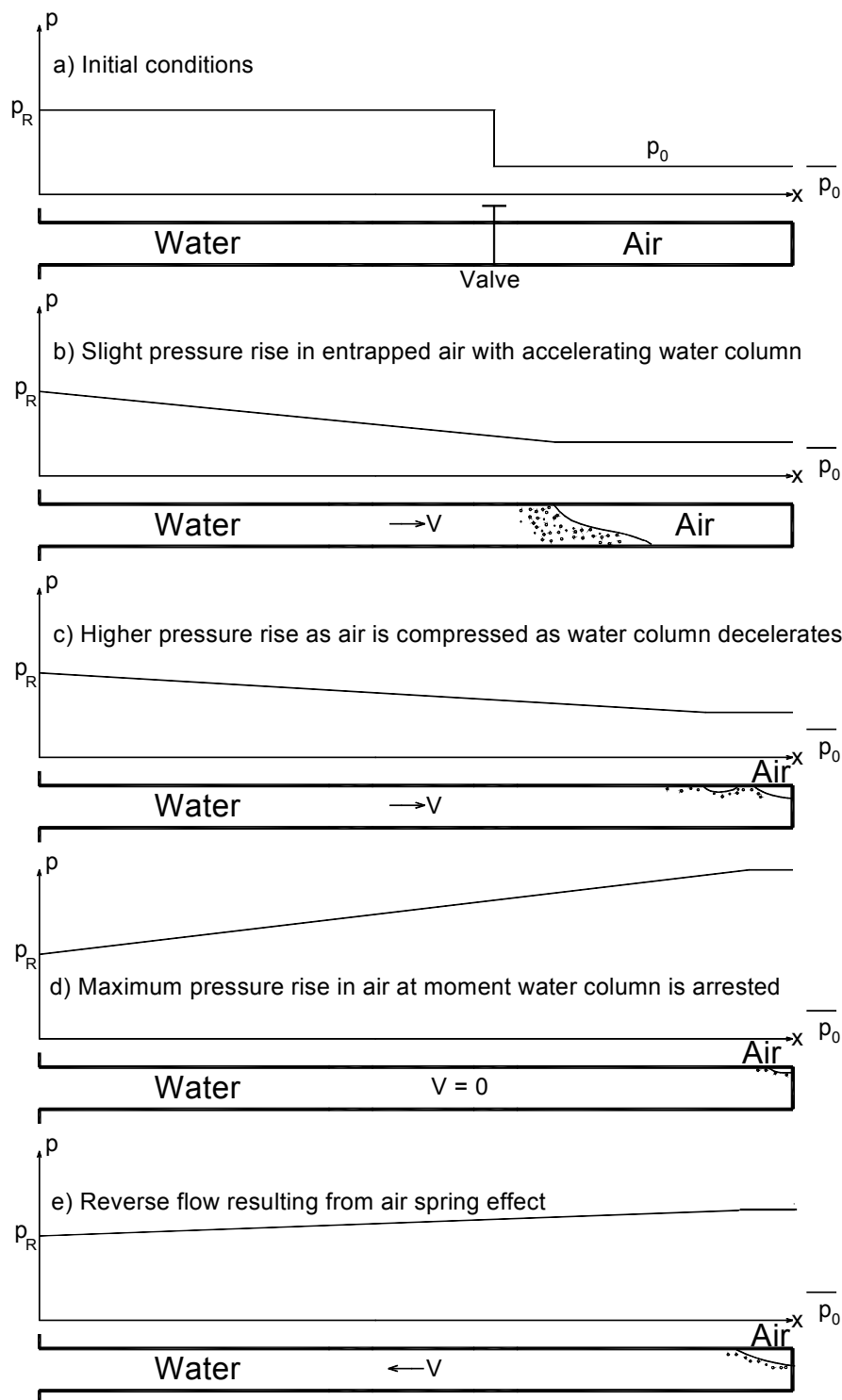


Figure 5.1 Schematic of Entrapped Transient Air Phases

Entrapped air experiments were performed with two arrangements of pressure transducer locations. The first setup was designed to confirm the validity of lumped gas assumptions, CASE I, II, and III, as defined in Chapter 2. For Setup 1 and 2 defined in Figure 4.1 and Table 4.1, pressure transducers were mounted at the dead end and middle point of the air pocket to see the pressure history. The third last pressure transducer was installed at the valve to get the reference information regarding valve opening time. For Setup 3, 4, and 5 there was no transducer mounted at the mid-air location.

### **5.1.1 Experimental Procedure**

For the particular entrapped air test to be conducted at the desired configuration listed in Table 4.1 the pipe from the pressure tank to the closed ball valve was filled with water, taking care to purge any air along the 20-ft long pipe. Downstream of the ball valve all water was removed and the pipe temporarily vented to ensure that the initial pressure was atmospheric to correspond to the initial condition of  $p_0$ . By means of a laboratory compressed air source and the pressure regulator at the pressure tank care was exercised to set the tank pressure  $p_T$  at the desired magnitude. The intent was to establish a definite ratio of absolute pressures  $P_R = p_R/p_0$ , where  $p_R$  is actually the pressure within the pressure tank at the centerline of the pipe. This necessitated an accurate knowledge of the barometric pressure as well as the liquid head in the tank, being recorded from the sight glass. The pressure ratio  $P_R$  was set at values ranging from 2 to 7 in increments of 0.5.

Once the tank pressure was accurately preset and the data acquisition system readied the experiment was initiated by applying pneumatic pressure to the ball valve actuator. For each test the data acquisition system recorded four signals at a rate of 2,000 readings/second.; namely, the ball valve angle  $\theta$ , and pressures at transducer locations PT1, PT2, and PT3 (Figures 4.1 and 4.2). Figure 5.2 shows plots of the ball valve angle  $\theta$  for seven typical tests. It is noted that (1) the opening mechanism, controlled by constant pneumatic pressure, was consistent, and (2) the nominal opening time is approximately 0.2

second. The dotted points shown on Figure 5.2 denote the approximation of the curves by five steps for analysis purposes outlined in Chapter 6.

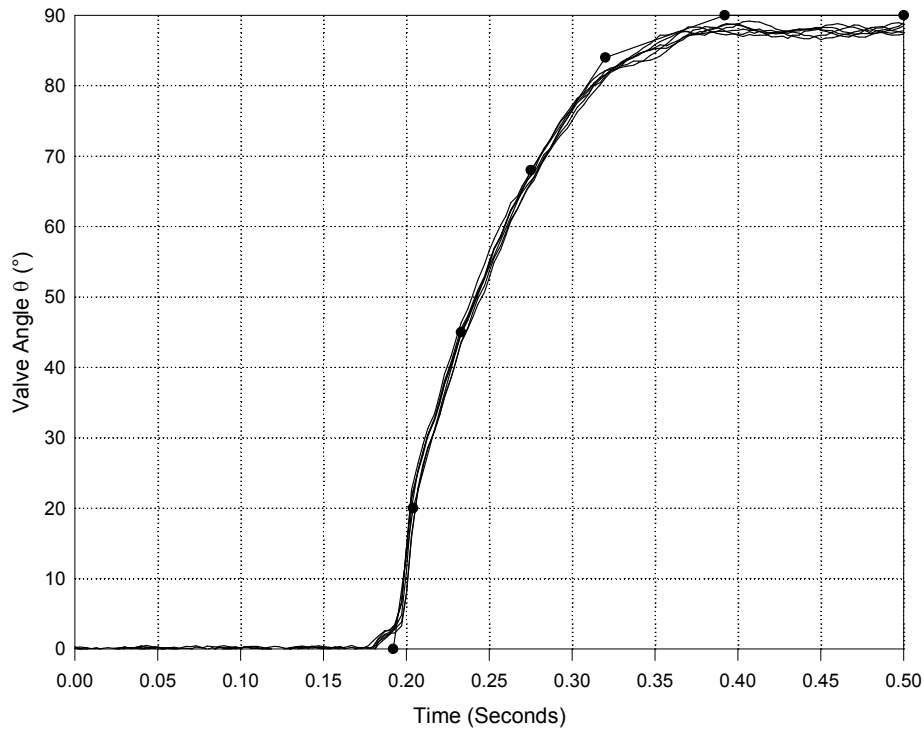


Figure 5.2 Typical Variation of Ball Valve Angle  $\theta$  During Opening

### 5.1.2 Entrapped Air Experimental Results

Entrapped air experiments were performed with two different pressure transducer setups, as defined in Figure 4.1. Setup 1-2 defined in Figure 4.1 refers to Table 4.1 wherein pressure transducer locations for PT1, PT2, and PT3 correspond to upstream of ball valve, mid-air location, and dead end, respectively. This configuration was employed for air lengths  $L_A = 16.23$  and  $10.1$  ft for Setup 1-2. The objective of this arrangement of pressure transducer location was to confirm the validity of lumped gas assumptions; that is, are there acoustic wave effects within the air space. For Setup 3-5 defined in Figure 4.1 pressure transducers were mounted at the dead end (PT3), upstream of ball valve (PT2), and mid-water point between pressure tank and ball valve (PT1). The entire set of pressure time

histories at the respective three locations are presented in APPENDIX A, Figures A.1 through A.7.

Experimental results of pressure time history at the dead end (PT3), middle point of the initial air pocket (PT2), and ball valve (PT1) are presented in Figure 5.3 for pressure ratio  $P_R = 2, 3, 4, 5, 6$ , and  $7$ . These results show that there are not major differences in the pressure traces at the dead end and middle point of the initial air pocket, with the exception of the highest values of  $P_R$ . These means that there is little acoustic wave action inside the air pocket as it is compressed and then expanded, which was pointed out theoretically in Chapter 3. In other words, pressure inside the air pocket can be treated as lumped gas for the circumstances that availed for these tests. The difference near the peak pressure time domain between the dead end and middle point of the initial air pocket happened as water passed the middle point of the initial air pocket. The lumped air assumption is verified both experimentally and theoretically.

The pressure recording upstream of the ball valve (PT1) illustrates the initial wave action within the water due to rapid opening of the valve (Figure 5.3( c) and Figures A.1 (c) and A.2 (c)). After some tenths of a second the trace at the open ball valve follows that of the other two transducers. Figures 5.4 and 5.5 show the results for Setup 3-5 on Figure 4.1, corresponding to initial air lengths  $L_A = 4.85$  and  $1.23$  ft, respectively. Figure A.4 shows the results for  $L_A = 2.77$  ft. For these runs the pressure transducer location PT1 was mid-water position; that is,  $10.9$  ft from the pressure tank. PT2 was located upstream of ball valve, and PT3 at the dead end. The recordings at PT1 clearly show pressure wave action within the water medium. Otherwise, the pressure traces are similar to those for the longer initial air lengths.

Figures 5.3 through 5.5 show that as air volume decreases or pressure ratio increases, the maximum entrapped pressure and frequency are increased. Experimental data also shows the dramatic damping mechanism between the first and second peaks. The time histories of

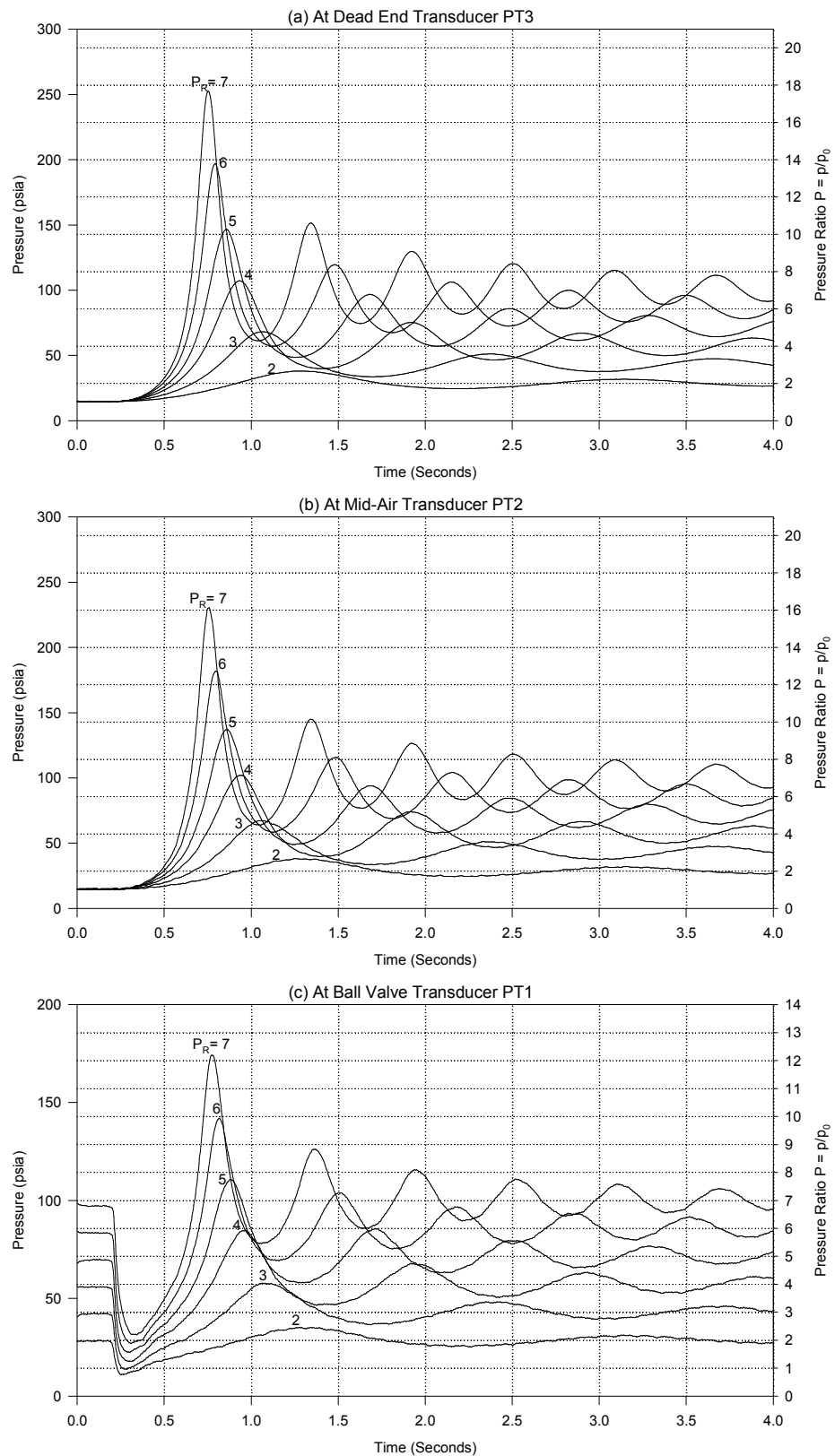


Figure 5.3 Entrapped Air Pressure Time Histories for  $L_A = 16.23$  ft ( $\alpha_0 = 0.4481$ )

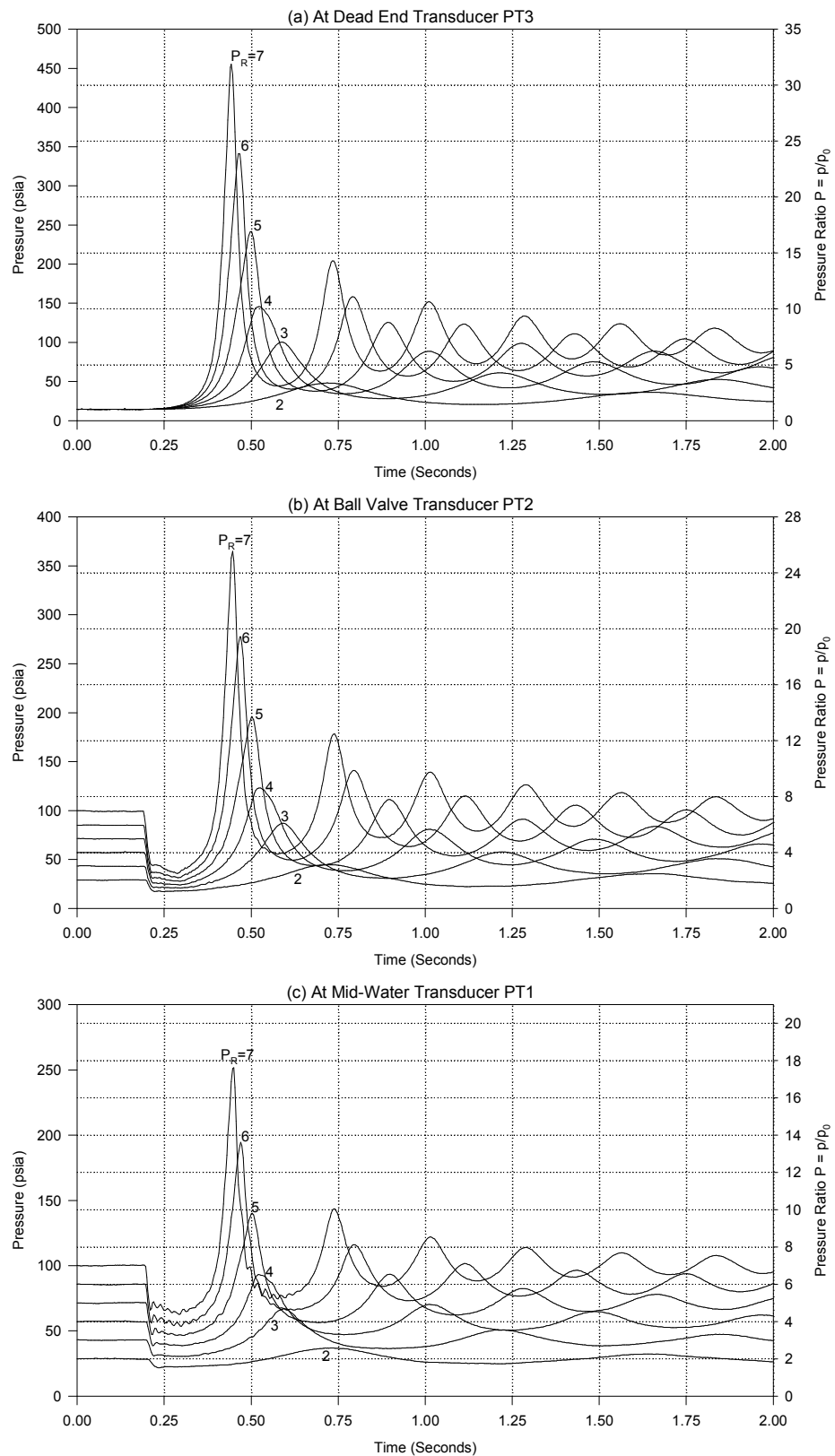


Figure 5.4 Entrapped Air Pressure Time Histories for  $L_A = 4.85$  ft ( $\alpha_0 = 0.1952$ )

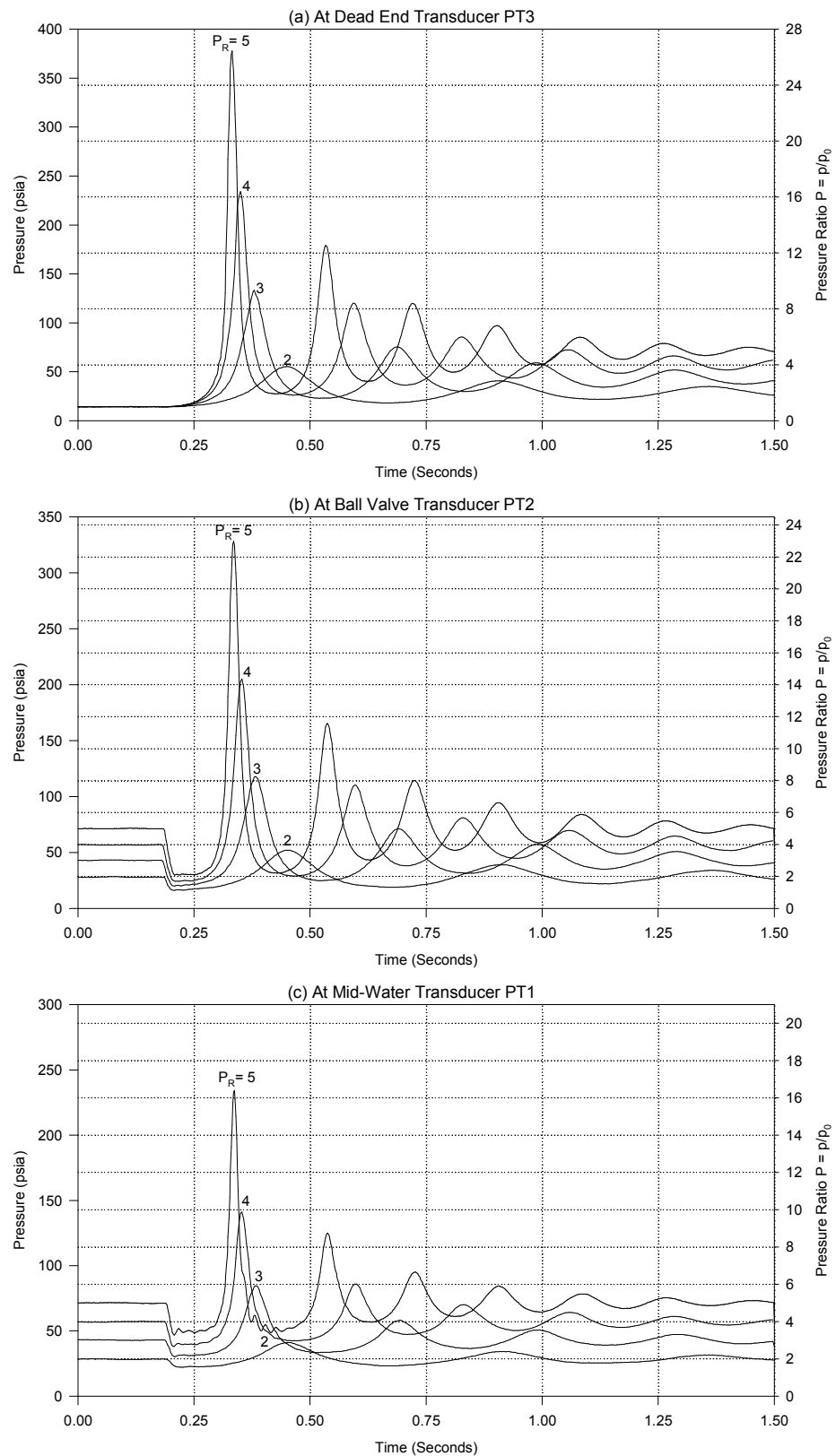


Figure 5.5 Entrapped Air Pressure Time Histories for  $L_A = 1.23$  ft ( $\alpha_0 = 0.0580$ )

pressure at the middle point of water in Figures 5.4 and 5.5 show wave action in the water as pressure ratio increases.

Another set of experimental conditions entailed partially filling the air pocket with water to study the relationship between maximum pressure and air pocket volume. The pressure time histories in this instance are plotted in Figure 5.6 and Figure A.7, which show results that appear similar to those with the entire space from ball valve to dead end occupied with air, Figures 5.3, 5.4, and 5.5. Indeed, for Figure 5.6 the initial void fraction  $\alpha_0$  was 0.1980, nearly identical to that for air length  $L_A = 4.85$  ft ( $\alpha_0 = 0.1980$ ).

### 5.1.3 Maximum Entrapped Air Pressures

The experimental maximum entrapped air pressures for different pressure ratios are plotted in Figure 5.7 indicate that initial air volume is the most important factor in deciding the magnitude of maximum entrapped pressure at a given pressure ratio. A general trend of pressure increase with both imposed pressure  $p_R$  and void fraction  $\alpha_0$  is noted. Also, the results for partial air, for which  $\alpha_0 = 0.1980$  (Figure 5.6) are very close to that for Figure 5.4, for which  $\alpha_0 = 0.1952$ .

### 5.1.4 Frequency of Oscillation

For an isentropic adiabatic process small amplitude theory will result in the period of oscillation  $T$  from rigid column (inelastic water) theory

$$T = 2\pi \sqrt{\frac{\rho_w L_w V_R}{k p_R A}} \quad (5-1)$$

where  $V_R$  is the volume of compressed air at the tank pressure  $p_R$ , computed from

$$p_0 V_0^k = p_R V_R^k \quad (5-2)$$

The period can now be written

$$T = 2\pi \sqrt{\frac{\rho_w L_w L_A P_R^{-\frac{k+1}{k}}}{k p_0}} \quad (5-3)$$

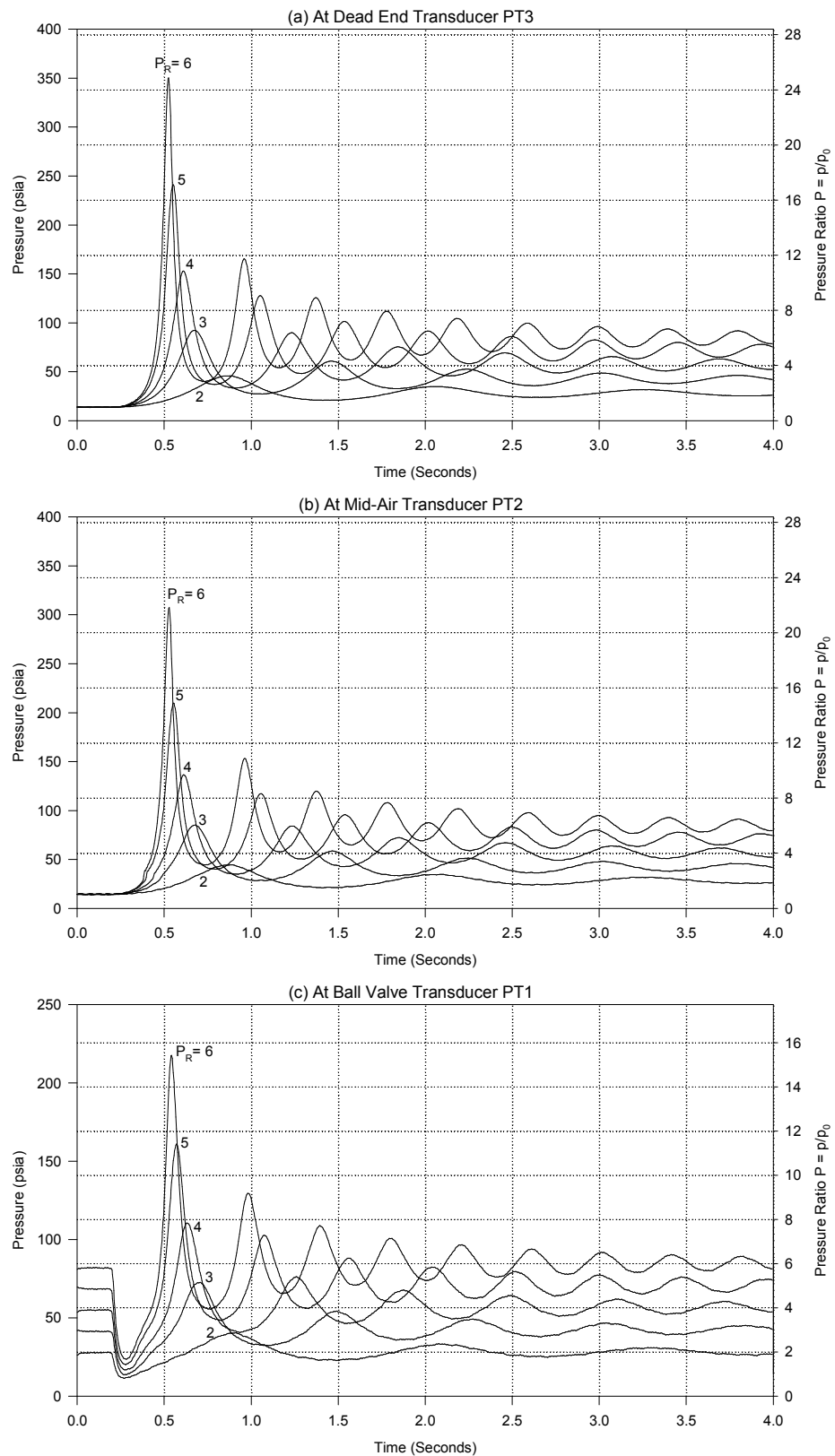


Figure 5.6 Entrapped Air Pressure Time Histories with Air Space Partially Filled with Water for  $L_A = 10.1$  ft ( $\alpha_0 = 0.1980$ ).

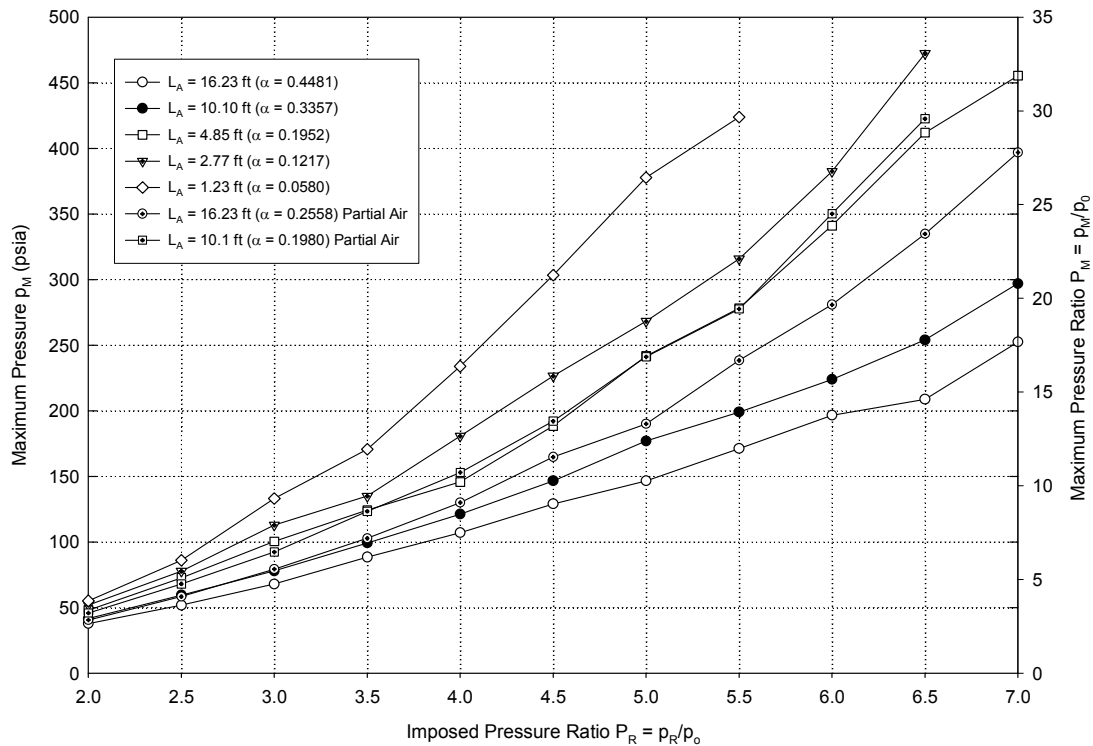


Figure 5.7 Correlation of Maximum Pressure with Pressure Ratio and Air Column Length

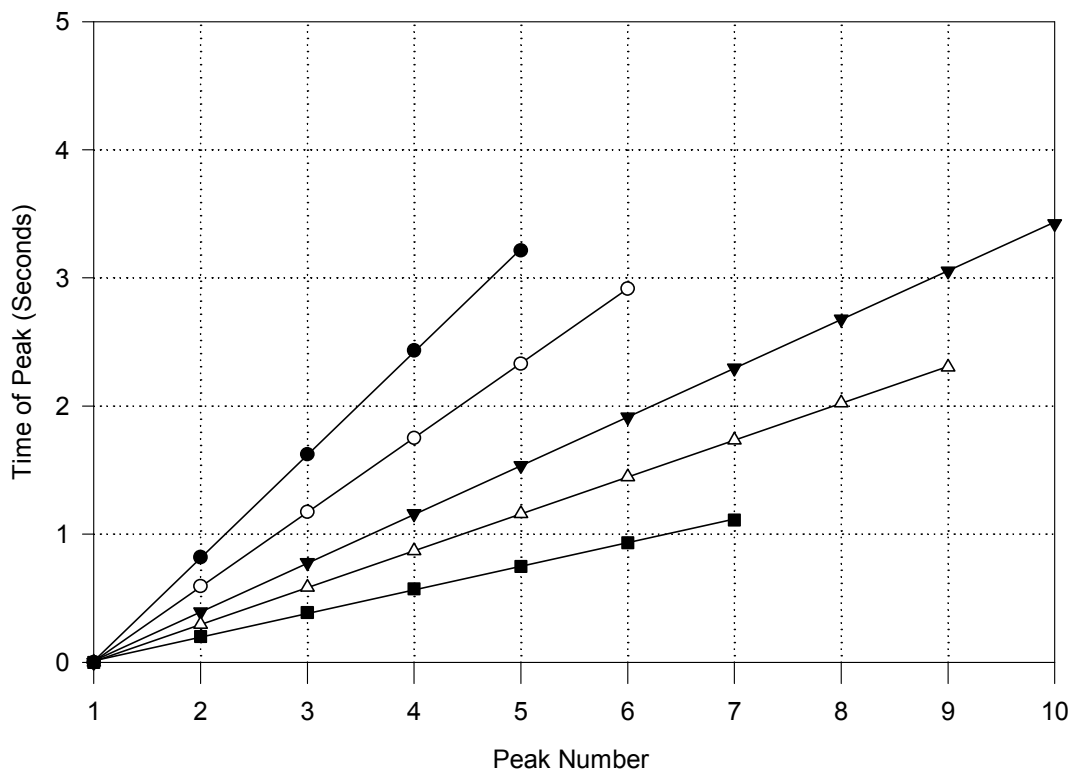


Figure 5.8 Determination of Measured Period of Oscillation for  $P_R = 5$

Numerical values for this theoretical period are listed in Table 5.1 for the five different initial void fractions  $\alpha_0$ , for which tests were specifically conducted for  $P_R = 2, 3$ , and  $5$  to ascertain frequency response for entrapped air. For  $P_R = 5$ , Figure 5.8 shows a definite linear relationship between time of peak and peak number, indicating a constant frequency, or period of oscillation. A comparison of recorded with theoretical period is presented in Figure 5.9 along with tabulated values in Table 5.1, indicating a higher measured period of oscillation (lower frequency) than predicted with theory. It should be noted that Equations (5-1) through (5-3) do not take into account the increase in the water column length  $L$  at reservoir pressure  $p_R$ .

Table 5.1 Period of Oscillation of Entrapped Gas Tests and Small Amplitude Theory

Void Fraction $\alpha_0$	Pressure Ratio $P_R$	Measured Period (Seconds)	Theoretical Period (Seconds)	Ratio of Measured to Theoretical
0.4481	2	1.846	1.619	1.141
	3	1.307	1.143	1.143
	5	0.804	0.738	1.089
0.3357	2	1.414	1.277	1.107
	3	0.974	0.902	1.080
	5	0.582	0.582	1.000
0.1952	2	0.915	0.885	1.034
	3	0.629	0.625	1.006
	5	0.380	0.403	0.942
0.1217	2	0.688	0.669	1.029
	3	0.477	0.472	1.009
	5	0.288	0.305	0.994
0.0580	2	0.450	0.446	1.011
	3	0.300	0.315	0.953
	5	0.184	0.203	0.905

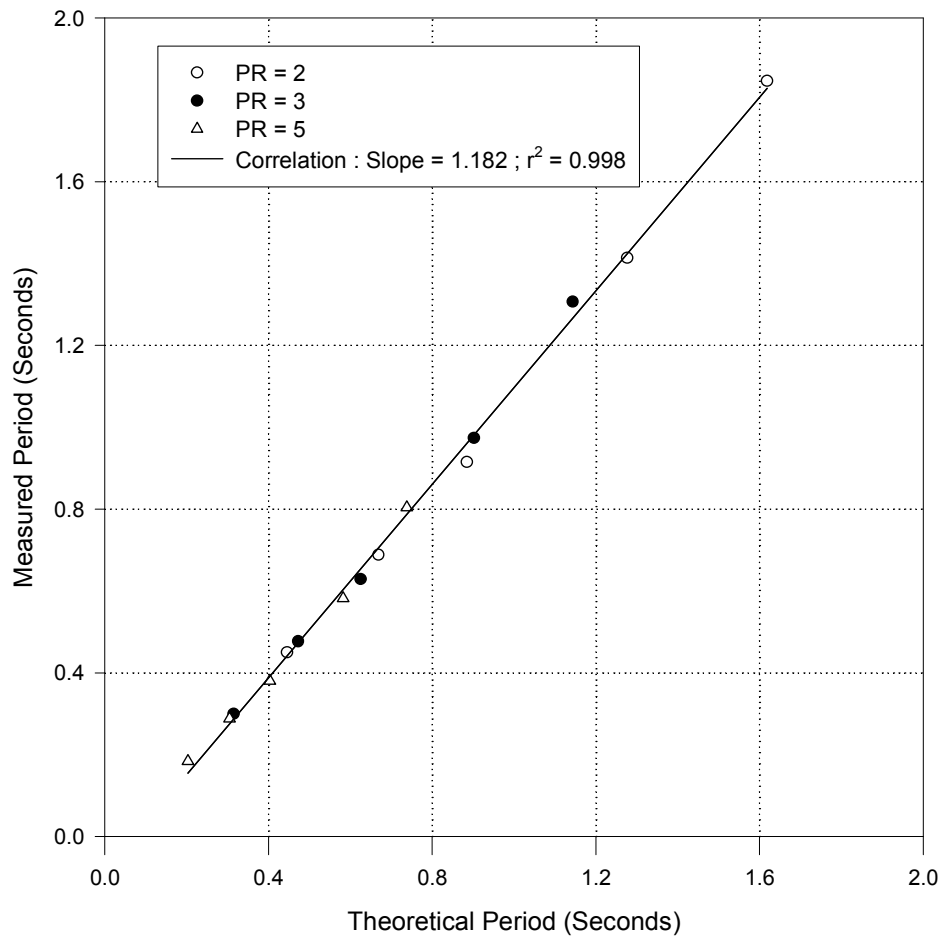


Figure 5.9 Correlation of Measured Period of Oscillation with Theoretical

## 5.2 Air Venting System

Pressure surges may occur when air vents through an opening too fast, causing a water column following the air to accelerate. Sudden deceleration at the exit may then produce dangerous transient pressures. When the water column following the air reaches the orifice, a small amount of mixed air and water can be trapped at the top of the orifice and compressed by the water column, causing extremely high entrapped air pressure surges. An experiment regarding air venting was set up as shown in Figure 4.2.

Physical observations of this experiment and the initial conditions for it are illustrated in Figure 5.10 and can be described as follows: (a) Initial condition of elevated pressure from tank to closed ball valve with atmospheric pressure from ball valve to orifice, which communicates directly with laboratory space; (b) Accelerating water column and venting air – the water column starts accelerating due to the ball valve opening and causes the air pocket to start venting; (c) The covered orifice leads to entrapped air – air can be trapped at the top of the orifice, the amount trapped depending on water tank pressure and the size of the orifice. A large amount of air can be trapped if either the orifice opening or the water tank pressure is small enough. All air can be vented if the orifice size is large enough. If the orifice size is not small or large enough, or if water tank pressure is small enough, then a small amount of air can be trapped at the top of an orifice; (d) Entrapped air at the covered orifice -- a very small amount of air trapped at the top of the orifice acts like an entrapped air problem. This can lead to very serious pressure surges; (e) Reverse flow followed by venting air -- the flow direction of the water column changes once it reaches maximum pressure while air continues to vent.

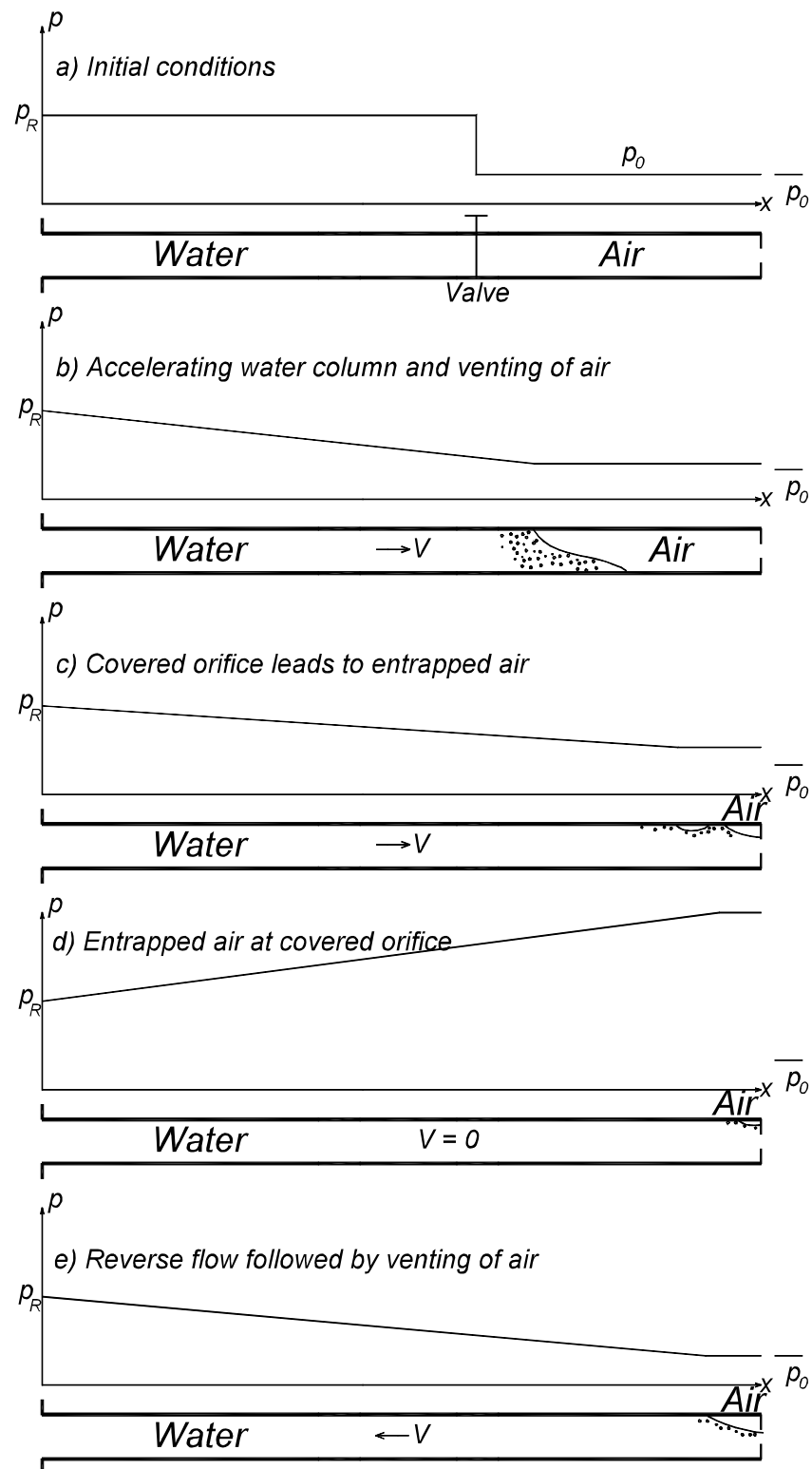


Figure 5.10 Schematic of Air Venting Transient Phases

Time histories of (a) pressure at the orifice (PT3), and b) water velocity 7 feet from the pressure tank, were collected using all five air lengths  $L_A$  listed in Table 4.2, corresponding to orifice sizes ranging in size from 1/16th to 1/2-inch. Although tests were conducted for the imposed pressure ratio  $P_R = 2, 3$ , and  $4$ , the flow meter ran out of range for  $P_R = 4$ . Hence, for these presentations, only tests for  $P_R = 2$  and  $3$  will be included in the main body of the thesis. The entire set of pressure and flow time histories for the air venting tests for  $P_R = 2$  and  $3$  are presented in Figures B.1 through B.18 in Appendix B. Only pressure traces are reported in Figures B.19 through B.22 for  $P_R = 4$  because the flow meter was out of range.

For purposes of comparison, test results for  $d = 0$  (dead end) are presented in Figure 5.11 for  $P_R = 2$ . These entrapped air results are similar to those reported in the entrapped air section of this chapter, with the major difference being no flow meter installed for the latter. Especially for these tests it should be mentioned that the turbine flow meter cannot ascertain flow reversal in terms of sign inasmuch as signal conditioning is based solely on speed of rotation of the propeller shaft. For example, for the air length  $L_A = 1.23$  ft, the flow signal at approximately 0.55 second shows an increase in output, which should drop below zero and indicate a negative voltage (reverse flow).

For  $P_R = 2$  transient time histories of pressure at the orifice transduce (PT3) and flow at the turbine meter are plotted in Figures 5.12, 5.13, 5.14, 5.15, and 5.16 for all five initial air lengths and for  $d = 1/16, 3/16, 1/4, 3/8$ , and  $1/2$ -inch orifice sizes. Except for an obvious time offset in the records for  $d = 1/16$ -inch and  $L_A = 16.23$  ft, the flow signal in the initial stages of the acceleration is nearly identical. This is especially true in Figures 5.13 - 5.16, where there is minimal pressure buildup until the water column nears the orifice due to the ability of the orifice to expel air for the larger orifice sizes.

With an orifice size  $d = 1/16$  inch ( $L_A = 1.23$  ft in Figure 5.12) the first peak is due to entrapped air effects as the orifice discharge of air is small. However, for  $L_A = 2.77$  ft a dip occurs in the record near  $T = 0.7$  second, suggesting that water had reached the orifice,

most likely causing air to be entrapped (Figure 5.10d) by covering the small hole. Due to relief provided by air flow the pressure surges may be reduced when compared to the closed systems shown in Figures 5.3 - 5.5. Pressure traces in Figure 5.12 are quite similar to those of entrapped air with a closed end orifice because a large portion of air is still trapped while air is continuously vented. This venting effect reduces the first peak pressure.

For the results for the larger orifices plotted in Figures 5.13, 5.14, 5.15, and 5.16, there is virtually no increase in air pressure during water column acceleration due to small resistance offered by larger openings. Existence of a sudden deceleration associated with a steep pressure rise again suggests entrapment of air at the orifice causing by covering of the hole. For the medium size orifices such as  $d = 3/16$  inch there is a small oscillation associated with the entrapped air, but within a short period of time it is evident that the air has been mostly expelled, resulting in the pressure to settle down to the reservoir level  $p_R$ . This effect is especially apparent for  $d = 1/2$ -inch (Figure 5.16).

Medium orifice sizes ranging from  $3/16$  to  $1/4$  of an inch generally produced higher pressure surges when compared to closed systems, as shown in Figures 5.13 and 5.14. Especially high pressures of the entrapped gas type were recorded in this range. For example, for given orifice sizes of  $3/16$  and  $1/4$  inch, pressure time history shows that there is an entrapped air effect based on the shape of the time trace from the first to the second peak, as shown in Figures 5.13 and 5.14. These velocity time history traces definitely show a tendency toward reverse flow as a result of entrapped air. A small amount of air is trapped at the orifice while most of the gas is venting, causing pressure to accumulate continuously. Martin and Lee (2000) also reported that compressing small amounts of air trapped at the orifice could cause significant pressure surges.

An impact type of surge, not unlike waterhammer can be observed in Figures 5.15 and 5.16 with orifice sizes from  $3/8$ -inch to  $1/2$ -inch.

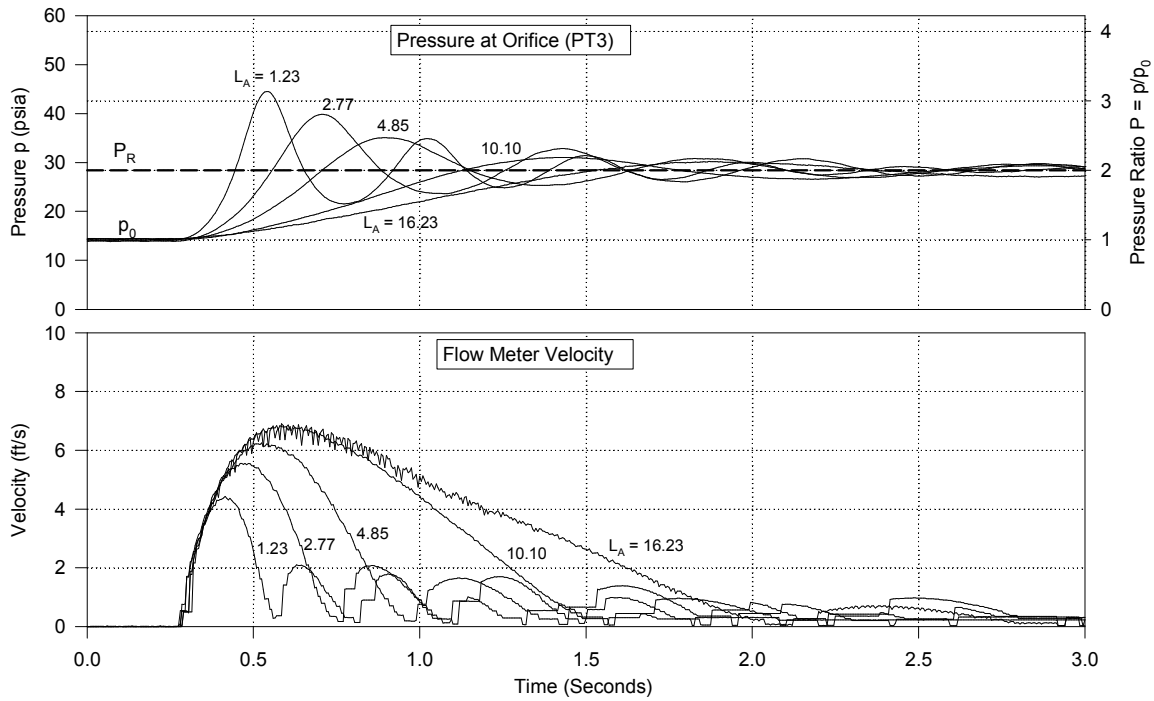


Figure 5.11 Pressure and Velocity Time Histories for Air Venting ( $P_R = 2$ ;  $d = 0$ )

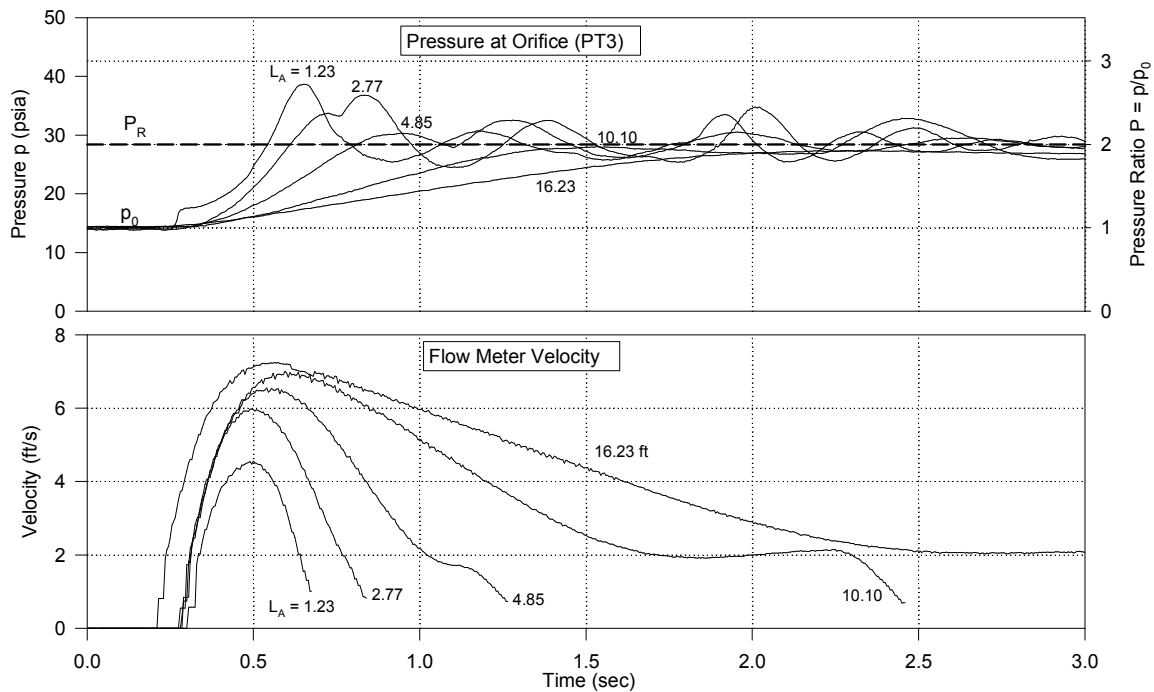


Figure 5.12 Pressure and Velocity Time Histories for Air Venting ( $P_R = 2$ ;  $d = 1/16$  Inch)

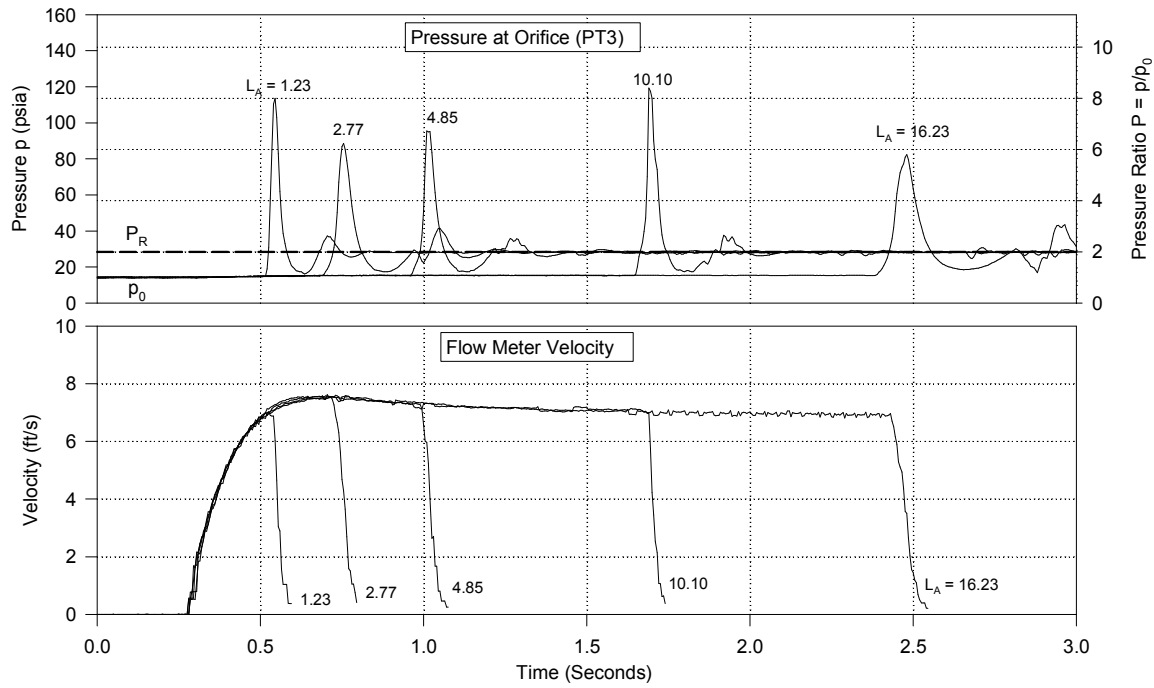


Figure 5.13 Pressure and Velocity Time Histories for Air Venting ( $P_R = 2$ ;  $d = 3/16$  Inch)

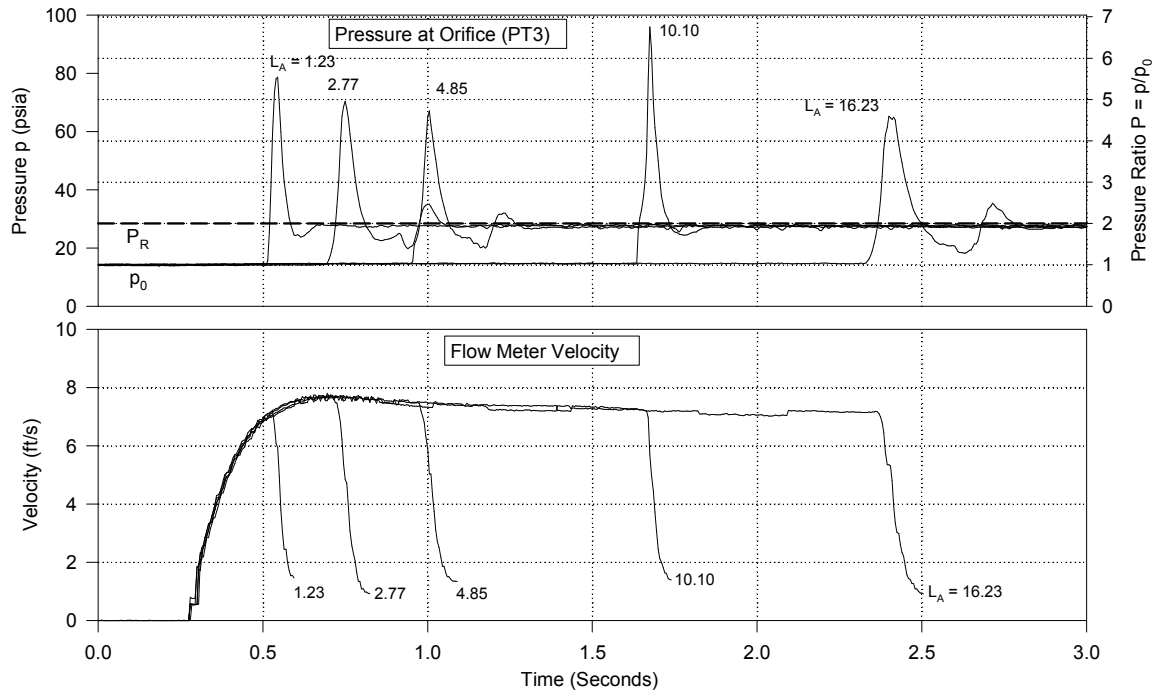


Figure 5.14 Pressure and Velocity Time Histories for Air Venting ( $P_R = 2$ ;  $d = 1/4$  Inch)

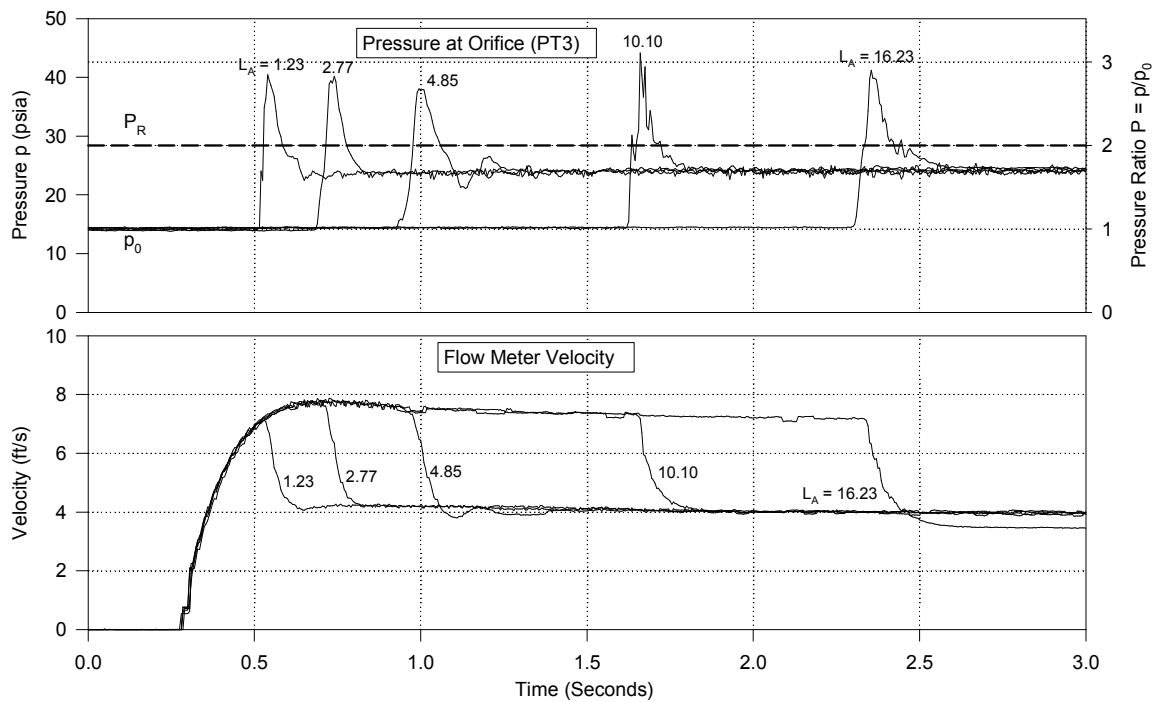


Figure 5.15 Pressure and Velocity Time Histories for Air Venting ( $P_R = 2$ ;  $d = 3/8$  Inch)

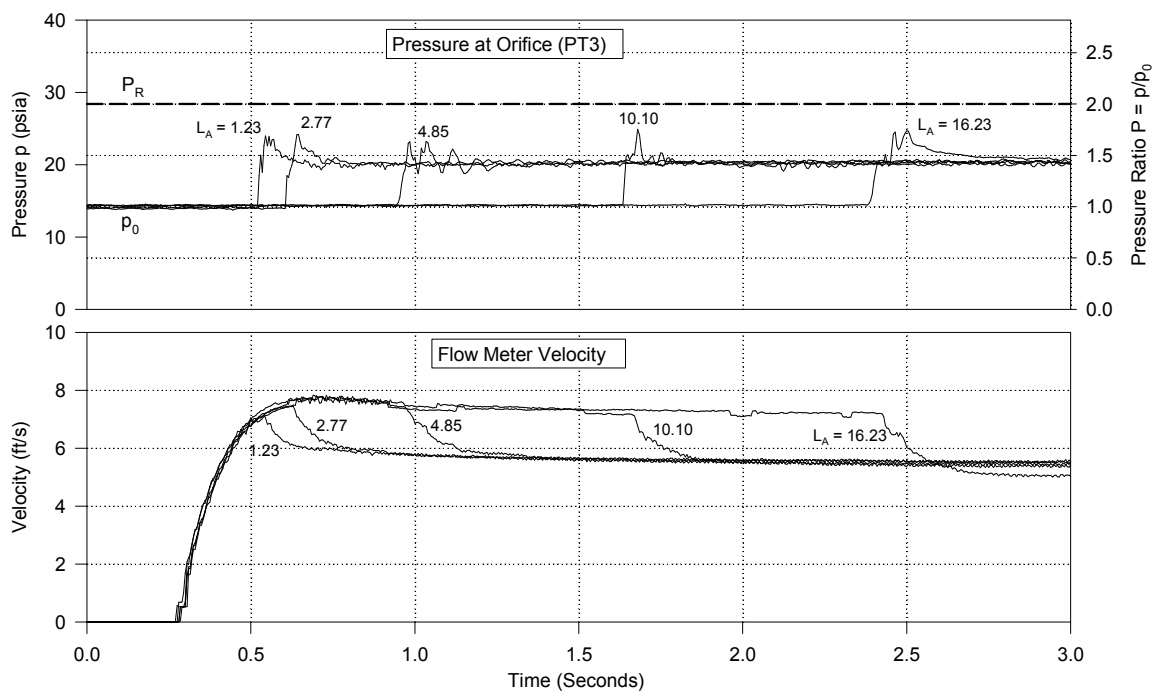


Figure 5.16 Pressure and Velocity Time Histories for Air Venting ( $P_R = 2$ ;  $d = 1/2$  Inch)

### 5.2.1 Maximum Venting Pressures

Maximum venting air pressures for each orifice are plotted for different pressure ratios corresponding to each set of air lengths. Results are presented in Figures 5.17 to 5.21 for the five air lengths  $L_A$  or initial void fraction  $\alpha_0$ . Maximum pressures at the orifice depend on the size of the orifice and the pressure ratio, more than the initial air volume. Maximum pressure was recorded with an orifice size of 3/16 of an inch, but extremely high pressure values were shown throughout the whole range of orifice sizes. Experimental results show that improper size of an orifice opening can cause higher transient pressures, either of the entrapped air or impact type, than occur in a closed system.

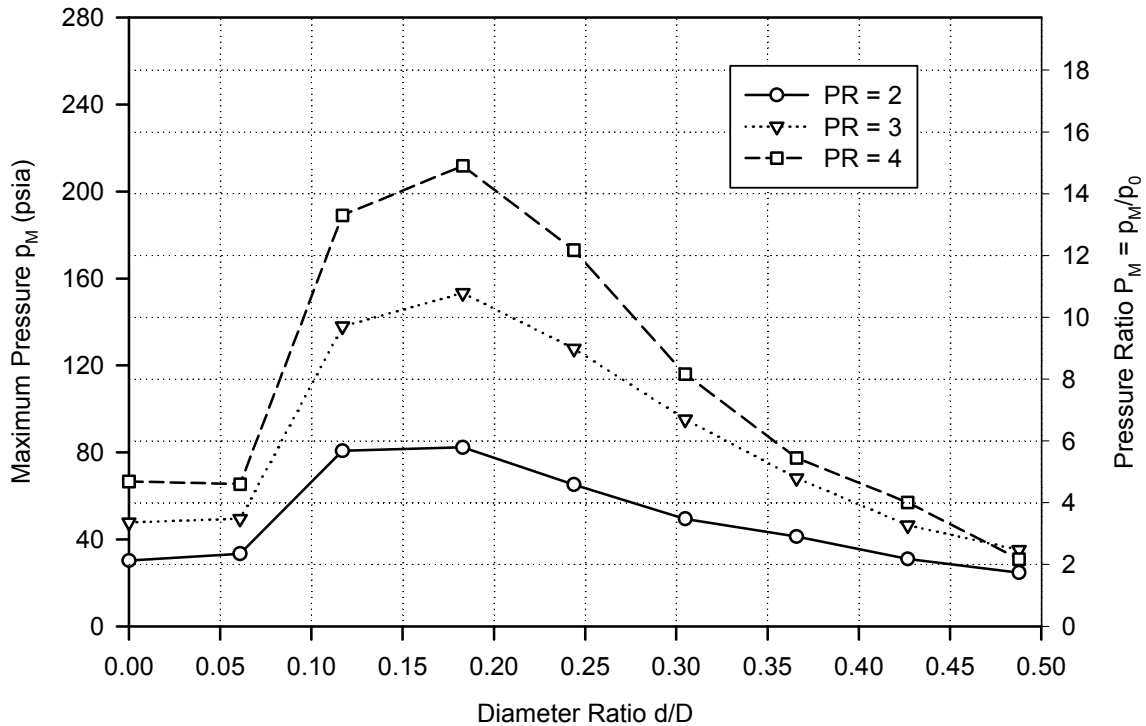


Figure 5.17 Maximum Pressure at Orifice (PT3) for  $\alpha_0 = 0.4481$

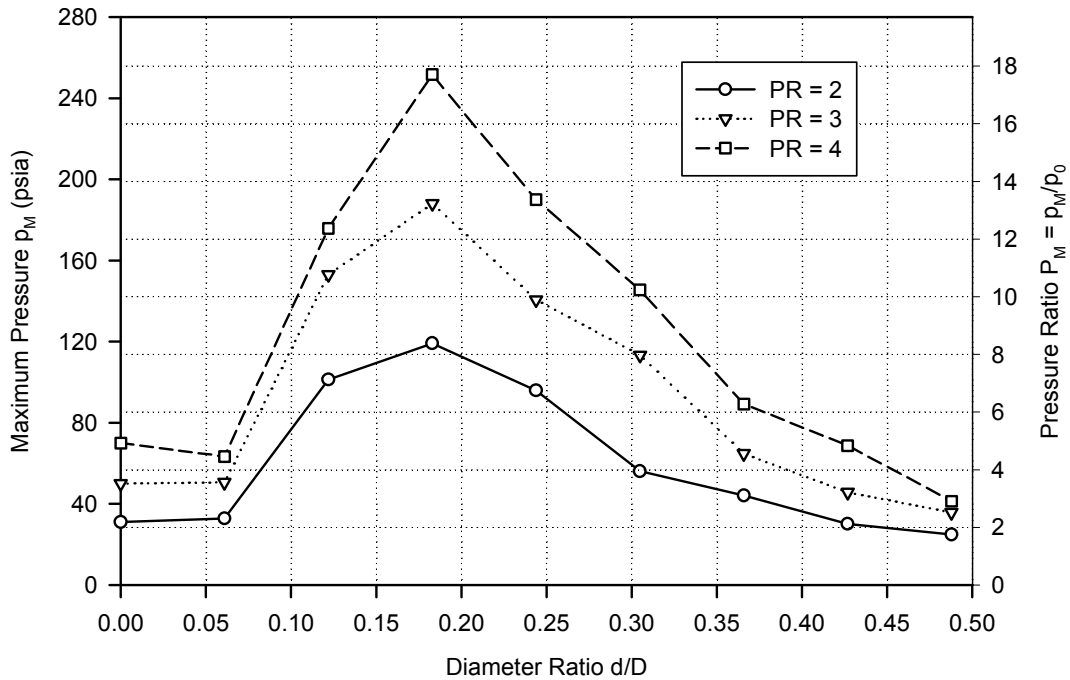


Figure 5.18 Maximum Pressure at Orifice (PT3) for  $\alpha_0 = 0.3357$

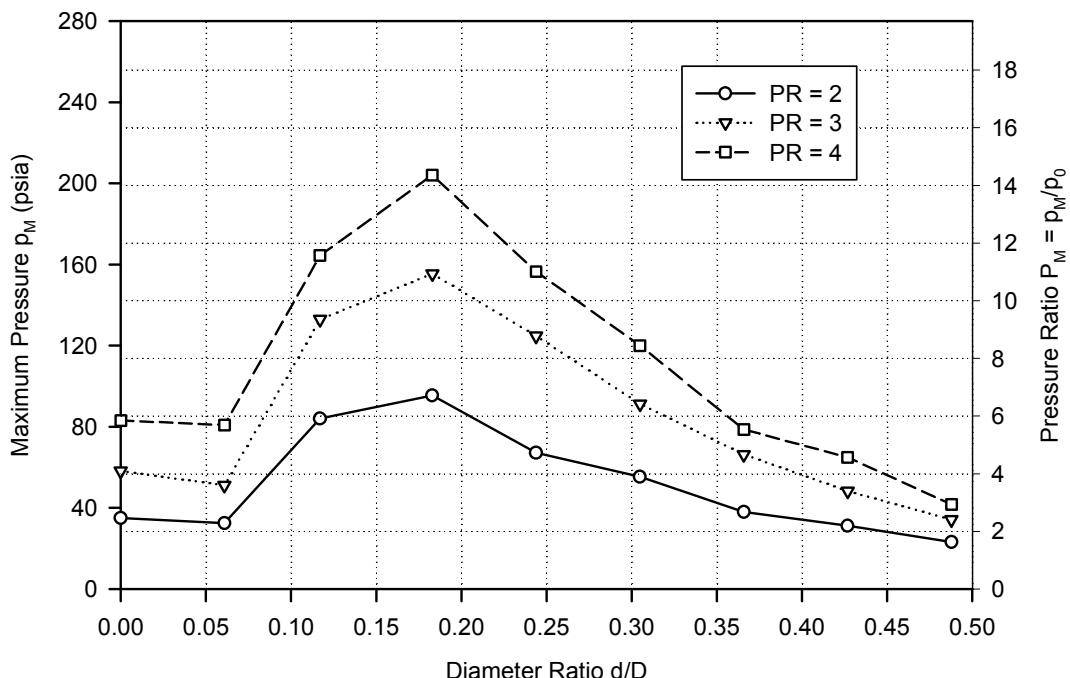


Figure 5.19 Maximum Pressure at Orifice (PT3) for  $\alpha_0 = 0.1952$

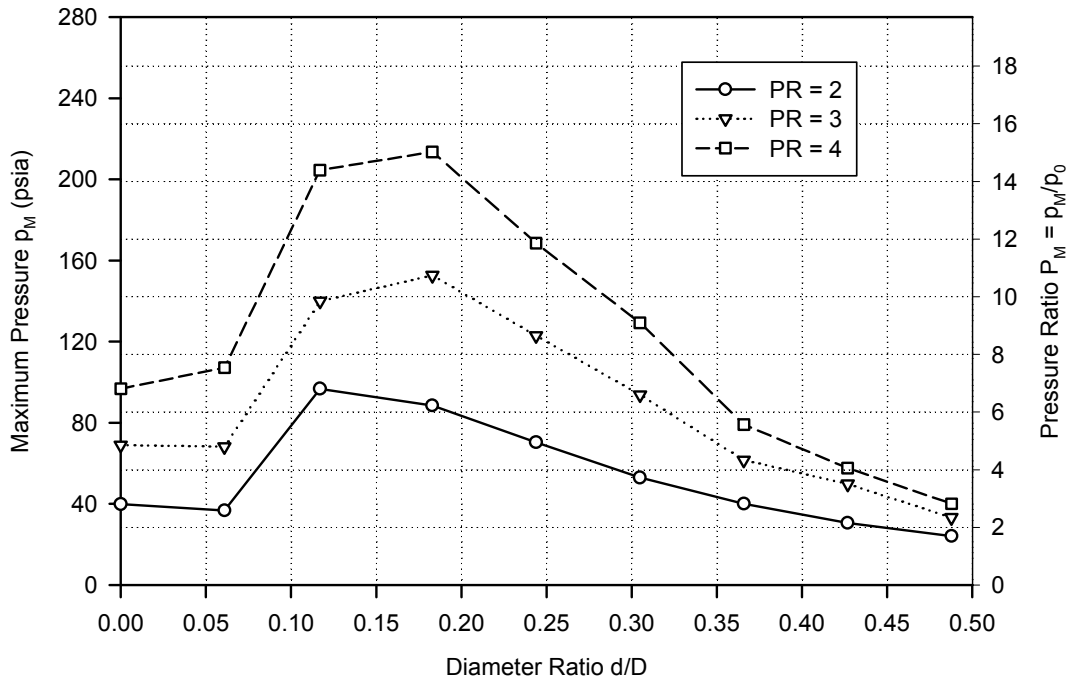


Figure 5.20 Maximum Pressure at Orifice (PT3) for  $\alpha_0 = 0.1217$

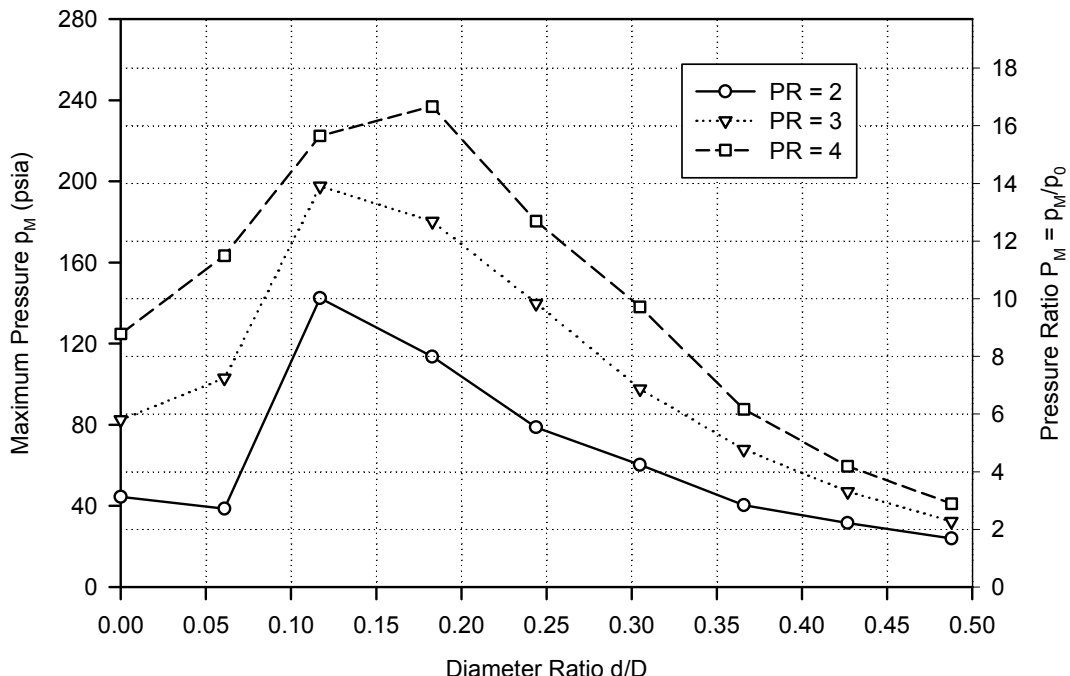


Figure 5.21 Maximum Pressure at Orifice (PT3) for  $\alpha_0 = 0.0580$

## CHAPTER 6

### COMPARISON BETWEEN ANALYTICAL AND EXPERIMENTAL RESULTS

#### 6.1 Confined System

Analytical models derived from both rigid column theory and waterhammer (MOC) were used to predict transient pressures. In both instances Equation (3-19) for linear momentum was employed

$$\frac{dV}{dt} = \frac{1}{\rho_t} \frac{p_R - p}{L} - \frac{V^2}{2L} - \frac{f}{2D} V|V| \quad (6-1)$$

However, for proper representation of the experiment described in Chapter 5, minor losses at the intake due to an isolation valve and resistance through the ball valve were included. Hence, Equation (6-1) was modified to be

$$\frac{dV}{dt} = \frac{1}{\rho_t} \frac{p_R - p}{L} - (1 + \Sigma K_L) \frac{V^2}{2L} - \frac{f}{2D} V|V| \quad (6-2)$$

where  $\Sigma K_L$  represents all minor losses. The rigid column solution with variable liquid length (Case I) was implemented employing Runge-Kutta finite differences techniques. The closed form solution utilizing incomplete gamma functions is only valid for solving Equation (6-1) and the attendant lumped gas relationships.

For the MOC solution the fixed and irregular grid depicted in Figure 3.3 was employed with lumped air at the interface labeled as Point C and D on the path line (Case III). Equation (6-2) constituted the momentum and the lumped air model assumed an adiabatic process with  $k = 1.4$ .

Comparisons of time traces between analytical model results and experimental

measurements of pressure time history at the dead end (PT3) are presented in Figures 6.1, 6.2, and 6.3 for air length  $L_A = 16.23$  ft for the imposed pressure ratio  $P_R = 2, 4,$  and  $6.$  Figures 6.4, 6.5, and 6.6 provide further results for air length  $L_A = 10.1$  ft. Additional graphs for other initial air lengths may be found in Appendix C. Both models agreed well with experimental measurements. For these two air lengths the two analytical models yield nearly identical results in terms of peak pressure. However, as shown Figure C.12 for  $L_A = 10.1$  ft and  $P_R = 6,$  the rigid column models predicts a higher peak pressure than MOC. Moreover, neither analytical model agrees with experimental measurements with respect to frequency, which will be addressed later with respect to Figures 5.8 and 5.9

### **6.1.1 Maximum Pressures**

Maximum entrapped air pressures predicted by the two different analytical models are plotted against experimental measurements in Figure 6.7. The trends of both the analytical models and the measurements indicate that maximum entrapped air pressure increases if air volume decreases at a given pressure ratio, or if pressure ratio  $P_R$  increases at a given air volume.

As air volume decreases or pressure ratio increases, the rigid column model predicts higher values than the waterhammer model. This is because the rigid column model does not account for the elasticity of water. As air volume decreases, the elasticity of water becomes more important theoretically. However, the experimental data indicate little effect of the elasticity of water.

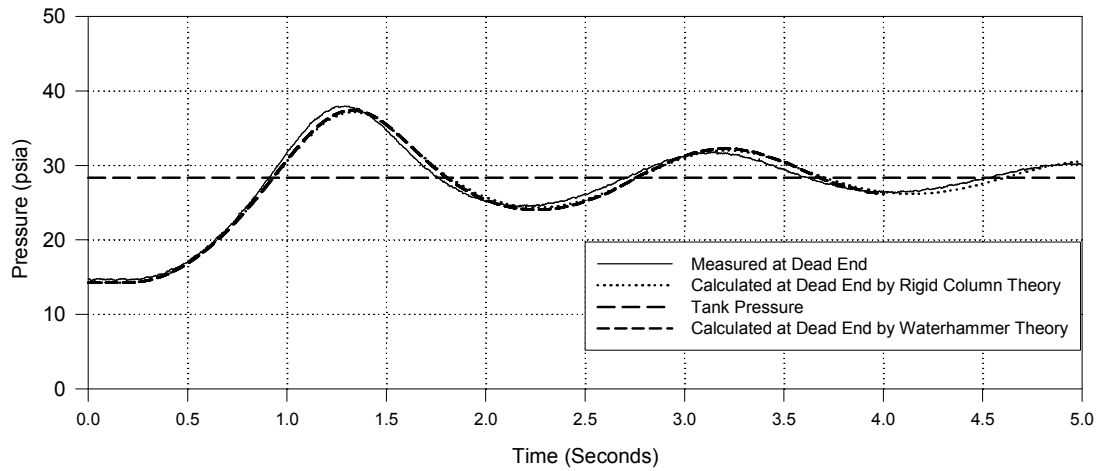


Figure 6.1 Entrapped Air Analysis for  $L_A = 16.23 \text{ ft}$  ( $\alpha_0 = 0.4481$ ) ;  $P_R = 2$

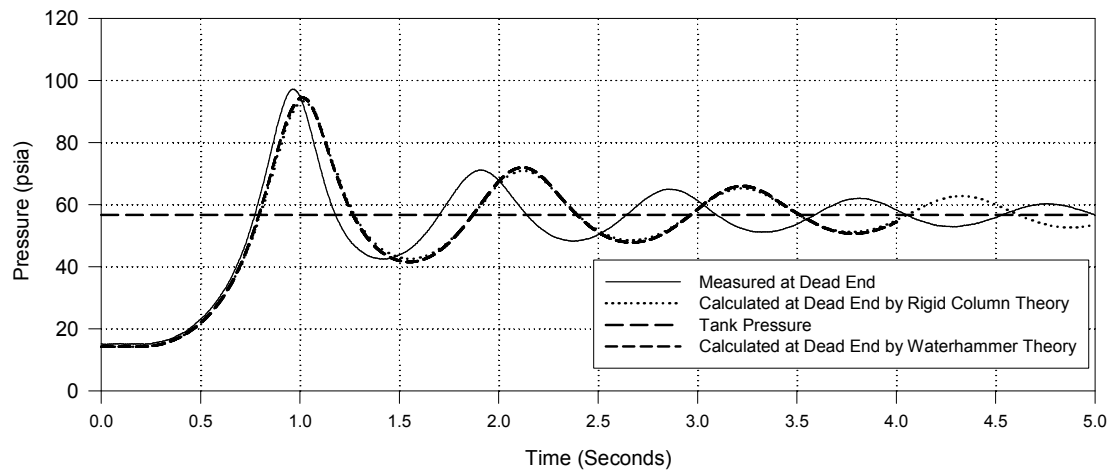


Figure 6.2 Entrapped Air Analysis for  $L_A = 16.23 \text{ ft}$  ( $\alpha_0 = 0.4481$ ) ;  $P_R = 4$

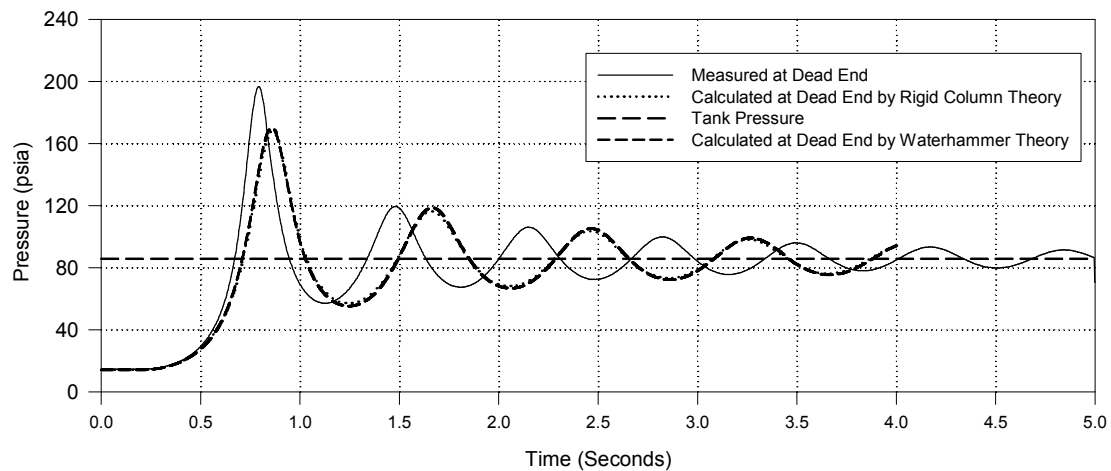


Figure 6.3 Entrapped Air Analysis for  $L_A = 16.23 \text{ ft}$  ( $\alpha_0 = 0.4481$ ) ;  $P_R = 6$

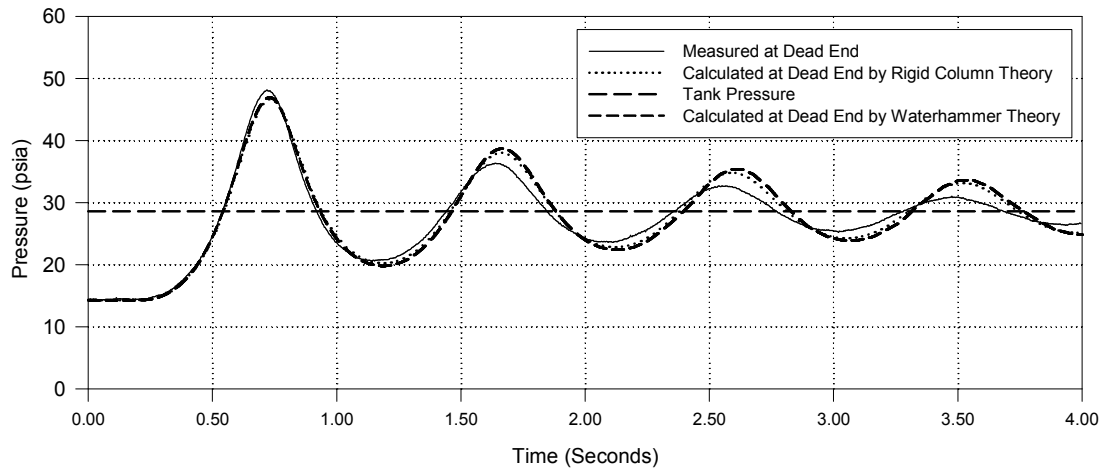


Figure 6.4 Entrapped Air Analysis for  $L_A = 10.1$  ft ( $\alpha_0 = 0.3357$ ) ;  $P_R = 2$

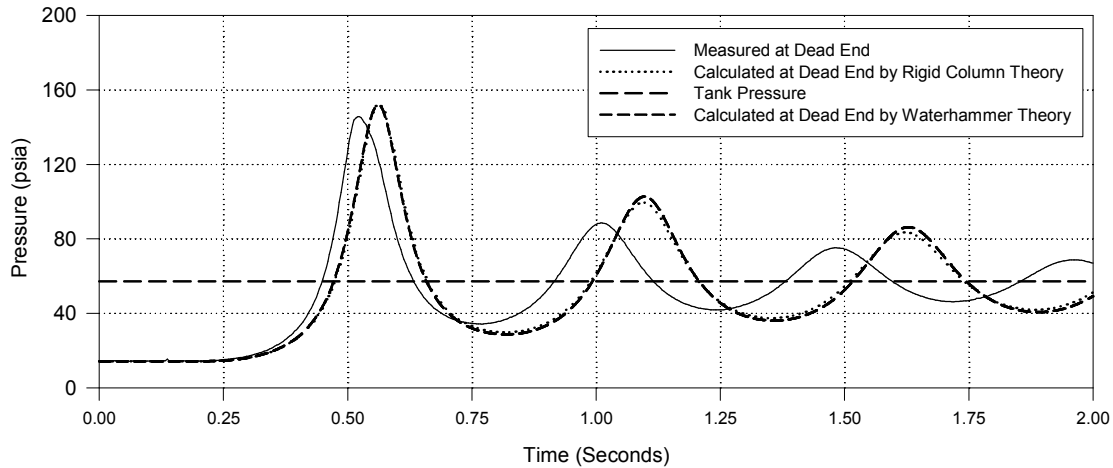


Figure 6.5 Entrapped Air Analysis for  $L_A = 10.1$  ft ( $\alpha_0 = 0.3357$ ) ;  $P_R = 4$

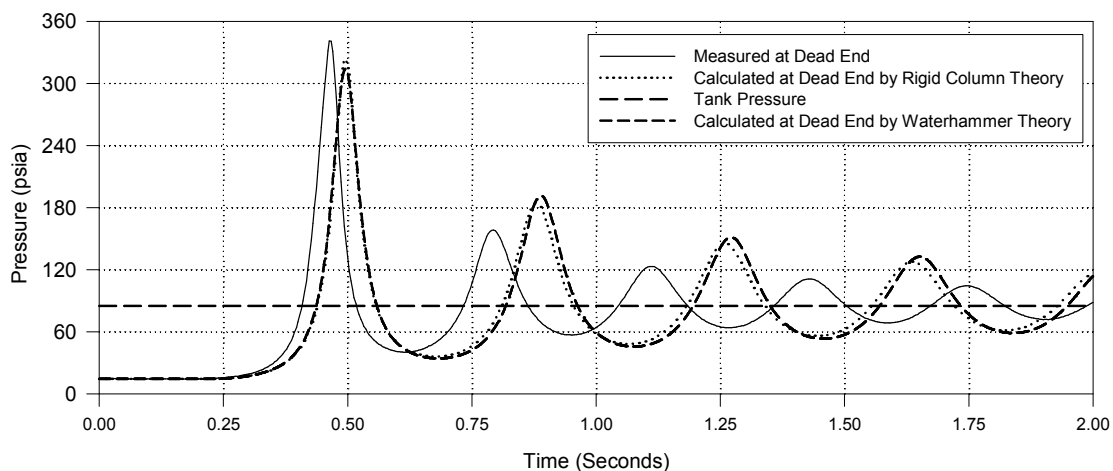


Figure 6.6 Entrapped Air Analysis for  $L_A = 10.1$  ft ( $\alpha_0 = 0.3357$ ) ;  $P_R = 6$

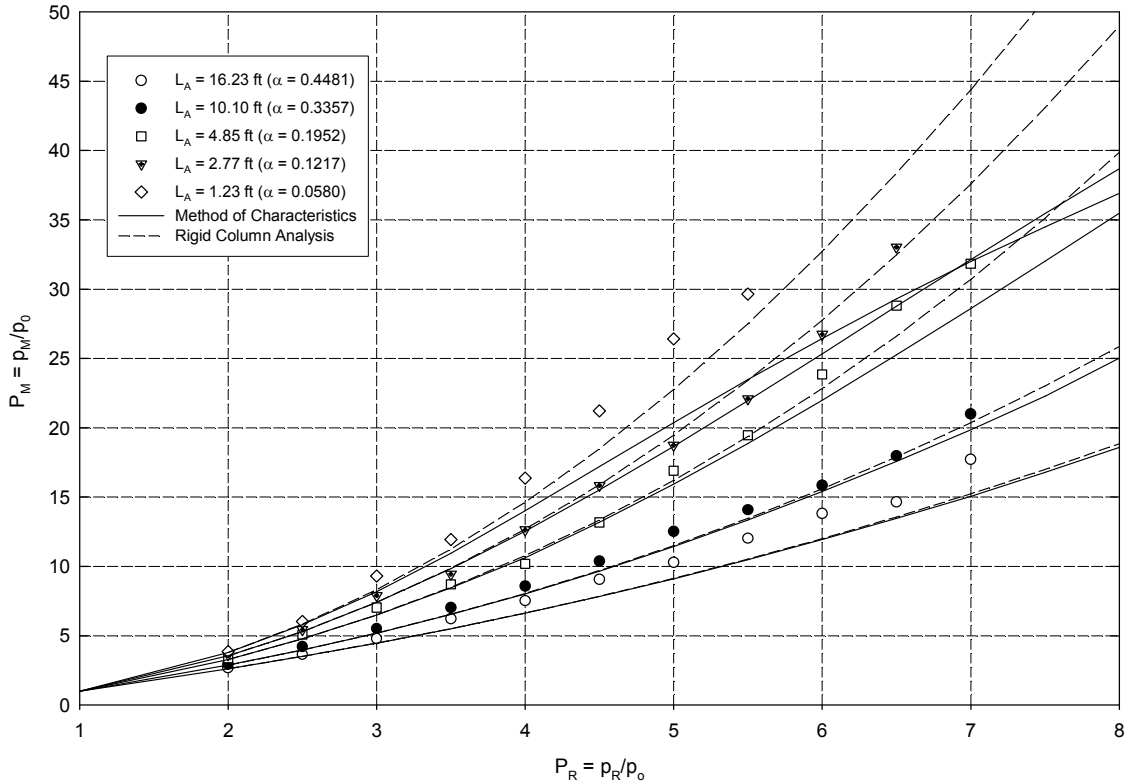


Figure 6.7 Analytical and Experimental Entrapped Air Results for Various Air Lengths  $L_A$  and Tank Pressures  $P_R$

### 6.1.2 Thermal Damping and Frequency

Lumped liquid and lumped gas mass model was applied to analyze the frequency of oscillation of the liquid column with entrapped air. Acoustic liquid and lumped gas mass model did not improve effectively the frequency of entrapped gas because it has an implicit form of internal moving boundary condition. The frequencies of analytical model were improved by applying thermal damping effect. Pipe friction and minor loss reduced only magnitude of pressure and velocity whereas thermal damping term did change the frequency because it is directly related to the stiffness of gas mass, as already mentioned.

Although both variable water length models – MOC waterhammer (Case III) and rigid column Model (Case I) – generated good agreement with peak pressures, damping and period of oscillation did not match that of measurement. One example is Figure 6.8, for which the air length  $L_A = 16.23$  ft and  $P_R = 2.5$ . The thermal damping model is based upon

solution of the energy Equation (3-145) based on theory by Moody (1990) with heat transfer coefficient  $H$  determined from work by Graze (1996), Equation (3-147). The thermal damping model improves the damping characteristics of the system compared to only the utilization of boundary resistance afforded by the head loss terms in Equation (6-2). The results in Figure 6.8 show that analytical model with thermal damping effect has better agreement to experimental results than those of analytical model without thermal damping effect.

In addition to improvement in damping compared with experiment, the inclusion of heat transfer enhances the comparison of theory with measurement in terms of the period of oscillation (frequency) as shown in Figure 6.9 for pressure ratios  $P_R = 2, 3$ , and  $5$ . Similar trends occurred with the other four air lengths.

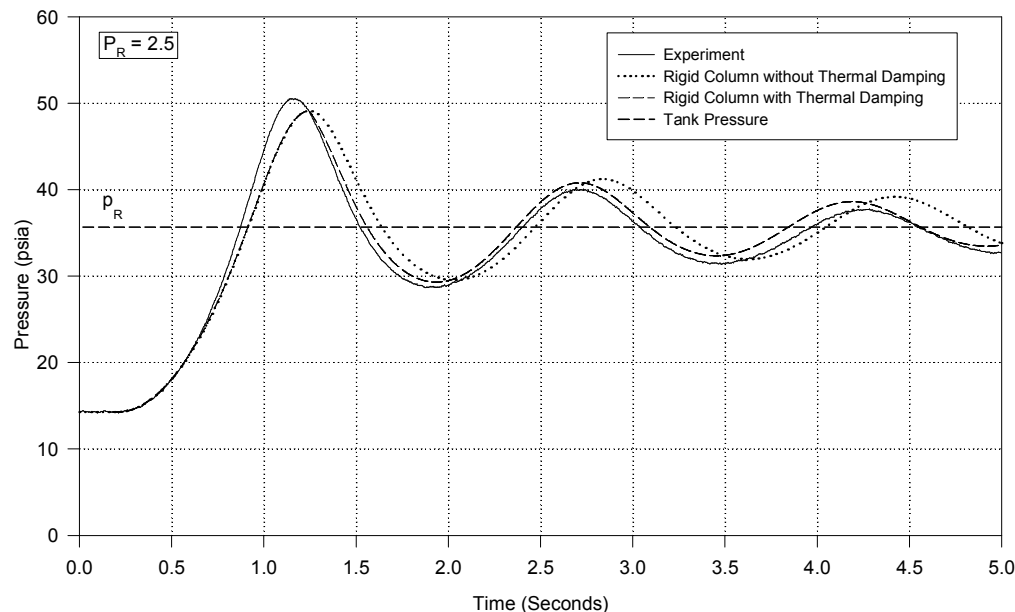


Figure 6.8 Effect of Thermal Damping on Entrapped Air for  $L_A = 16.23 \text{ ft}$

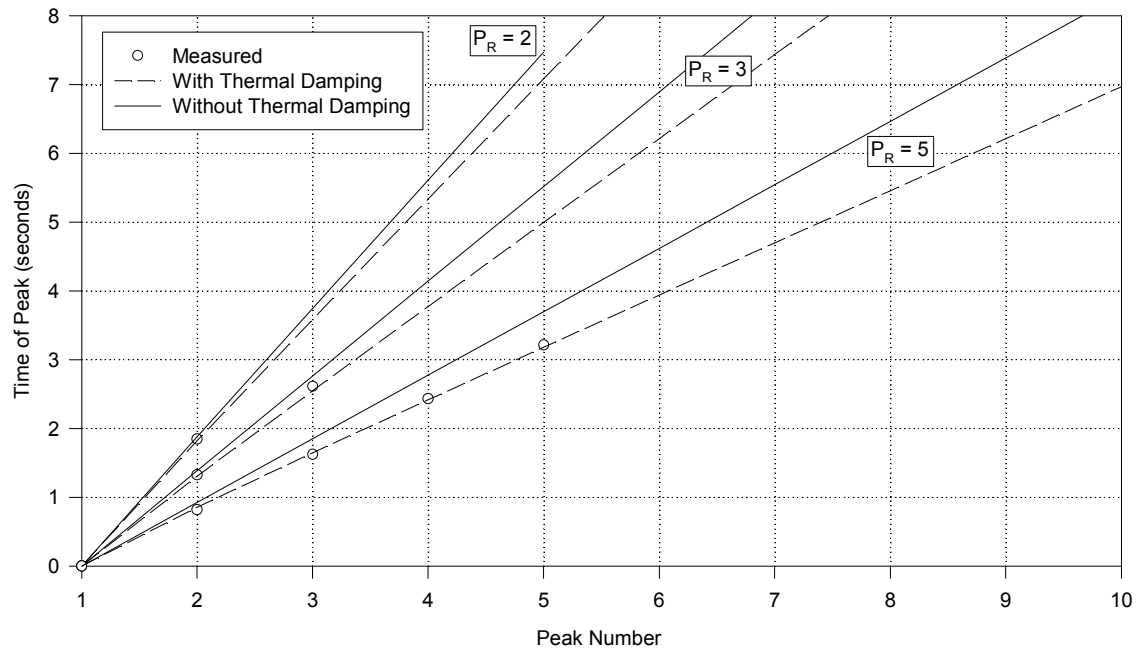


Figure 6.9 Effect of Thermal Damping on Entrapped Air Frequency for  $L_A = 16.23$  ft

## 6.2 Air Venting System

The physical phenomena of gas venting systems is a very complex problem. This was described earlier in Section 5.2. Only a few researchers have studied this field. Furthermore, there are few published articles that describe how maximum transient pressure develops in the case of orifices of medium size, that is, for the current experimental configuration, in the range of an 1/8-inch to 1/4-inch. Experimental data obtained using medium-sized orifices indicate the most extreme maximum pressure at the orifice. Analysis was focused on the entrapped type of pressure surges rather than waterhammer. Orifice sizes from 1/16-inch to 1/4-inch were selected for experiments designed to understand the physics behind the air venting system and were compared with analytical results.

The difficulties in developing an analytical model are as follows: Firstly, when the leading mixture of water and air reaches the orifice, there is an impact time. Secondly, what are the density and acoustic speed of the air-water mixture? Thirdly, how does this two-phase flow behave?

A modified entrapped gas model that neglects the effect of distributed two-phase flow was developed as an analytical model to verify that entrapped air plays a major role in the maximum pressure at the orifice. The impact time used in the analytic model was chosen from experimental results. Firstly, gas venting system equations as shown in Section 3.2.2 were adopted in the analytical model to simulate the period before impact time. Secondly, entrapped air equations were applied to predict maximum peak pressure.

A comparison of the analytic model and experimental results is presented in Figures 6.10, 6.11, and 6.12 for the longest initial air length  $L_A = 16.23$  ft,  $P_R = 3$ , and  $d = 1/16$ -inch, 1/8-inch, and 1/4-inch, respectively. Simulation results showed that the amount of entrapped air plays an important role in determining the magnitude of peak pressure. Impact time is the critical parameter in determining the entrapped air volume at the top of an orifice. The velocity profiles shown by both the analytical model and the experimental results agree well.

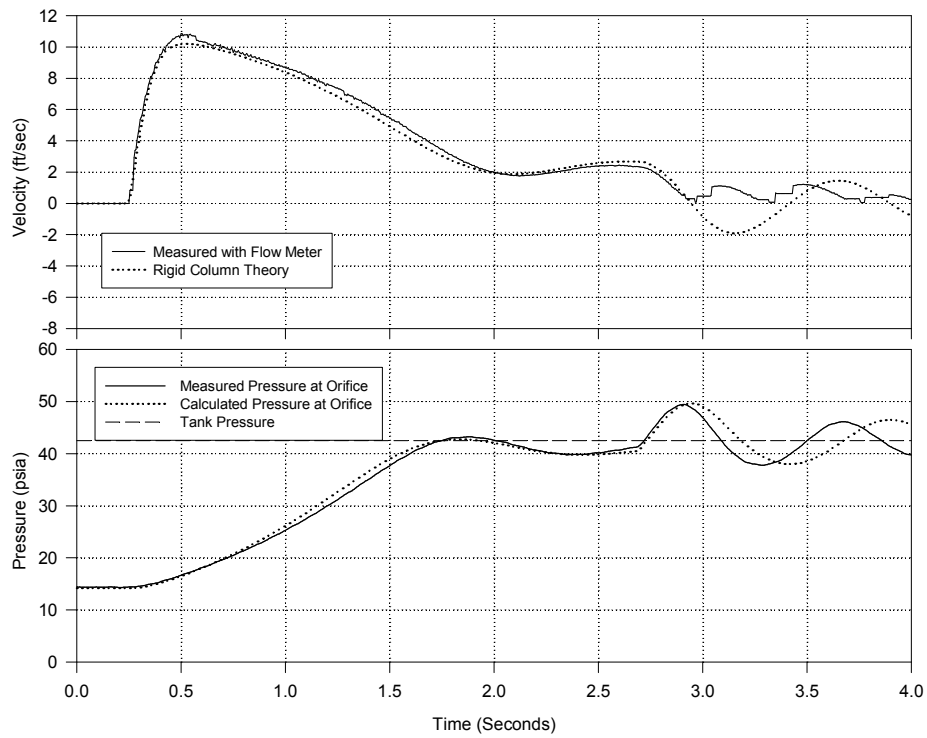


Figure 6.10 Venting Analysis for  $\alpha_0 = 0.4481$ ;  $P_R = 3$ ; and  $d = 1/16$  Inch

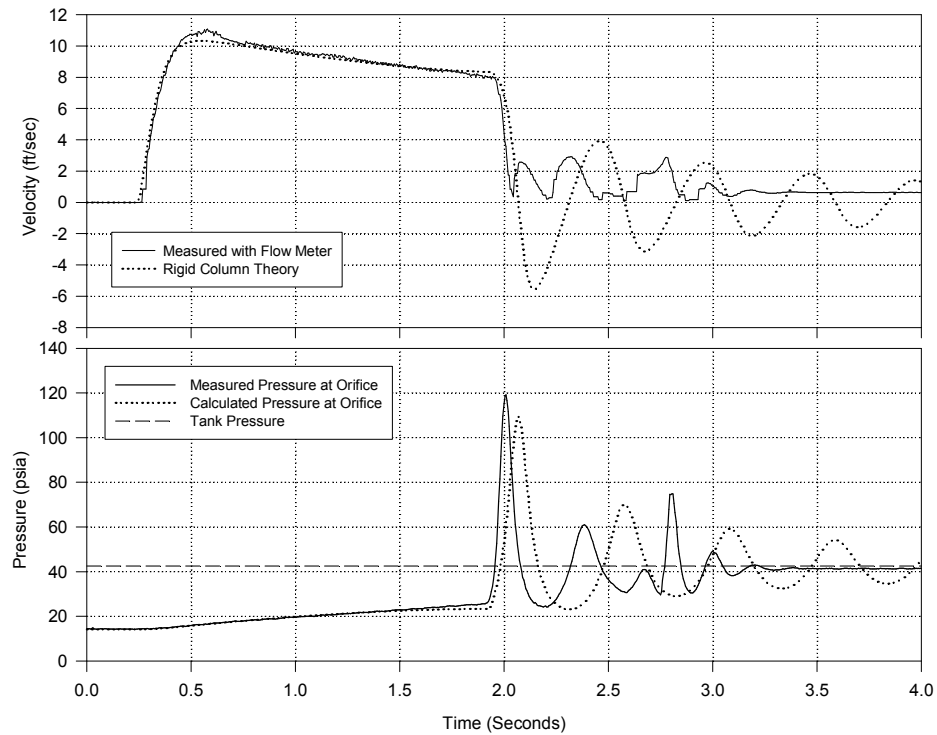


Figure 6.11 Venting Analysis for  $\alpha_0 = 0.4481$ ;  $P_R = 3$ ; and  $d = 1/8$  Inch

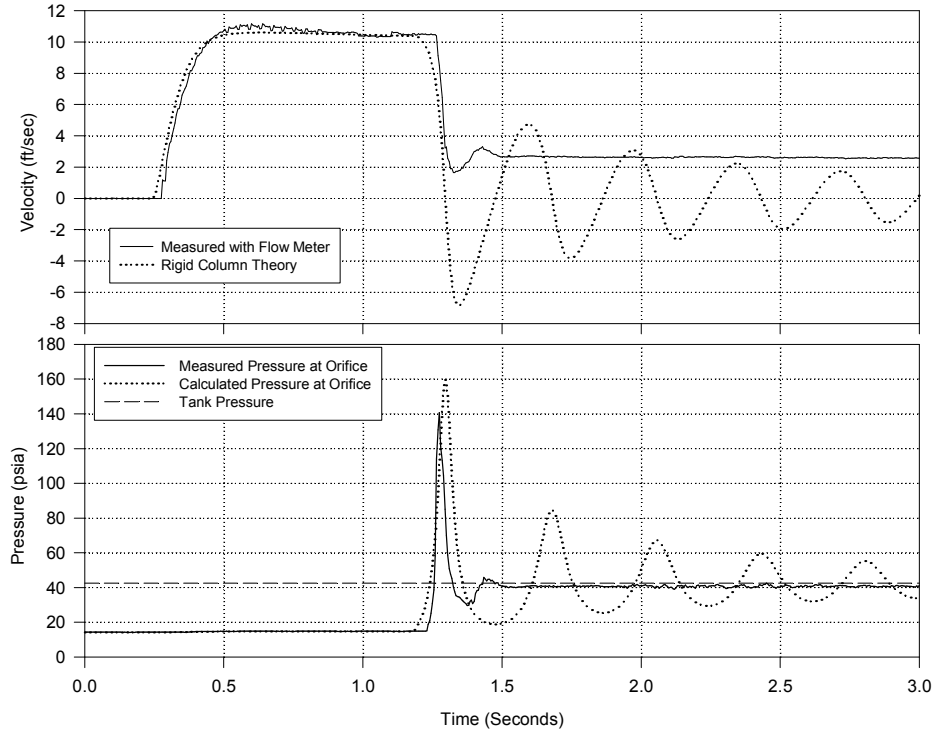


Figure 6.12. Venting Analysis for  $\alpha_0 = 0.4481$ ;  $P_R = 3$  ; and  $d = 1/4$  Inch

Indeed, for the smallest orifice, for which  $d = 1/6$ -inch (Figure 6.10), both the flow and orifice pressure are very well modeled using gas venting relationship and momentum Equation (6-2). It should be mentioned that the minor loss term is significantly increased because of the contribution of the turbine flow meter, for which  $K_{LM}$  is greater than 26. Initially, there is pressure buildup akin to entrapped air because of relatively low rate of air being expelled at the orifice. Peak pressure occurs slightly before  $t = 2$  seconds, followed by a discontinuity at  $t \sim 2.65$  seconds, attributed to the orifice hole being closed off or covered by the water. The smaller amount of air remaining within the pipe leads to a higher frequency of oscillation.

For  $d = 1/8$ -inch (Figure 6.11) a lesser pressure increase compared to  $d = 1/16$ -inch, but higher water flow leads to the orifice hole being covered at  $t \sim 1.9$  seconds, sudden deceleration, and a higher peak pressure, which can be principally related to an entrapped air phenomenon, as predicted by rigid column mode with air. It is claimed that the orifice hole is uncovered after  $t > 2.5$  seconds, resulting in more air being expelled, and associated

higher frequency of oscillation shown in Figure 6.11.

Higher impact pressures occur as the orifice diameter  $d$  is increased to 1/4-inch (Figure 6.12). Because of the greater air flow there is not much pressure buildup before the water column reached the orifice. The pressure rise due to impact is reasonably modeled employing the same technique of applying entrapped air modeling once the orifice hole is temporarily covered. For this experiment, however, the larger hole size did not inhibit the expulsion of air, as the pressure at PT3 settled down to tank pressure  $p_R$  at  $t \sim 1.5$  seconds

## CHAPTER 7

### CONCLUSION AND RECOMMENDATIONS

Analytical models were studied and experiments were performed in the cases of pipelines with dead ends and orifices. In the dead end case, analytical models were developed for the Case I :Lumped constant liquid length and lumped gas mass; Case II : Lumped variable liquid length and lumped gas mass; Case III : Acoustic liquid and lumped gas mass, and Case IV : Acoustic liquid and acoustic gas. Analytical models predicted initial peak pressure and time well. Both analytical models and experiments showed that an "entrapped gas pocket can reduce or increase pressure rise depending on the flow acceleration", which was also stated by Lee and Martin (1999). Findings are as follows:

- The analytical model study showed that the lumped gas mass method is adequate to investigate the entrapped gas study because there is little acoustic wave action inside a gas pocket as that gas pocket is compressed and expanded. This was verified both theoretically and experimentally.
- Closed forms of solutions were developed for both the lumped variable liquid length and lumped gas mass, and for the lumped constant liquid length and lumped gas mass. Closed form solutions have shown that both models yield the same values of maximum interface pressure and minimum gas volume if the pipeline is horizontal.
- Frequency analysis for a closed system was investigated with respect to thermal damping, which accounts for frequency shortening and additional damping other than that caused by pipe friction and minor loss. Investigation of thermal damping showed that the heat transfer term changes the stiffness of the entrapped gas system. However, pipe friction and minor loss do not change the stiffness of the entrapped gas system.

- During the gas venting experiments, a small amount of gas covering the top of an orifice was shown to be able to cause a significant pressure surge of the entrapped gas type. Analytical models also show that small amounts of gas can cause severe pressure. This agrees well with experimental measurements.
- Only orifices of the smallest and largest (greater than critical value) size recorded lower pressure of the pressure surge type than occurs in a closed system.

Further research is recommended. The heat transfer coefficient relating to thermal damping needs to be carefully measured experimentally and theoretical study is needed to define the heat transfer coefficient between gas and liquid. Analytical models need to be applied to study two-phase flow in order to predict the impact time on a gas venting system. This time was taken from experimental results in the modified entrapped gas model.

# **APPENDIX A**

## **ENTRAPPED AIR EXPERIMENTAL RESULTS**

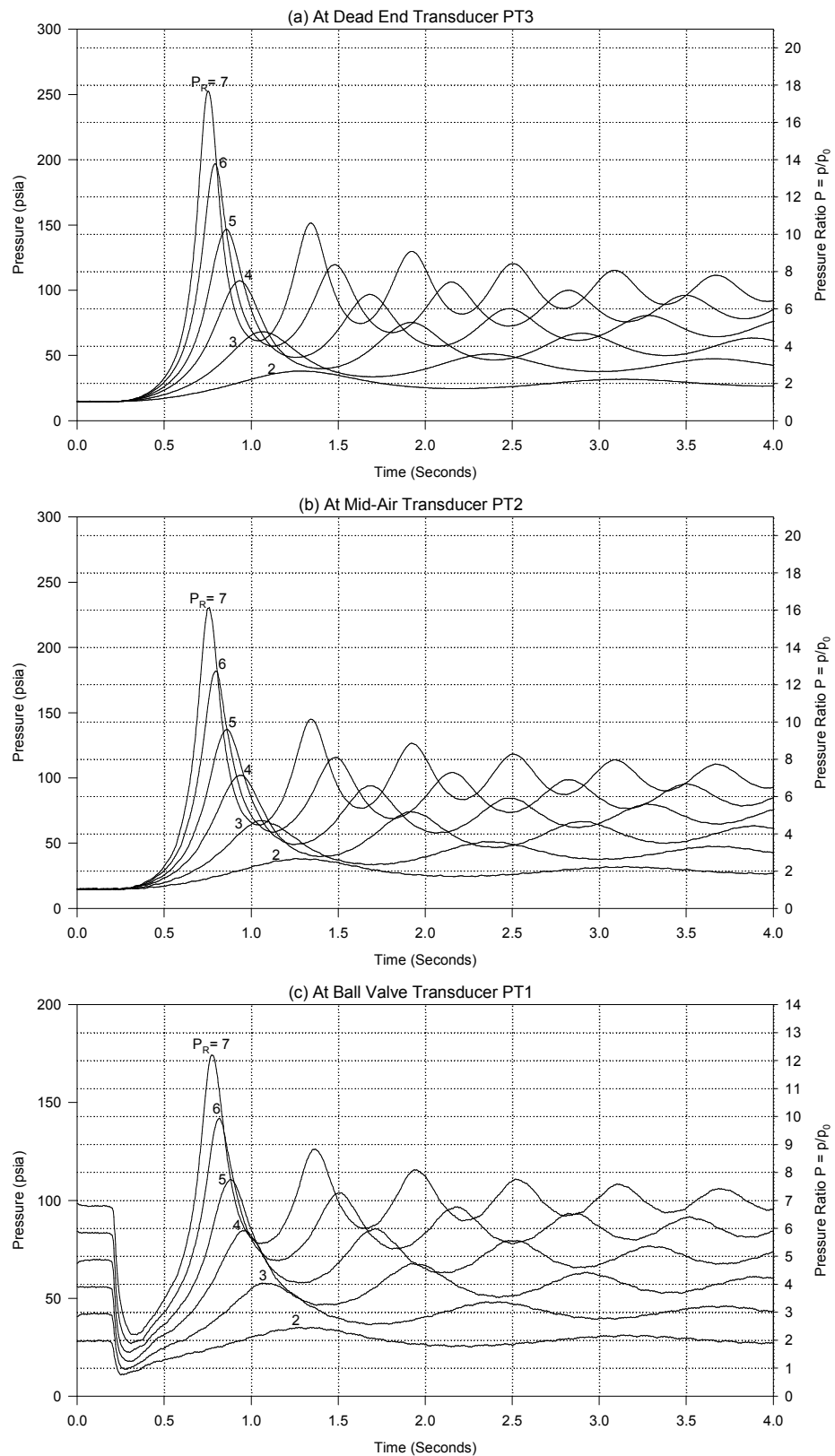


Figure A.1 Entrapped Air Pressure Time Histories for  $L_A = 16.23 \text{ ft}$  ( $\alpha_0 = 0.4481$ )

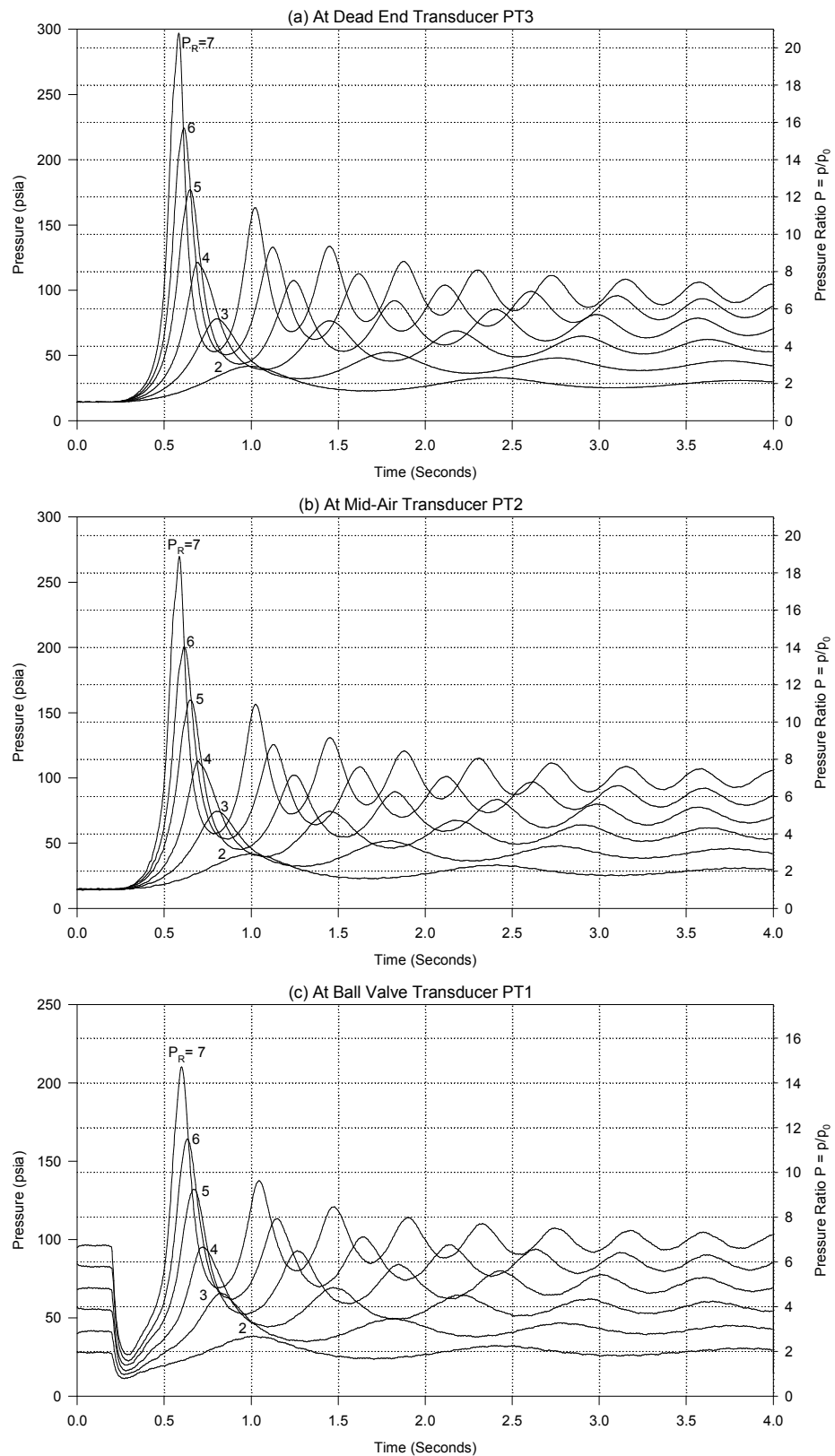


Figure A.2 Entrapped Air Pressure Time Histories for  $L_A = 10.1$  ft ( $\alpha_0 = 0.3357$ )

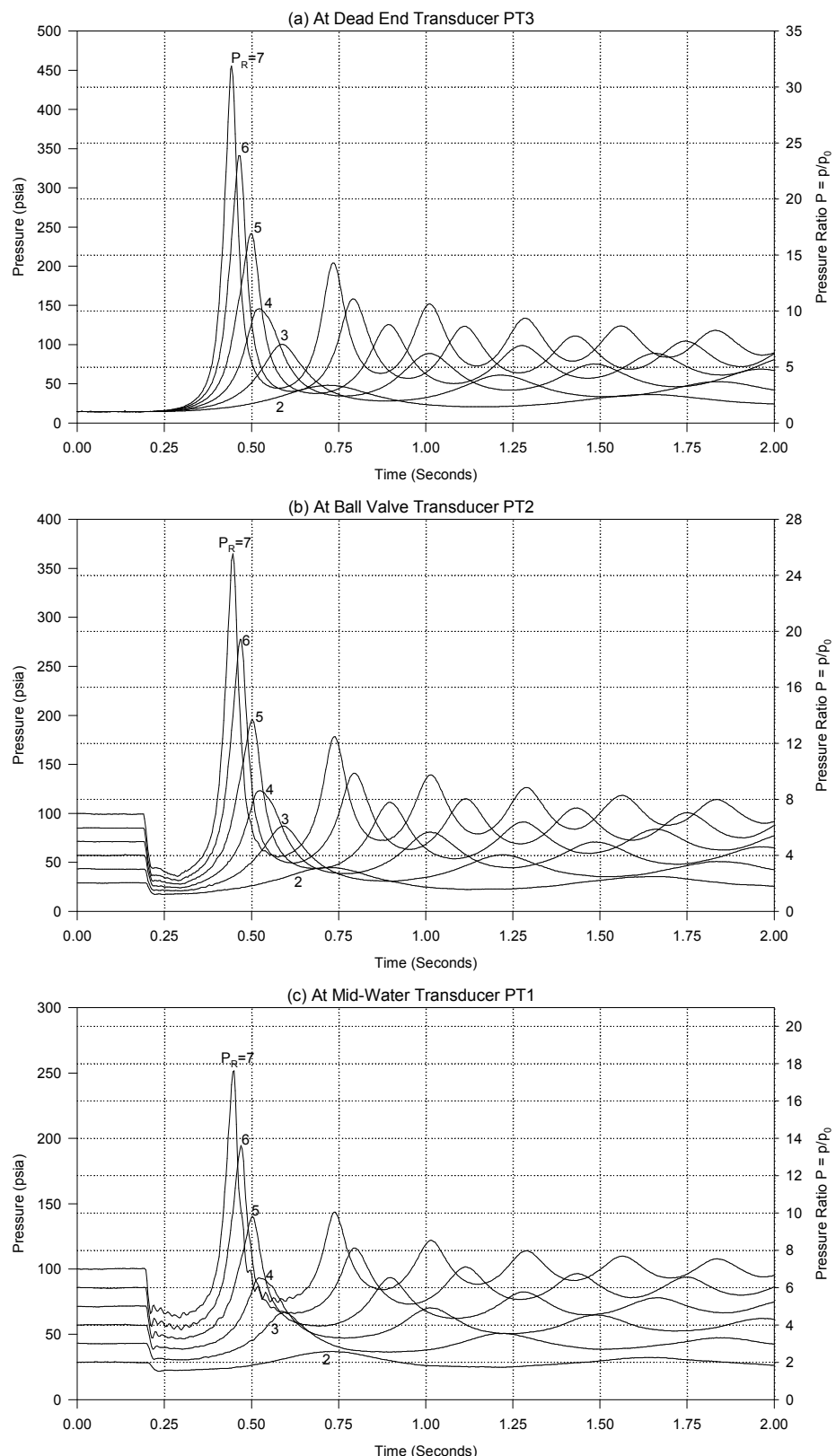


Figure A.3 Entrapped Air Pressure Time Histories for  $L_A = 4.85$  ft ( $\alpha_0 = 0.1952$ )

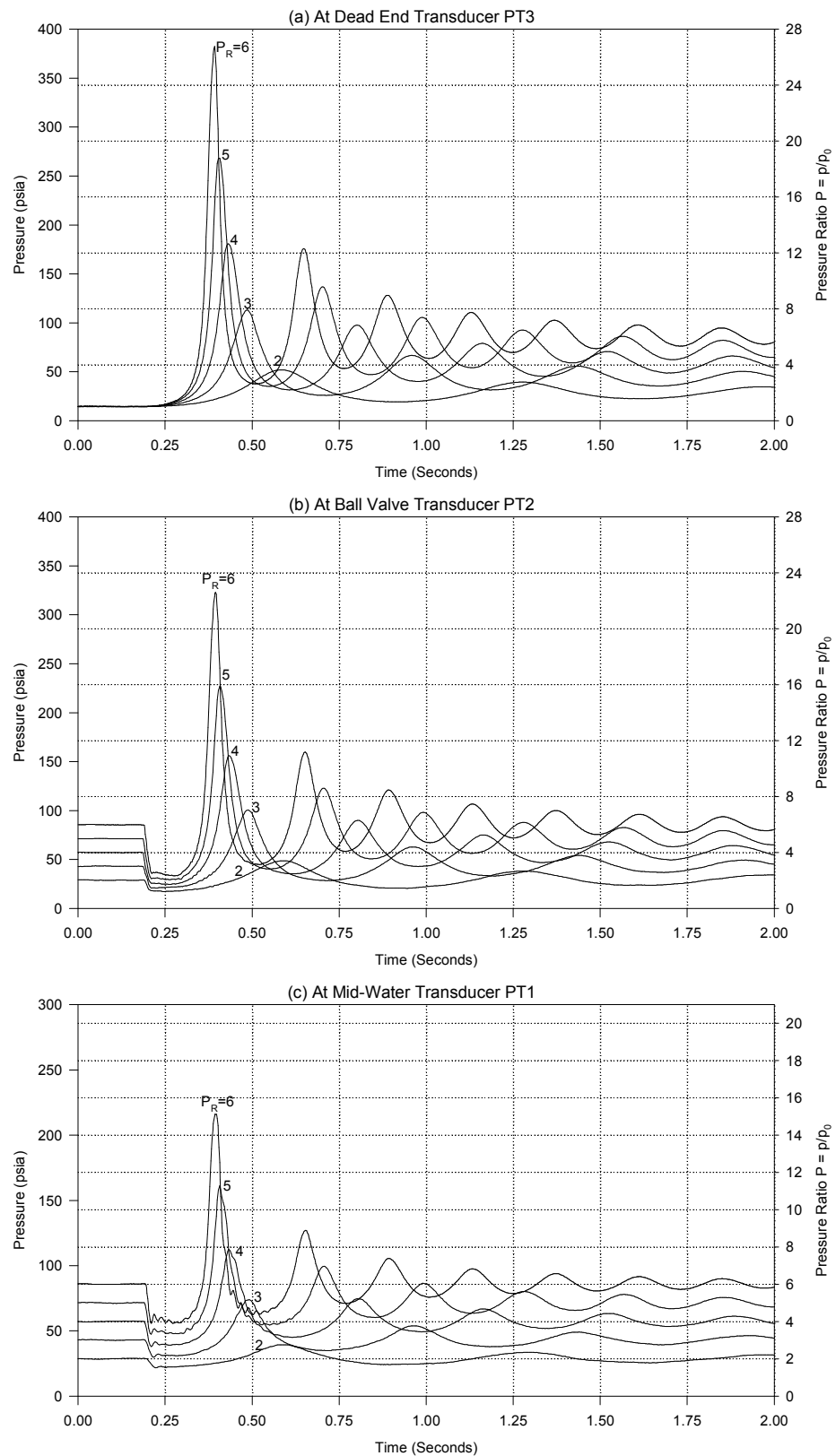


Figure A.4 Entrapped Air Pressure Time Histories for  $L_A = 2.77$  ft ( $\alpha_0 = 0.1217$ )

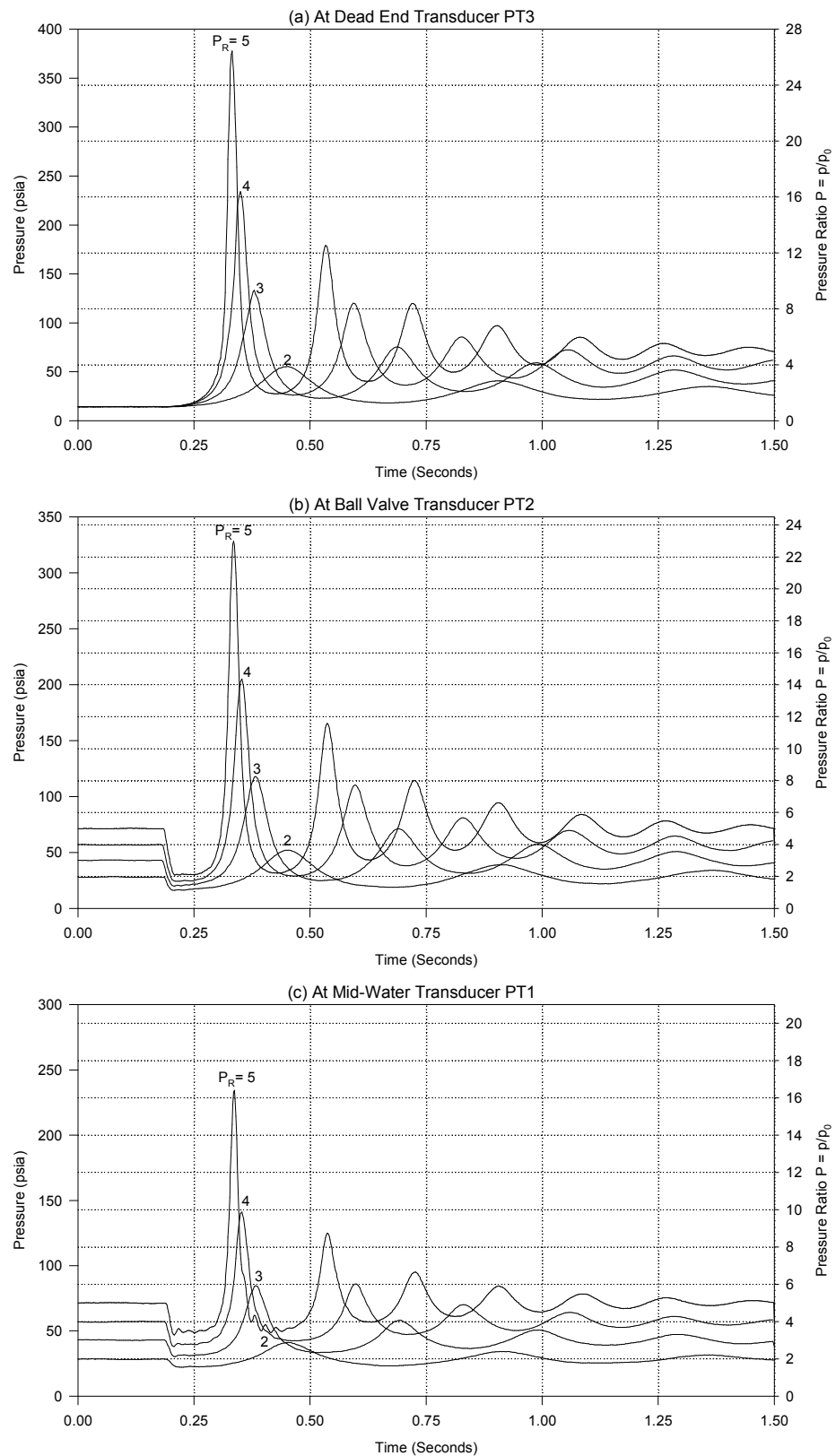


Figure A.5 Entrapped Air Pressure Time Histories for  $L_A = 1.23$  ft ( $\alpha_0 = 0.0580$ )

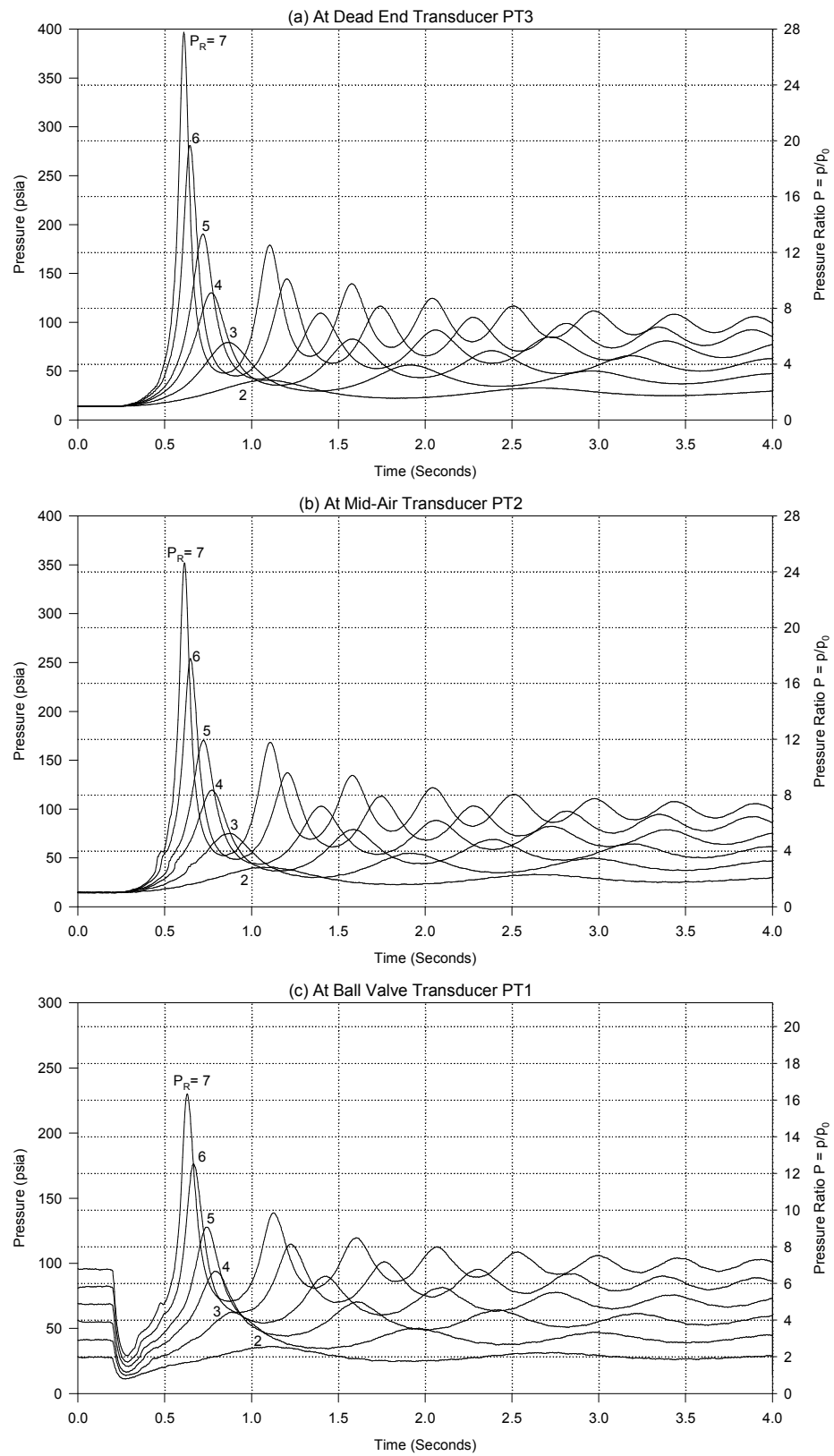


Figure A.6 Entrapped Air Pressure Time Histories with Air Space Partially Filled with Water for  $L_A = 16.23$  ft ( $\alpha_0 = 0.2558$ )

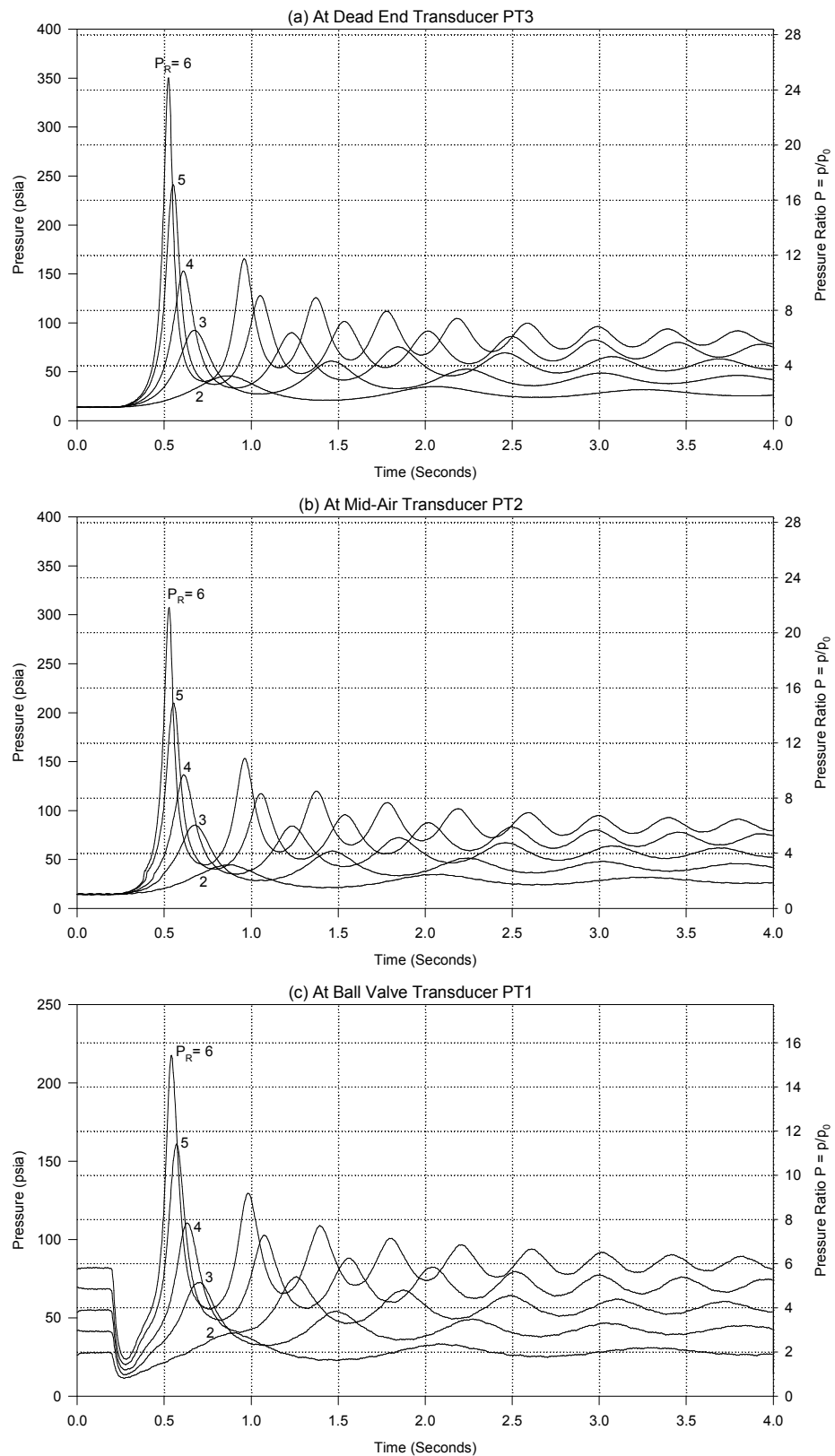


Figure A.7 Entrapped Air Pressure Time Histories with Air Space Partially Filled with Water for  $L_A = 10.1$  ft ( $\alpha_0 = 0.1980$ )

## APPENDIX B

### AIR VENTING EXPERIMENTAL RESULTS

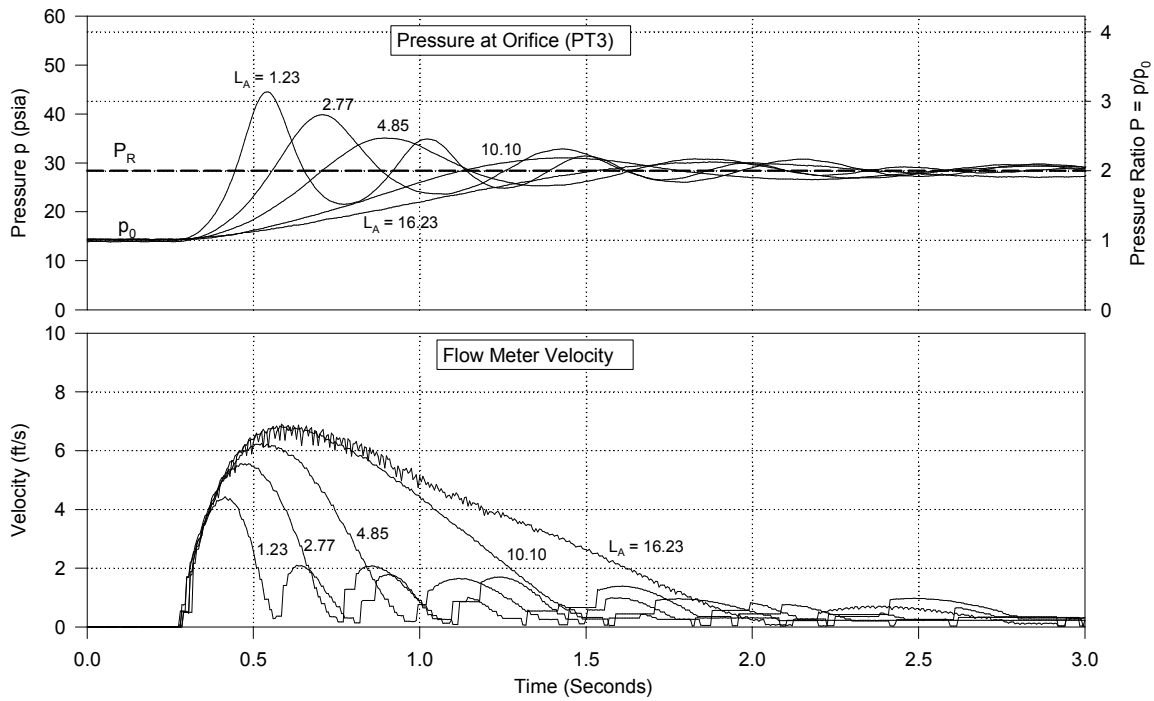


Figure B.1 Pressure and Velocity Time Histories for Air Venting ( $P_R = 2$ ;  $d = 0$ )

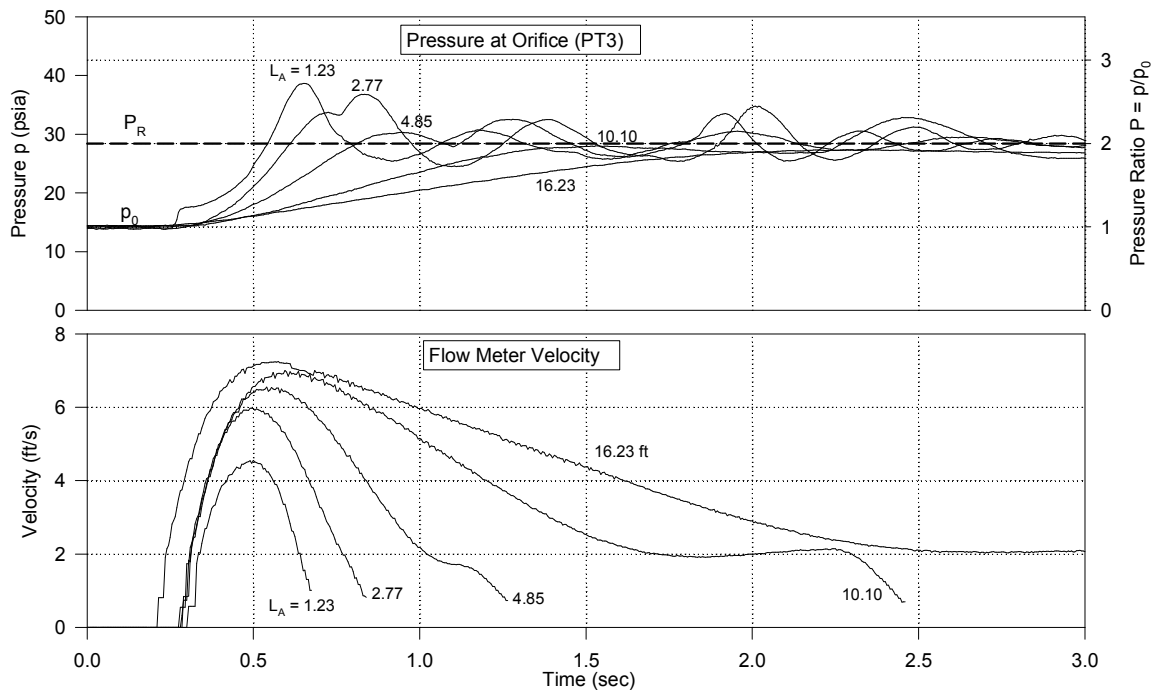


Figure B.2 Pressure and Velocity Time Histories for Air Venting ( $P_R = 2$ ;  $d = 1/16$  Inch)

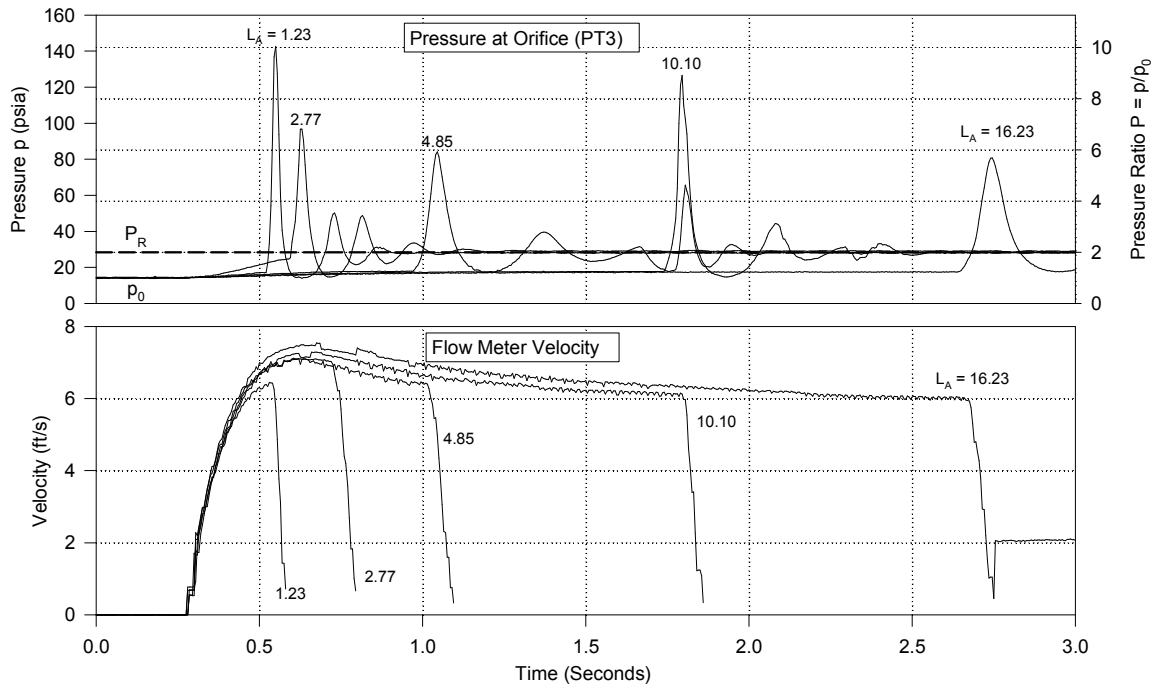


Figure B.3 Pressure and Velocity Time Histories for Air Venting ( $P_R = 2$ ;  $d = 1/8$  Inch)

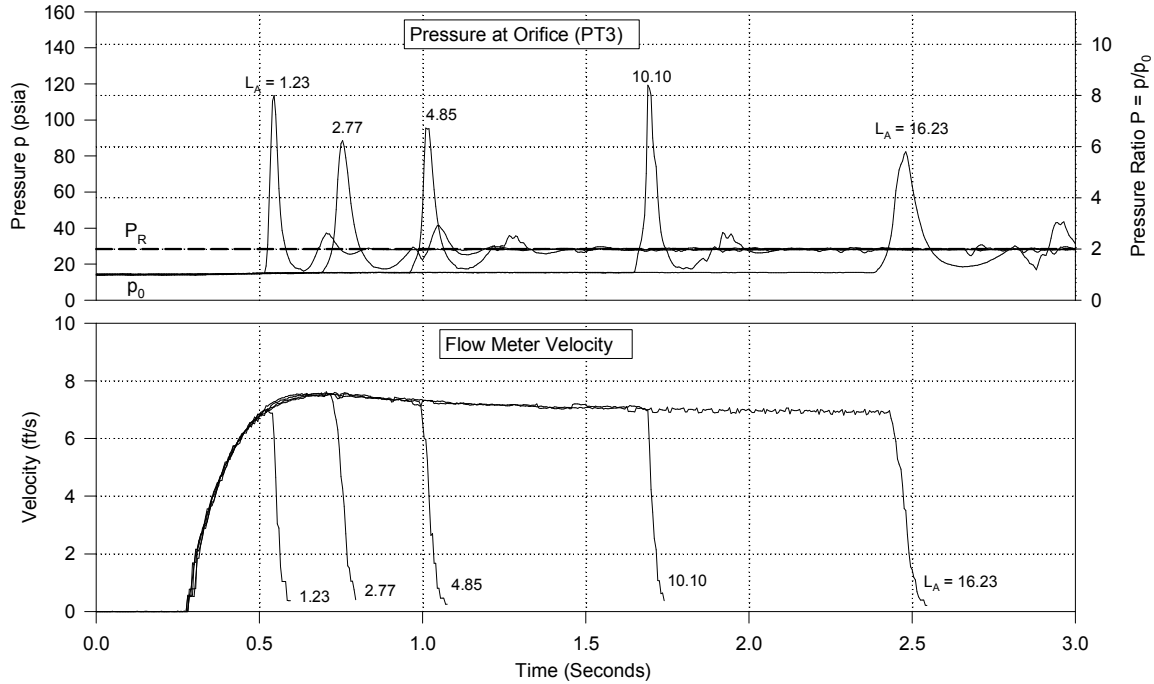


Figure B.4 Pressure and Velocity Time Histories for Air Venting ( $P_R = 2$ ;  $d = 3/16$  Inch)

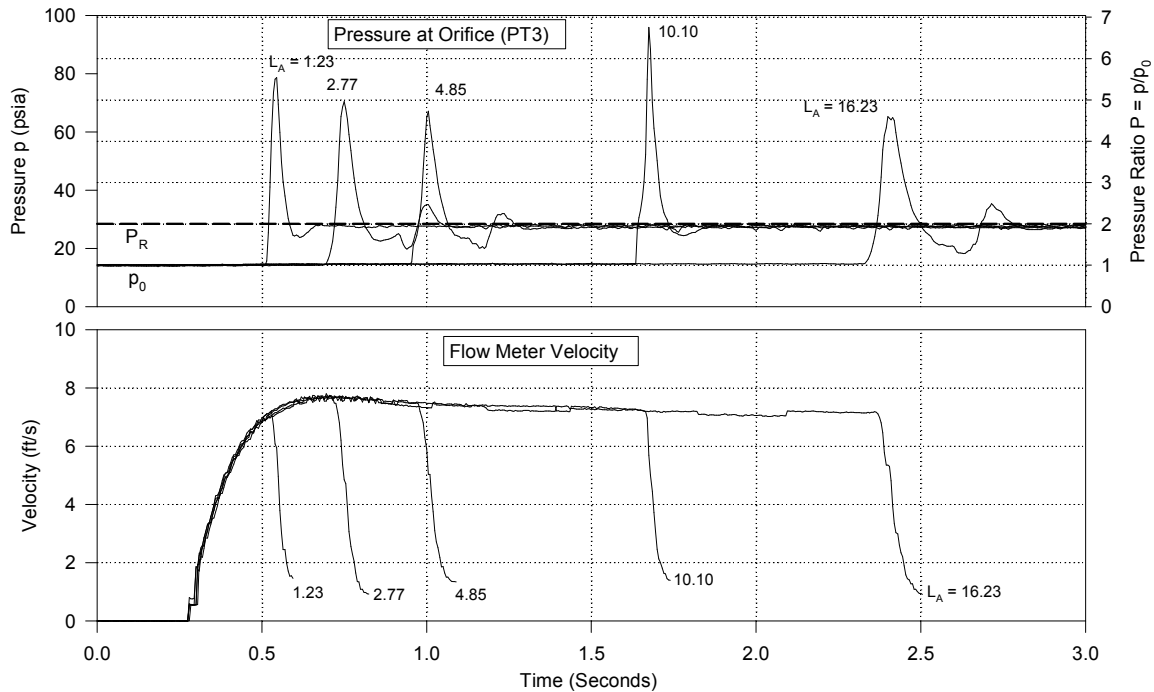


Figure B.5 Pressure and Velocity Time Histories for Air Venting ( $P_R = 2$ ;  $d = 1/4$  Inch)

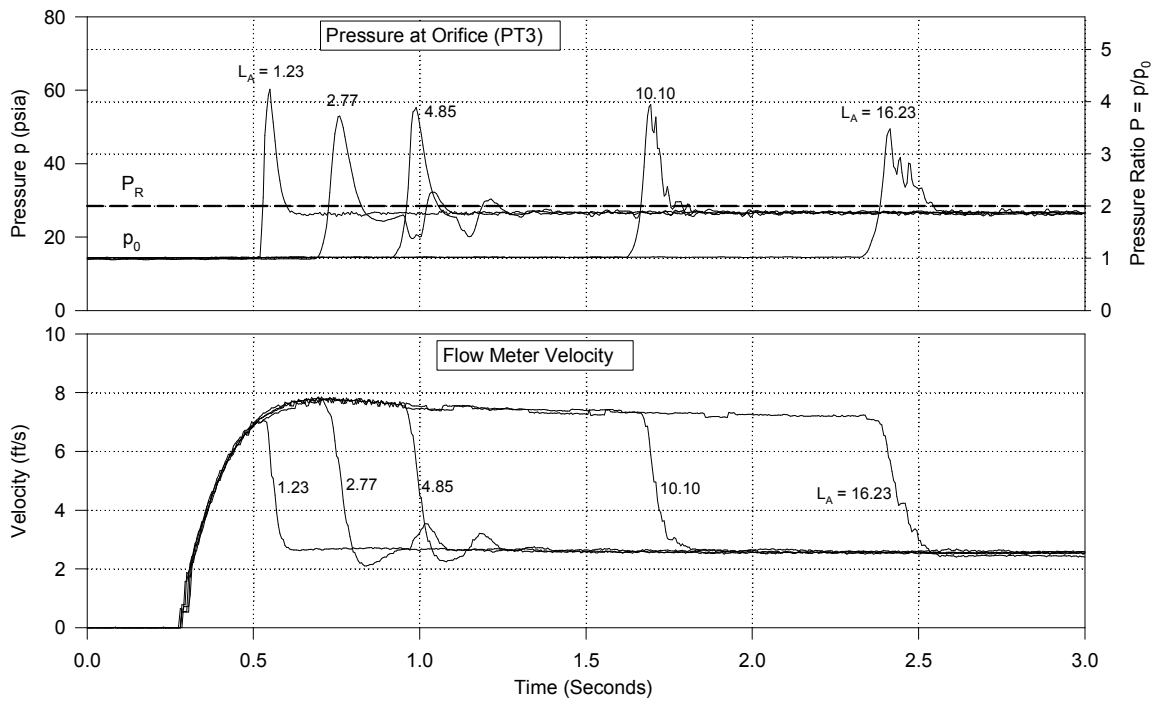


Figure B.6 Pressure and Velocity Time Histories for Air Venting ( $P_R = 2$ ;  $d = 5/16$  Inch)

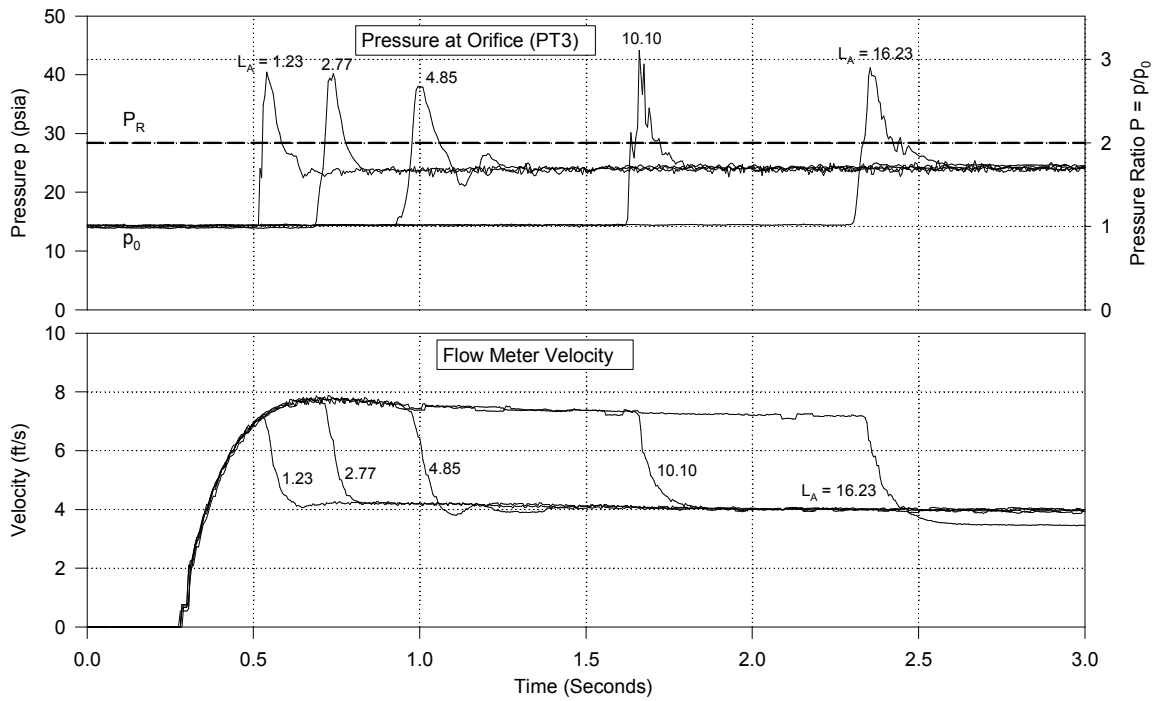


Figure B.7 Pressure and Velocity Time Histories for Air Venting ( $P_R = 2$ ;  $d = 3/8$  Inch)

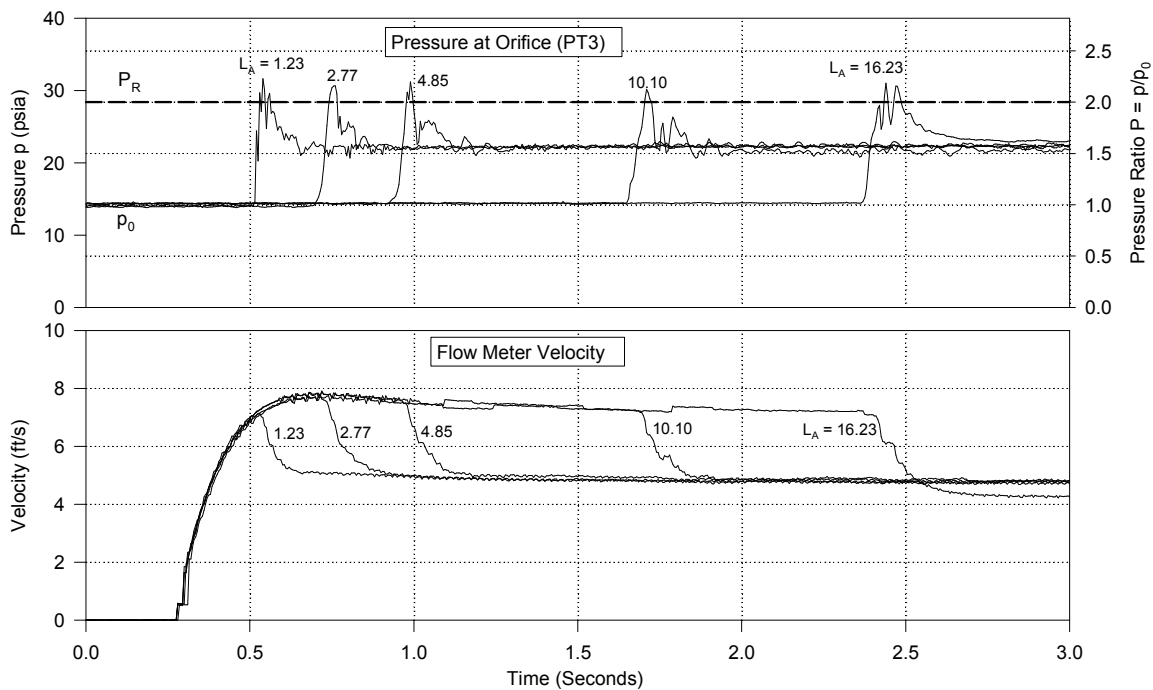


Figure B.8 Pressure and Velocity Time Histories for Air Venting ( $P_R = 2$ ;  $d = 7/16$  Inch)

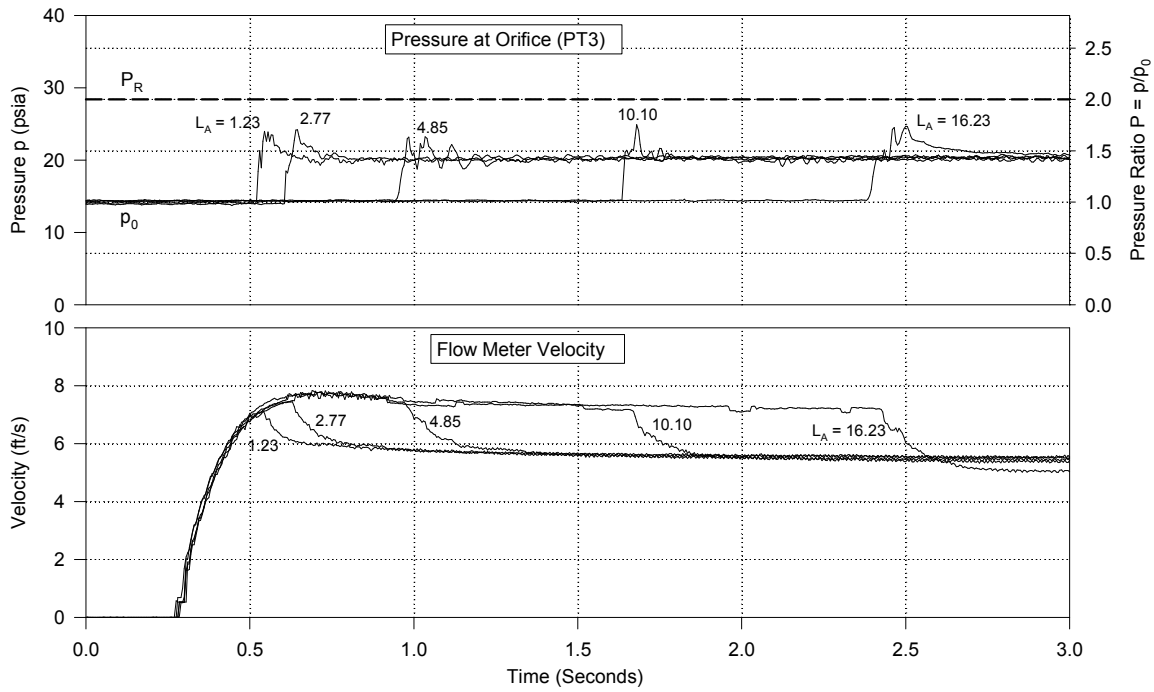


Figure B.9 Pressure and Velocity Time Histories for Air Venting ( $P_R = 2$ ;  $d = 1/2$  Inch)

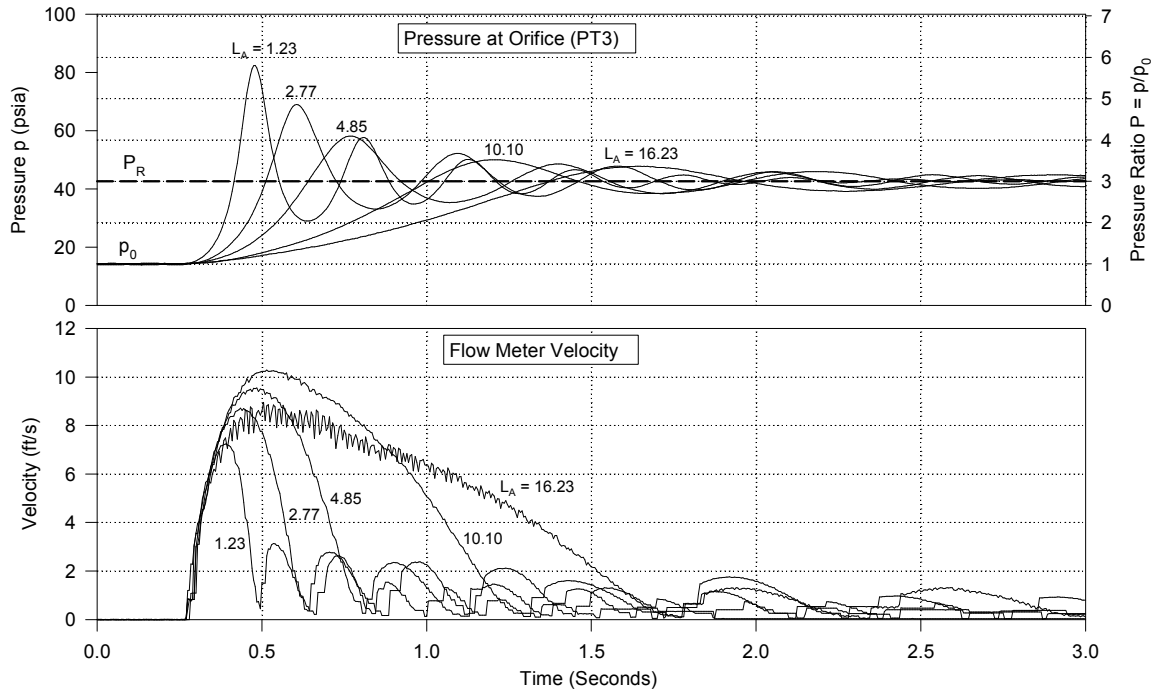


Figure B.10 Pressure and Velocity Time Histories for Air Venting ( $P_R = 3$ ;  $d = 0$ )

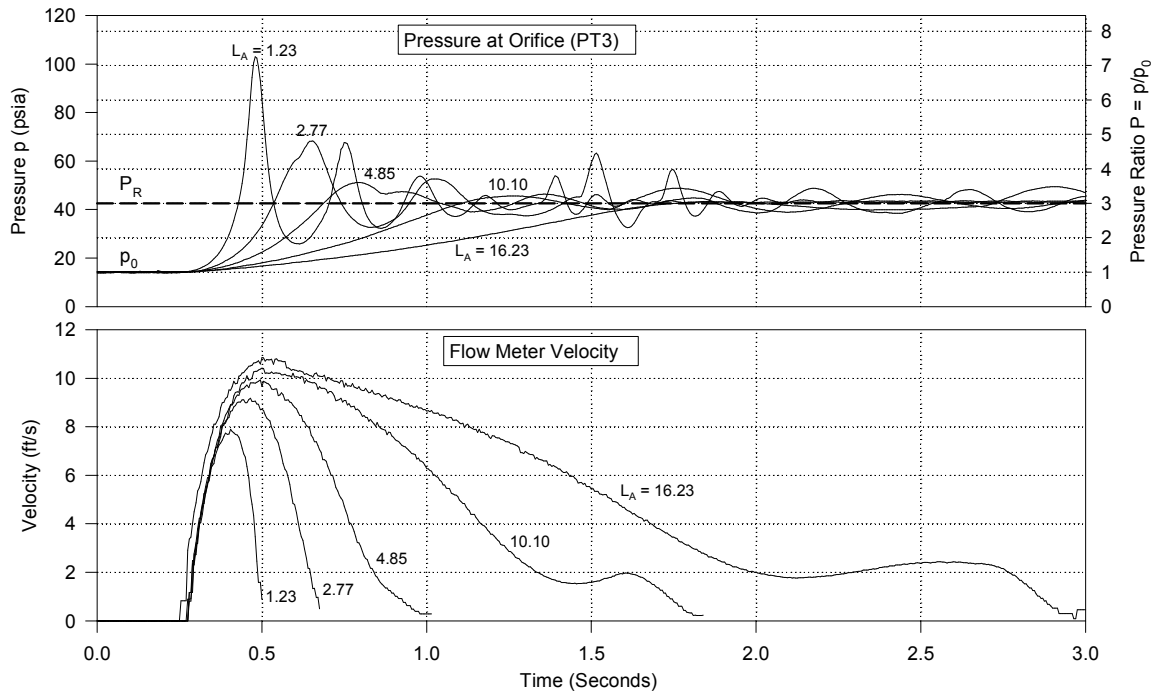


Figure B.11 Pressure and Velocity Time Histories for Air Venting ( $P_R = 3$ ;  $d = 1/16$  Inch)

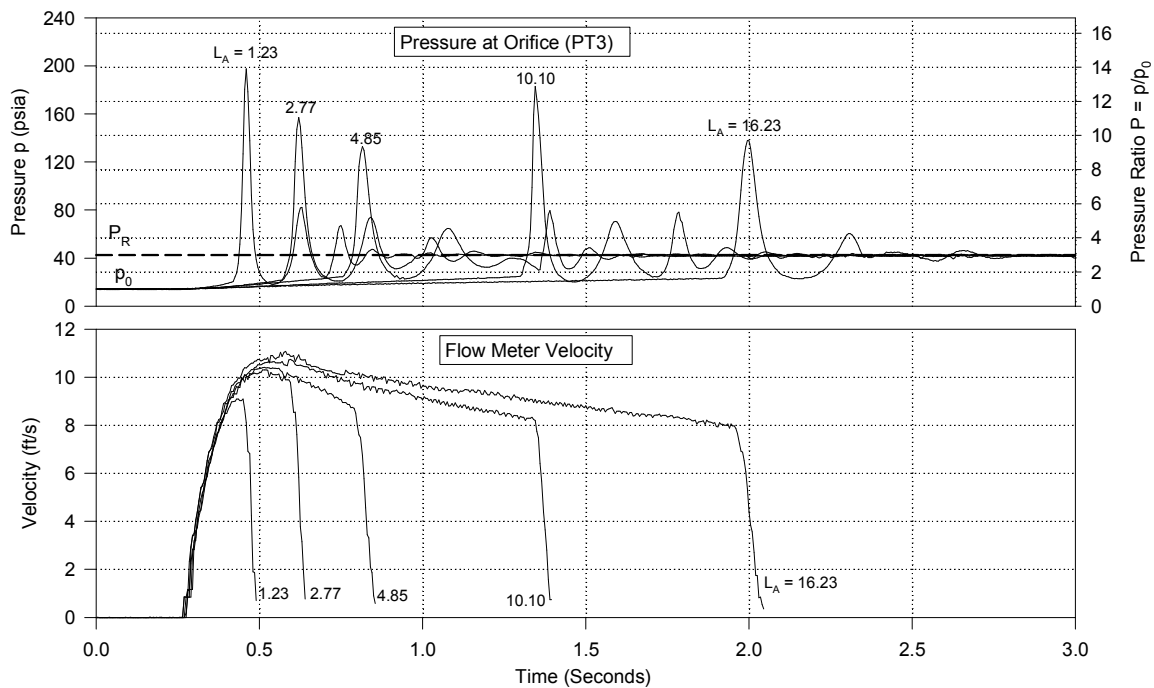


Figure B.12 Pressure and Velocity Time Histories for Air Venting ( $P_R = 3$ ;  $d = 1/8$  Inch)

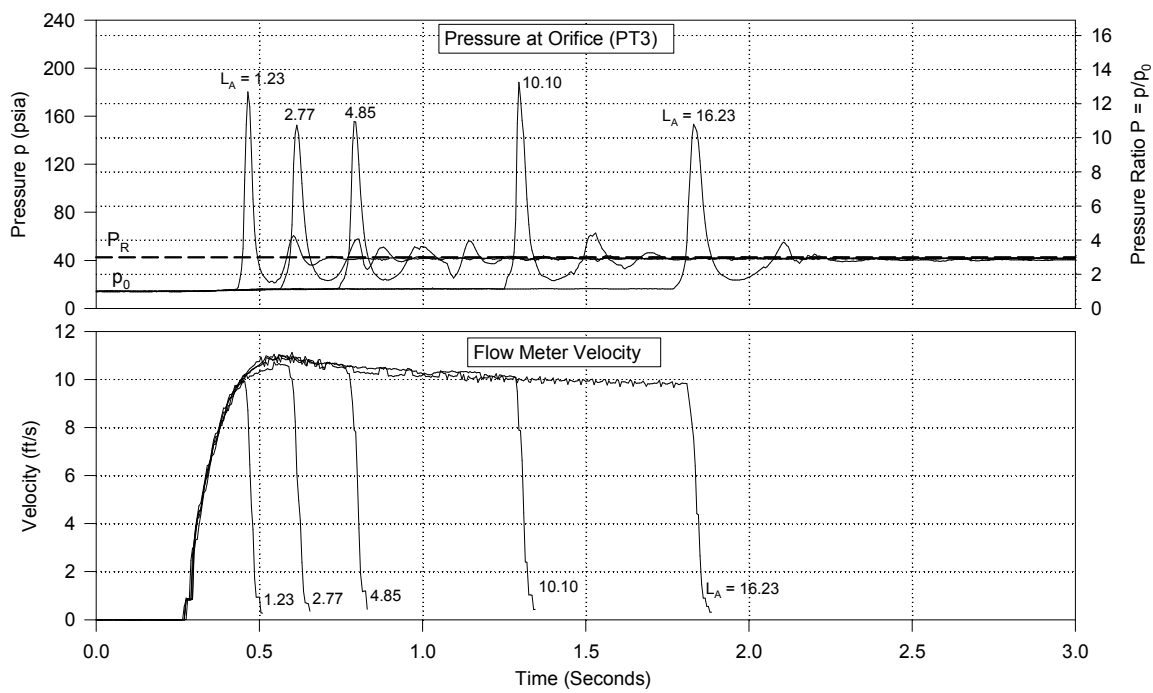


Figure B.13 Pressure and Velocity Time Histories for Air Venting ( $P_R = 3$ ;  $d = 3/16$  Inch)

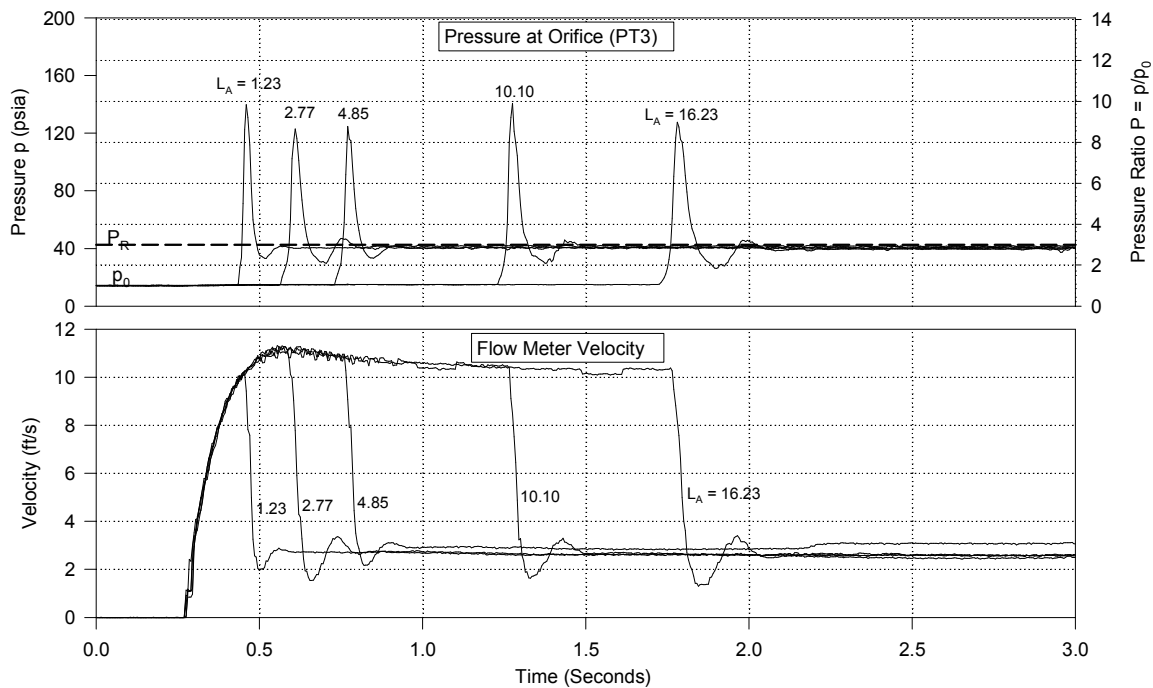


Figure B.14 Pressure and Velocity Time Histories for Air Venting ( $P_R = 3$ ;  $d = 1/4$  Inch)

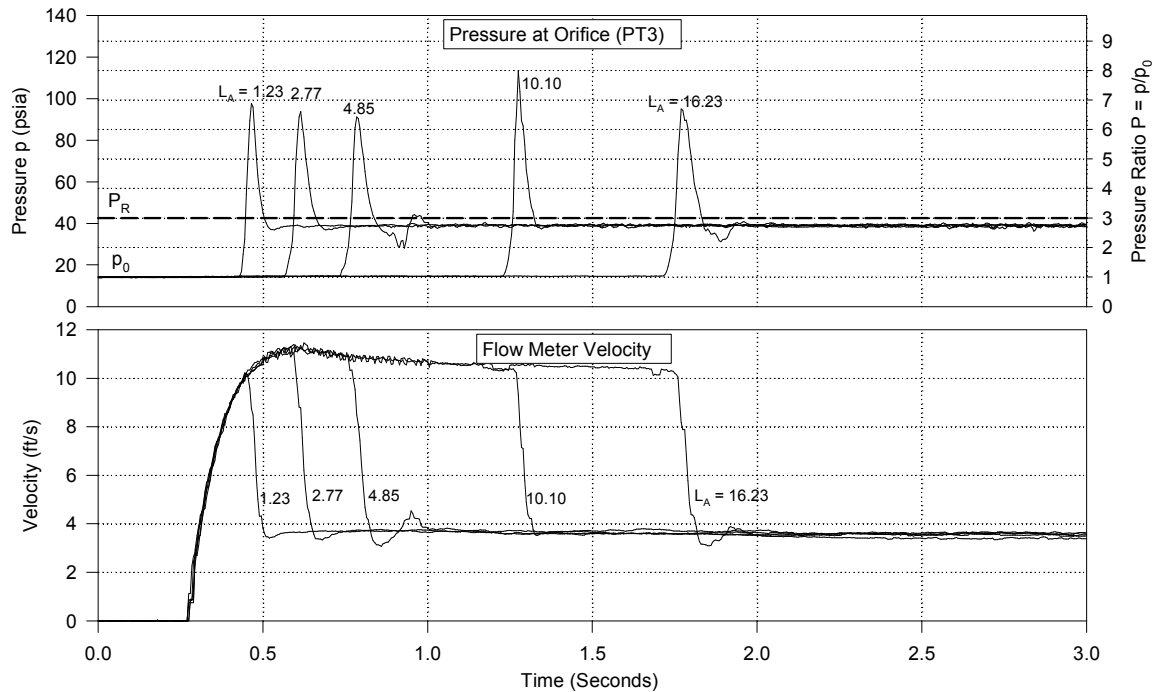


Figure B.15 Pressure and Velocity Time Histories for Air Venting ( $P_R = 3$ ;  $d = 5/16$  Inch)

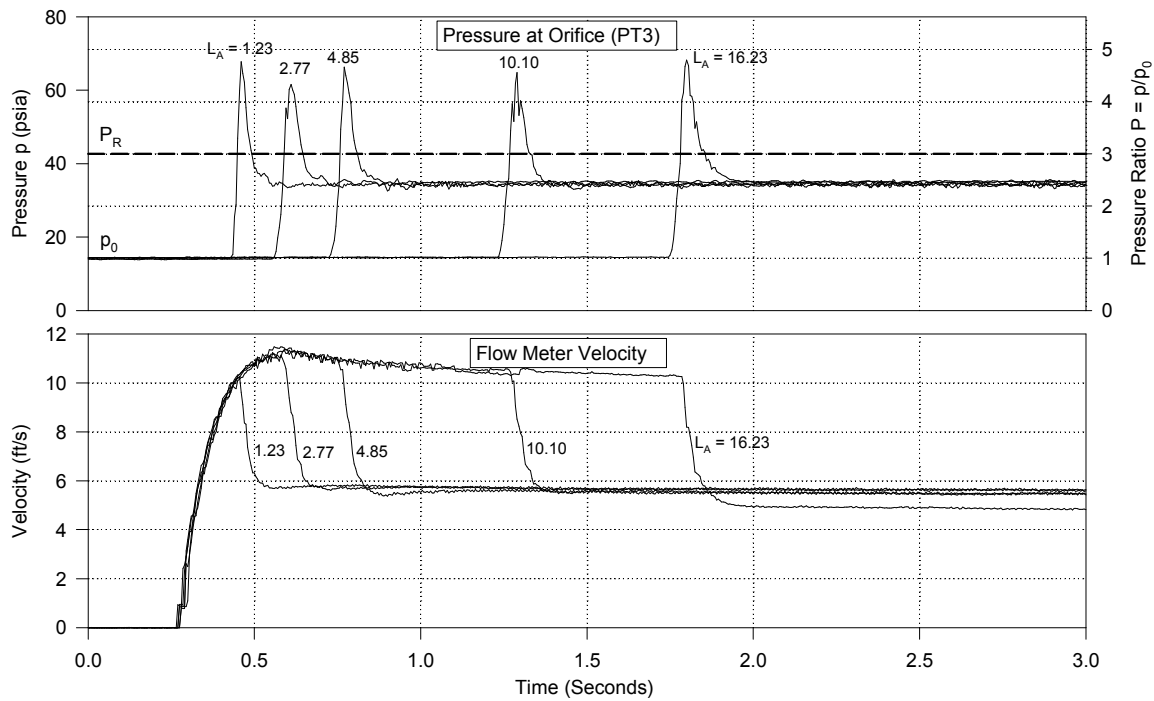


Figure B.16 Pressure and Velocity Time Histories for Air Venting ( $P_R = 3$ ;  $d = 3/8$  Inch)

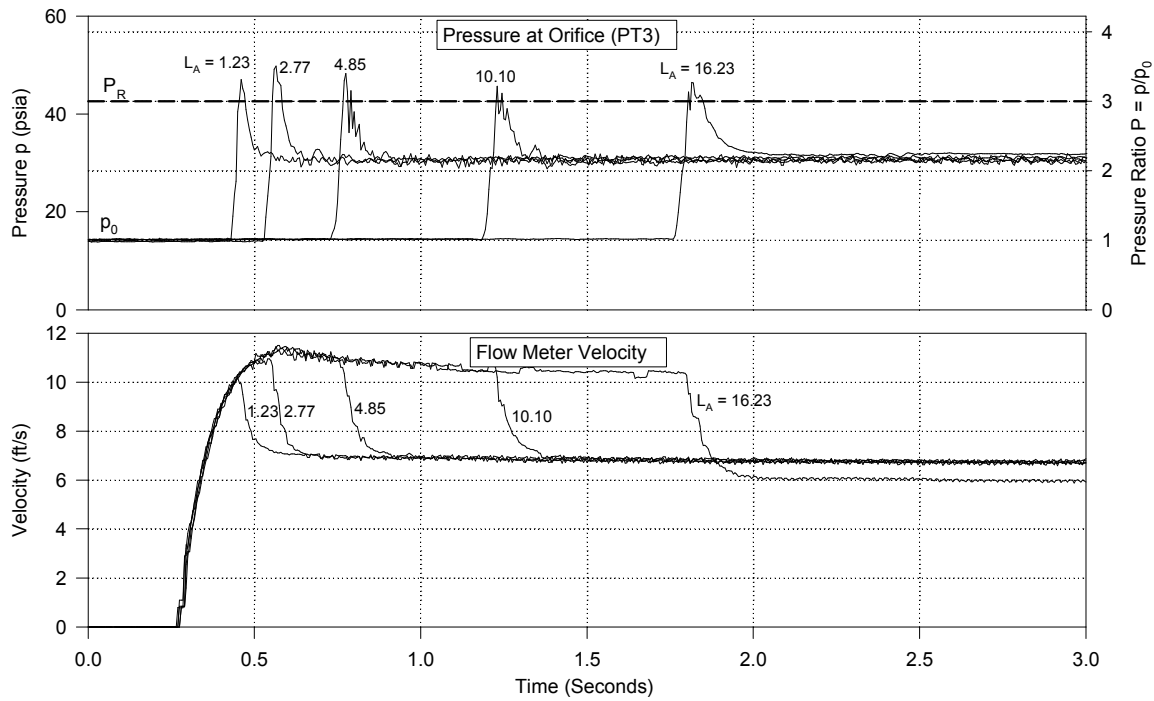


Figure B.17 Pressure and Velocity Time Histories for Air Venting ( $P_R = 3$ ;  $d = 7/16$  Inch)

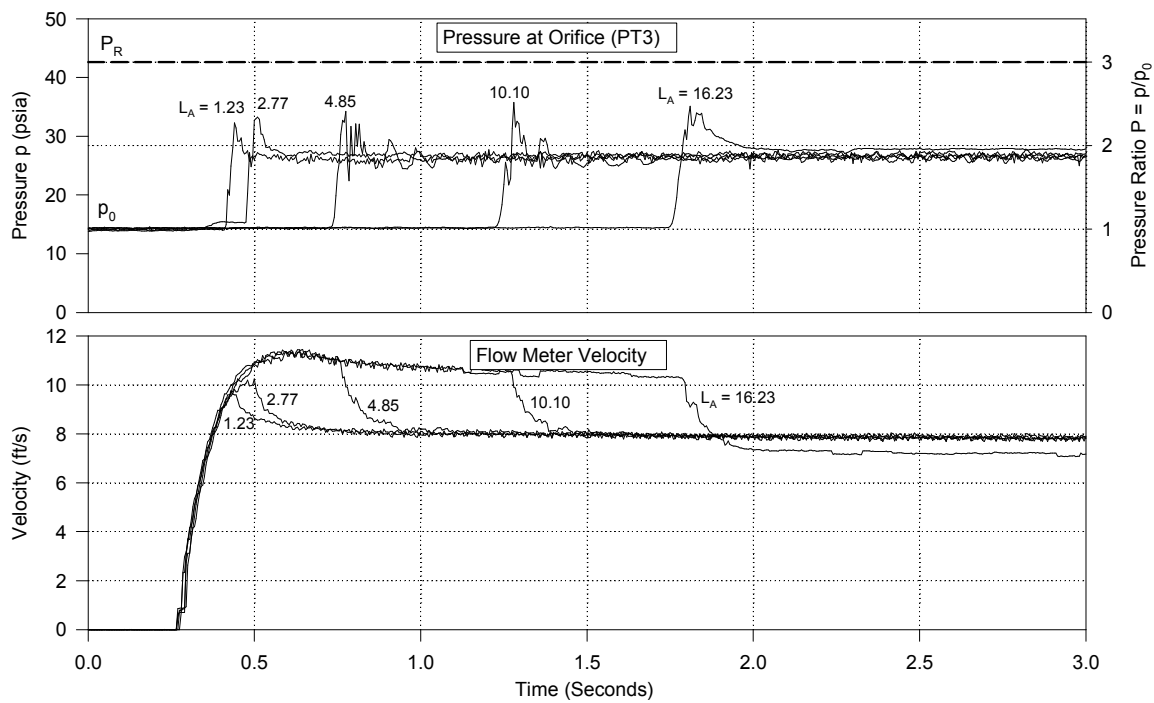


Figure B.18 Pressure and Velocity Time Histories for Air Venting ( $P_R = 3$ ;  $d = 1/2$  Inch)

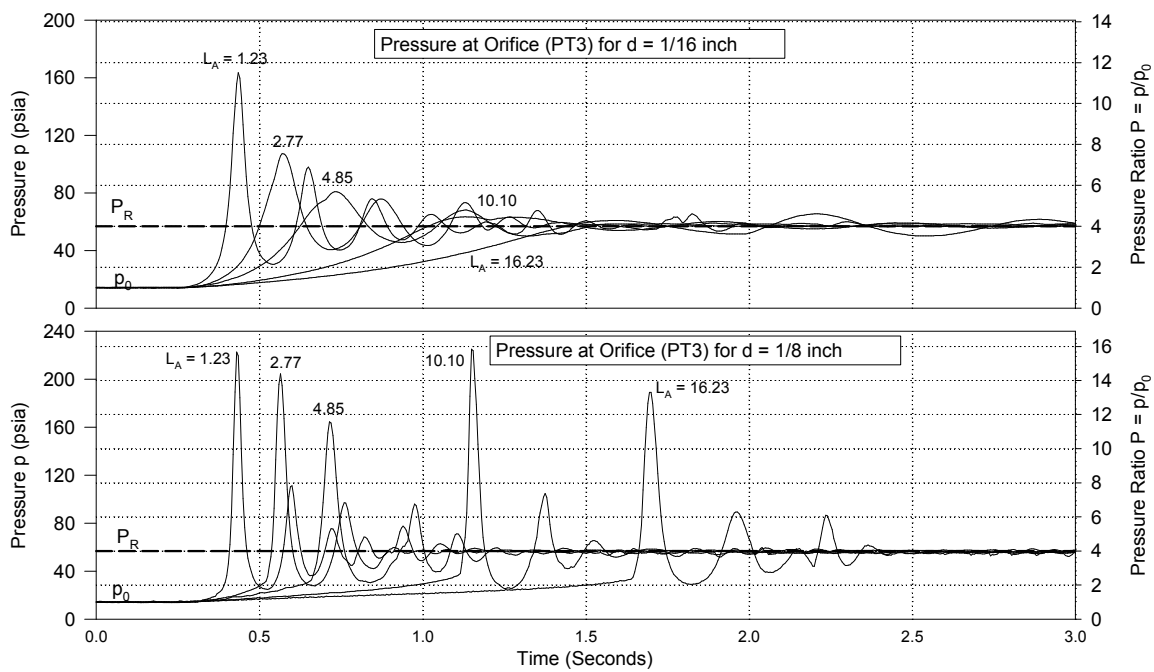


Figure B.19 Pressure and Velocity Transients for Air Venting ( $P_R = 4$ ;  $d = 1/16, 1/8$  Inch)

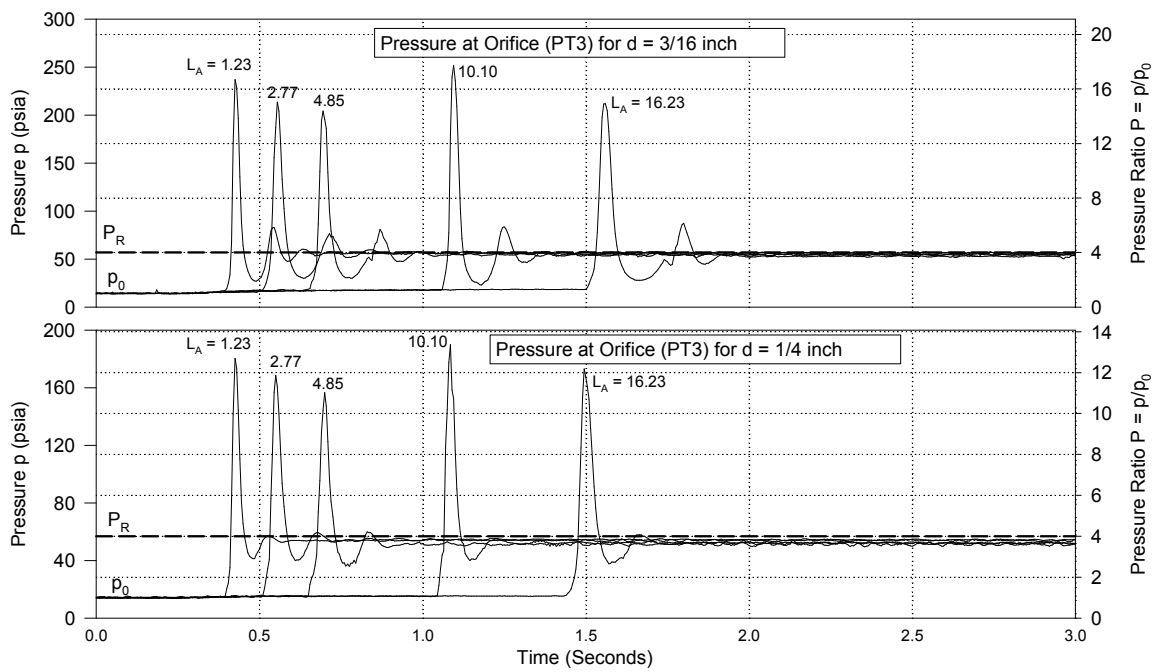


Figure B.20 Pressure and Velocity Transients for Air Venting ( $P_R = 4$ ;  $d = 3/16, 1/4$  Inch)

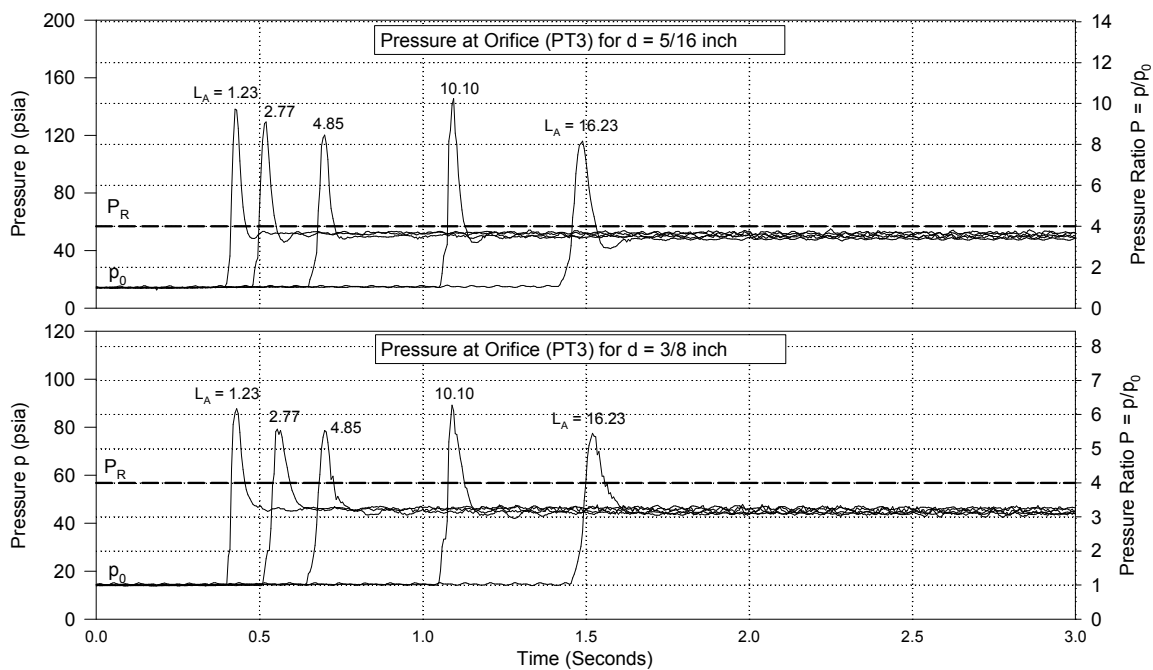


Figure B.21 Pressure and Velocity Transients for Air Venting ( $P_R = 4$ ;  $d = 5/16, 3/8$  Inch)

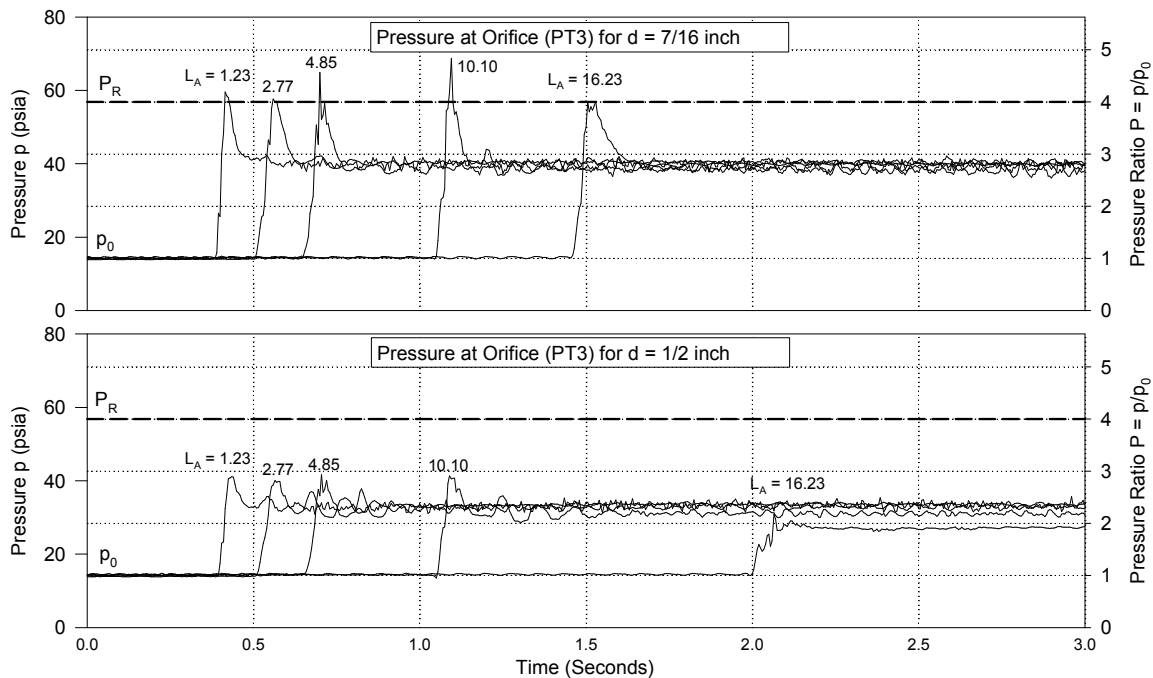


Figure B.22 Pressure and Velocity Transients for Air Venting ( $P_R = 4$ ;  $d = 7/16, 1/2$  Inch)

## APPENDIX C

### ENTRAPPED AIR ANALYSIS

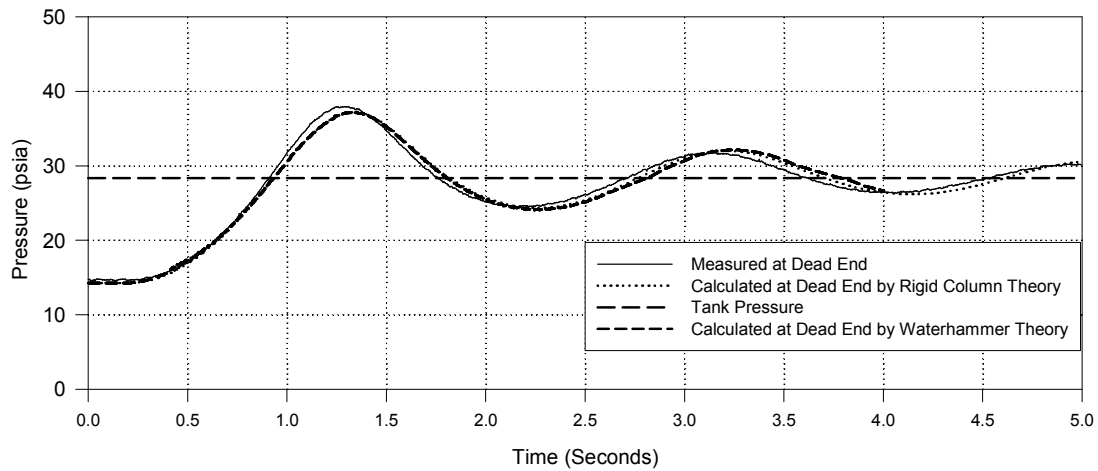


Figure C.1 Entrapped Air Analysis for  $L_A = 16.23 \text{ ft}$  ( $\alpha_0 = 0.4481$ ) ;  $P_R = 2$

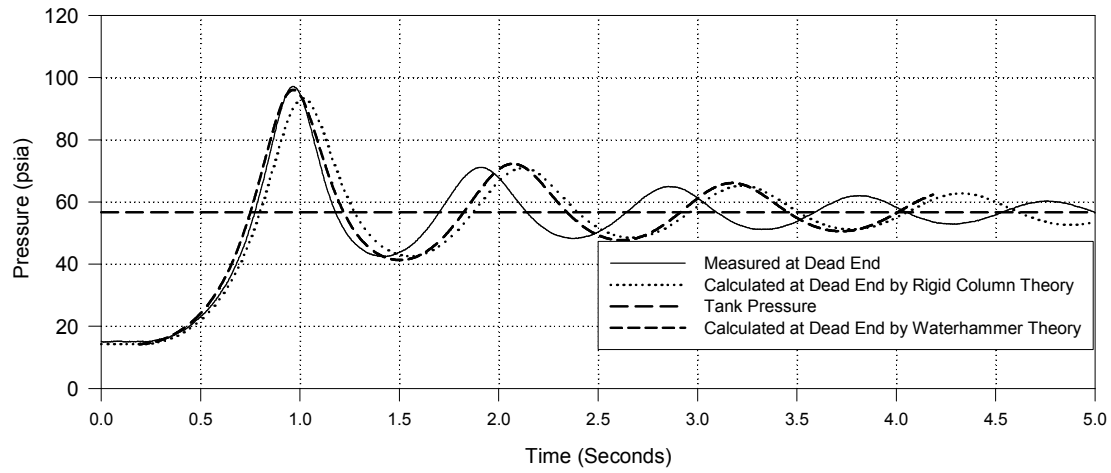


Figure C.2 Entrapped Air Analysis for  $L_A = 16.23 \text{ ft}$  ( $\alpha_0 = 0.4481$ ) ;  $P_R = 4$

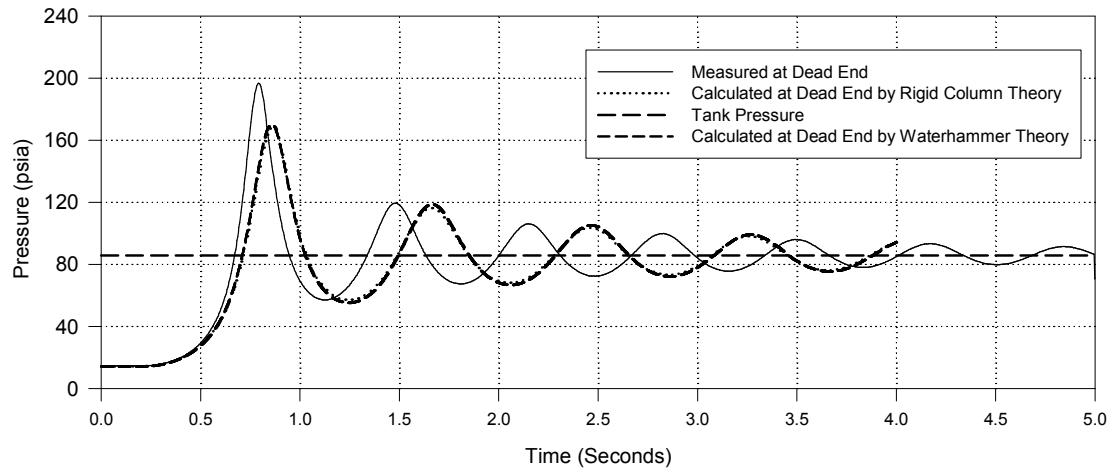


Figure C.3 Entrapped Air Analysis for  $L_A = 16.23 \text{ ft}$  ( $\alpha_0 = 0.4481$ ) ;  $P_R = 6$

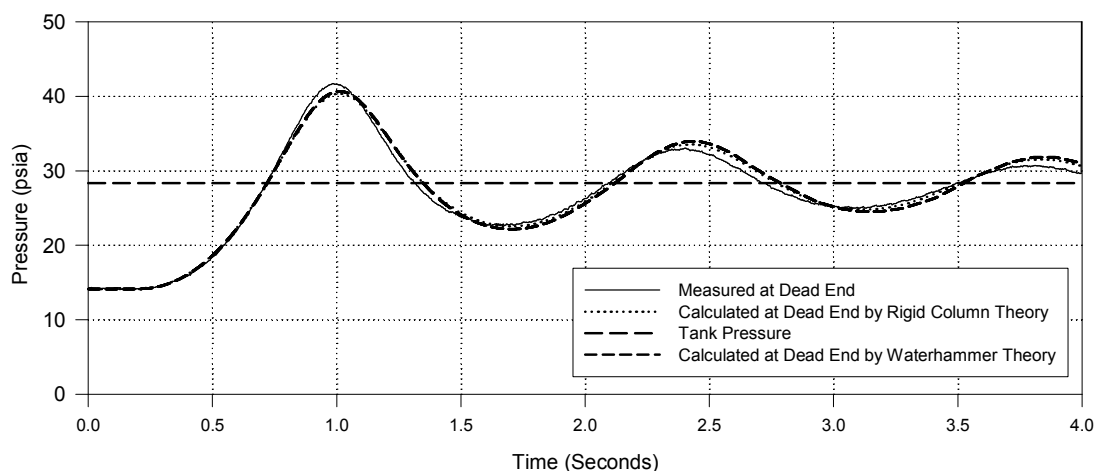


Figure C.4 Entrapped Air Analysis for  $L_A = 10.1$  ft ( $\alpha_0 = 0.3357$ ) ;  $P_R = 2$

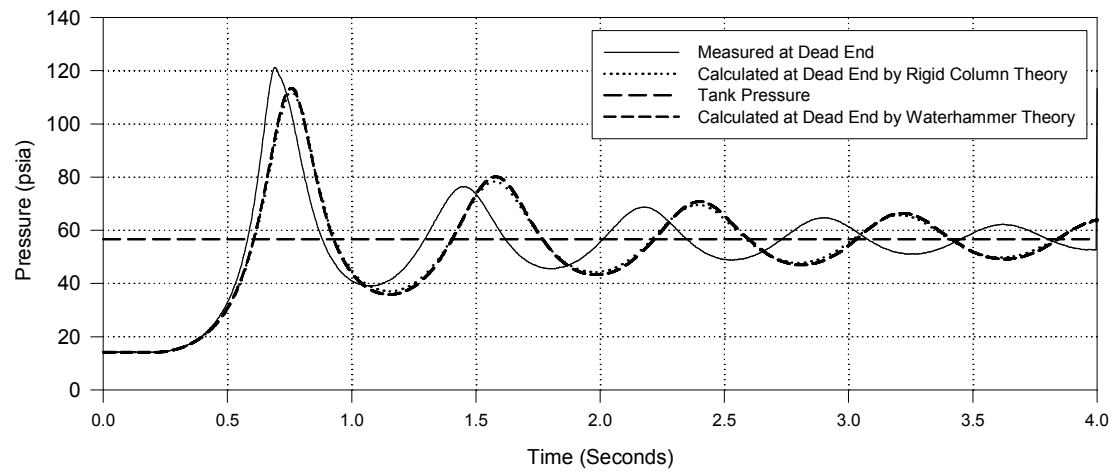


Figure C.5 Entrapped Air Analysis for  $L_A = 10.1$  ft ( $\alpha_0 = 0.3357$ ) ;  $P_R = 4$

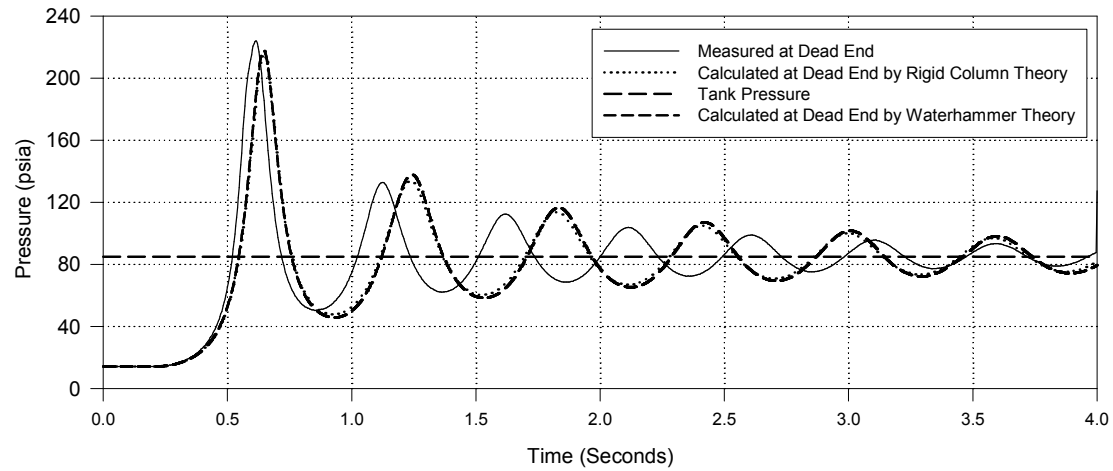


Figure C.6 Entrapped Air Analysis for  $L_A = 10.1$  ft ( $\alpha_0 = 0.3357$ ) ;  $P_R = 6$

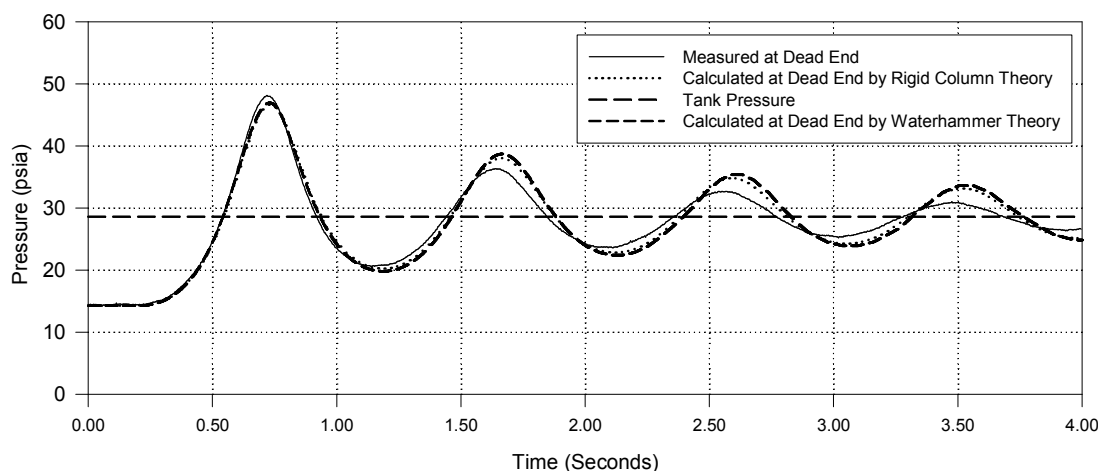


Figure C.7 Entrapped Air Analysis for  $L_A = 4.85 \text{ ft}$  ( $\alpha_0 = 0.1952$ ) ;  $P_R = 2$

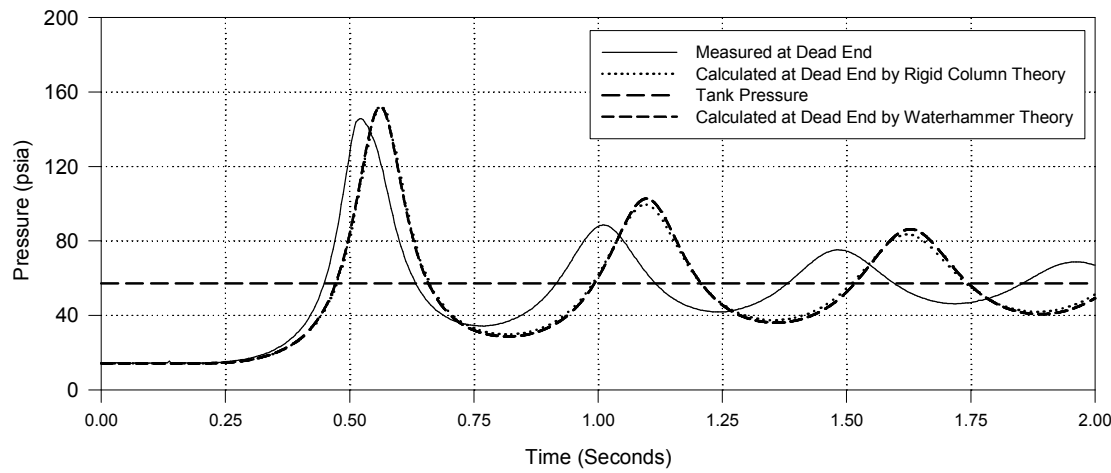


Figure C.8 Entrapped Air Analysis for  $L_A = 4.85 \text{ ft}$  ( $\alpha_0 = 0.1952$ ) ;  $P_R = 4$

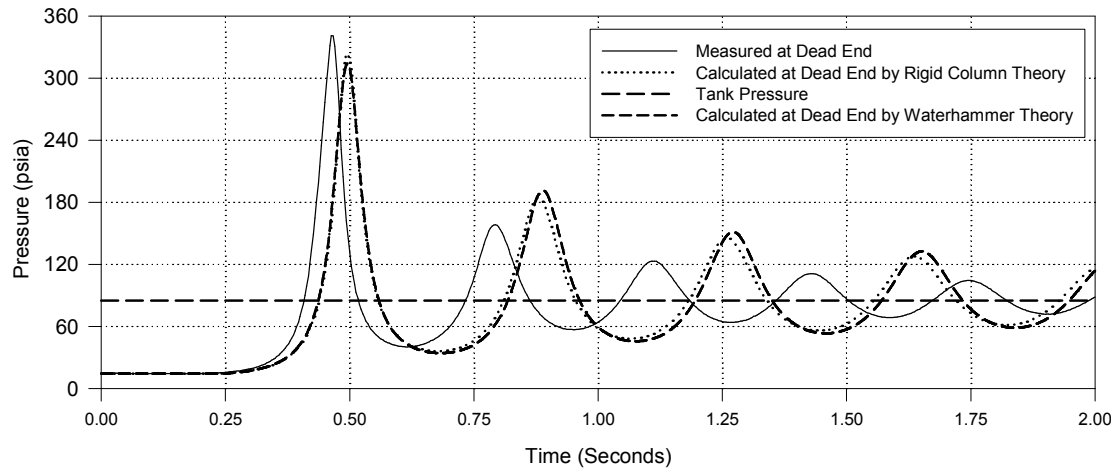


Figure C.9 Entrapped Air Analysis for  $L_A = 4.85 \text{ ft}$  ( $\alpha_0 = 0.1952$ ) ;  $P_R = 6$

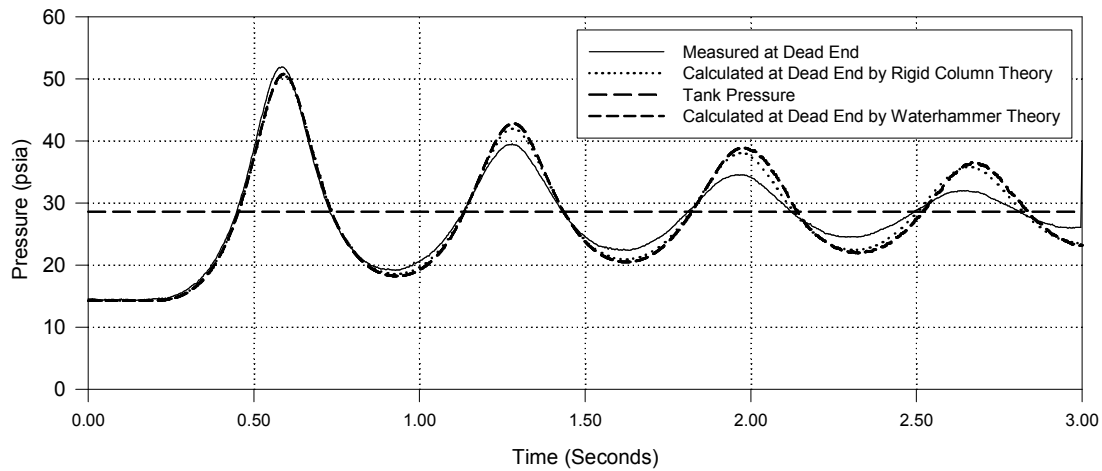


Figure C.10 Entrapped Air Analysis for  $L_A = 2.77$  ft ( $\alpha_0 = 0.1212$ ) ;  $P_R = 2$

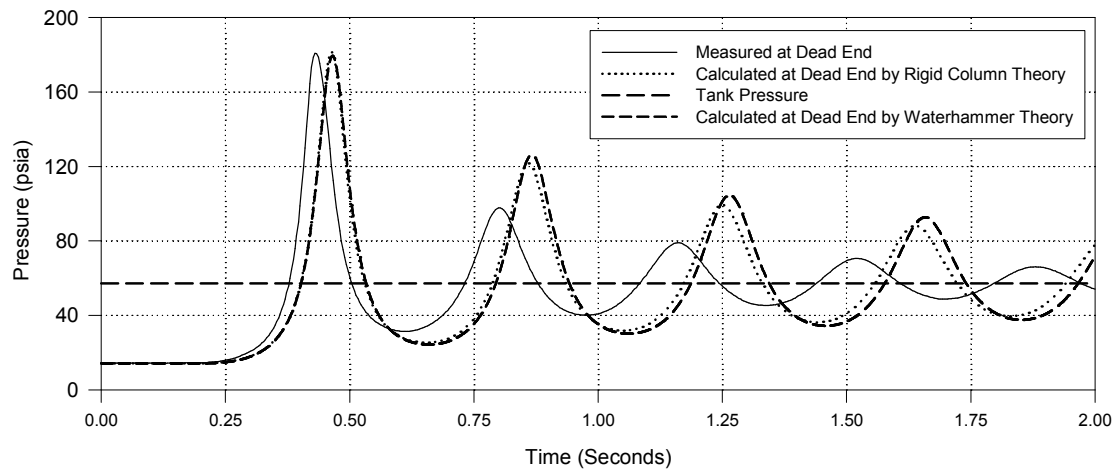


Figure C.11 Entrapped Air Analysis for  $L_A = 2.77$  ft ( $\alpha_0 = 0.1212$ ) ;  $P_R = 4$

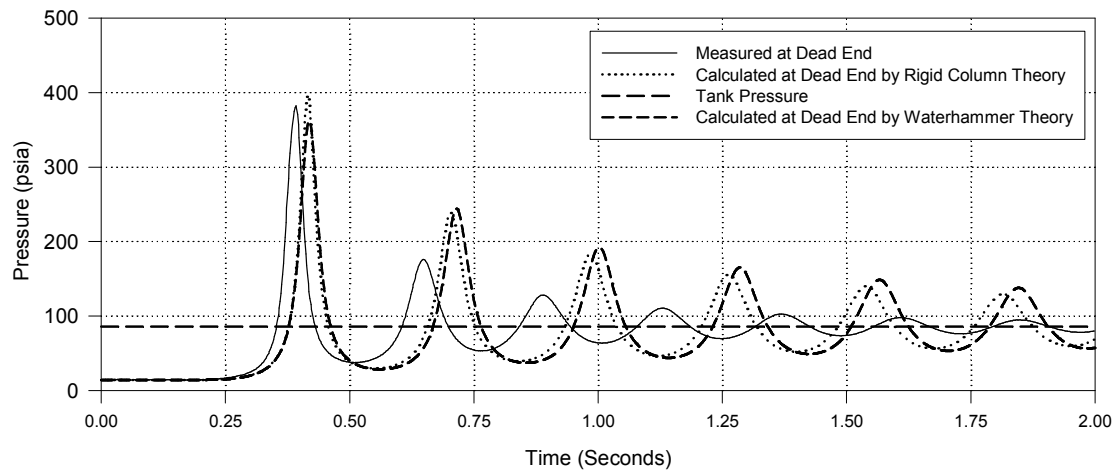


Figure C.12 Entrapped Air Analysis for  $L_A = 2.77$  ft ( $\alpha_0 = 0.1212$ ) ;  $P_R = 6$

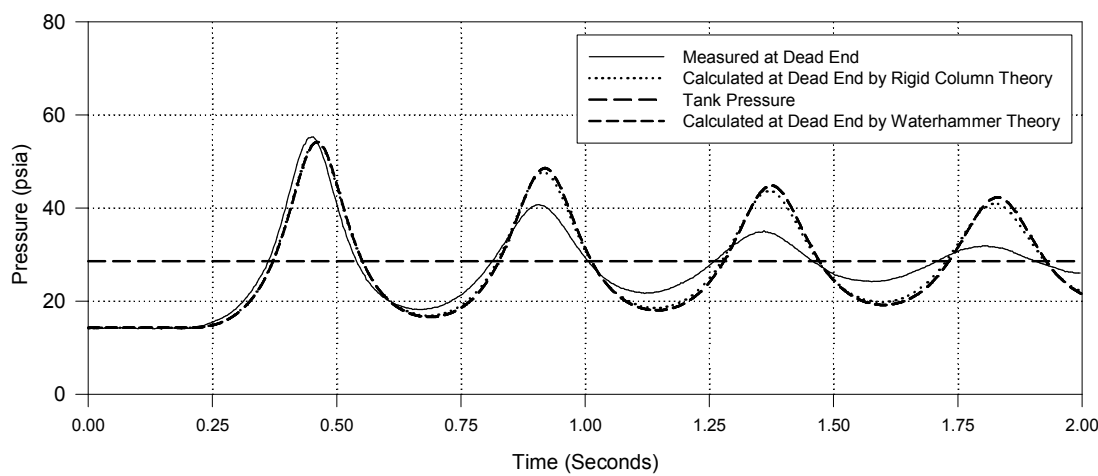


Figure C.13 Entrapped Air Analysis for  $L_A = 1.23$  ft ( $\alpha_0 = 0.0580$ ) ;  $P_R = 2$

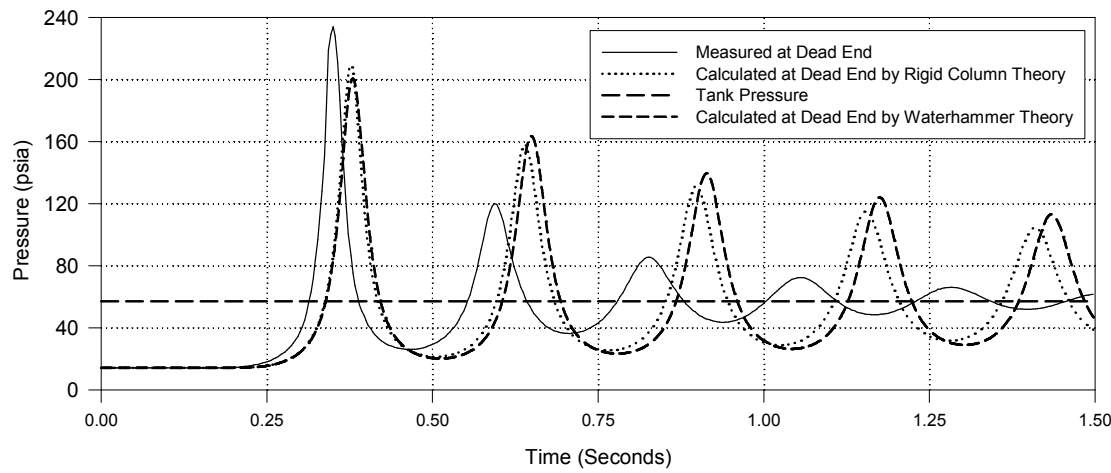


Figure C.14 Entrapped Air Analysis for  $L_A = 1.23$  ft ( $\alpha_0 = 0.0580$ ) ;  $P_R = 4$

## APPENDIX D

### AIR VENTING ANALYSIS

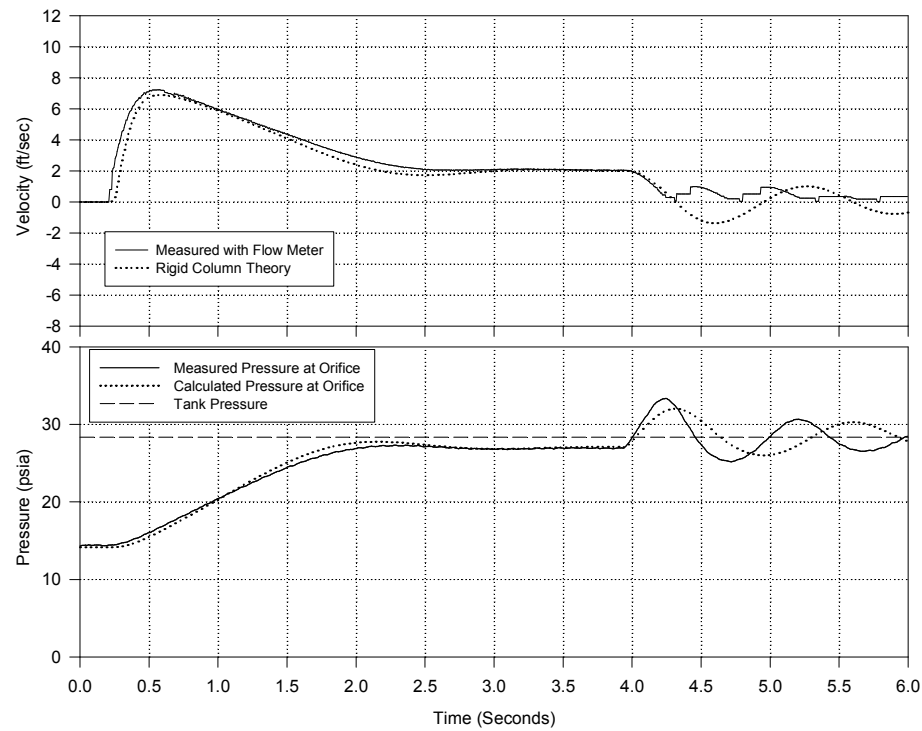


Figure D.1 Venting Analysis for  $L_A = 16.2$  ft ( $\alpha_0 = 0.4481$ ) ;  $P_R = 2$  ;  $d = 1/16$  Inch

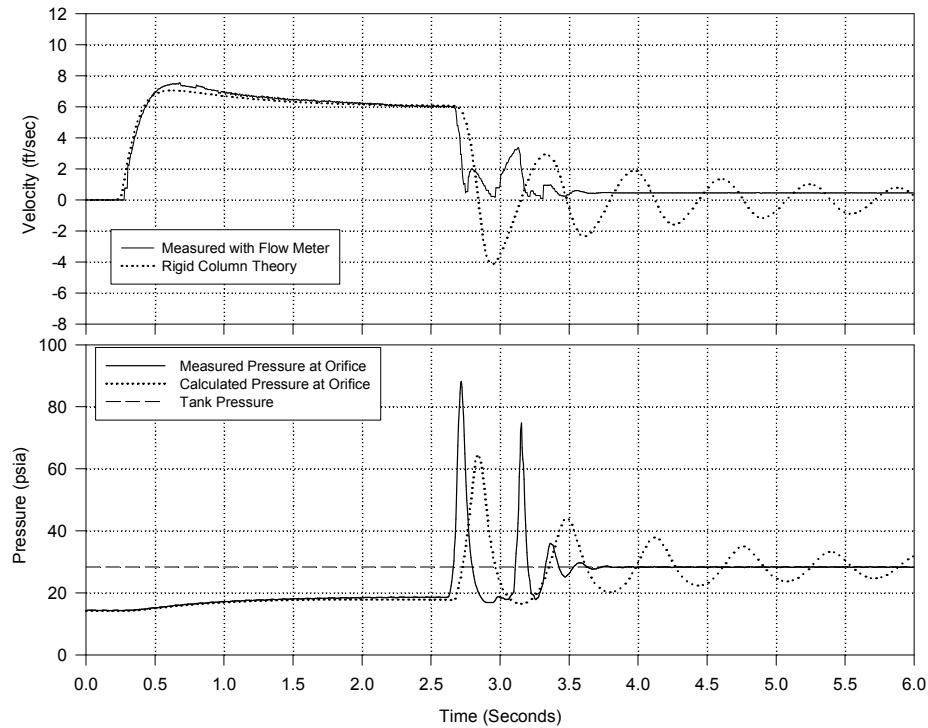


Figure D.2 Venting Analysis for  $L_A = 16.2$  ft ( $\alpha_0 = 0.4481$ ) ;  $P_R = 2$  ;  $d = 1/8$  Inch

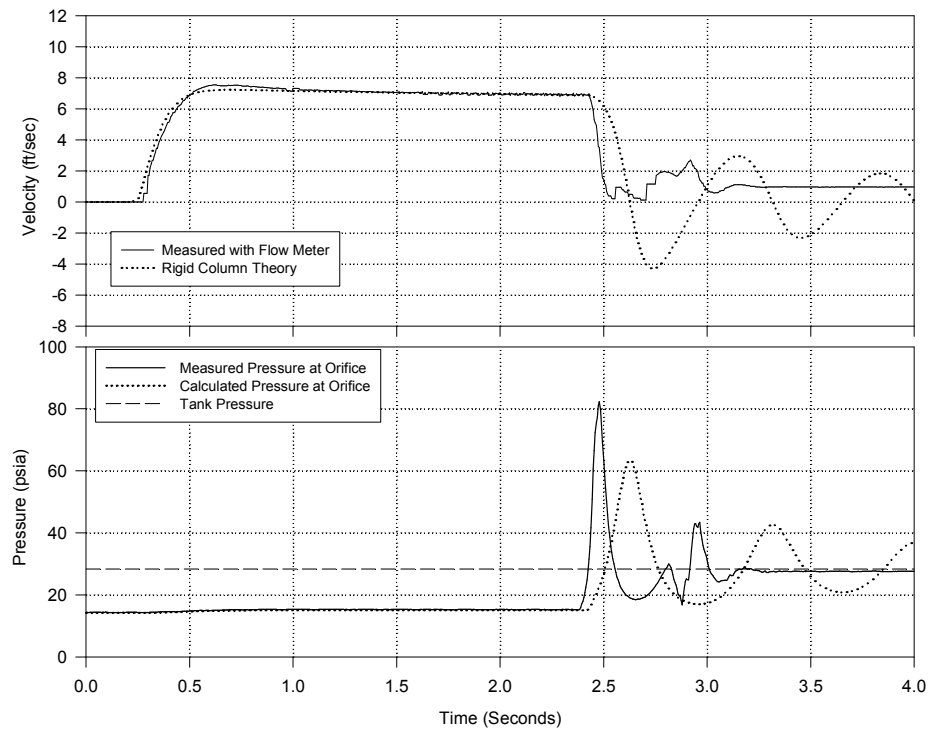


Figure D.3 Venting Analysis for  $L_A = 16.2$  ft ( $\alpha_0 = 0.4481$ ) ;  $P_R = 2$  ;  $d = 3/16$  Inch

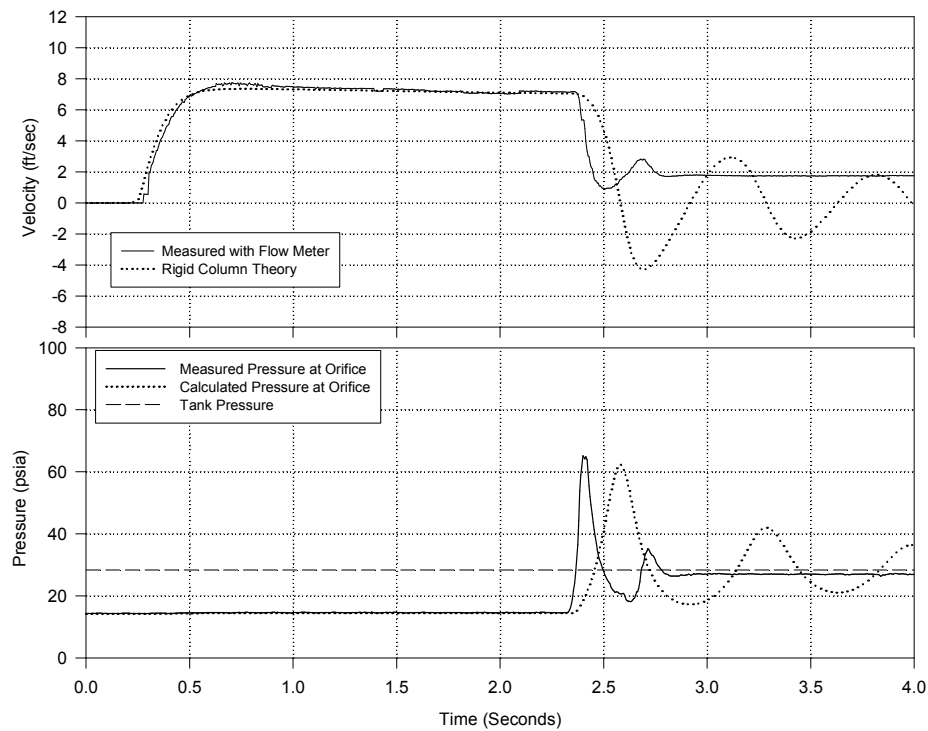


Figure D.4 Venting Analysis for  $L_A = 16.2$  ft ( $\alpha_0 = 0.4481$ ) ;  $P_R = 2$  ;  $d = 1/4$  Inch

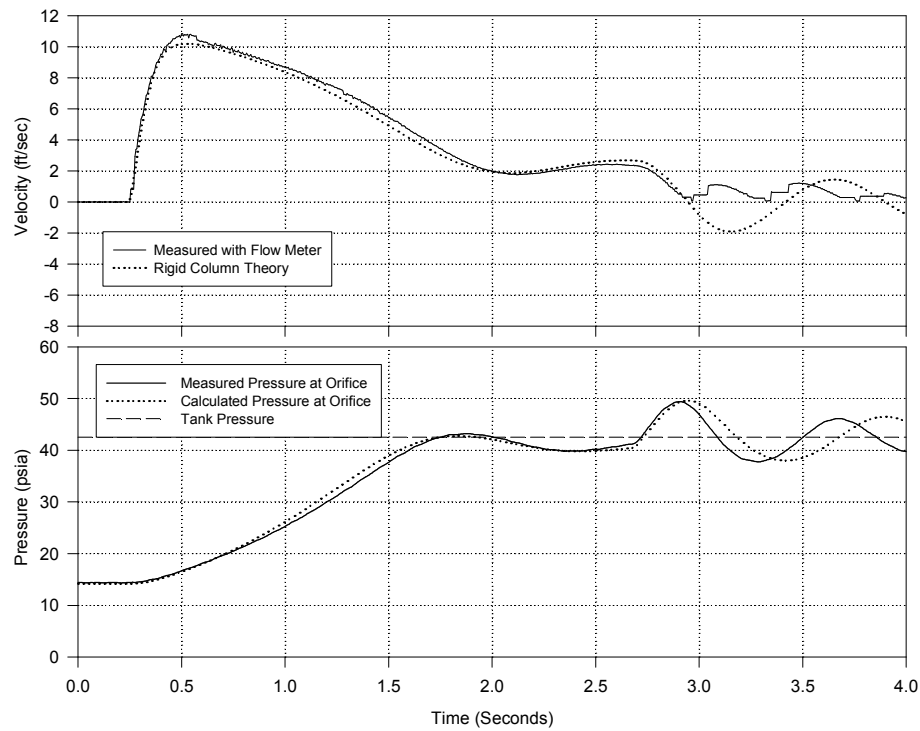


Figure D.5 Venting Analysis for  $L_A = 16.2$  ft ( $\alpha_0 = 0.4481$ ) ;  $P_R = 3$  ;  $d = 1/16$  Inch

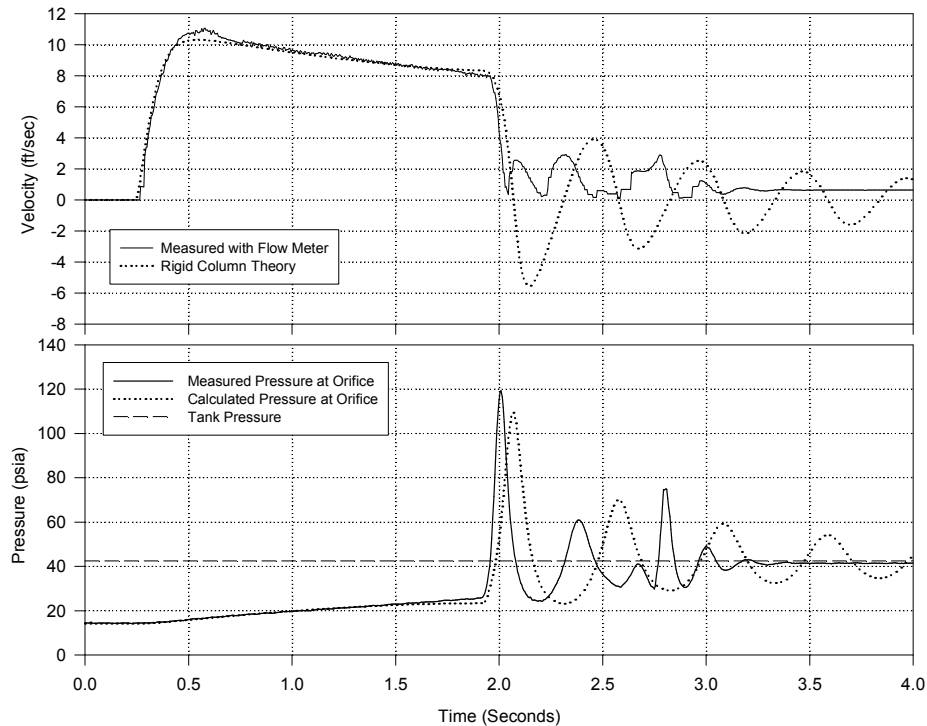


Figure D.6 Venting Analysis for  $L_A = 16.2$  ft ( $\alpha_0 = 0.4481$ ) ;  $P_R = 3$  ;  $d = 1/8$  Inch

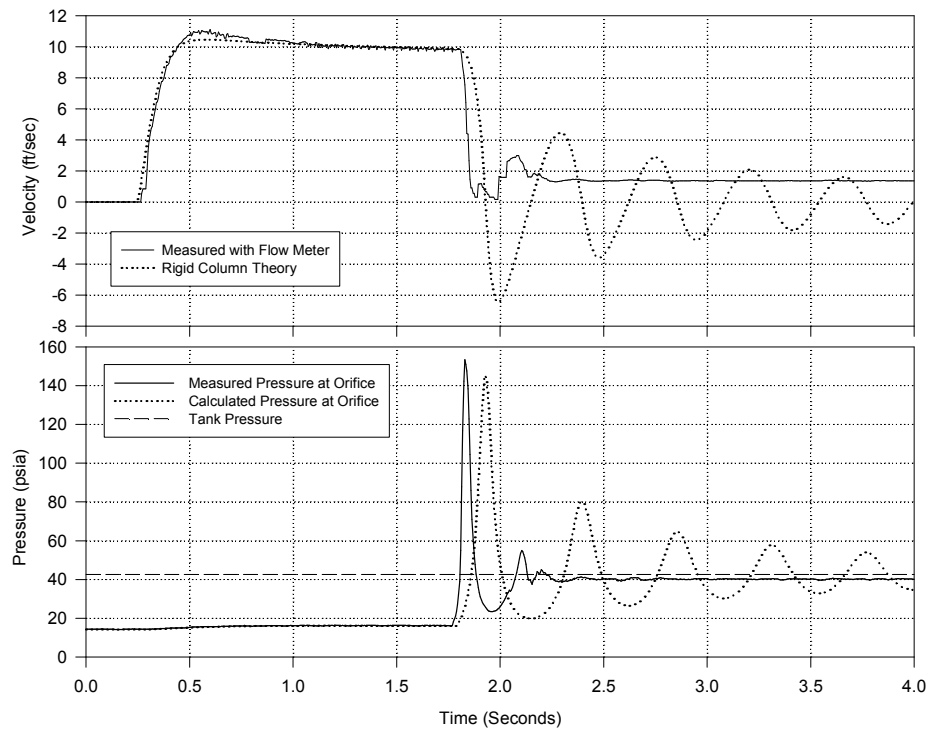


Figure D.7 Venting Analysis for  $L_A = 16.2$  ft ( $\alpha_0 = 0.4481$ ) ;  $P_R = 3$  ;  $d = 3/16$  Inch

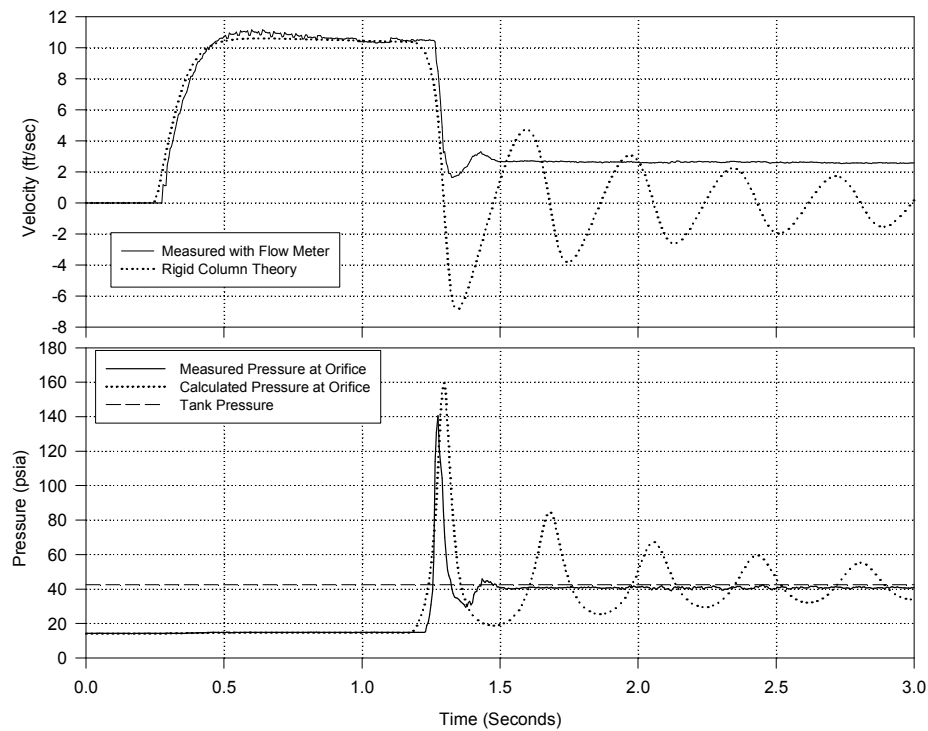


Figure D.8 Venting Analysis for  $L_A = 16.2$  ft ( $\alpha_0 = 0.4481$ ) ;  $P_R = 3$  ;  $d = 1/4$  Inch

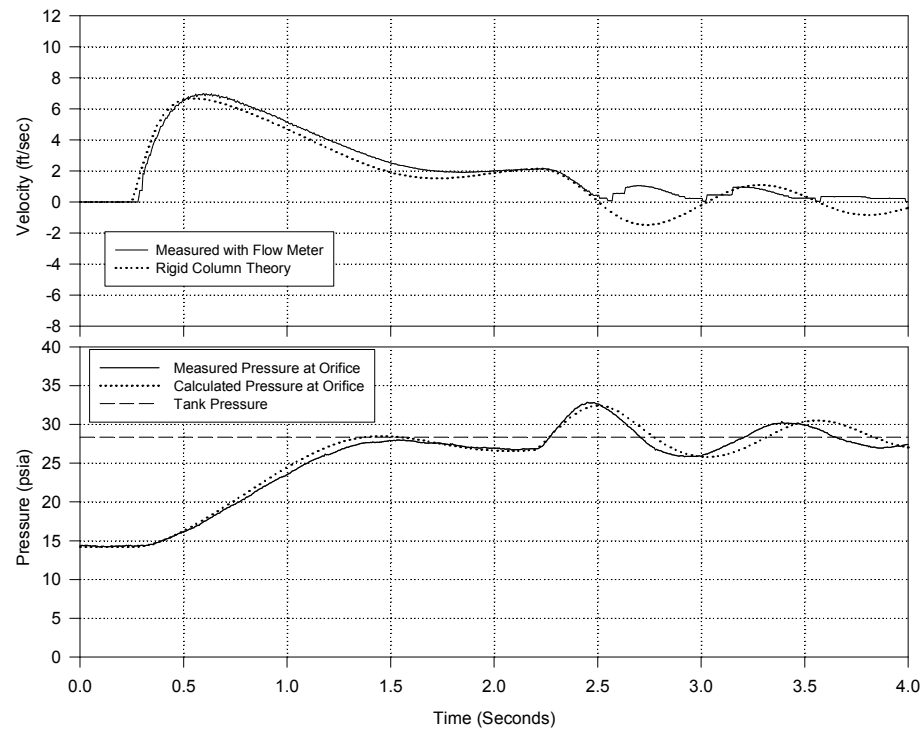


Figure D.9 Venting Analysis for  $L_A = 10.1$  ft ( $\alpha_0 = 0.3357$ ) ;  $P_R = 2$  ;  $d = 1/16$  Inch

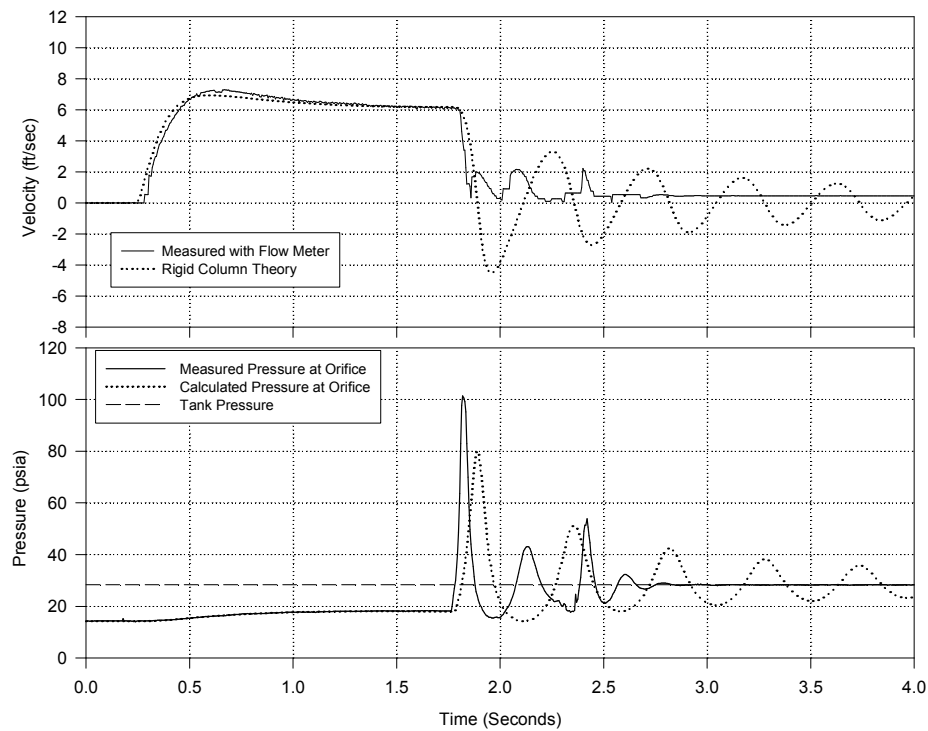


Figure D.10 Venting Analysis for  $L_A = 10.1$  ft ( $\alpha_0 = 0.3357$ ) ;  $P_R = 2$  ;  $d = 1/8$  Inch

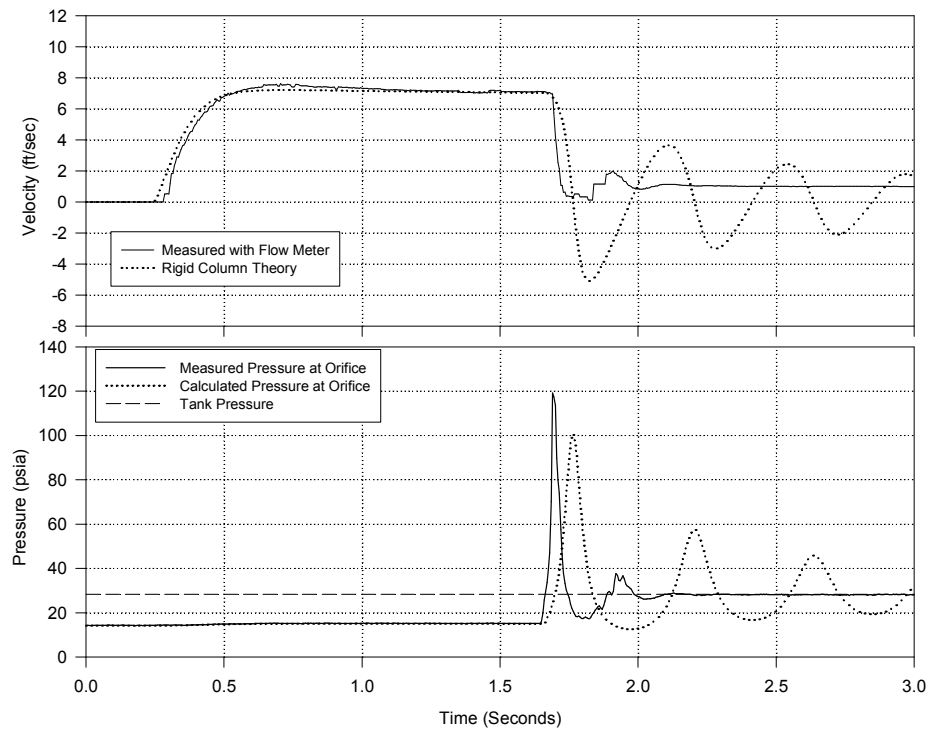


Figure D.11 Venting Analysis for  $L_A = 10.1$  ft ( $\alpha_0 = 0.3357$ ) ;  $P_R = 2$  ;  $d = 3/16$  Inch

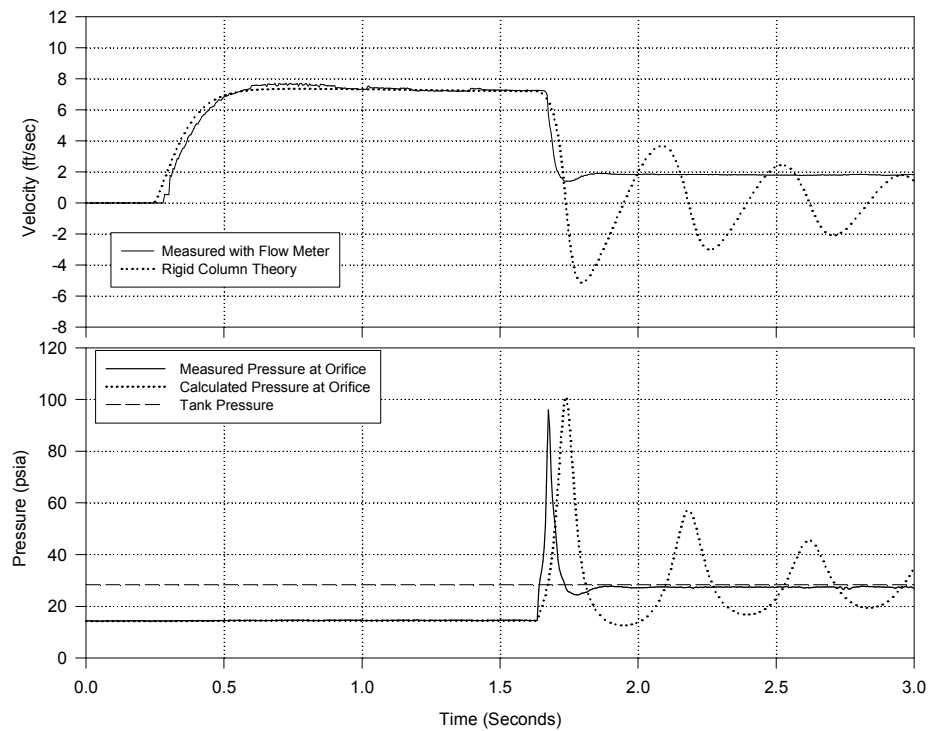


Figure D.12 Venting Analysis for  $L_A = 10.1$  ft ( $\alpha_0 = 0.3357$ ) ;  $P_R = 2$  ;  $d = 1/4$  Inch

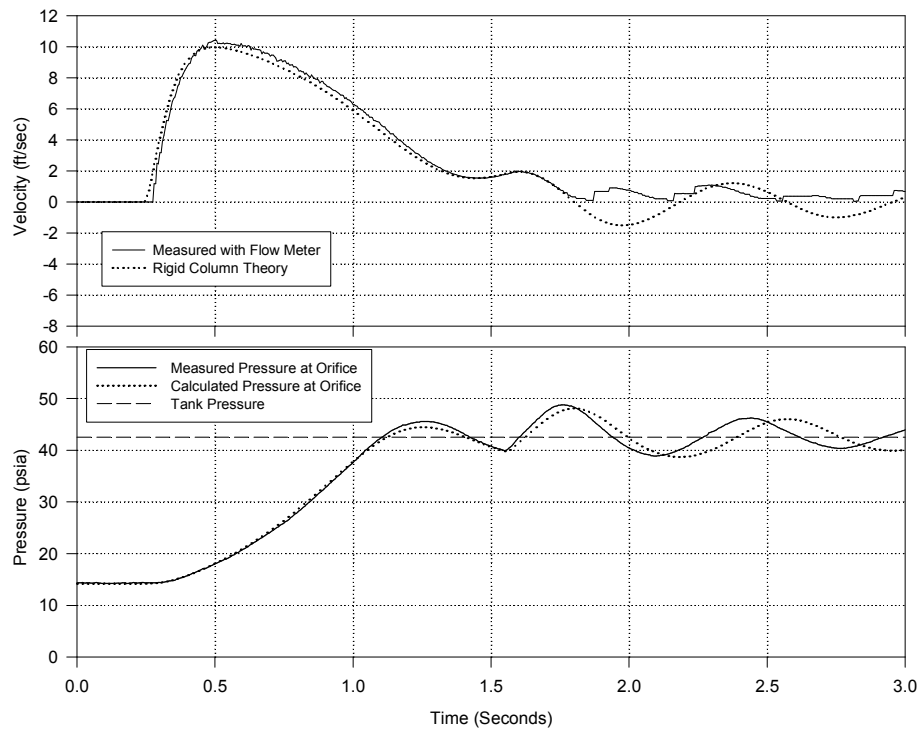


Figure D.13 Venting Analysis for  $L_A = 10.1$  ft ( $\alpha_0 = 0.3357$ ) ;  $P_R = 3$  ;  $d = 1/16$  Inch

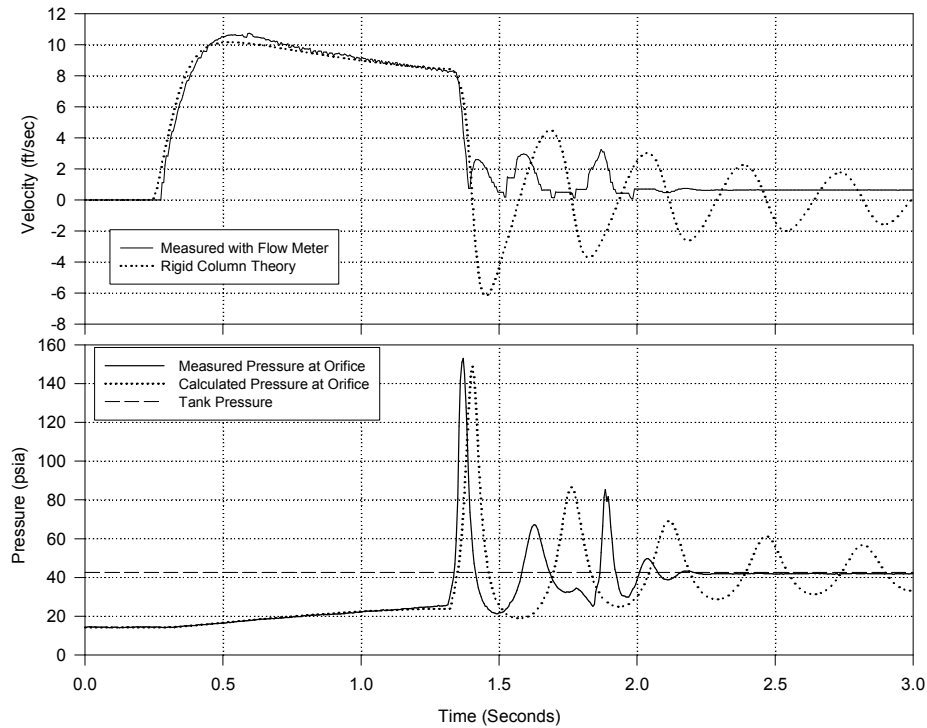


Figure D.14 Venting Analysis for  $L_A = 10.1$  ft ( $\alpha_0 = 0.3357$ ) ;  $P_R = 3$  ;  $d = 1/8$  Inch

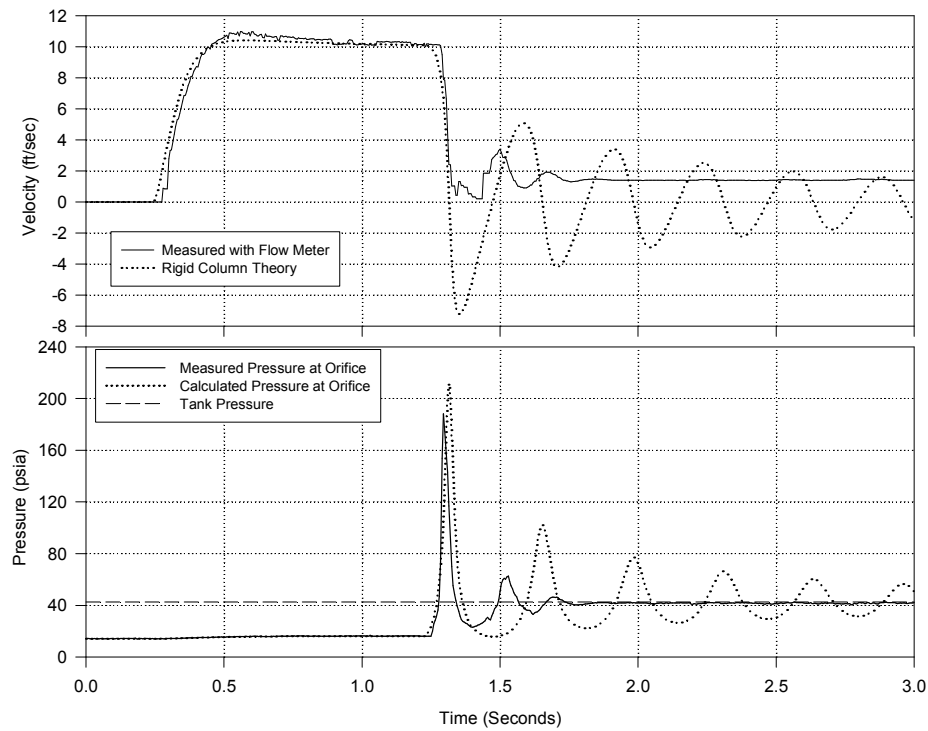


Figure D.15 Venting Analysis for  $L_A = 10.1$  ft ( $\alpha_0 = 0.3357$ ) ;  $P_R = 3$  ;  $d = 3/16$  Inch

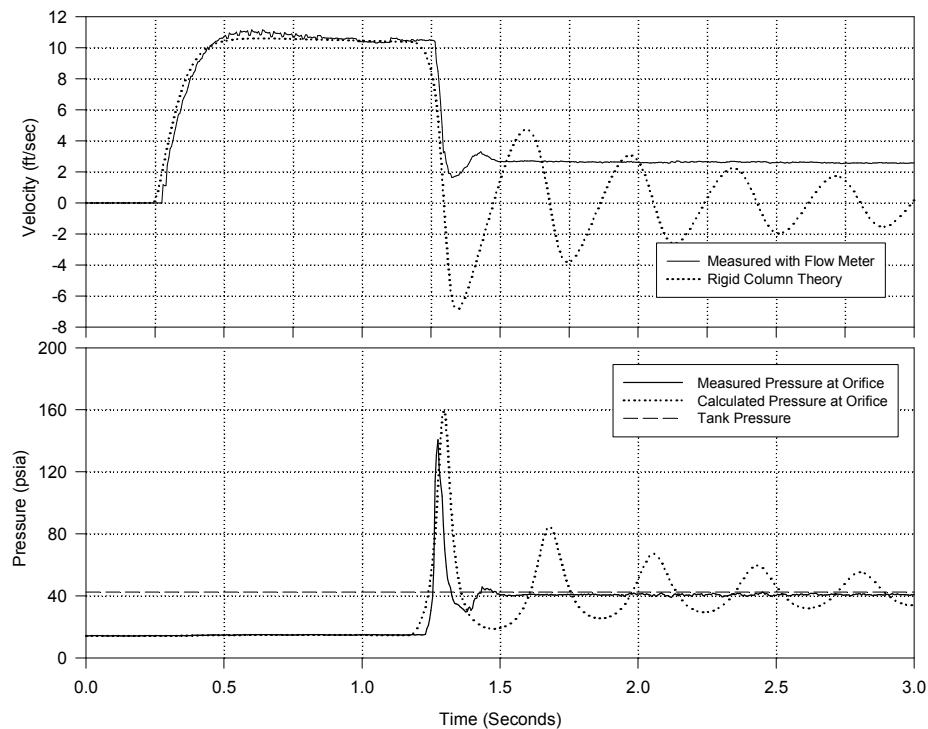


Figure D.16 Venting Analysis for  $L_A = 10.1$  ft ( $\alpha_0 = 0.3357$ ) ;  $P_R = 3$  ;  $d = 1/4$  Inch

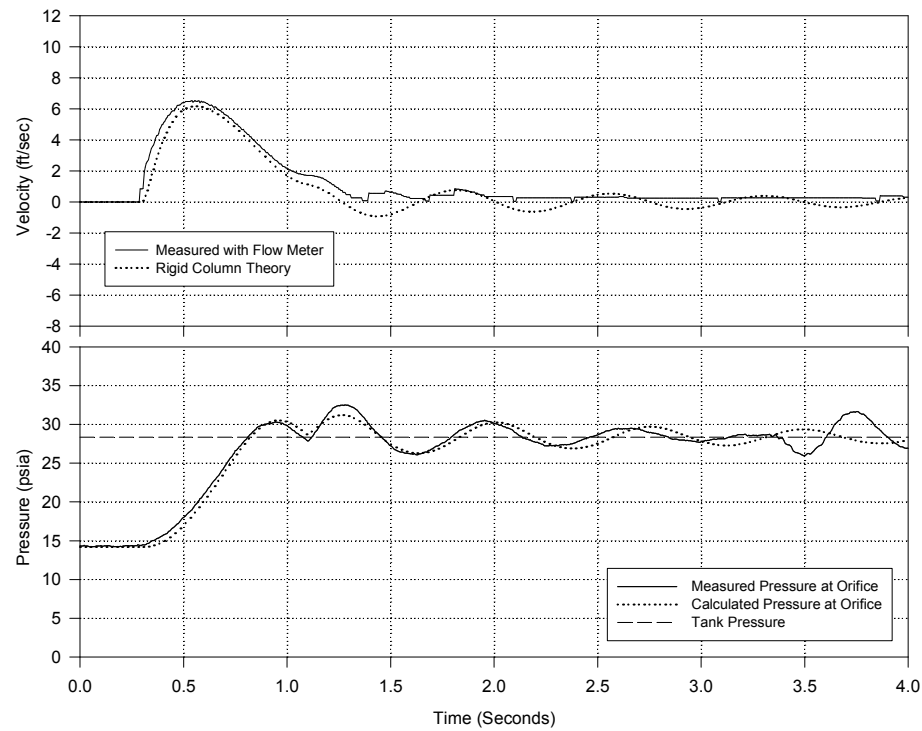


Figure D.17 Venting Analysis for  $L_A = 4.85$  ft ( $\alpha_0 = 0.1952$ ) ;  $P_R = 2$  ;  $d = 1/16$  Inch

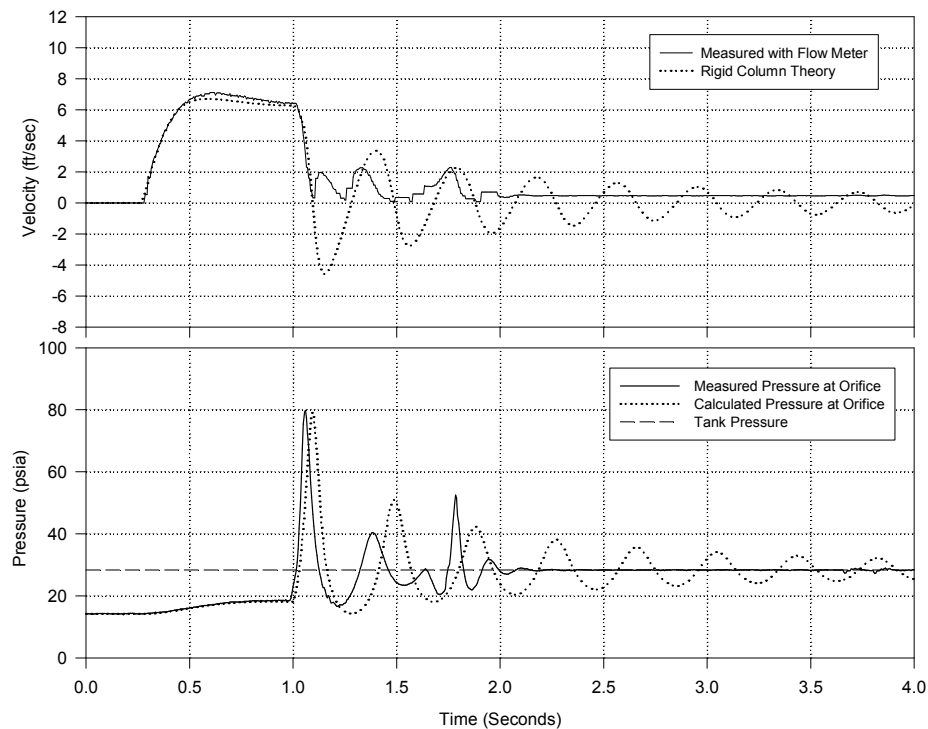


Figure D.18 Venting Analysis for  $L_A = 4.85$  ft ( $\alpha_0 = 0.1952$ ) ;  $P_R = 2$  ;  $d = 1/8$  Inch

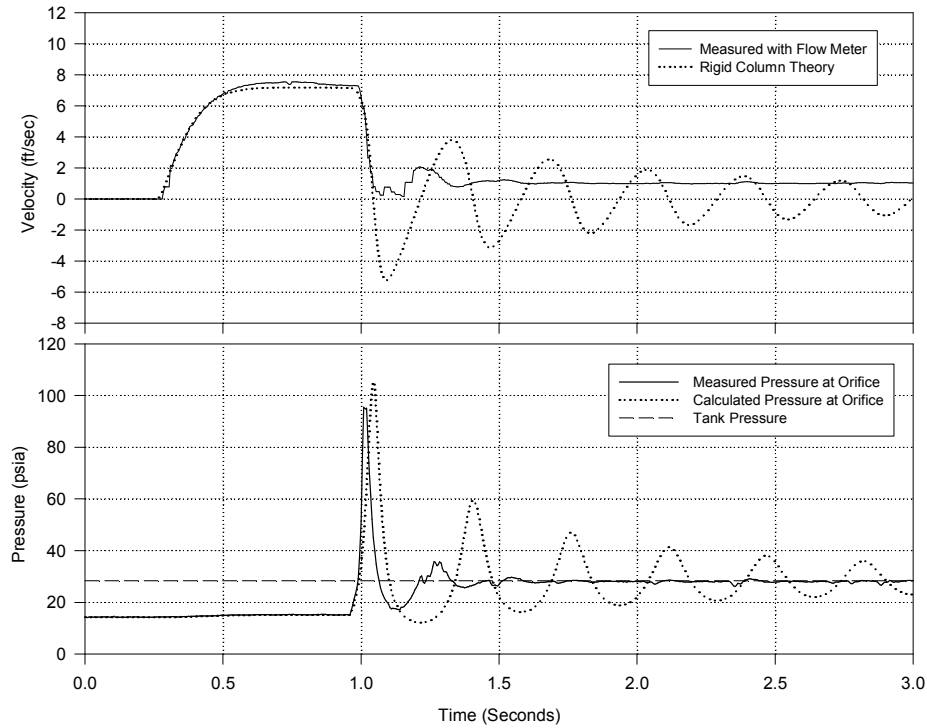


Figure D.19 Venting Analysis for  $L_A = 4.85$  ft ( $\alpha_0 = 0.1952$ ) ;  $P_R = 2$  ;  $d = 3/16$  Inch

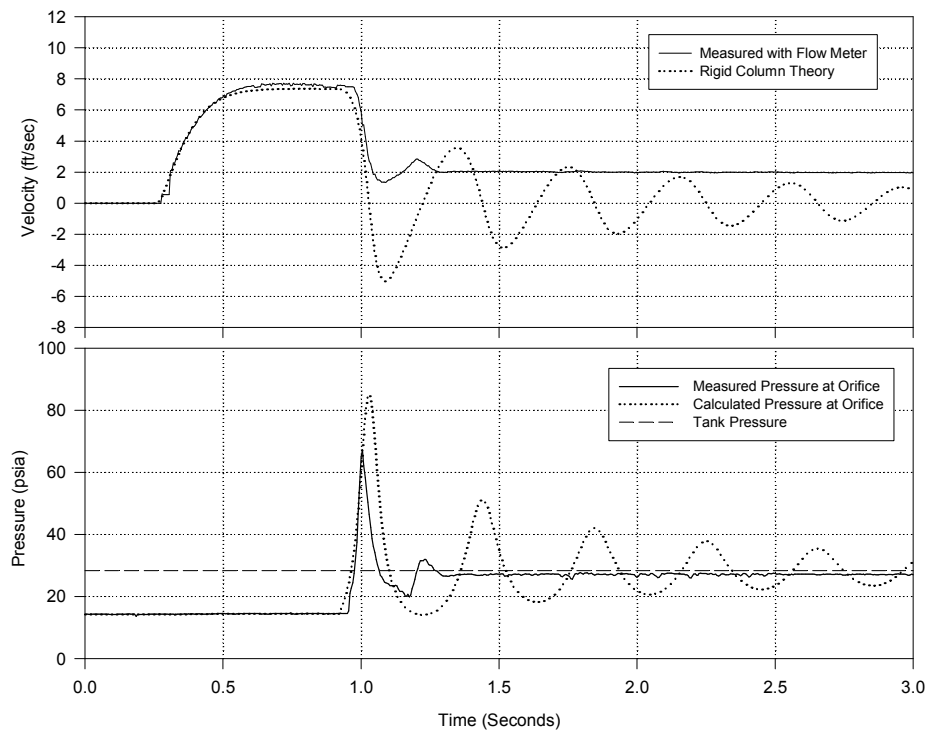


Figure D.20 Venting Analysis for  $L_A = 4.85$  ft ( $\alpha_0 = 0.1952$ ) ;  $P_R = 2$  ;  $d = 1/4$  Inch

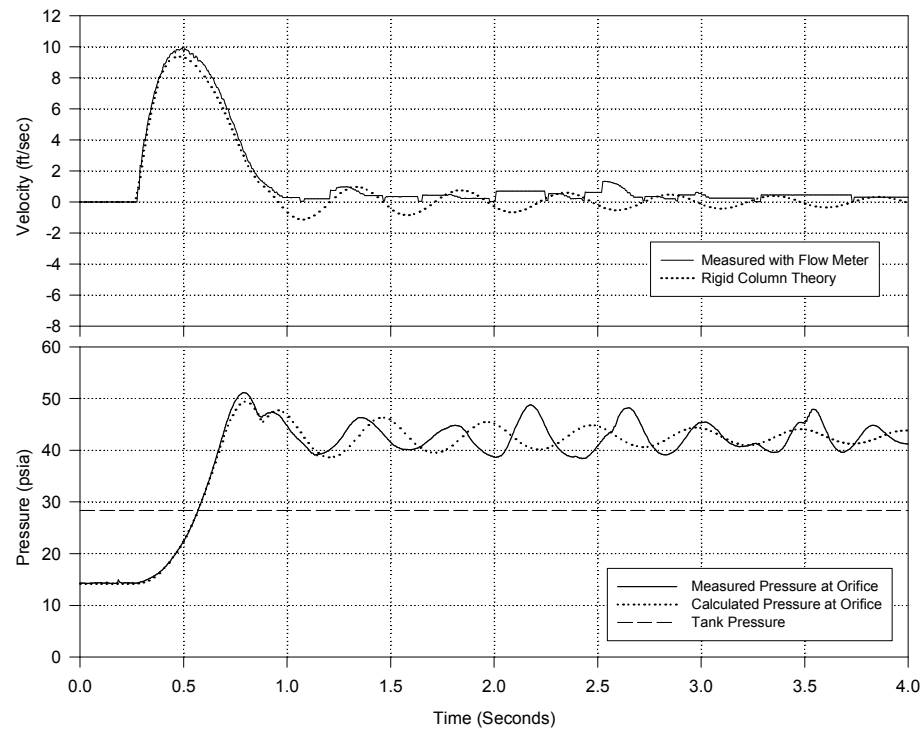


Figure D.21 Venting Analysis for  $L_A = 4.85$  ft ( $\alpha_0 = 0.1952$ ) ;  $P_R = 3$  ;  $d = 1/16$  Inch

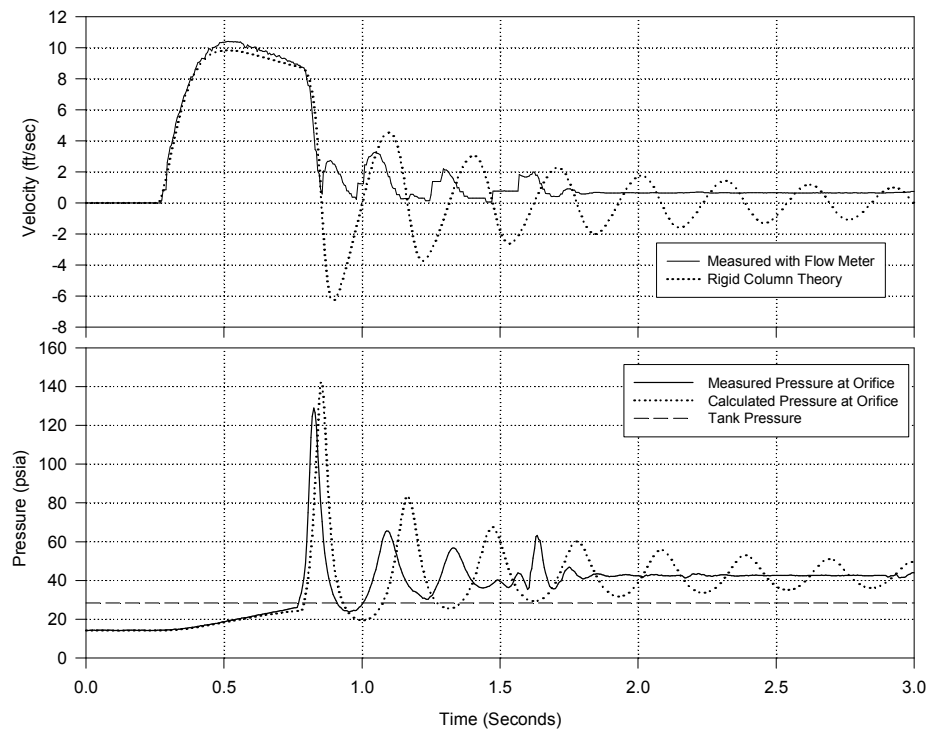


Figure D.22 Venting Analysis for  $L_A = 4.85$  ft ( $\alpha_0 = 0.1952$ ) ;  $P_R = 3$  ;  $d = 1/8$  Inch

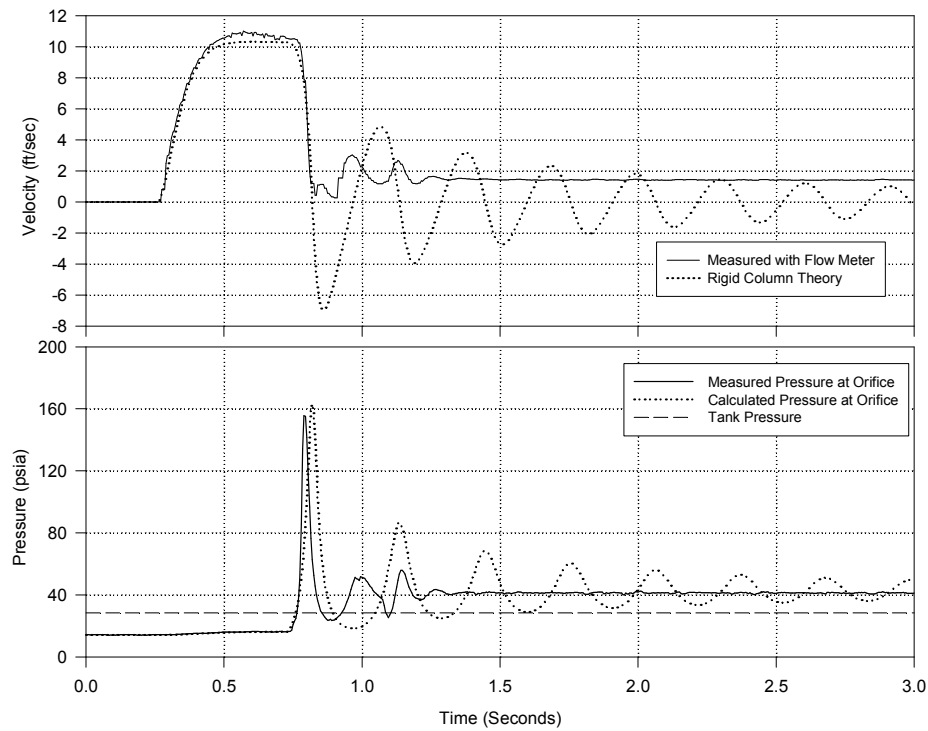


Figure D.23 Venting Analysis for  $L_A = 4.85$  ft ( $\alpha_0 = 0.1952$ ) ;  $P_R = 3$  ;  $d = 3/16$  Inch

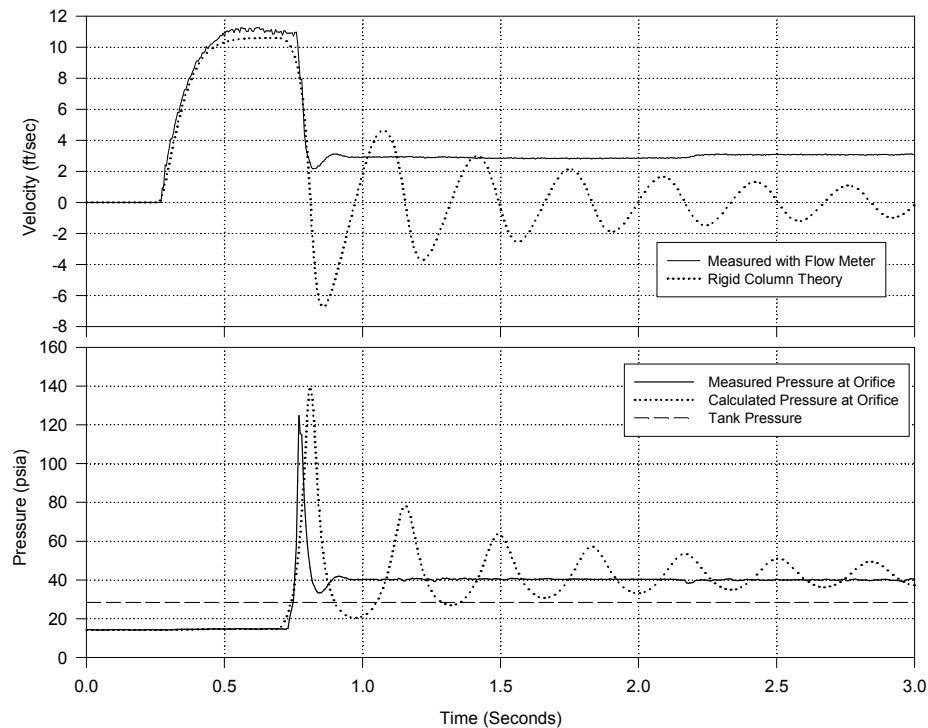


Figure D.24 Venting Analysis for  $L_A = 4.85$  ft ( $\alpha_0 = 0.1952$ ) ;  $P_R = 3$  ;  $d = 1/4$  Inch

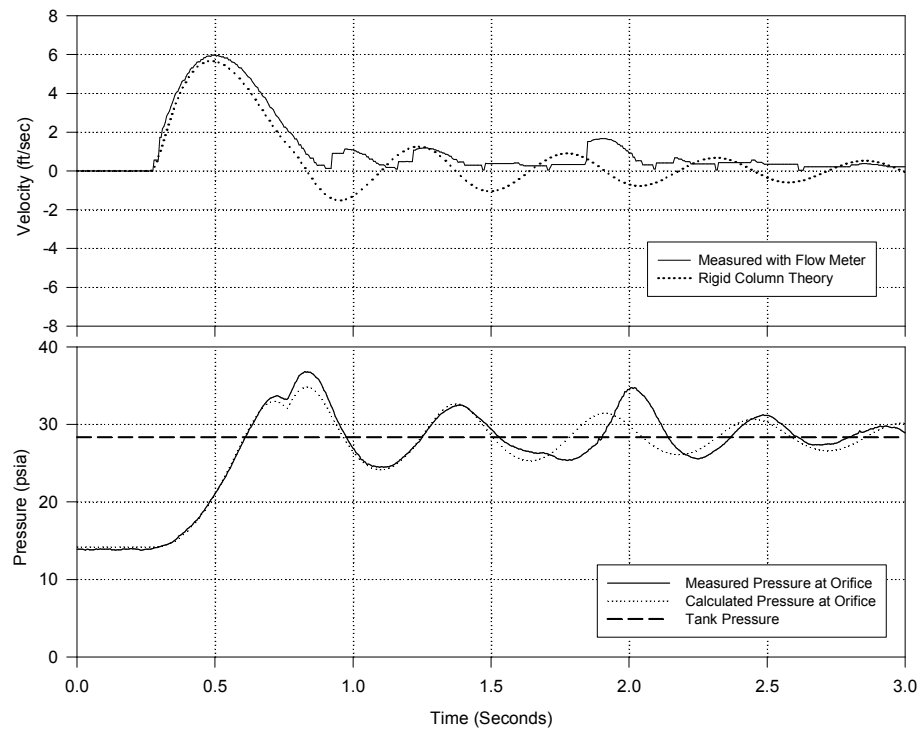


Figure D.25 Venting Analysis for  $L_A = 2.77$  ft ( $\alpha_0 = 0.1217$ ) ;  $P_R = 2$  ;  $d = 1/16$  Inch

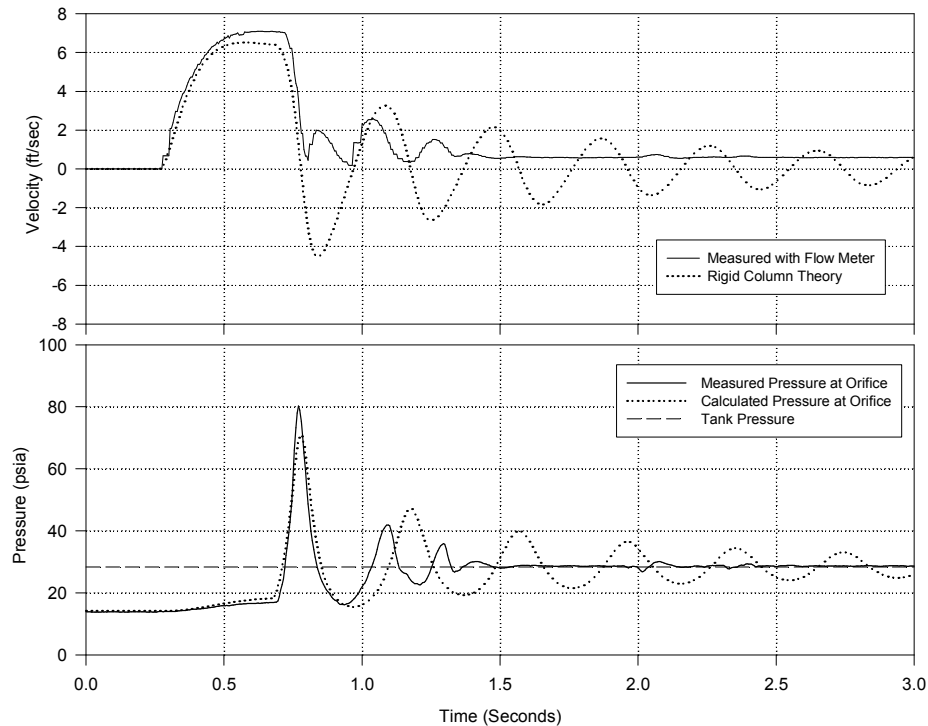


Figure D.26 Venting Analysis for  $L_A = 2.77$  ft ( $\alpha_0 = 0.1217$ ) ;  $P_R = 2$  ;  $d = 1/8$  Inch

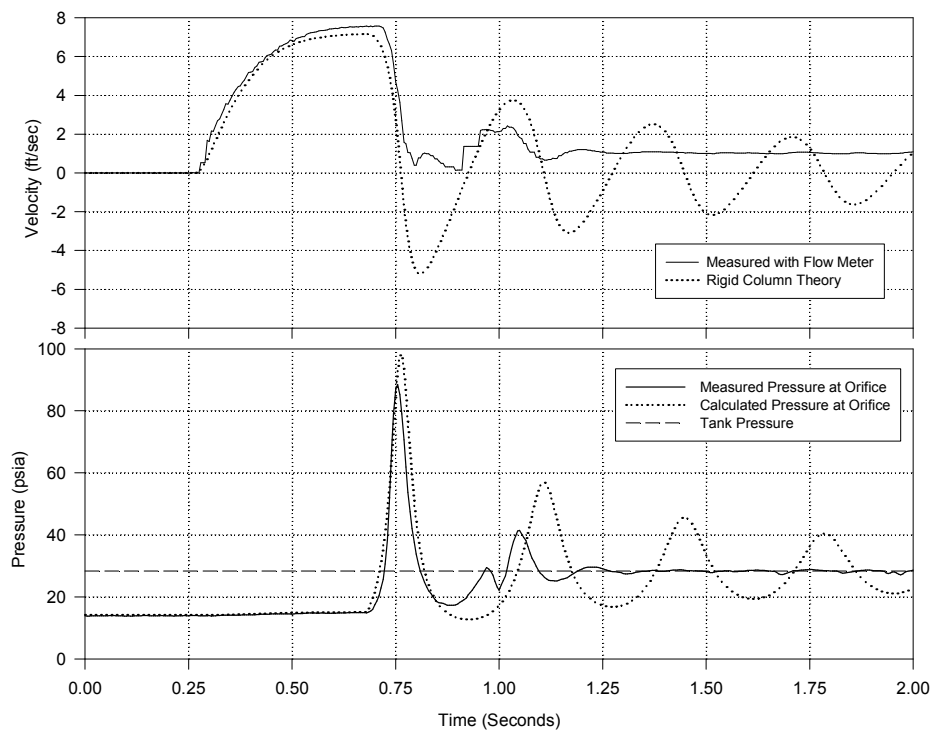


Figure D.27 Venting Analysis for  $L_A = 2.77$  ft ( $\alpha_0 = 0.1217$ ) ;  $P_R = 2$  ;  $d = 3/16$  Inch

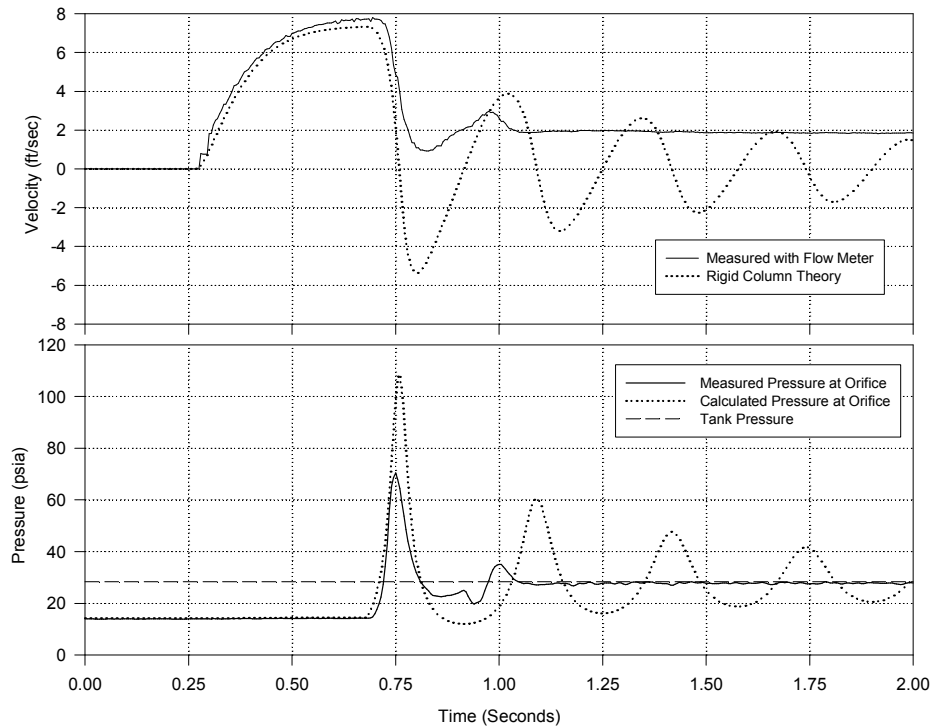


Figure D.28 Venting Analysis for  $L_A = 2.77$  ft ( $\alpha_0 = 0.1217$ ) ;  $P_R = 2$  ;  $d = 1/4$  Inch

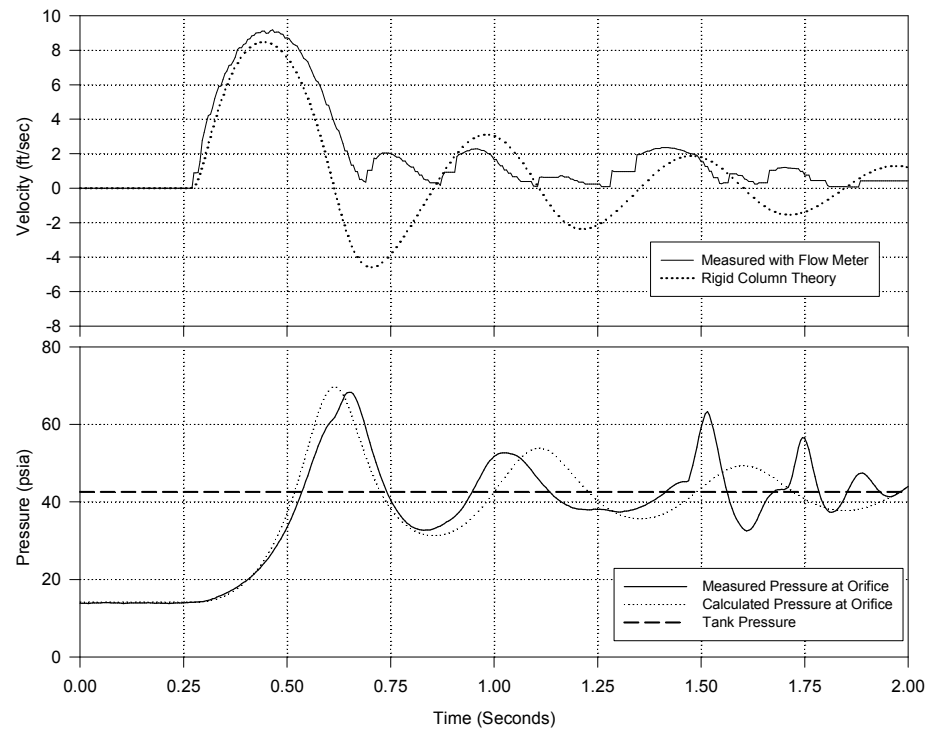


Figure D.29 Venting Analysis for  $L_A = 2.77$  ft ( $\alpha_0 = 0.1217$ ) ;  $P_R = 3$  ;  $d = 1/16$  Inch

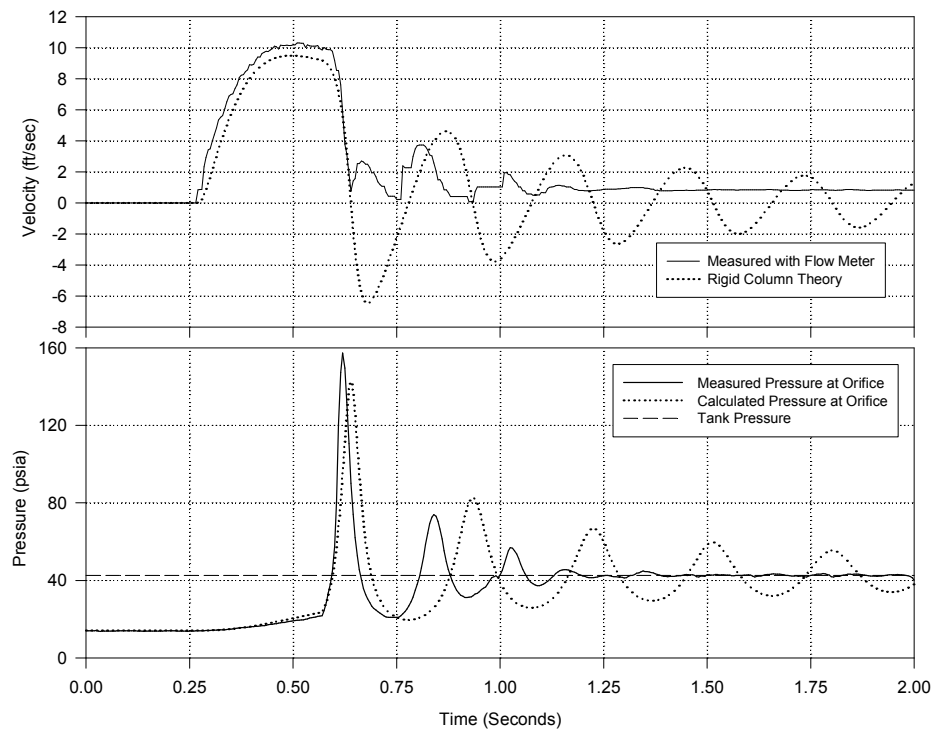


Figure D.30 Venting Analysis for  $L_A = 2.77$  ft ( $\alpha_0 = 0.1217$ ) ;  $P_R = 3$  ;  $d = 1/8$  Inch

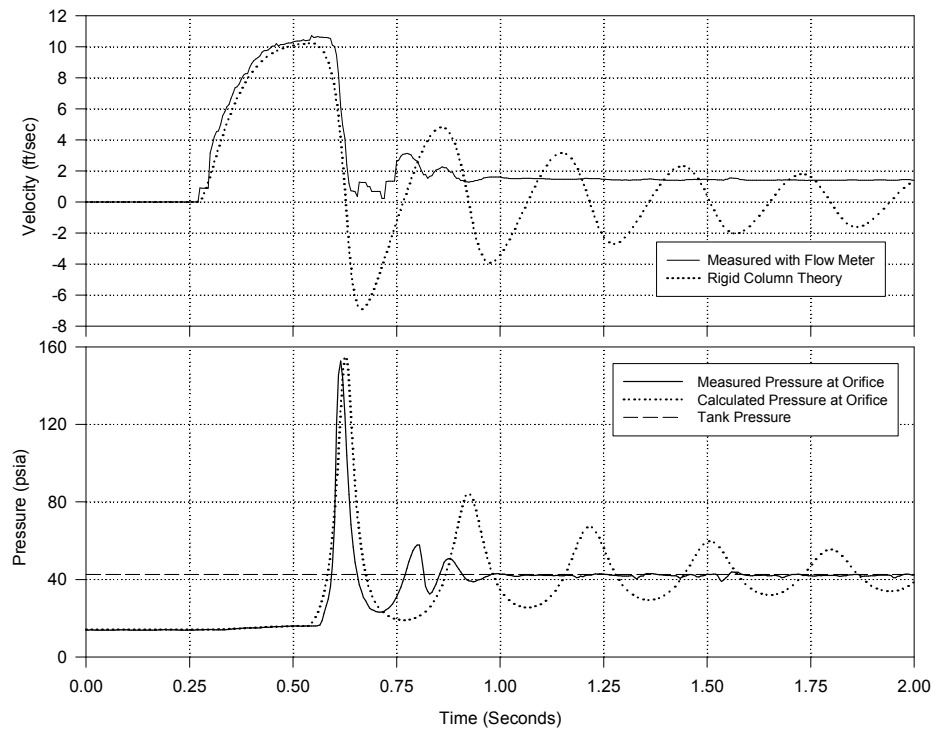


Figure D.31 Venting Analysis for  $L_A = 2.77$  ft ( $\alpha_0 = 0.1217$ ) ;  $P_R = 3$  ;  $d = 3/16$  Inch

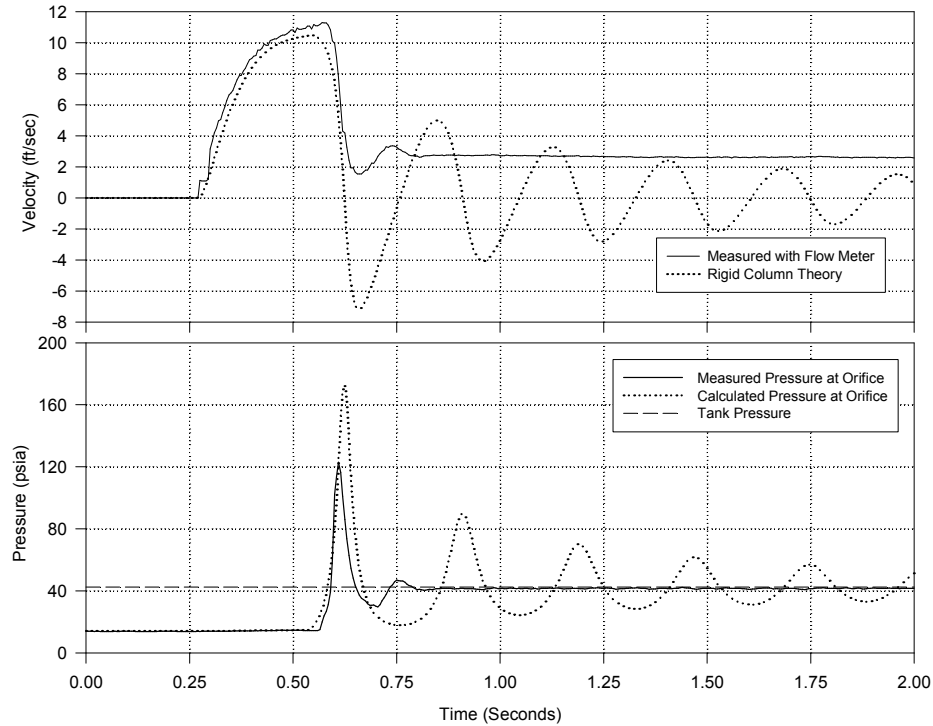


Figure D.32 Venting Analysis for  $L_A = 2.77$  ft ( $\alpha_0 = 0.1217$ ) ;  $P_R = 3$  ;  $d = 1/4$  Inch

## REFERENCES

- Abramowitz, M., and Stegun, I. A. (1964). "Handbook of Mathematical Functions", National Bureau of Standards, Applied Mathematics No. 55, Washington, D. C.
- Albertson, M.L. and Andrews, J. S. (1971). "Transients Caused by Air Release", Control of Flow in Closed Conduits (Edited by J.P. Tullis), Colorado State University, pp 315-340.
- Agudelo, J. F. (1988). "Entrapped Air in Water Pipelines", *Special M. S. Research Report*, School of Civil Engineering, Georgia Institute of Technology, 41 pages.
- Anderson J. D. (1960). "Modern Compressible Flow With Historical Perspective", McGraw-Hill.
- Atkinson K.E. (1989). "An Introduction to Numerical Analysis", John Wiley & Sons.
- Cabrera, E. *et al* .(1991). "Boundary Between Elastic and Inelastic Models in Hydraulic Transients Analysis with Entrapped Air Pocket", 9th Round Table of IAHR Group on Hydraulic Transients with Water Column Separation, Valencia, September, pp 159-179.
- Cabrera, E. *et al* .(1992). "Influence of Liquid Length Variation in Hydraulic Transients", *Journal of Hydraulic Engineering*, ASCE, Vol. 118, No. 12, pp 1639-1650.
- Conte S. D. (1980). "Elementary Numerical Analysis an Algorithmic Approach", McGraw-Hill.
- Edwards, D. G. and Farmer, G.P. (1984). "A Study of Piston-Water Impact in an Impulsive Water Cannon", *Seventh International Conference on Jet Cutting Technology*, Ottawa, Canada, BHRA, Paper D1-163-178.
- Ghidaoui, M.S. and Karney, B.W. (1994). Discussion on "Influence of Liquid Length Variation in Hydraulic Transients," *Journal of Hydraulic Engineering*, ASCE, 118(12), 661-666.

- Graze, H.R. (1968). "A Rational Thermodynamic Equation for Air Chamber Design", *Proceedings of the Third Australian Conference on Hydraulics and Fluid Mechanics*, Sydney, Australia, pp 57 - 61.
- Graze, H.R. (1972). "The Importance of Temperature in Air Chamber Operations", *First International Conference on Pressure Surges*, University of Kent, Canterbury, BHRA, Paper F2-13-20.
- Graze, H.R. (1996). "Thermodynamic Behavior of Entrapped Air in an Air Chamber", *Seventh International Conference on Pressure Surges*, BHR Group, Harrogate, England, pp 549-560.
- Griffiths, P.T.A. (1972). "Surge Problems of the Hydro-Electric Commission of Tasmania", *First International Conference on Pressure Surges*, Canterbury, England, BHRA, Paper E5-73-82.
- Guara, R. et al. (1996). "Dynamic Compression of Entrapped Air Pockets by Elastic Water Columns", 17th IAHR Symposium on Hydraulic Machinery, Valencia, Vol. II, pp. 710-719.
- Hashimoto, K. et al. (1988). "Transients of Fluid Lines Containing an Air Pocket or Liquid Column", *Journal of Fluid Control*, Vol. 18, No. 4, pp 38 - 54.
- Jönsson, L. (1985). "Maximum Transient Pressures in a Conduit with Check Valve and Air Entrainment", *International Conference on pumping Stations*, Manchester, England, Paper 55-76
- Kinsler L. E. and Frey A. R. (1962). "Fundamentals of Acoustics", John Wiley & Sons.
- Kitagawa A. (1979)."A Method of Absorption for Surge Pressure in Conduits", Bulletin of the JSME, Vol. 22, No. 165, pp 348-355.
- Lee, Nahm and Martin, C. S. (1999). "Experimental and Analytical Investigation of Entrapped Air in a Horizontal Pipe", Proceedings of the 3rd ASME/JSME Joint Fluids Engineering Conference, San Francisco, California.

McAdams W. H. (1954). "Heat Transmission", McGraw-Hill.

Martin, C. S. (1976). "Entrapped Air in Pipelines", *Second International Conference on Pressure Surges*, London, England, BHRA, Paper F2-15-28.

Martin, C. S. (1993). "Pressure Wave Propagation in Two-Component Flow", NATO Advanced Study Institute on Computer Modeling of Free Surface and Pressurized Flows, Washington State University, Pullman, Washington, pp 1- 33.

Martin, C. S. (1996). "Two-Phase Gas-Liquid Experiences in Fluid Transients", *Seventh International Conference on Pressure Surges*, BHR Group, Harrogate, England, pp 65-81.

Martin, C. S. and Lee, Nahm H. (2000). "Rapid expulsion of Entrapped Air Through an Orifice", 8th International Conference on Pressure Surges, The Hague, The Netherlands, BHR.

Moody, F. J. (1990). "Introduction to Unsteady Thermofluid Mechanics", John Wiley & Sons.

Munson B. R., Young D. F., and Okiishi T. H. (1990). "Fundamentals of Fluid Mechanics", Wiley.

Nakagawa, M. and Takenaka, T. (1993). "Damping and Peak Period Shortening of a Waterhammer in Collapse of a Cooling Cavity", Vol. 59, *Nippon Kikai Gakkai Ronbunshu B. Hen.*, Vol. 59 No. 559, pp 157 - 162.

Nakagawa, M. and Takenaka, T. (1993). "Waterhammer in Quick Opening of a Closed Pipe with a Cooling Cavity", JSME International Journal, Series B, Vol 36, No. 2, pp 261-265

Nakagawa, M. and Takenaka, T. (1994). "Modeling and Analysis of a Waterhammer in Collapse of a Cooling Cavity including Heat Transfer", Vol. 60, *Nippon Kikai Gakkai Ronbunshu B. Hen.*, Vol. 60, No. 570, pp 357 - 365.

Norman, T. and Sorenson, S.C. (1996). " A Simulation of the Influence of Air Cavities in a Pipeline", *Seventh International Conference on Pressure Surges*, BHR Group, Harrogate, England, Paper 265-280.

Ocasio, J. A. (1976). "Pressure Surging Associated with Pressurization of Pipelines Containing Entrapped Air", *Special M. S. Research Report*, School of Civil Engineering, Georgia Institute of Technology, 67 pages.

Parmakian, J. (1963). "Waterhammer Analysis", Dover.

Paynter, H.M. (1961). "Fluid Transients in Engineering Systems", Chapter 20, *Handbook of Fluid Dynamics*, McGraw Hill.

Prandtl and Tietjens (1957). "Fundamentals of Hydro- and Aeromechanics", Dover.

Qui, D. Q. and Burrows, R. (1996). "Prediction of Pressure Transients with Entrapped Air in a Pipeline", *Seventh International Conference on Pressure Surges*, BHR Group, Harrogate, England, Paper 251-263.

Sarpkaya, T.M. (1962). "Unsteady Flow of Fluids in Closed Systems", *Journal of Engineering Mechanics Division*, ASCE, Vol. 88, No. EM3, pp 1 - 15.

Safwat, H.H. (1972). "Experimental Study of Pressure Surges in Condenser Cooling Water Systems", *First International Conference on Pressure Surges*, Canterbury, England, BHRA, Paper D2-17-32.

Thorley, A. R. D. and Main, B.G. (1986). "Spontaneous Combustion in Vapor Cavities Subjected to Fluid Transients in Pipelines", *Fifth international Conference on Pressure Surges*, Hannover, F. R. Germany, BHRA, Paper 139-147.

Thorley, A. R. D. and Spurrett, R. P. (1990). "Cavity Dynamics and the Risk of Explosive Combustion in Pipelines", *Sixth international Conference on Pressure Surges*, Cambridge, England, BHRA, Paper 357-370.

Thornton, R E. (1983). "High Gas Temperatures Associated with Pressure Surges in a Pipeline", *Fourth international Conference on Pressure Surges*, Bath, England, BHRA, Paper B2-59-76.

Watters G. Z. (1980). "Modern Analysis and Control of Unsteady Flow in Pipelines", Ann Arbor Science.

Wylie E. B. and Streeter V. L. (1993). "Fluid Transients in Systems", Prentice Hall.

Zhao, T. *et al.* (2005). "On the Effect of Trapped Air in a Liquid Conduit on the Transient Flow Rate", Bulletin of the JSME, Vol. 28, No. 242, pp 1603-1609.

## **VITA**

Nahm Lee was born in Seoul, Korea, on September 2, 1960. After he graduated Dongguk University at Seoul, Korea, he worked as a scientific software developer for two years. He decided to study further in the United States. He entered the Graduate School of The Georgia Institute of Technology in March 1991. He continued to study as a doctoral student after receiving Master degree. During the academic years of 1993 and 2001 he worked as a teaching assistant and a research assistant. Currently he is working for Santa Clara Valley Water District in San Jose California as a civil engineer since July 2001.